Probing the Early Phase of High Energy Heavy Ion Collisions with ϕ Meson and Correlations at RHIC

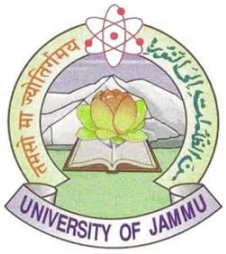

by

Mukesh Kumar Sharma

Post Graduate Department of Physics & Electronics

University of Jammu, Jammu Tawi

J&K - 180006 (INDIA)

A

THESIS

SUBMITTED TO THE UNIVERSITY OF JAMMU

FOR

THE AWARD OF THE DEGREE OF

DOCTOR OF PHILOSOPHY

IN

PHYSICS

(September 2015)

Dedicated

To

My Loving Family

DECLARATION

I, **Mukesh Kumar Sharma**, declare that the work reported in this thesis entitled "Probing the Early Phase of High Energy Heavy Ion Collisions with ϕ Meson and Correlations at RHIC" has entirely been done by me under the supervision of Prof. Anju Bhasin in the Department of Physics and Electronics, University of Jammu, Jammu. No part of this work has been submitted in part or full for the award of the degree in any other University.

Dated: **Mukesh Kumar Sharma**

POST GRADUATE DEPARTMENT OF PHYSICS & ELECTRONICS

UNIVERSITY OF JAMMU, JAMMU TAWI - 180006

CERTIFICATE

It is certified that **Mr. Mukesh Kumar Sharma**, worked under my supervision and the work is worthy of consideration for the award of Ph.D Degree in Physics. It is further certified that:

1. the thesis embodies the work of the candidate himself;
2. the candidate worked under my supervision for the period required under statutes;
3. the candidate has put in the required attendance during that period in the Department;
4. the conduct of the candidate remained satisfactory during that period;
5. the candidate has fulfilled the statutory conditions as laid down in Section 18 of statutes governing degree of Doctor of Philosophy issued vide notification no. 4 dated 04-03-2013.

(**Prof. Vivek K. Gupta**)
Head of the Department

(**Prof. Anju Bhasin**)
Supervisor

List of Publications/Preprints

[1] **A Review on ϕ Meson Production in Heavy-Ion Collision.**

Md. Nasim, Vipul Bairathi, Mukesh Kumar Sharma, Bedangadas Mohanty and Anju Bhasin

Advances in High Energy Physics (197930) 2015.

[2] **Higher harmonic flow of ϕ meson in STAR at RHIC.**

Mukesh Kumar Sharma (for the STAR collaboration)

Proceedings for the "7^{th} International Conference on Physics and Astrophysics of Quark Gluon Plasma". Submitted in Proceedings of Science (2015).

[3] **Effect of event selection on jetlike correlation measurement in d+Au collisions at $\sqrt{s_{NN}}$ = 200 GeV.**

L. Adamczyk, ... **Mukesh Kumar Sharma**, ... et al., (for the STAR Collaboration).

Phys. Lett. B **743**, 333-339 (2015).

[4] **Charged-to-neutral correlation at forward rapidity in Au+Au collisions at $\sqrt{s_{NN}}$ = 200 GeV.**

L. Adamczyk, ... **Mukesh Kumar Sharma**, ... et al., (for the STAR Collaboration).

Phys. Rev. C **91**, 034905 (2015).

[5] **$\Lambda\Lambda$ Correlation Function in Au+Au collisions at $\sqrt{s_{NN}}$ = 200 GeV.**

L. Adamczyk, ... **Mukesh Kumar Sharma**, ... et al., (for the STAR Collaboration).

Phys. Rev. Lett. **114**, 022301 (2015).

[6] **Centrality and transverse momentum dependence of elliptic flow of multi-strange hadrons and ϕ meson in Au+Au collisions at $\sqrt{s_{NN}}$ =**

200 GeV.

L. Adamczyk, ... **Mukesh Kumar Sharma**, ... et al., (for the STAR Collaboration).

e-Print:arxiv:1507.05247, July (2015)

[7] **Beam-Energy Dependence of Charge Balance Functions from Au+Au Collisions at RHIC.**

L. Adamczyk, ... **Mukesh Kumar Sharma**, ... et al., (for the STAR Collaboration).

e-Print:arxiv:1507.03539, July (2015)

[8] **Probing Parton Dynamics of QCD Matter with Ω and ϕ Production.**

L. Adamczyk, ... **Mukesh Kumar Sharma**, ... et al., (for the STAR Collaboration).

e-Print:arxiv:1506.07605, June (2015)

[9] **Azimuthal anisotrophy in U+U and Au+Au collisions at RHIC.**

L. Adamczyk, ... **Mukesh Kumar Sharma**, ... et al., (for the STAR Collaboration).

e-Print:arxiv:1505.07812, June (2015)

[10] **Observation of charge asymmetry dependence of pion elliptic flow and the possible chiral magnetic wave in heavy-ion collisions.**

L. Adamczyk, ... **Mukesh Kumar Sharma**, ... et al., (for the STAR Collaboration).

Published in Phys. Rev. Lett. **114** (2015) 25, 252302

[11] **Measurements of Dielectron Production in Au+Au Collisions at $\sqrt{s_{NN}}$ = 200 GeV from the STAR Experiment.**

L. Adamczyk, ... **Mukesh Kumar Sharma**, ... et al., (for the STAR Collaboration).

Published in Phys. Rev. C **92** (2015) 2, 024912

[12] **Leptonic decay of the ϕ(1020) meson in Au+Au collisions at $\sqrt{s_{NN}}$ = 200 GeV measured with the STAR experiment.**

L. Adamczyk, ... **Mukesh Kumar Sharma**, ... et al., (for the STAR Collaboration).

e-Print:arXiv:1503.04217 March (2015).

[13] **Long-range pseudorapidity dihadron correlations in d+Au collisions at $\sqrt{s_{NN}}$ = 200GeV.**

L. Adamczyk, ... **Mukesh Kumar Sharma**, ... et al., (for the STAR Collaboration).

Published in Phys. Lett. B **747** (2015) 265-271

[14] **Energy dependence of acceptance-corrected dielectron excess mass spectrum at mid rapidity in Au+Au $\sqrt{s_{NN}}$ 19.6 and 200 GeV.**

L. Adamczyk ..... **Mukesh Kumar Sharma**, ... et al., (for the STAR Collaboration).

Published in Phys. Lett. B **750** (2015) 64-71

[15] **Constraining Sea Quark Distributions Through $W^{\pm}$ Cross Section Ratios Measured at STAR.**

M. Posik ..... **Mukesh Kumar Sharma**, ... et al., (for the STAR Collaboration).

e-print:arXiv:1507.07854 July (2015).

[16] **Measurement of longitudinal single-spin asymmetries for $W^{\pm}$ boson production in polarized p+p collisions at $\sqrt{s_{NN}}$=510 GeV at STAR.**

Devika Gunarathne ..... **Mukesh Kumar Sharma**, ... et al., (for the STAR Collaboration).

e-Print:arXiv:1507.07835 January (2015).

[17] **Measurement of interaction between antiprotons.**

Richard Witt.....**Mukesh Kumar Sharma**, ... et al., (for the STAR Collaboration).

e-Print:arXiv:arXiv:1507.07158 July (2015)

[18] **Baryon Resonances in the STAR Experiment at RHIC.**

L. Adamczyk ..... **Mukesh Kumar Sharma**, ... et al., (for the STAR Collaboration).

Published in EPJ Web Conf. 97 (2015) 00031.

[19] **K^{*0}(892) and ϕ(1020) resonance production at RHIC**

Lokesh Kumar ..... **Mukesh Kumar Sharma**, ... et al., (for the STAR Collaboration).

Published in EPJ Web Conf. 97 (2015) 00017

[20] **Quarkonia production in the STAR experiment.**

Barbara Trzeciak..... **Mukesh Kumar Sharma**, ... et al., (for the STAR Collaboration).

Published in EPJ Web Conf. 95 (2015) 04070

[21] **Pion-kaon femtoscopy in Au+Au collisions at STAR.**

Katarzyna Poniatowska ..... **Mukesh Kumar Sharma**, ... et al., (for the STAR Collaboration).

Published in EPJ Web Conf. 95 (2015) 04051

[22] **Spin physics highlights from STAR.**

(A. Gibson ..... **Mukesh Kumar Sharma**, ... et al., (for the STAR Collaboration).

Published in EPJ Web Conf. 95 (2015) 03013

[23] Overview of results from phase I of the Beam Energy Scan program at RHIC.

(Daniel McDonald ..... **Mukesh Kumar Sharma**, ... et al., (for the STAR Collaboration).

Published in EPJ Web Conf. 95 (2015) 01009

[24] Pion-kaon femtoscopy in Au+Au collisions at STAR.

(Katarzyna Poniatowska ..... **Mukesh Kumar Sharma**, ... et al., (for the STAR Collaboration).

Published in J. Phys. Conf. Ser. 612 (2015) 1, 012045

[25] Measurement of Υ production in p+p collisions at $\sqrt{s}_{NN}$ = 500 GeV in the STAR experiment.

(Leszek Kosarzewski ..... **Mukesh Kumar Sharma**, ... et al., (for the STAR Collaboration).

Published in J. Phys. Conf. Ser. 612 (2015) 1, 012022

[26] Directed Flow of Charged Kaons in Au+Au Collisions from the BES Program at RHIC.

(Yadav Pandit ..... **Mukesh Kumar Sharma**, ... et al., (for the STAR Collaboration).

Published in J. Phys. Conf. Ser. 636 (2015) 1, 012001

[27] STAR results on central exclusive production in proton-proton collisions.

Mariusz Przybycien ..... **Mukesh Kumar Sharma**, ... et al., (for the STAR

Collaboration).

Published in AIP Conf. Proc. 1654 (2015) 040006

[28] **Observation of Transverse Spin-Dependent Azimuthal Correlations of Charged Pion Pairs in p+p at $\sqrt{s}_{NN}$ =GeV.**

(L. Adamczyk ..... **Mukesh Kumar Sharma**, ... et al., (for the STAR Collaboration).

e-Print: arXiv:1504.00415

[29] **Upgrade of the STAR Silicon Detectors.**

(Michal Szelezniak ..... **Mukesh Kumar Sharma**, ... et al., (for the STAR Collaboration).

Published in PoS Vertex 2014 (2015) 015

[30] J/ψ **measurements in the STAR experiment.**

(Barbara Trzeciak ..... **Mukesh Kumar Sharma**, ... et al., (for the STAR Collaboration).

e-Print: arXiv:1412.7345

[31] J/ψ **and** ψ**(2S) measurement in p+p collisions at** $\sqrt{s}_{NN}$**= 200 and 500 GeV in the STAR experiment.**

(Barbara Trzeciak ..... **Mukesh Kumar Sharma**, ... et al., (for the STAR Collaboration).

Published in J. Phys. Conf. Ser. 612 (2015) 1, 012038

[32] **Higher harmonic flow of** ϕ **meson in STAR at RHIC.**

Mukesh Kumar Sharma (for the STAR collaboration)

Proceedings of the XXI DAE-BRNS HEP Symposium, Guwahati. Published in Springer Proceeding in Physics (2015)

[**33**] **Measurement of higher harmonic flow of ϕ meson in STAR at RHIC.**

Mukesh Kumar Sharma (for the STAR Collaboration)

XXIV QUARK MATTER Poster Presentation, DARMSTADT (2014)

ACKNOWLEDGEMENT

First and foremost I would like to thank God. You have given me the power to believe in my passion and pursue my dreams. I could never have completed this thesis without the faith I have in you, the Almighty. Thank you for the strength and courage you provided me.

I would like to express my sincere appreciation to my supervisor Prof. Anju Bhasin for her guidance and support throughout my research period. Her wide knowledge and her logical way of thinking have been of great value for me. She guided me through the adventure of research with her inspiring ideas, patience in mentoring, prudent attitude towards data analysis, and critical feedback on the results.

My regardful thanks are due to Prof. Vivek Gupta, Head, Department of Physics & Electronics, University of Jammu, for providing me the necessary infrastructure, help, support and other facilities required for carrying out my research work.

I extend my heartfelt thank to Prof. Sanjeev Singh Sambyal for his valuable guidance, encouragement and support during the period of my research work.

I would also like to thank Er. Anik Gupta (Scientist G) for his kind support, encouragement during my stay in HEP Group.

I would like to take this opportunity to express my sincere and heartfelt thanks to Dr. Bedangadas Mohanty, Associate Professor, National Institute of Science Education and Research, Bhubaneswar, for his timely help in the completion of my analysis work. Had he not allowed me to work in his group, this thesis work would never be possible. I have learnt a lot from him, not only about physics but also about life in general. I also express my sincere gratitude to Dr. Lokesh Kumar, Assistant Professor, Panjab University, Chandigarh, for his valuable guidance, timely help and for assisting me in the analysis work and helped me see it through to its completion.

I am also thankful to the STAR team leaders, Dr. Nu Xu, former Spokesperson

and Dr. Zhangbu Xu, present Spokesperson for providing me a great opportunity to work at Brookhaven Lab, USA and helping me in excelling in this field of science.

I would like to thanks Dr. Md. Nasim and Mr. Shikshit Gupta for introducing me about the STAR analysis frame work and lots of physics discussions.

I am also thankful to other members of Jammu HEP Group; viz. Dr. Ramni Gupta, Dr. P.V.K.S Baba, Er. Sanjay Mahajan and Dr. Saroj Nayak for their good wishes.

I take this opportunity to thank all the faculty members of Department of Physics & Electronics, University of Jammu for their support and guidance.

I wish to thank all the members of the RCF at BNL, VECC grid, NERSC center at LBNL and HEP grid, Jammu University for providing the computing resources and help.

I am extremely thankful to my India-ALICE collaborators, Dr. Y. P. Viyogi, Dr. Subhasis Chattopadhyay and Dr. T. K. Nayak of VECC, Kolkata, Prof. P. K. Sahu of IOP, Bhubaneswar, Prof. M. M. Aggarwal of Panjab University, Chandigarh, Prof. Raghav Varma and Dr. B. K. Nandi of IIT Bombay, Prof. Sudhir Raniwala and Dr. Rashmi Raniwala of Rajasthan University, Jaipur for their suggestions, physics discussions during my research work.

I also wish to thank whole STAR Collaboration with particular emphasis on members of the Bulk-Correlation group for their productive suggestions, discussions during the meetings and conferences.

I am also thankful to my collaborative friends and seniors Dr. Chitrasen Jena, Dr. M. M. Mondal, Dr. Natasha Sharma , Dr. Nihar Ranjan Sahoo, Dr. Md. Nasim, Dr. Sudipan De, Ms. Sabita Das, Dr. Subhash Singha, Dr. Rihan Haque, Mr Vipul Bairathi, Mr. Kishora Nayak, Dr. Prakhar Garg, Mr. Arindam and Mr. Srikanta for their kind help and fruitful discussions.

I also offer my sincere gratitude to Dr. Renu Bala, CSIR SRA (Pool Officer), Jammu University and for their help and encouragement during my research period.

Deep regards to my seniors Dr. Satish Sharma, Dr. Ranbir Singh, Mr. Shikshit Gupta for their help, good wishes and kind support towards me. I am also very thankful to my seniors Dr. S. M. Dogra, Dr. Chaman Lal and Dr. Ramesh Sachdeva for their support at every stage of the work.

My special thanks go to my senior Dr. Ranbir Singh, Scientific Officer, NISER, Bhubaneswar, for introducing me to this field of experimental HEP and his help, immense support and encouragement during my research period.

I would also like to thank my best friends Mr. Arun Sharma, Mr. Ahsan Elahi, Mr. Rohit, Mr. Sandeep (Sandy), Capt. Prateek (Monty), Mr. Neeraj, Mr. Sahil, Mr. Atul, Mr. Arun (Chotu) and Mr. Piyush for their help, good wishes and kind support towards me.

I would like to express my loving regards and thanks to all HEP labmates-Mr. Inayat, Rohni, Jagjeet, Ankita, Sonia, Monika, Mandeep, Sakshi, Ajay and Sandeep for sharing such a good time with me and also for their keen affection, support, good wishes and help for me. Thanks are also due to Sahil, Iftar, Rakesh, Bhanu, Lakshmi, Abhinav, Mona and Shagun Siotra for their good wishes and regards. It was good time to spend with Abhinav at BNL during the STAR Experimental Shifts.

I sincerely thank all the members of technical and non-technical staff of HEP Group, especially Mr. Vivek Chalotra, Mr Satpaul, Mr. Surinder, Mrs. Rita Sharma, Mrs. Anju Kapoor, Mrs. Neelam Sharma, Mr. Tarseem, Mr. Ravi, Mr. Ravinder Sharma and Gaja Singh for their affection and kind co-operation.

I would also like to thank Department of Science & Technology (DST), Government of India for providing me financial assistance during my research work.

Last but most importantly, I would like to express my due respect and sincere

thanks to my parents for their immense patience and encouragement. Without their love and support, this thesis would not have been possible. I'll never forget the continue support and understanding from my brothers and Bhabi's; Manoj Sharma (bhai), Shivam, Sunny, Sahil, Ankush and Sachin, Meena Sharma (Bhabi), Simta Sharma (Bhabi), Sneh Sharma (Bhabi) and my sisters and Jiju's; Anita (Neetu) & Vinod Sudan, Vandana (Popli) & Vinod Raina, Nishu & Akshaya Vasishth, Seema & Gourav Taneja, Arti Gupta, Shilpa and Shikha. I am also very thankful to my elder brothers Mr. Navneet Sudan (Vicky), Mr. Manoj Sharma (Lovely), Mr. Amit Sudan (Sonu), Mr. Dushyant Sudan (Bittu), Vinod Sudan (Rinku) and Madan Bhai for their good wishes. Let me express my heart felt thanks to my fiancee (Indu) for her continuous and unwavering support and encouragement during the later stages of my Ph.D work. Finally, I would like to venerate GuruJi, the Almighty for his benevolence, thanks galore for seeing me through the trials and tribulations of life till now.

Deepest gratitude to everyone ! Thank You !

Mukesh Kumar Sharma

Contents

List of Figures

List of Tables

ABSTRACT

Title of Thesis : Probing the Early Phase of High Energy Heavy Ion Collisions with ϕ Meson and Correlations at RHIC

The Universe went through a series of phase transitions after the Big Bang. These transitions mark the most important epochs of expanding universe after the Big Bang. At 10^{-11} secs and a temperature T $\sim$ 100 GeV ($\sim 10^{10}$ K), the electroweak transition took place where most of the elementary particles acquired their masses through Higg's mechanism. At 10^{-5} secs and T $\sim$ 200 GeV ($\sim 10^{12}$ K), the strong phase transition took place where the quarks and gluons become confined into hadrons and where the approximate chiral symmetry was spontaneously broken. Quarks are not observed as free particles and are confined in hadrons by the inter quark potential. Baryons are made up of three quarks and mesons consist of a quark-antiquark pair. Deep-inelastic electron scattering experiments showed that constituent quarks have fractional electric charges, $+2/3$ or $-1/3$, and carry effective mass (m) of about one third of the nucleon mass and only half of the nucleons momentum. It was proposed that the other half of the nucleons momentum is ascribed to the force carriers called gluons which are responsible for the inter quark binding. These quanta are called gluons, since they serve to "glue" quarks together. Gluons themselves also carry colour which permits them also to interact among themselves, a property which is believed to ultimately be responsible for confinement. The resulting fundamental theory describing the strong interaction between quarks is called Quantum Chromo Dynamics(QCD). In anology to QED the elementary particles having quark and antiquarks interact via a bosonic gauge fields. Although the fundamental degress of freedom (quarks and gluons) cannot be observed as free particles but the QCD Lagrangian is well established.

One of the key features of QCD is self coupling of the gluons which cause the

coupling constant to increase with decreasing momentum transfer. This gives rise to asymptotic freedom and confinement at large and small momentum transfer respectively. At small momentum transfer non-perturbative corrections become important but are hard to calculate and thus the two important non-perturbative properties of QCD viz. *Confinement* and *Chiral Symmetry* breaking are still poorly understood from first principles.

One of the key questions in QCD phenomenology is what are the properties of matter at extreme temperature and densities where quarks and gluons are in deconfined state, known as the Quark Gluon Plasma (QGP). Basic arguments allow us to estimate the energy density $\epsilon \sim 1$ GeV$/fm^3$ and temperature T ~ 200 GeV at which the strong phase transition takes place, which implies that this occurs in the regime where coupling constant is large and thus one cannot rely on perturbative QCD. Better understanding of the non-perturbative domain comes from lattice QCD calculation, which provide's information on QCD transition and Equation of State (EoS) of the deconfined state. The ultra-relativistic heavy-ion collisions provide an indispensable laboratory for investigating the behavior of nuclear matter under extreme conditions of temperature and pressure as these exist a few moments after the "Big Bang". In these collisions very hot and dense nuclear matter is produced having an estimated temperature of about trillion degrees and density several times higher than that of normal nuclear matter. Under these conditions, a phase transition is believed to occur leading to the "deconfinement" of partons, a state where quarks and gluons are no longer bound in individual hadrons but instead can freely move inside the whole interaction region and form a QGP. Thus one can create and study hot QCD matter and its phase transition under controlled conditions. As in the early universe, this hot and dense matter created in heavy-ion collisions will expand and cool down. During this evolution the system probes a range of energy densities and

temperatures, and possibly different phases.

The Relativistic Heavy Ion Collider (RHIC) is the first machine in the world capable of colliding heavy-ions as well as nucleons and its complex is composed of long chain of particle accelerators and detectors. Its main purpose is to study the nuclear matter under extreme conditions of temperature and density. The RHIC accelerated heavy-ions up to 100 A GeV, and based upon results in the first few years, RHIC later planned a Beam Energy Scan programme to accelerate heavy-ions at various energies (from 7.7 A GeV to 39 A GeV) to search for the critical point of the QCD phase diagram. Besides, RHIC, there are various other experiments world wide viz. SPS, LHC at CERN Geneva, FAIR at GSI, Germany etc. serving in their own specified objectives pertaining to the field of high energy physics.

This thesis work pertains to data collected by the Solenoidal Tracker At RHIC (STAR) detector at the RHIC accelerator facility. Three other experiments which are also part of the heavy-ion programme are; Pioneering High Energy Nuclear Interaction eXperiment (PHENIX), Broad RAnge Hadron Magnetic Spectrometer (BRAHMS) and PHOBOS. STAR is designed primarily for charged hadron production measurements with high precision tracking and momentum over a large solid angle. The whole detector is enclosed in a solenoidal magnet that provides a uniform magnetic field of 0.5 T parallel to the beam direction. The primary tracking device in the STAR is the Time Projection Chamber (TPC) which performs the role of 3-D camera capturing the images of the emitted sub-atomic particles.

The analysis work embodied in thesis is mainly based on data analysis of Au+Au and U+U collisions at $\sqrt{s}_{NN} = 200$ and 193 GeV collected by STAR in the year 2011 and 2012 respectively. The main aim of this work is to study the properties of the deconfined hadronic matter at a very high temperature produced by colliding the nuclei at ultra-relativistic high energies. One of the spectacular findings of RHIC was

that the matter generated in heavy-ion collisions flows like a liquid with very low internal resistance to the flow, almost at the limit of what is allowed for any material in nature. This tells us that the constituents of this matter are quite different from freely interacting quarks and gluons. This almost perfect fluid has been found to be opaque to even the most energetic partons (quarks and gluons), which appear as jets of particles from the collisions-an effect known as jet quenching. The physical mechanisms underlying these phenomena are not fully understood. The thesis work is divided into two parts:

In the first part of the thesis, the azimuthal anisotropy (Flow) of ϕ meson and the higher harmonic ratio in mid-rapidity region are studied. At such high temperature and energy densities in heavy-ion collisions, the quarks and gluons undergo multiple interactions and the system will thermalize and form QGP which subsequently undergoes a collective expansion and eventually becomes too dilute that it hadronizes. This collective expansion is called "Flow" which provides experimental information on EoS and the transport properties of the created QGP. The azimuthal anisotropy in particle production is the cleanest experimental signature of collective flow in heavy-ion collisions. The anisotropic flow is caused by the initial asymmetries in the geometric overlap of colliding nuclei in non-central collisions. This initial spatial asymmetry is converted via multiple interactions and the pressure gradient created into an anisotropic momentum distribution of the produced particles. The azimuthal anisotropy is usually characterized by the Fourier co-efficients given by v_n= $< \cos[n(\phi - \psi_n)]>$ where ϕ is the azimuthal angle of the particle, ψ_n is the angle of the initial state spatial plane of symmetry and n is the order of the harmonic. Since the hadronic interaction cross section of ϕ-meson is smaller than the other hadrons, its v_n coefficients remain almost unaffected by the later stage interactions. Therefore ϕ-meson v_n will reflect the collective motion of the partonic phase. This makes the

ϕ-meson a clean probe for the study of the properties of the matter created in heavy-ion collisions. The large magnitude of 2^{nd} harmonic called elliptic flow (v_2) observed at the RHIC and LHC provides compelling evidence for strongly interacting matter which appears to behave like an almost perfect fluid. Deviations from this ideal case are controlled by the ratio of shear viscosity to entropy density (η/s). Because the effect of shear viscosity is to dampen all the flow co-efficients, with a larger decrease for higher order co-efficient, it has been argued that the magnitude and transverse momentum dependence of the higher flow co-efficients (v_3, v_4, and v_5) is a more sensitive measure of η/s. The ratio v_4/v_2^2 is studied for ϕ meson. The ratio v_4/v_2^2 is proposed as a probe of ideal hydrodynamic behavior and it is directly related to the degree of thermalization.. We find that the ratio v_4/v_2^2 is greater than unity, which is larger than the ideal hydrodynamic prediction. This may be due to the fluctuation of the measured v_2 and v_4 and that may indicate the incomplete thermalization of the system.

Significant dynamic event-by-event fluctuations in apparent temperature, mean transverse momentum, multiplicity and conserved quantities as the net charge are predicted to be produced in the QGP phase created in heavy-ion collisions. In the second part, measurement of two charged particle transverse momentum correlations in U+U at $\sqrt{s}_{NN} = 193$ GeV is done. The study of event-by-event fluctuations provide evidence for the production of QGP in relativistic heavy-ion collisions. In this thesis, the results are compared with the published results of Au+Au and Cu+Cu collisions to study the system size dependence. The p_T correlation is an important tool to understand thermalization in heavy-ion collisions. The non-monotonic change in transverse momentum (p_T) correlations as a function of centrality has been proposed as a possible signal of the Quark Gluon Plasma (QGP) formation. The p_T correlations measured are finite and decreases with increase in number of participants. This

decrease in p_T correlations could be due to correlations being dominated from pair of particles coming from the same nucleon-nucleon collision which get diluted with increasing the number of participants. The p_T correlations scaled by dN/dη increases with collision centrality and then saturate in central U+U collision indicating the sign of thermalization. It is also observed that square root of p_T correlations scaled by mean p_T is independent of colliding ion size, but decrease with increase in collision centrality.

This thesis is divided into eight chapters and the brief contents of the chapters are :

Chapter 1 : In this chapter an introduction to basic particle physics is discussed in brief. An introduction to QGP and the theory for strong interaction, QCD and its phase diagram is given. The comparison of physics results of RHIC and LHC are also shown.

Chapter 2 : This chapter gives an overview of the Relativistic Heavy Ion Collider (RHIC) and will focus primarily on the STAR detector.

Chapter 3 : In this chapter the review of the measurements of ϕ-meson production in heavy-ion experiments is presented. The energy dependence of ϕ-meson invariant yield and the production mechanism, strangeness enhancement, parton energy loss, and partonic collectivity in nucleus-nucleus collisions are discussed. Effect of later stage hadronic re-scattering on elliptic flow (v_2) of proton is also discussed relative to corresponding effect on ϕ-meson v_2.

Chapter 4 : In this chapter the data set, various kinematical cuts like event cuts, track cuts and particle identification method are discussed. The invariant mass technique to reconstruct ϕ meson ($\phi \rightarrow K^+K^-$), event mixing technique to construct background are also discussed.

Chapter 5 : This chapter compiles all previous results on elliptical flow and the

various method to obtain ϕ-meson flow are discussed.

Chapter 6 : In this chapter different types of corrections for obtaining the final higher harmonics (v_n) are given. The detailed procedure of each correction is given along with their corresponding results. The final ϕ meson v_n as a function of p_T and centrality dependence in Au+Au collisions at $\sqrt{s}_{NN} = 200$ GeV is presented. In addition, the ϕ higher harmonic ratio and their possible implications are also discussed in this chapter.

Chapter 7 : The results of transverse momentum correlations for U+U collisions at $\sqrt{s}_{NN} = 193$ GeV are discussed in this chapter. These results are compared with the published results from Au+Au and Cu+Cu collisions at $\sqrt{s}_{NN} = 200$ GeV.

Chapter 8 : All the results presented in the thesis are summarized and concluded in this chapter. The implications of these results in the field of high energy heavy-ion collision experiments are also discussed.

Chapter 1

Introduction to high energy physics

1.1 Introduction to Strangeness

A relatively simple picture of elementary particles emerged with the discovery of the pion in 1947. However, this simple interpretation did not go unchallenged for long. In the same year, two cloud-chamber pictures of cosmic rays, obtained by Rochester and Butler [1], indicated the decay of neutral particles. One of the pictures showed a "V-track", indicating the decay of a neutral particle into two charged particles. The other picture showed a track with a kink, indicating the decay of a charged particle into another charged particle and a neutral.

In 1953, the Cosmotron, went into operation at the Brookhaven National Laboratory (BNL) in USA which was capable of producing the new particles. This machine permitted a systematic study of the particle production and decay reactions. Both the cosmic-ray experiments and those done at the accelerators showed the decay lifetimes of the new particles to be on the order of 10^{-10} sec, extremely long compared to the particle production time of 10^{-23} sec. To account for this descrepancy, Pais [2] suggested the concept of associated production. This concept was formalized by Gellmann and Nishijima [3] with the introduction of a "strangeness" quantum number.

1.1.1 Role of strangeness in Quark Gluon Plasma

Strangeness has been linked to studies of the Quark Gluon Plasma[1]. The existence and behaviour of the QGP phase transition is linked to the mass of the strange quark [4]. As its dynamical mass is somewhat higher than the QGP phase transition temperature, and its bare mass somewhat below [5, 6], it plays a key role in determining the behaviour of the system close to the phase boundary. Strangeness, can be produced either in the first interactions of colliding matter, or in the many ensuing less-energetic collisions. The mass of the strange quark m_s is comparable in magnitude to the temperatures reached in heavy-ion interactions and the numerous "soft" collisions of secondary partons dominate the production of strangeness. The production of strangeness is a dynamical time dependent process. In the QGP, strangeness pair production is mainly due to gluon fusion processes, $gg \rightarrow s\bar{s}$, but light quarks also contribute $q\bar{q} \rightarrow s\bar{s}$. The QCD Feynmann diagrams for strangeness production are shown in Figure 1.1. All of these are annihilation processes, and so the threshold energy is simply the bare mass of strange quarks. The threshold energy is of the order of 300 MeV, but has since been reduced to roughly 100 MeV, strongly favouring thermal production in a system believed to have temperature $>$ 150 MeV. The impact of Pauli blocking can change the equilibration time slightly. As quarks are fermions, they are subject to Pauli exclusion [8], which states that two fermions cannot be in the same quantum state. This has little effect in pp collisions, but in heavy ion collisions where the quark densities are higher, production can be suppressed as the available energy levels fill up. Hwa and Yang have shown that this causes around 6% of quark-antiquark pairs to be created as strange quarks rather than light quarks when comparing the initial stages of a heavy ion collision to

[1] A deconfined state of matter which is beleived to exist at extreme temperature and density. It will be extensively explained in section 1.4

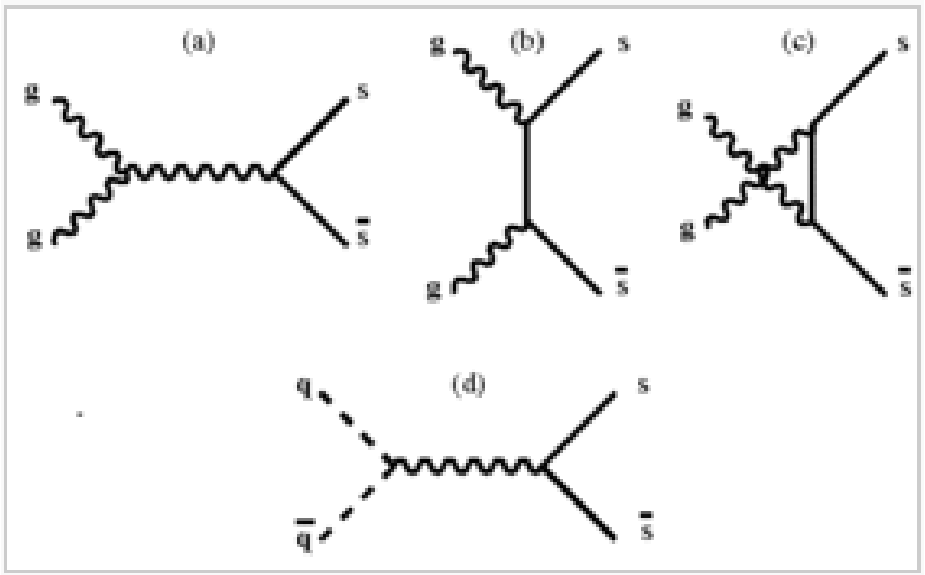

Figure 1.1: *QCD diagrams for $s\bar{s}$ production-Feynmann diagrams for (a-c) $gg \rightarrow s\bar{s}$ (d) $q\bar{q} \rightarrow s\bar{s}$ [7]*

a pp collision, slightly speeding the early stages of strange quark equilibration [9]. At higher temperatures, where strange quarks rapidly reach equilibrium, Pauli blocking of strange quarks can increase equilibrium time by around 10%. In 1982, Johann Rafelski and Berndt Muller suggested "strangeness enhancement" as a possible signature for the formation of a QGP in a heavy-ion collision [10] which is discussed in section 1.6.

1.2 Standard Model of particle physics

The Standard Model (SM) [11] of Particle Physics evolved throughout the 20th century due to a fertile interplay between fundamental theoretical developments and experimental input guiding the way. It describes the dynamics and interactions of all currently known elementary particles. SM classify elementary particles into two categories: *Fermions*, the particles that compose matter are characterized by an in-

trinsic angular momentum (spin) with a value equal to an half-integer multiple of the reduced planck constant. Fermions obey Fermi-Dirac statistics, which follows from the inability of two fermions to be in the same quantum state and the force mediators of the fundamental interactions, *gauge Bosons*, which have integral spin and follow Bose-Einstein statistics. Figure 1.2 shows the elementary particles described by the Standard Model. Fermions are composed of two families, each including six particles

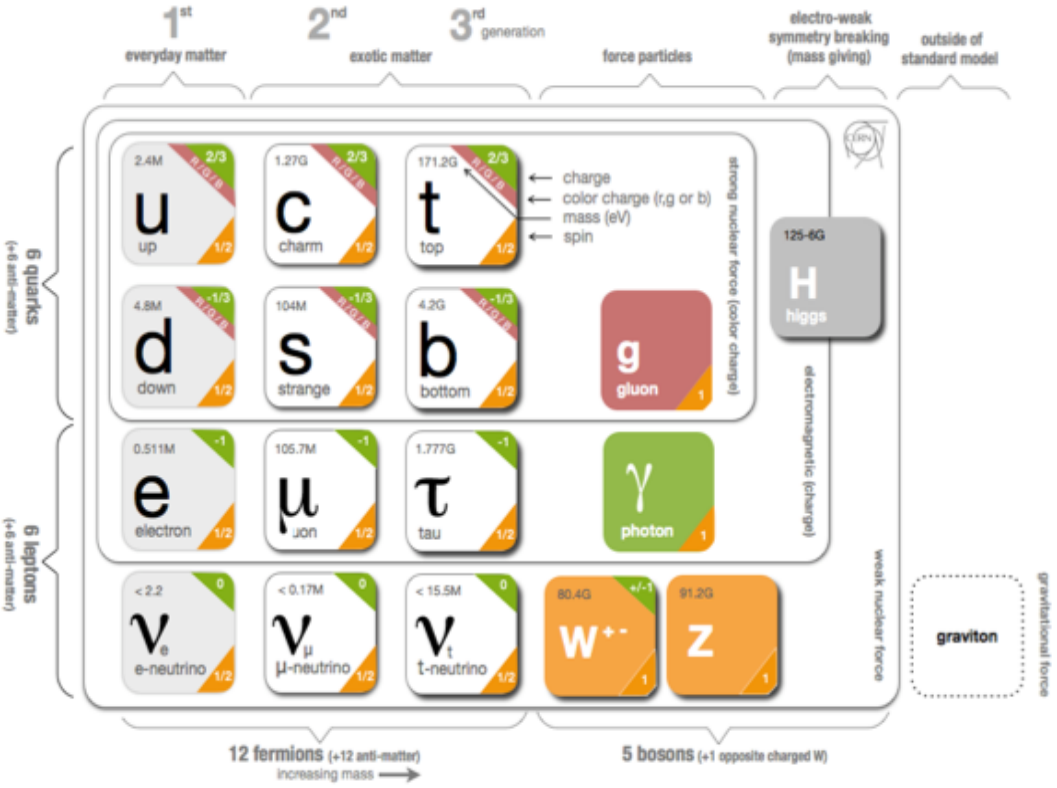

Figure 1.2: *Table of fundamental particles as described by the standard model, with the quantum numbers that characterize those particles*

spread in three generations as well as their antiparticles. The first family, leptons, do not participate directly in the strong interaction; it is composed of doublets of the quantum number called weak isospin, with the upper part of the doublets filled by electrons, muons and tau, which can interact via the electromagnetic and potentially

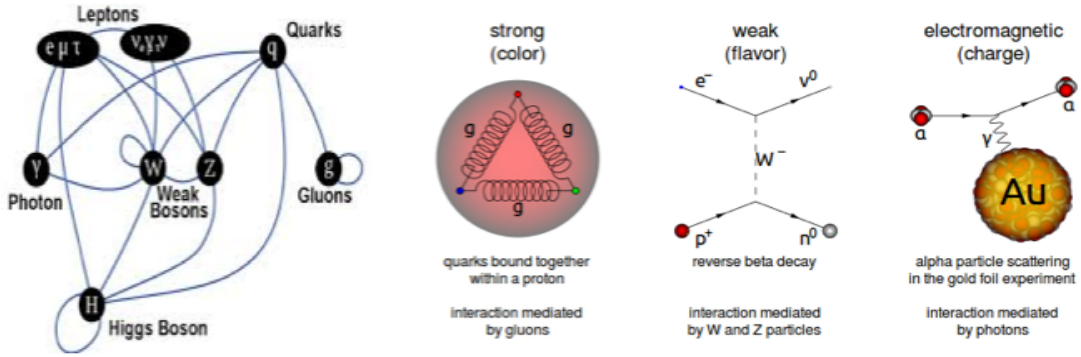

Figure 1.3: *Summary of interactions between particles (first), and characterization of strong (second), weak (third) and electromagnetic (fourth)*

weak interactions, depending on their handedness, and the lower parts are filled by their corresponding neutrinos, which are only sensitive to weak interactions. The other family, quarks, is composed of three generations of two quarks. Quarks carry a fractional electric charge and are thus sensitive to the electromagnetic interaction; they also participate in the weak and strong interactions.

The three fundamental interactions described by the model are called gauge bosons. Those three interactions are the electromagnetic interaction, the weak interaction, and the strong interactions. The gravitational force, the fourth of the fundamental interactions, is not included in the SM as its strength is so faint so that its effect on fundamental particles is not measurable with present day experiments The gauge bosons are the force carriers that mediate the electromagnetic, weak, and strong interactions in the Standard Model. These spin 1 particles can be separated according to the interaction types, and the number of gauge bosons in each interaction is determined by the dimension of their gauge group. The electromagnetic mediator is the photon (γ), which is a massless and chargeless particle that couples to electric charge and is well described by Quantum Electrodynamics (QED). The mediators of the weak interaction are the neutral Z^0 boson, and the $W^{\pm}$ bosons, which carry a

charge of ±1e. The strong force mediators are the gluons, which are massless and interact with the color charge of quarks. There are eight types of gauge gluons for each non-vanishing color-anticolor charge combination, and the non-zero color charge of the gluons means that they are also self-interacting. The Standard Model also predicts the existence of Higgs Boson [12, 13] with a mass of about 125 GeV/c^2 at Large Hadron Collidor (LHC) at CERN in July 2012. The Higgs boson gives mass to fundamental particles using the Higgs mechanism. The fundamental interactions between particles and characterization of strong, weak and electromagnetic are summarized in Figure 1.3

The strong force between the color charge of quarks and gluons is responsible for the binding of nucleons into a nucleus, and also for the binding of quarks into hadrons. The theory of Quantum Chromodynamics (QCD) is used to describe the strong interaction between quarks and gluons, and is discussed in detail in the following section:

1.3 Quantum Chromodynamics

Quantum Chromodynamics (QCD) [14] is the non-Abelian SU(3)[2] Yang-Mills gauge theory of the strong interaction, and describes the fundamental force experienced by color charged fermions (quarks) and mediated by gluon exchange in the Standard Model. It is similar to the theory which describes the electromagnetic force, Quantum Electrodynamics (QED), with photons as the quanta of the Electrodynamic field.

[2]is a non-Abelian group which means that its elements do not systematically commute. In particular, different generators of SU(3) never commute with each other. In QCD, these generators correspond to gluons, which are themselves carriers of the strong charge. This is in contrast with QED, in which photons do not carry the electric charge. Unlike photons, gluons interact directly with each other.

The gauge invariant QCD Lagrangian, which describes the dynamics of the quarks and gluons, is:

$$\mathcal{L} = -\frac{1}{4}F^C_{\mu v}F^{\mu v}_C + \sum_f \bar{\psi}_f(i\gamma^\mu D_\mu - m_f)\psi_f \tag{1.1}$$

where C is the color index that runs from $C = 1$ to $N_C^2 - 1 = 8$, corresponding to the dimensionality of $SU(3)$, the index f runs over the fermions (in the Standard Model, these are the six quark flavors) with bare mass m_f and Dirac spinor ψ_f, and γ_μ are the four Dirac matrices. The fermion fields have a color index $\psi_f^{(A)}$ that runs from $A = 1$ to $N_C = 3$ but it is suppressed in the following notation for brevity. The field tensor $F^C_{\mu v}$ is related to the eight gauge fields A^C_μ, called gluon fields, through

$$F^A_{\mu v} = \partial_\mu A^A_\nu - \partial_\nu A^A_\mu - g f_{ABC} A^B_\mu A^C_\nu \tag{1.2}$$

where f_{ABC} are the structure constants of SU(3) defined by $[t_A, t_B] = i f_{ABC} t_C$ for the eight 3×3 generators t_A of SU(3), and g is the QCD coupling constant (more commonly referred to by $\alpha_s = g^2/4\pi$. The covariant derivative is defined as

$$D_\mu = \partial_\mu - igt^C A^C_\mu \tag{1.3}$$

The gluon field in the covariant derivative reflects local gauge symmetry. The Eq. 1.3 contains one dimensionless coupling constant g, and Eq. 1.1 provides no scale, QCD predicts only the ratios of physical quantities, not absolute values in terms of physical units. The QCD coupling constant $\alpha_s = g^2/4\pi$, which is analogous to $\alpha = 1/137$ in QED describes the strong interaction strength depending on the momentum transfer Q, i.e. $\alpha_s \sim 0.1$ for 100 GeV-TeV range. In perturbative QCD (pQCD) coupling constant (α_s) can be written as:

$$\alpha_s(Q^2) = \frac{1}{\beta_0 \ln(Q^2/\Lambda^2_{QCD})} \tag{1.4}$$

where Λ^2_{QCD} is the QCD scale, $\beta_0 = \frac{33-2N_f}{12\pi}$ is a positive-definite coefficient, and N_f is the number of flavor. The measurements of the QCD coupling is presented as a func-

tion of the energy scale Q in Figure 1.4, which demonstrates the agreement of measurements with the specific energy dependence of α_s predicted by QCD. Figure 1.4 shows

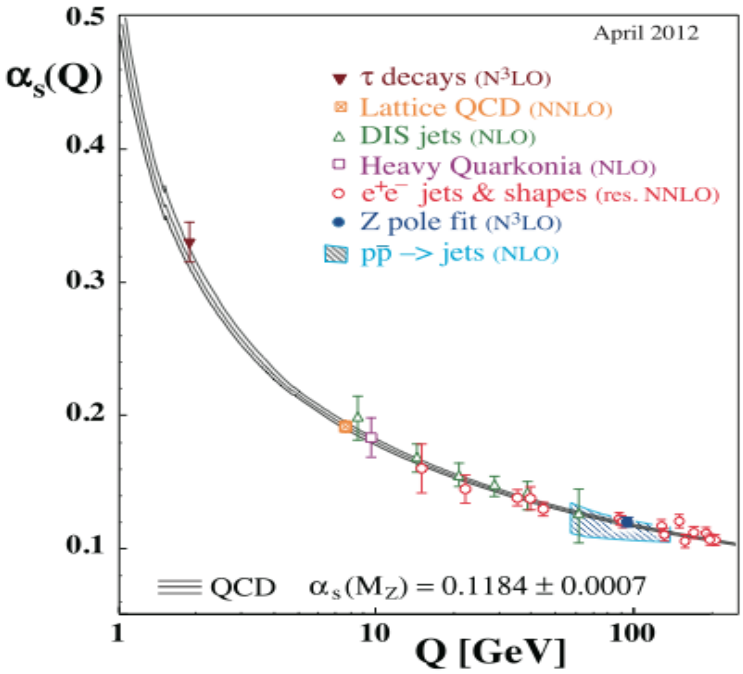

Figure 1.4: *The QCD renormalization coupling constant,α_s, as a function of energy (or momentum) transfer. The plots is taken from Ref. [15]*

that the coupling constant becomes smaller as the momentum transfer increases. At α_s approaching zero, the partons [3] interact very weakly and can behave as if they are free. This feature of the strong interaction is called *asymptotic freedom*. On the contrary, at low momentum transfers, the coupling constant α_s becomes larger and the perturbative approach is not valid anymore. In the normal world, the quarks and gluons are confined in the hadrons. This property is known as *confinement*. The another explanation is given by the coupling strength between two interacting quarks which increases with the distance. The potential of the strong force between $q\bar{q}$ pair

[3]The basic constituents of hadrons, namely quarks and gluons

as a function of distance **r** can be approximated by [16]:

$$V_s(r) = -\frac{4}{3}\frac{\alpha_s}{r} + kr \tag{1.5}$$

where r is the separation between the interacting quarks and k an effective string constant for the long distance force. It concludes that the QCD potential between two quarks does not vanish for large distances but grows linearly with **r**. The third characteristic associated with QCD is **chiral symmetry restoration** which is associated to the fact that the masses of the $\bar{u}$ and $\bar{d}$ quarks are small compared to the relevant scales of QCD. Thus, these masses can be taken as zero for many practical applications. The theory assumes that a massless quark with its spin pointing into the direction of the momentum preserves its helicity for all times in spite of the interaction with other quarks and likewise for a massless quark with its spin opposite to the direction of motion. This symmetry is called chiral symmetry because the conserved spin alignment with the quark's direction of motion can be associated with the right and left-handedness respectively. They are so-called chiral partners under parity transformation. Chiral symmetry predicts for every particle the existence of a mirror reflected particle with the same properties such as mass, hence, the spectrum of hadrons should group into parity partners with identical properties. This, however, is not observed in nature. Actually, the parity partners exhibit large differences in their masses. Hence, in nature chiral symmetry is observed to be spontaneously broken. But at high temperature or densities a transition to the chirally restored phase is expected. This fact would imply dramatic changes in the properties of certain hadrons in the medium in the vicinity of the phase transition. In the chirally restored phase each particle and its parity partner have to become alike. In particular, their masses have to become similar.

1.4 The QCD Phase Transition

The ordinary matter in the world, is made up of quarks and gluons, confined into hadrons by the strong interactions. As discussed in section 1.3, the quarks and gluons is expected to be in a deconfined state based on the asymptotic property of QCD at extremely high temperatures and/or short distances. This deconfined state of quarks and gluons is called **Quark-Gluon Plasma** (QGP) [17], which is defined as a locally thermally equilibrated state of matter in which quarks and gluons are deconfined from hadrons, so that color degrees of freedom become manifest over nuclear, rather than merely nucleonic, volumes [18].

1.4.1 Lattice QCD

The phase transition of ordinary matter to a QGP state is best studied in QCD thermodynamics within the framework of lattice QCD. The phase transitions are related to extended range phenomena in a thermal medium, to the collective behaviour and spontaneous breaking of global symmetries. In order to study such mechanisms in QCD a calculation approach able to deal with all non-perturbative aspects of the theory of strong interactions is needed, this is precisely the purpose of lattice QCD [19]. In lattice QCD, the Lagrangian associated with the theory is discretised onto a finite space-time grid. This procedure is described in detail in [20]. Figure 1.5 shows the energy density as a function of temperature. The energy densities measured at the fixed target experiments at the Super Proton Synchrotron (SPS) at CERN, and higher energy collider experiments at RHIC and LHC at several accelerators are indicated on the diagram, as well as equivalent temperatures that lattice QCD predicts. The energy density is estimated using the Bjorken formula [21], which relates the energy density at thermalisation to the transverse energy density in the detector. Overall, the lattice QCD calculations suggest, firstly, that a phase transition at around $T_c \geq$

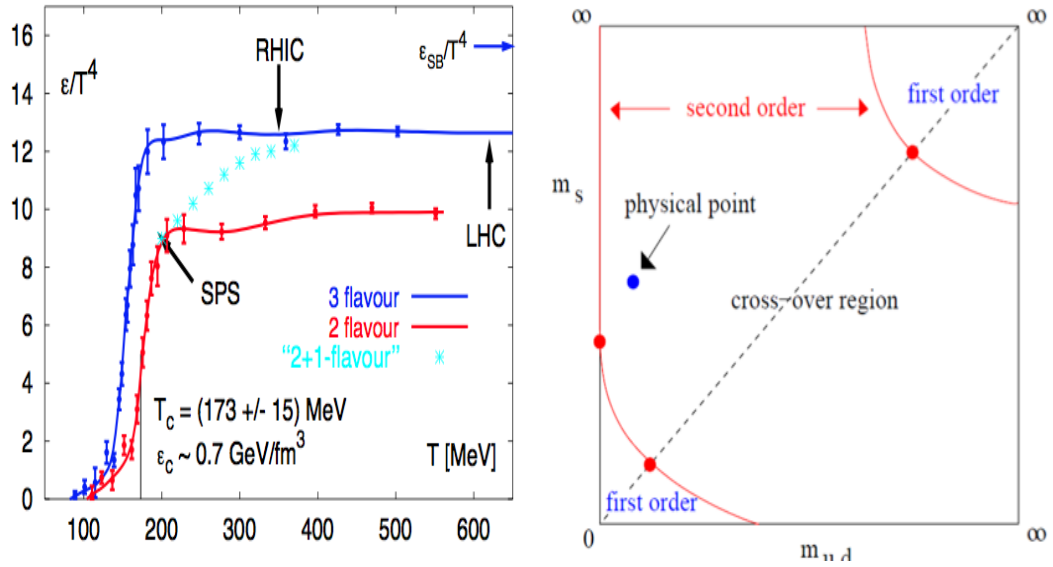

Figure 1.5: *Left: Lattice QCD calculations for the energy density as a function of the system temperature (T). A phase transition occurs when T reaches the critical temperature (T_c). The system transfers from hadronic matter to Quark−Gluon Plasma (QGP) where quarks and gluons are deconfined, Right: Order of the phase transition for finite temperature and $\mu_B = 0$.*

170 MeV (2×10^{12}) [25, 26] is to be expected depending on the collisions used to calculate this, and that collisions of heavy ions at RHIC, and particularly at the LHC, should reach temperatures well over this transition point. Another important Lattice QCD prediction is that the mass of quarks in a QGP is effectively lower than in the QCD vacuum [22]. As low energy QCD is non-perturbative, it is impossible to approximate through perturbation theory the gluon clouds surrounding any real quark. Instead, the theory is renormalised and the fundamental parameters are expressed in terms of experimentally measured properties. This leads to effective quark masses in the vacuum known as dynamical masses, approximately 300 MeV for up and down quarks, and around 500 MeV for strange quarks [23]. As the strong coupling drops, the effective quark masses also drop, and in a QGP they reach their bare masses; a few MeV for the up and down quarks and around 100 MeV for the strange quark [15].

This is important for the behaviour of QGP, as it may speed chemical equilibrium, the statistically most likely distribution of quark flavours in the medium.

The order of the phase transition, strongly depend on the quark masses, can be seen on the right plot of Figure 1.5. The n^{th} order phase transition means that the n^{th} derivative of the free energy, $\partial^n F/\partial T^n$ is discontinuous, while the lower derivatives in T are continuous. Due to the light mass of the u and d quarks and the heavier s quark, the physical point is located in a region indicating that the phase transition is a rapid, but smooth cross-over [24].

1.4.2 QCD phase diagram

A phase transition from the confined hadronic matter to the deconfined QGP matter is expected to happen at either high temperature (T) or large baryon chemical potential (μ_B) which can be thought of as a measure of the imbalance between quarks and antiquarks in the system. Figure 1.6 shows the QCD phase diagram of strongly interacting matter in T-μ_B space. When heated, nuclei eventually break up into protons and neutrons, while at the same time thermally created light hadrons, predominantly pions, start filling up the space between the nucleons. When the hadron gas that has formed is sufficiently heated or compressed, the finite size hadrons begin to overlap and the partons start experiencing the effect of Debye screening. Zones with free quarks and gluons form which at a certain critical temperature, T_C, spread over the entire volume of the hadron gas. The phase boundary with the QGP state is represented by the solid white line in Figure 1.6. As discussed earlier, in Lattice QCD calculations, a certain critical point is reached as $\mu_B \rightarrow 0$, beyond which the transition is expected to become a rapid crossover. This is the region which is experimentally accessible in heavy-ion collisions at the Relativistic Heavy Ion Collider (RHIC) and at the Large Hadron Collider (LHC) at CERN. At $\mu_B \rightarrow 0$, along the line where the

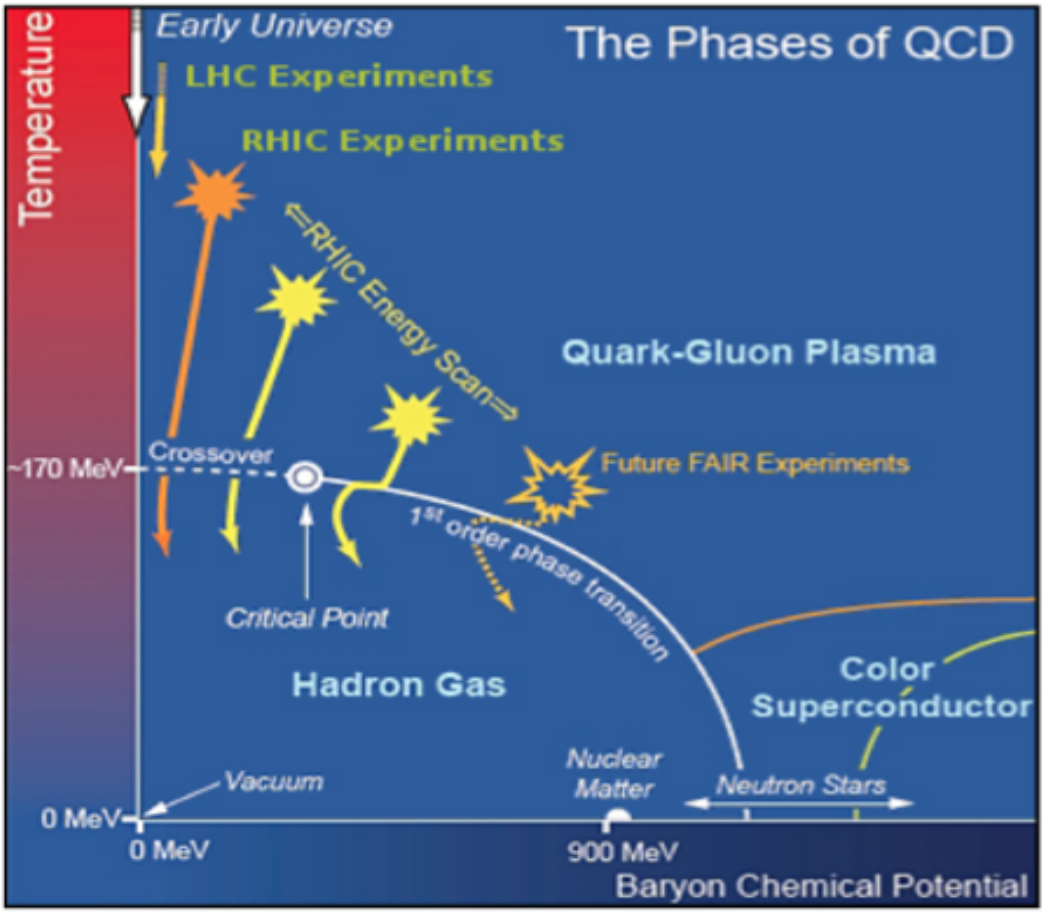

Figure 1.6: *Schematic of QCD phase diagram. The solid lines show the phase boundaries for the indicated phases. The solid circle depicts the critical point where sharp distinction between the hadronic gas and QGP phases cease to exist. Possible trajectories for systems created in the QGP phase at different accelerator facilities are also shown.*

early universe evolved, the transition is predicted to happen at a critical temperature of $T_C \approx 170$ MeV (2×10^{12}) [25, 26]. The region of the RHIC beam energy scan is also indicated in the phase diagram in Figure 1.6. During the RHIC beam energy scan, the collision energy was lowered in multiple steps down to 7.7 GeV in order to learn more about the onset of deconfinement [27]. The future Facility for Anti-proton and Ion Research (FAIR) accelerator will be operated at similar center-of-mass energies in order to investigate equation-of-state, phase transition and the critical end point at high μ_B. The FAIR will explore the phase diagram at high baryonic densities. At very high densities and very low temperatures, correlated quark-quark pairs (Cooper pairs) are predicted to form a color superconductor [28]. This color-superconductive phase has already been seen early in the study of quark matter [29]. The transition from a hadron gas to a QGP is also interesting for cosmology and astrophysics. Today it is believed that in the Big Bang scenario for the origin of the universe the elementary particles were produced in the freeze-out from a QGP phase with high temperature and low baryon density around 1 μs after the Big Bang. Furthermore, it can be seen in the phase diagram that a phase transition to the QGP, or even to more exotic states of matter at zero temperature, is expected for large baryon densities. It is assumed that these densities are reached in the center of neutron stars [30]. Here, the possible super conducting phase and the QGP can play an important role in the stability of neutron stars.

In a relativistic heavy ion collision, two nuclei are accelerated close to the speed of light (99.995% c) and are thus Lorentz contracted. When they collide with each other, the nuclei slow down through, naively speaking, multiple inelastic nucleon-nucleon collisions, depositing energy into the collision zone. If the energy density reaches the critical value ($\sim$1 GeV/fm^3 predicted from QCD [32]) of the phase transition, the QGP is predicted to form. In nucleus-nucleus collisions, the system evolves

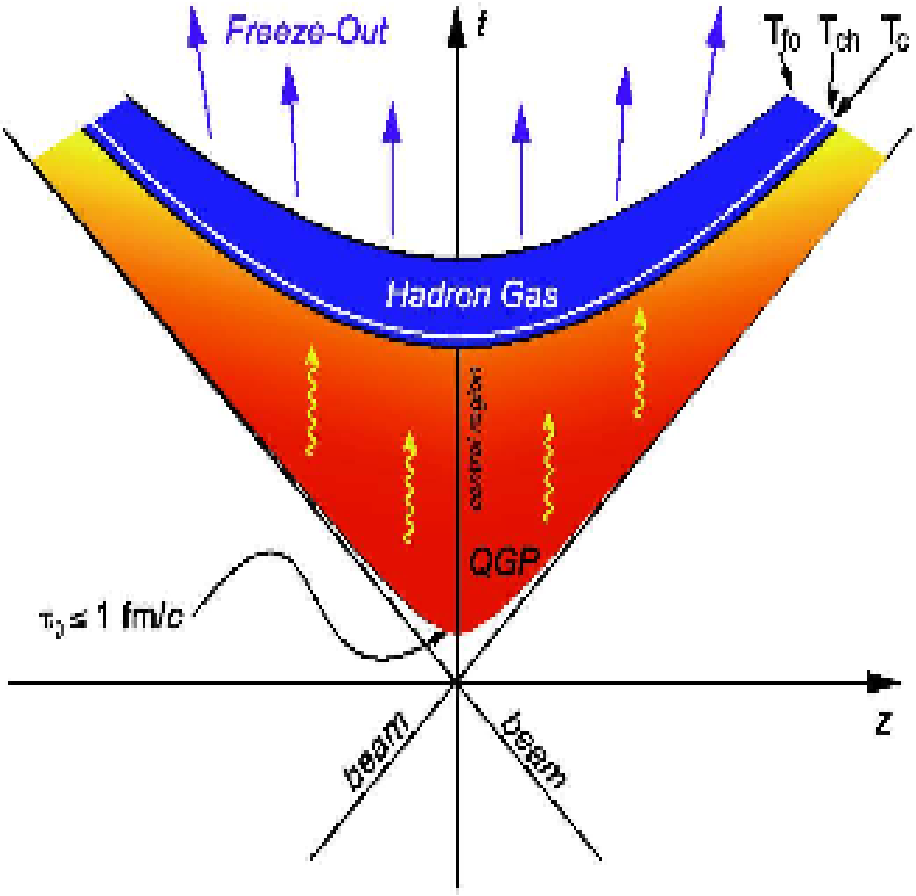

Figure 1.7: *space-time evolution in ultra-relativistic nuclear collision. [31]*

through several space-time stages as depicted in Figure 1.7. The inelastic nucleon-nucleon collision happens through parton-parton (quark or gluon) scattering. The QGP is formed within ∼1fm/c after the collision. The system begins to thermalize by further partonic scattering. As the scattering continues, the system expands in both longitudinal and transverse directions. The temperature decreases as the system expands. The photons and leptons radiated from the color QGP medium leave the system without further (strong) interactions in the QGP. When the temperature drops below the phase transition critical value, the system starts to convert back into a hadronic state, in the form of baryons and mesons. The hadronization happens at ∼10 fm/c. After hadronization, the system enters the hadron gas state. In the hadron gas state, hadronic inelastic scatterings change the particle species at the level of hadrons instead of partons. When further hadronic inelastic scattering ceases, particle species is frozen. As the system further expands, the average distance between particles increases. Particle elastic scatterings continue until their distance is too large. Finally, the elastic scattering ceases and particles stream freely into the detector and are recorded. The experimental observables are the charge, momentum and energy of each final state particle reconstructed with the detectors. The final state particles carry the information about the QGP as well as the various stages of evolution.

1.5 Kinematic Observables

1.5.1 Centrality Definition

Nuclei are extended objects and thus the geometry of the collision plays an important role. Most of the observables depend on the initial collision geometry. The impact parameter (b), defined as the distance between the centres of two colliding nuclei in

the transverse plane describes the geometry of the collision. Figure 1.8 provides a sketch that is helpful to understand this quantity. The volume of the overlap region between the two nuclei can be computed from the value of the impact paremeter. The framework commonly used to describe the collision geometry is the Glauber Model [33]. The main assumption of this model states that a collision between nuclei can be seen as superposition of independent binary collisions between the nucleons. Nucleons that suffer at least one collisions are called participants, while the other are called spectators. When the collision occurs it is described in terms of single interactions between the constituent nucleons.

The Glauber model allows to describe the features of the collisions as the impact parameter, the number of participants and the number of binary collisions among the participants. The participant nucleons will transfer the fraction of their energy to the collisions region providing the energy needed to possibly create the QGP, while the spectators will simply continue their flight (almost) unaffected by the collision. In a collision of two nuclei, the impact parameter (b) can carry values from 0 to $R_a + R_b$ where R_a and R_b are the radii of the two nuclei. When b = 0 i,e the overlap region between nuclei is large, it is called central collision. In this case most of the nucleons are involved. This means that a large amount of energy will be transferred to the collision region and whereform matter, also called fireball (which has a good chance of creation of QGP). Alternatively if b is large, it is called peripheral collisions, where energy available is small and thus we do not expect QGP formation. A good knowledge of geometry is important to understand many collective and hydrodynamical effects such as collective motion generally called flow are strongly affected by intial geometrical distribution of the collision of nucleons and it is discussed extensively in Chapter 6. When collisions with $0 \leq b \leq (R_a + R_b)$ are allowed, it is called minimum-bias collision. System created in a central collision can be qualitatively as well as

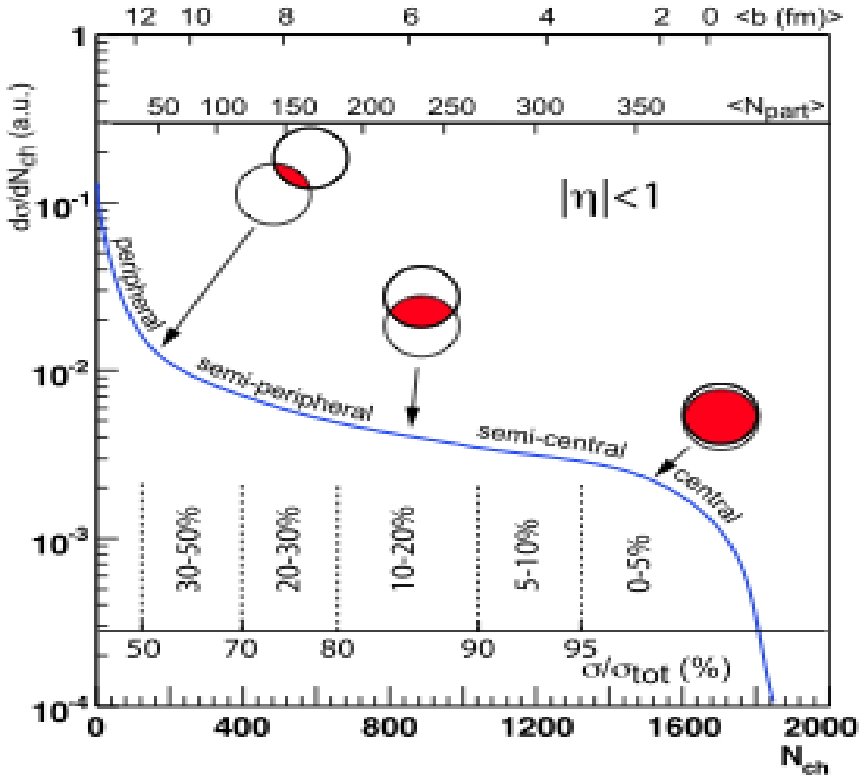

Figure 1.8: *Centrality definition from charged particles multiplicity distribution in minimum bias nucleus-nucleus collision and its correlation with impact parameter(b) and the number of participating nucleons (N_{part}) in a collision*

quantitatively different from the system created in a peripheral collision. Different aspects of reaction dynamics can be understood if heavy ion collisions are studied as a function of impact parameter. But experimentally it is not possible to directly measure the initial geometric quantities such as impact parameter. However there is one to one correspondence between impact parameter of the collision and some experimental observable. e.g. particle multiplicity, transverse energy (E_T) and the number of spectactor nucleons (measured by a Zero-Degree Calorimeter (ZDC)). On an average the particle multiplicity is proportional to the energy released in the collision. One can measure the particle multiplicity distribution or the transverse energy for minimum-bias collisions. The high values of particle multiplicity correspond to central collisions and lower values correspond to more peripheral collisions. Hence the minimum-bias multiplicity distribution could be used for centrality determination in a collision experiment. Figure 1.8 shows the minimum-bias multiplicity (N_{ch}) distribution used for the selection of collision centrality. The minimum bias yield has been cut into successive intervals starting from the maximum value of N_{ch}. The first 5% of the high N_{ch} events correspond to top 5% central collisions.

1.5.2 Rapidity and Pseudorapidity

Two variables that are in common use in accelerator physics are rapidity (y) and pseudorapidity (η). These are derived from the fact that in accelerators the incident velocities of particles taking part in collision are along the beam axis. This leads to the definition of various quantities that are either with respect to boosts to the rest frame of observers moving at different velocities parallel to the beam axis or others that although they are not invariant have transformation properties that are easy to handle and useful for analysis. The usual convention in accelerator physics is to take

z-axis as beam axis. Rapidity of the particle is defined as

$$y = \frac{1}{2}\ln(\frac{E + p_z c}{E - p_z c}) \tag{1.6}$$

Where p_z is the momentum in z-direction. In highly relativistic region, if the particle is directed in XY plane perpendicular to beam axis, than p_z will be small and rapidity will be close to zero. Now if the particle which is highly relativistic be directed predominantly down the beam axis, say in +z direction then E$\approx$ p_zc and y$\rightarrow$ + ∞. Similarly if the particle is travelling down the beam in the -ve axis, E$\approx$ -p_z c and y = -∞. So rapidity is zero when the particle is close to transverse beam axis and moves to $\pm\infty$ when particle is close to beam axis in either direction. Rapidity is related to angle between XY plane and the direction of emission of product of the collision.

Upon lorentz transformation parallel to the beam velocity v = βc, the equation for transformation in rapidity is a particular simple one.

$$y' = y - \tanh^{-1}\beta \tag{1.7}$$

This simple transformation implies that the difference between rapidities of two particles is invariant with respect to lorentz boosts along the z-axis. This is the key reason why rapidity is important in accelerator physics. Rapidity difference are invariant with respect to lorentz boost along the beam axis.

The only problem with rapidity is that it can be hard to measure for highly relativistic particles. One need energy and the total momentum in reality, however, it is often difficult to get total momentum vector of a particle, especially at high values of rapidity where the z component of momentum is large and the beam pipe can be in the way of measuring it precisely. This leads to the concept of pseudorapidity (η) which is calculated by defining in the same way as rapidity but easier to measure for highly energetic particles.

We start from the definition of y

$$y = \frac{1}{2}\ln(\frac{E + p_z c}{E - p_z c}) \tag{1.8}$$

$$y = \frac{1}{2}\ln(\frac{(\sqrt{p^2c^2 + m^2c^4} + p_z c}{\sqrt{p^2c^2 + m^2c^4} - p_z c}) \tag{1.9}$$

For highly relativistic particles, $p_c \gg mc^2$

$$y = \frac{1}{2}\ln(\frac{pc\sqrt{1 + \frac{m^2c^4}{p^2c^2}} + p_z c}{pc\sqrt{1 + \frac{m^2c^4}{p^2c^2}} - p_z c}) \tag{1.10}$$

$$y = \frac{1}{2}\ln(\frac{pc + p_z c + \frac{m^2c^4}{2pc} + ...}{pc - p_z c + \frac{m^2c^4}{2pc} + ...}) \tag{1.11}$$

Now p_z/p is $\cos\theta$ where θ is the angle made by particle's trajectory with beam pipe. Thus

$$1 + \frac{p_z}{p} = 1 + \cos\theta = 2\cos^2\theta/2 \tag{1.12}$$

$$1 - \frac{p_z}{p} = 1 - \cos\theta = 2\sin^2\theta/2 \tag{1.13}$$

$$y = \frac{1}{2}\ln\frac{2\cos^2\theta/2}{2\sin^2\theta/2} \simeq -\ln\tan\theta/2 \tag{1.14}$$

We define pseudorapidity as $\eta \simeq$-ln tan$\theta/2$ thus for highly relativistic particles $\eta \simeq$ y.

1.6 Experimental Search for QGP

1.6.1 Signature and Observables

The study of relativistic heavy-ion collision thus provides a unique opportunity to search for the predicted state of matter known as the QGP which is an extremely short-lived state of matter with lifetime some 10^{-23} sec. A number of experimental signatures of the transition to the QGP phase have been proposed. They are extensively studied in several experiments at Relativistic Heavy Ion Collider (RHIC) at the Brookhaven National Laboratory (BNL) and at Large Hadron Collider (LHC) at CERN, Geneva.

1.6.1.1 Nuclear Modification Factor

The energy loss by energetic partons in the dense medium formed in high-energy heavy-ion collisions is predicted to be proportional to both the initial gluon density and the lifetime of the dense matter. High-p_T suppression results are usually presented in terms of a nuclear modification factor (R_{CP}), defined as

$$R_{CP} = \frac{Yield_{central}}{Yield_{peripheral}} \times \frac{< N_{bin} >_{peripheral}}{< N_{bin} >_{central}} \tag{1.15}$$

where $< N_{bin} >$ is the average number of binary collisions to the corresponding centrality. The value of N_{bin} was calculated from the Monte Carlo Glauber simula-

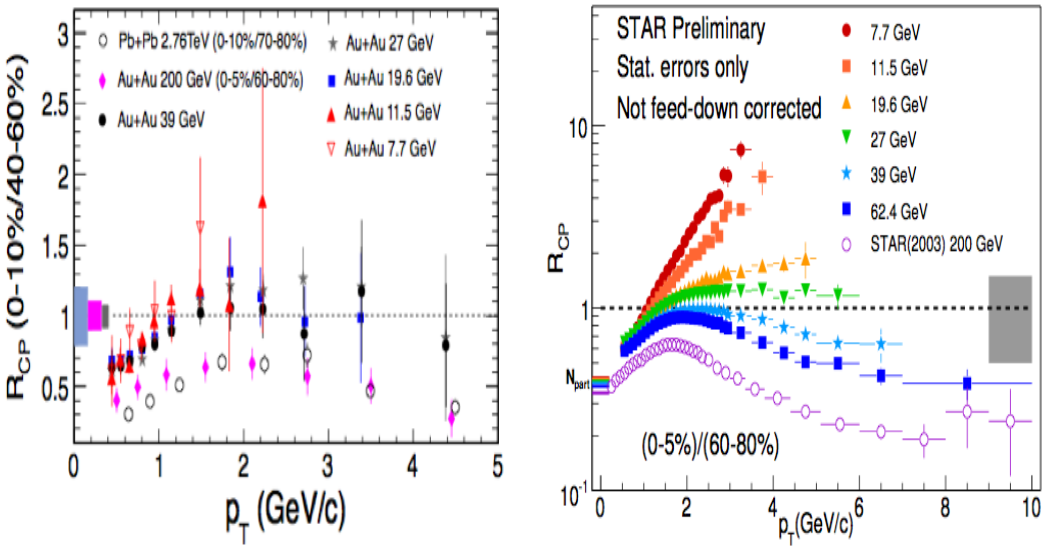

Figure 1.9: *Left: The ϕ meson R_{CP} as a function of p_T in Au+Au [34, 35] and Pb + Pb [36] collisions at various beam energies Right: Nuclear modification factor versus transverse momentum for inclusive charged hadrons from Au+Au collisions at various $\sqrt{s}_{NN}$ at RHIC. The yield ratios for charged hadrons are taken for $0-5\%$ to $60-80\%$ collision centrality.*

tion [33]. $R_{\rm CP}$ is equal to one when a nucleus-nucleus collision are simply a superposition of nucleon-nucleon collisions. Therefore deviation of $R_{\rm CP}$ from the unity would imply contribution from the nuclear medium effects specifically jet-quenching [37].

Nuclear modification factors (R_{CP}) of ϕ mesons at midrapidity in $Au+Au$ collisions at $\sqrt{s}_{NN}$ = 7.7, 11.5, 19.6, 27, 39, and 200 GeV [34, 35] and in $Pb+Pb$ collisions at $\sqrt{s}_{NN}$ = 2.76 TeV [36] are shown in Figure 1.9 (left). Figure 1.9 (Right) shows the nuclear modification factor for inclusive charged hadrons from Au+Au collisions at each BES-I energy. The results at high p_T ($>$ 2 GeV/c) show a smooth transition from strong enhancement at low beam energies to strong suppression at high beam energies. While it is clearly established that the suppression is related to the opacity of a deconfined medium of quarks and gluons, the source of enhancement could have multiple physics interpretations mostly related to dominance of hadronic interactions, like the Cronin effect, cold matter effects, or strong radial flow.

1.6.1.2 Photons

The photons are produced in all the different stages of a heavy-ion collisions and owing to their small electromagnetic coupling, they do not interact with the surrounding matter [38, 39]. In QGP phase, thermal photons are produced either by annihilation process of quark, anti-quark pairs ($q+\bar{q} \rightarrow \gamma+g$) or by compton scattering process of quark and anti-quark with gluons ($q+g \rightarrow \gamma+g$). Once produced, they interact with the surrounding matter only electromagnetically. Also when photons are produced in the quark-gluon plasma region, they do not participate much in the strong interactions with the quarks and gluons. Consequently, their mean free path is quite large and they may not suffer a collision after it is produced. Thus, photons can escape from the system immediately after their production, storing in memory the history of the early stages of collisions. Also, there are several other important photons contributing sources through out the evolution process; viz., photons from hard scattering in the QGP phase, photons from the particle decay, Bremsstrahlung photons etc. Thus, by filtering out the photons from these background processes, the measured direct

photons reflect the thermodynamics of quarks and gluons in the systems and serve as signal of QGP. Figure 1.10(a) shows the invariant direct photon multiplicity for

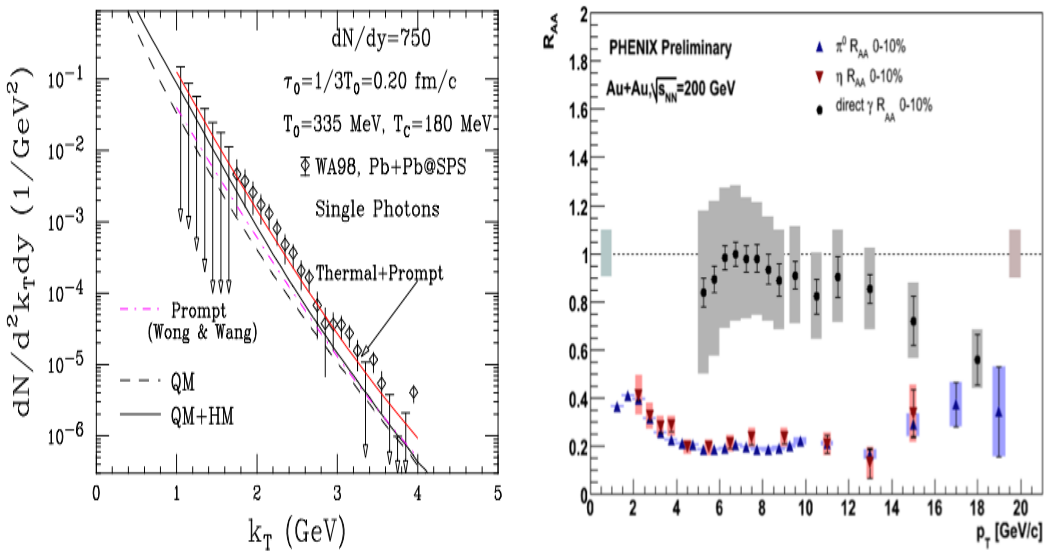

Figure 1.10: *a)The invariant direct photon multiplicity for central Pb+Pb collisions at* $\sqrt{s_{NN}}$ *= 17.3 GeV [40]. The model calculations [41] are shown in the form of lines. QM represents the radiations from quark matter in the QGP and mixed phase. HM represents the radiations from the hadronic matter in the mixed and hadronic phase.* T_0 *is the initial temperature of the system and* τ_0 *is the initial time, b) Nuclear modication factors (*R_{AA}*) for photons,* π^0 *and* η *in 0-10 % central Au+Au collisions at* $\sqrt{s_{NN}}$ *= 200 GeV.*

central Pb+Pb collisions at $\sqrt{s_{NN}} = 17.3$ GeV [40]. The figure also shows the model calculations with the assumption that a chemically and thermally equilibrated quark-gluon plasma is formed at $\tau_0 = 1/3T_0$. The QGP is assumed to expand, cool, enter into a mixed phase and attain freeze-out from a hadronic phase. The nuclear modification factor R_{AA} of direct photons measured by the PHENIX Collaboration is also shown in Figure 1.10(b) [42]. R_{AA} for direct photons is shown to be close to one, a possible indication of direct photons unmodified by the medium.

1.6.1.3 Dileptons

Another important tool for probing the temperature and the dynamical properties of the matter during the evolution of a relativistic heavy-ion collision is the production of lepton pairs, the so-called dileptons. If we consider the dileptons mass range, above pair mass M$\sim$ 2 GeV/c^2 the prompt contribution is dominated by semi-leptonic decays of heavy-flavour mesons and by the Drell-Yan process ($q\bar{q} \rightarrow l^+l^-$). Since these leptons originate from hard scatterings, their rates can be calculated in perturbative QCD. Also at leptons pair masses above $\sim$1.5 GeV/c^2, since the thermal radiation is very sensitive to temperature variations, the dileptons production is expected to originate from the early hot phases, probably from $q\bar{q}$ annihilation. Similarly to the photons case, the thermal QGP radiation has to be discriminated from the large prompt background. finally at low masses, less than 1.5 GeV/c^2, thermal dileptons spectra are dominated by the radiation process from the hot hadronic phase. The potential of thermal dilepton as a signature for a phase transition to the QGP is described in detail in reference [43]

1.6.1.4 Quarkonium Suppression

Quarkonia are the important probes of the QGP since they are produced early in the collision and their survival is affected by the surrounding medium [44]. The bound states of charm and bottom quarks are predicted to be suppressed in heavy ion collisions in comparison with pp, primarily as a consequence of deconfinement in the QGP [45]. The magnitude of the suppression for different quarkonium states should depend on their binding energy, with strongly bound states such as the Υ showing less or no modification. However, J/ψ production, the classical deconfinement signal, has puzzled expectations and interpretations ever since the first nuclear suppression was measured with Oxygen beams at the SPS, now attributed to cold nuclear matter

effects rather than deconfinement. The "anomalous" suppression seen later with heavier beams turned out to be rather similar in magnitude at SPS and RHIC. This could indicate suppression of only the high mass charmonium states ψ' and χ_c, which populate about 40% of the observed J/ψ, and which should dissociate very close to or even below the critical transition temperature. Alternatively, it has been suggested that the increasing (with energy) J/ψ suppression is more or less balanced by enhance production via recombination of two independently produced charm quarks [46, 47]. A compilation of first LHC results on quarkonia production for both (a) J/ψ and

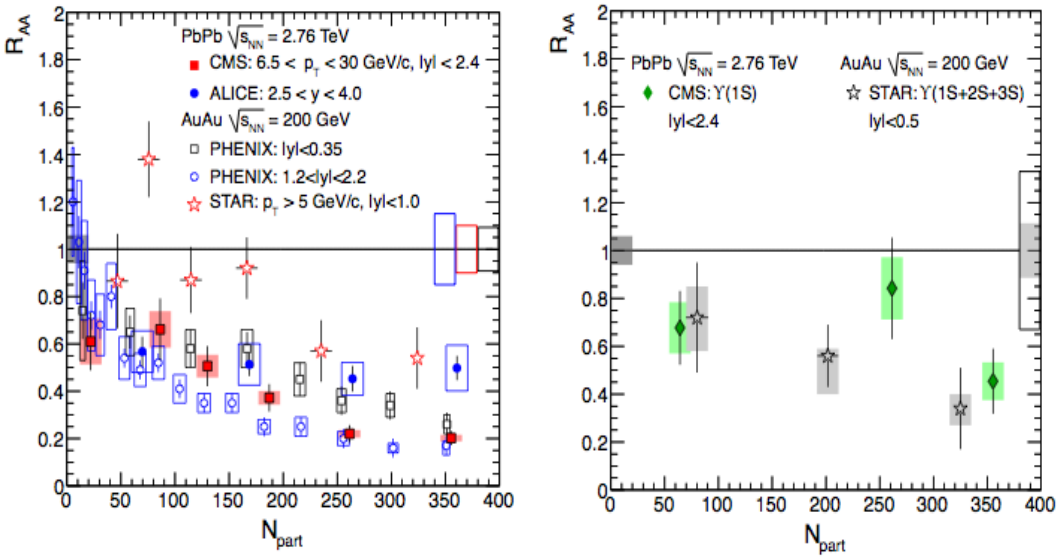

Figure 1.11: *Nuclear modification factor R_{AA} as a function of centrality for J/ψ (Left) and Υ (Right).*

b) Υ is shown in Figure 1.11 as a function of centrality (N_{part}), together with data from RHIC. While errors are still large, and the overall amount suppression at LHC remains qualitatively similar to RHIC. The p_T integrated R_{AA} measured for the J/ψ at forward rapidity (closed circles) of about 0.5 depends very little on centrality and is almost a factor of two larger than the one measured at RHIC in central collisions, also at forward rapidity (open circles); the difference is smaller but still significant when comparing with RHIC midrapidity data (open squares). On the contrary, the

high p_T data at LHC (full squares), which are compatible with an independent R_{CP} measurement, show a stronger suppression than the high p_T RHIC results (open stars). While such a pattern would be unexpected in a pure suppression scenario, it is qualitatively consistent with the recombination model, which predicts substantial regeneration effects only at low transverse momentum. The Υ suppression (right panel) is very similar at RHIC and LHC. As only about 50% of the observed Υ(1S) are directly produced, and the Υ(2S/3S) states seem to be more suppressed than the ground state, the measured R_{AA} is compatible at both RHIC and LHC with suppression of the high mass bottonium states only.

1.6.1.5 Strangeness Enhancement

One of the first signatures of the QGP was the strangeness enhancement in A-A collisions that is an increased production of strange hadrons with respect to pp interactions. In A-A collisions the initial content of strangeness is zero because nucleons are only made of up and down quarks, so the strange matter that is detected after a nucleus-nucleus collision can only be created by the collision. Besides this, strangeness is a conserved quantity, implying that each strange quark (s) has to be created together with its antiparticle. As mentioned before, the transition from ordinary nuclear matter to the QGP is expected to be accompanied by a restoration of the chiral symmetry, so the threshold energy to produce a $s\bar{s}$ pair would be much lower than in elementary hadronic collisions. As a consequence, the production of (anti)hyperons would be greater in heavy-ion collisions relative to pp or pA. This effect is often called strangeness enhancement.

The strangeness enhancement in a baryon rich matter can also be a result of the Pauli principle:suppression of $u\bar{u}$ and $d\bar{d}$ pair production in favour of $s\bar{s}$ pairs in initial u and d-rich environment remaining from incident nuclei. Furthermore, the $\bar{u}$

and $\bar{d}$ anti-quarks annihilate with u and d quarks, while $s\bar{s}$ annihilation occurs less frequently until saturation of the s and $\bar{s}$ abundances. Most calculations predict an enhancement in the observable yield as a signature of plasma formation while s quark yields, although enhanced, differ only slightly in a plasma compared to a hadron gas.

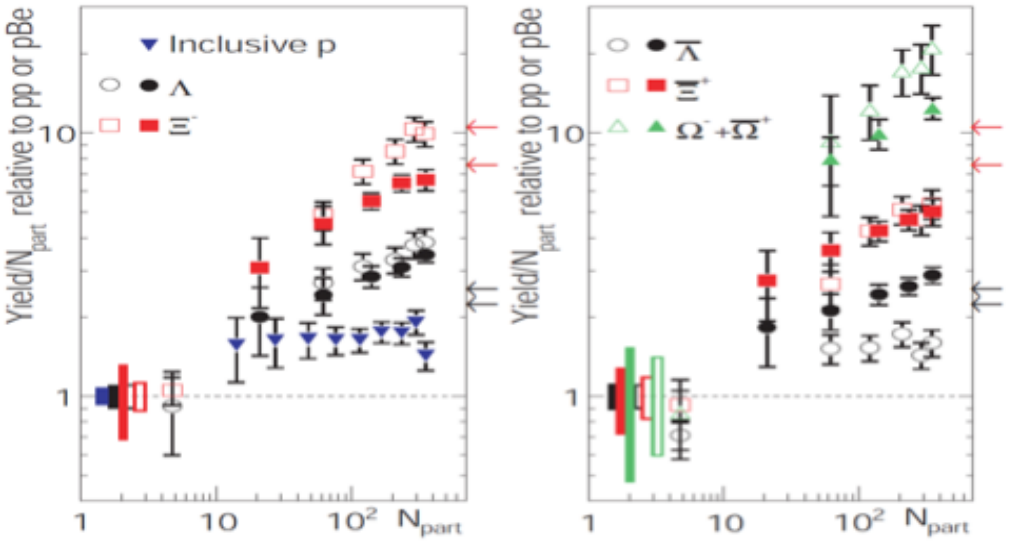

Figure 1.12: *Observed (anti)hyperon yields normalized to pp or pBe collisions as a function of the centrality of the collision; open and closed points correspond to measurements performed at SPS and RHIC, respectively. The arrows on the right axis are the predictions from a Grand Canonical formalism for different chemical freeze-out temperatures.*

In Figure 1.12, it is possible to appreciate the yield of (anti)hyperons compared to pp or pBe that are used as benchmarks. A clear hierarchy in the scale of enhancements, which grows with the increased strangeness content of the baryon, is observed [48]. The phenomenon of strangeness enhancement has indeed been observed. The ratio of the strange quark pairs with respect to the non-strange quark pairs was proposed by Wroblewski [49]. This ratio is strongly dominated by the most abundant strange particle, the kaon, and its ratio to the pion. The energy dependence

of this ratio λ_s e.g estimated here [50, 51], has a maximum at $\sqrt{s} = 6$ GeV.

$$\lambda_s = \frac{2 < s\bar{s} >}{< u\bar{u} >< d\bar{d} >} \tag{1.16}$$

where the quantities in brackets represent the number of quark-antiquark pairs. One way to quantify strangeness enhancement is by λ_S going from ≈ 0.2 in elementary collisions to ≈ 0.45 in central heavy-ion collisions. This effect becomes more important as the strangeness content of the particle increases. This was notified by Rafelski and others who predicted that the strangeness enhancement should be even stronger for multiple-strange anti-baryons.

1.6.1.6 Hanbury Brown-Twiss (HBT) Technique

Phase transitions from hadronic degrees of freedom to the quark-gluonic degrees of freedom require changes in the equation of state [52]. The information of the QCD equation of state can be extracted from the collective dynamics studies of heavy-ion collisions. Lattice QCD simulations suggest that the speed of light (c_s) is expected to reach a minimum near the critical temperature, T_c and then increase in the hadronic gas domain. At T_c, the equation of state is expected to be softest. If the matter is produced near this point, it will expand slowly due to internal pressure which results in the increased lifetime of the emission source or fireball [53]. So it is important to know about the space-time configuration of the source or fireball created in the heavy-ion collisions and system lifetime of the nuclear collisions. The technique used to extract information about the space-time configuration of the source is called the Hanbury Brown-Twiss (HBT) effect. It is based on the two-particle intensity interferometry and was first applied by Robert Hanbury Brown and Richard Twiss, in astrophysics to measure sizes of stars [54]. Later on, HBT became a very useful method to understand the crucial mechanisms and equation of state of the particle emitting source in relativistic heavy-ion collisions, where the QGP is expected to be

formed.

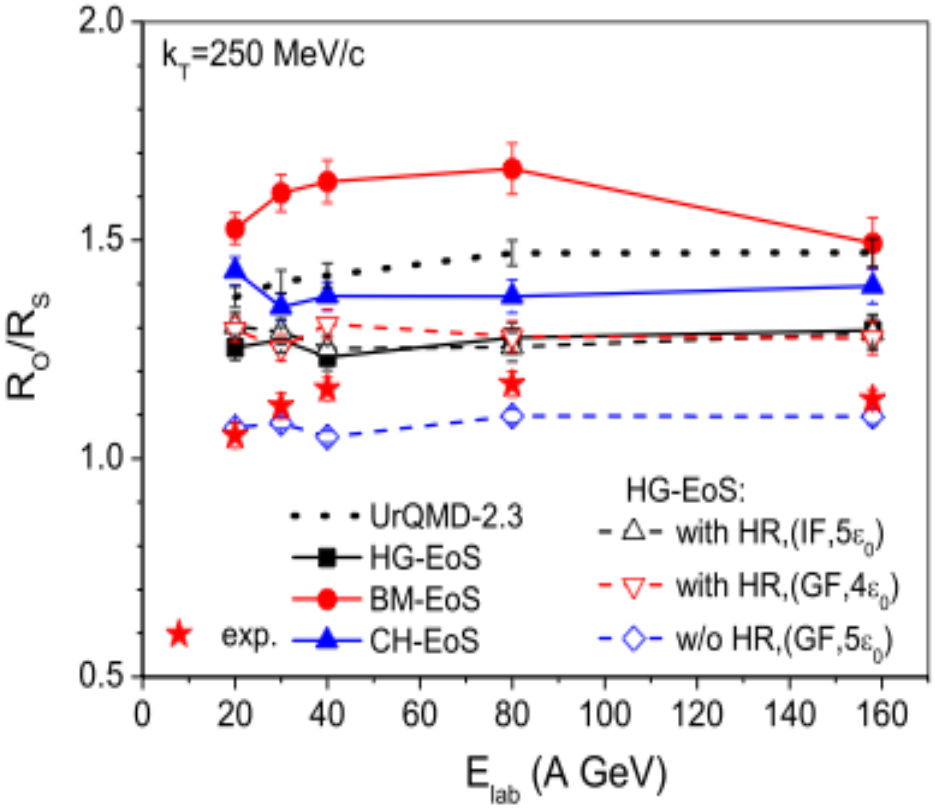

Figure 1.13: *Ratio R_O/R_S as function of lab frame energy (E_{lab}) for negatively charged pions as source. The NA49 data are indicated by solid stars. UrQMD cascade calculation is shown by dotted line. Hybrid model calculations with equation of state of Hadron Gas (HG), Bag Model (BM), and Chiral + HG (CH), with Hadronic rescattering and Resonance decays (HR) are shown by lines with solid symbols. The HG equation of state (HG-EoS) is shown for various freeze-out criteria with HR and without HR by dashed lines with open symbols.*

The observable used to measure the lifetime of fireball (or as signature of QGP) is the ratio of the HBT radii R_{out} (R_O) and R_{side} (R_S). These radii are obtained from the inverse of widths of the two-particle correlation functions in the outward and the sideward directions, respectively. It is proposed that the ratio R_{out}/R_{side} will be enhanced in case of first order phase transition with respect to the ideal gas case, where there is no such transition [55]. In heavy-ion collisions, the HBT correlation functions are mainly studied with pions (most abundantly produced) and direct photons (carry the initial information of collision system). Figure 1.13 shows the ratio R_O/R_S as function of lab frame energy (E_{lab}) for negatively charged pions [56].

It is clearly seen that the ratio R_O/R_S is sensitive to the equation of state, but not to the HG-EoS with different freeze-out prescriptions when HR is included (open triangles and open inverted triangles). With increasing latent heat which corresponds to softness of equation of state, the ratio R_O/R_S is increased. The "excessively" large latent heat in BM-EoS results in a long duration time of the pion source and hence a large R_O/R_S ratio. The chiral equation of state (CH-EoS) exhibits a lower R_O/R_S ratio because the first order phase transition is less pronounced. The calculation with HG model (line with solid squares) leads to smallest R_O/R_S ratio due to the most stiffest equation of state among the three cases. The result of the cascade calculation lies between the CH and BM models, which implies a relatively soft equation of state.

1.6.1.7 Parton Energy Loss

In the nucleus-nucleus collisions, parton energy loss, gives influence to the final particle production by medium modifications of partons fragmentation pattern and hadronization [55]. The partons created in the early stage of nucleus-nucleus collisions via hard scatterings go through the hot and dense medium formed in these collisions and lose a large fraction of their energy due to the interactions between partons inside

the medium. A first attempt to calculate the energy loss of a fast parton in the hot and dense QCD medium was made by J. D. Bjorken [57]. However, this calculation did not include the currently known dominant effect at high energies, namely, gluon radiation (gluon bremsstrahlung) energy loss [58, 59]. Recently, a new interaction mechanisms, collisional energy loss, is usually considered as the dominant mechanism especially at low energies. In a general way, the total energy loss of a parton going through the QCD medium is the sum of collisional and radiative term, written as:

$$\Delta E = \Delta E_{rad} + \Delta E_{coll} \tag{1.17}$$

where ΔE_{rad} is the gluon bremsstrahlung energy loss contribution via medium-induced multiple gluon emission, and ΔE_{coll} is the collision energy loss with the medium constituents. The Figure 1.14 shows different processes of energy loss of a quark of energy E traversing the quark gluon medium.

- **Gluon radiation energy loss**: From the left panel of Figure 1.14, the fast partons lose their energy with gluon radiation energy loss through inelastic scatterings within the medium dominantly at higher momentum. The quantity of energy transfered by radiative energy loss from a parton to medium is expressed as Δ E $\propto \alpha_s \; c_R \overrightarrow{q} \; L^2$. In this formula c_R is cashmir factor, which depends on colour charge of parton (4/3 for quark-quark scattering and 3 for gluon-gluon scattering). $\overrightarrow{q}$ is medium transport coefficient proportional to glun density and L is distance travelled in medium. For RHIC conditions, a parton travelling the fireball length will lose 40 GeV which is huge energy.

- **Collision energy loss**: The collision energy loss via elastic scatterings with the medium constituents dominates at low particle momentum as shown in the right panel of Figure 1.14. Thus if there is QGP medium, we expect high p_T hadrons to be produced near the fireball border, because partons produced in

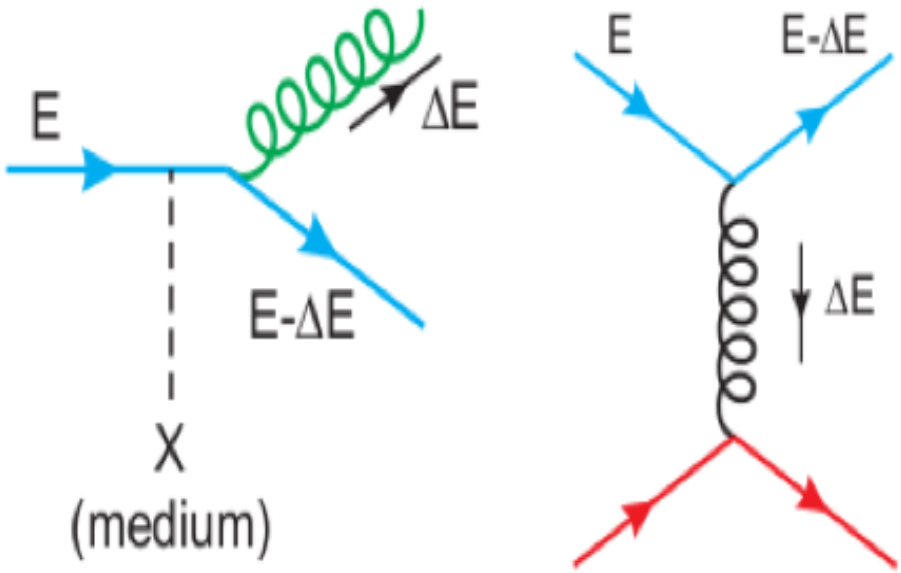

Figure 1.14: Diagrams for radiative (left) and collisional (right) energy losses of a quark of energy E traversing the quark-gluon medium.

the center of fireball will loose too much energy before escaping the fireball. This means that in heavy-ion collisions we expect the away side jet to be likely absorbed while in p-p these are produced back to back. This was observed at RHIC and LHC experiments.

For light flavor partons, the medium-induced gluon radiation has been shown to be more important than the collisional energy loss. However, for heavy quarks, the collisional energy loss is usually considered as the dominant mechanism especially at low energies due to the large masses of heavy quarks which suppress the phase space of gluon radiation [60]. However, at the LHC energies region, heavy quarks become ultra-relativistic as well and thus are expected to behave similarly as light partons for significantly considering the radiative energy loss corrections [61].

Due to parton energy loss in the medium we expect the p_T distribution of produced particles to be softer when there is medium and being harder when no medium is creared like in p-p collisions. This effect is quantified using the nuclear modification factor as

$$R_{AA}(p_t) = \frac{1}{N_{coll>}} \frac{dN_{AA}/dp_T}{dN_{pp}/dp_T} \tag{1.18}$$

From definition if nucleus-nucleus is just superposition of proton-proton collisions, then R_{AA} =1. if no QGP is created then R_{AA} value will increase from around 1/6 more or less the rate between the participants and collisions to a value close to 1 with increasing p_T. These effects can be estimated in pA collisions and are called cronin enhancement. R_{AA} as a function of p_T is used to estimate the modification of parton distribution function for nucleons in a nucleus. These are seen at RHIC and LHC.

1.6.1.8 Hydrodynamics and Collective Flow

Another important observable that can provide information about the evolution of the matter in the heavy-ion collisions is the Flow. The term flow refers to a collective

expansion of the bulk matter. It arises from the density gradient from the center to the boundary of the created fireball in nuclear collisions. Interactions among constituents push matter outwards, frequent interactions lead to a common constituent velocity distribution. Thus $Collective flow$ is sensitive to the strength of interaction and degree of freedom. Collectivity is defined as all particles moving with a common velocity, it is additive and thus accumulated over the whole system evolution, making it potentially sensitive to the equation of state of the expanding matter. At lower energies, the collective flow reflects the properties of dense hadronic matter, while at RHIC energies, a large contribution from the pre-hadronic phase is anticipated. The

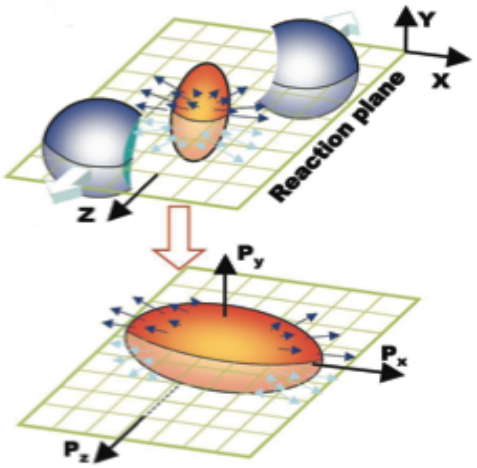

Figure 1.15: *Sketch of an almond shape fireball in spatial and momentum space with respect to the reaction plane determined from the x (impact parameter) and z (beam) directions.*

collision geometry is shown in Figure 1.15. In non-central collisions, the overlap area of two nuclei in the transverse plane has a short axis, which is parallel to the impact parameter (b), and a long axis perpendicular to it. The reaction plane is defined by the impact parameter (x) and beam (z) directions. We usually study the azimuthal anisotropy of in the momentum space with respect to the reaction plane. Since the initial anisotropy in the spatial space has an almond shape with respect to the reaction

plane, this almond shape of the initial profile is converted by the pressure gradient into a final anisotropy in the momentum space. As shown on the top of Figure 1.15, the length in x direction is shorter than that in y direction in the spatial space. This results in larger density gradient in x direction than in y direction. The projection of all particles on one dimension (x or y direction) is shown in Figure 1.16. The areas

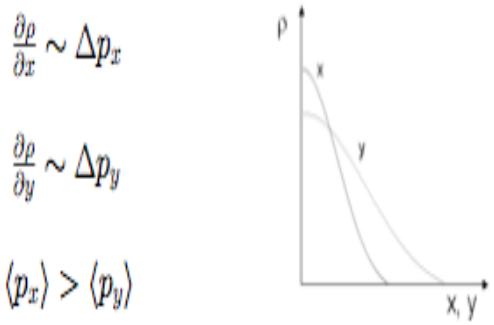

Figure 1.16: *A sketch map of initial particle density in x and y direction.*

under the density curves in x and y directions are same, they are equal to total number of particles. The larger density gradient in horizontal direction (x) leads to the larger pressure gradient in this direction, if we compare with vertical direction (y). The larger pressure gradient further results in larger collective velocity. As shown at the bottom of Figure 1.15, The anisotropy in the initial spatial space will translate into the anisotropy in the momentum space. In this process, the initial spatial anisotropy will be washed out by the momentum space anisotropy during the system expansion, or we can say, the spatial anisotropy only exists at the early stage of the collisions. As

Figure 1.17: *Two components of hydrodynamic flow.*

illustrated in Figure 1.17, the term of flow has two important aspects: (i) collectivity of produced hadrons and (ii) the local thermalization among these hadrons. Through

the interactions among constituents, collectivity will be built up provided that the initial profile of the system is anisotropic. If the interactions are strong enough, the system will finally reach local equilibrium and develop hydrodynamic type flow. The anisotropy in momentum space is usually studied by the Fourier expansion of azimuthal angle distribution of produced particles with respect to the reaction plane

$$E\frac{d^3N}{d^3p} = \frac{1}{2\pi}\frac{d^2N}{p_T dp_T dy}(1 + \sum_{n=1}^{\infty} 2v_n \cos(n(\phi - \psi_R))) \tag{1.19}$$

where p_T and y are the transverse momentum and rapidity of a particle,ϕ is its azimuthal angle, v_n is the n^{th} harmonic coefficient and ψ_R is the azimuthal angle of the reaction plane. The different harmonic coefficients represent different aspects of the global flow behavior. v_1 is called directed flow, v_2 is called elliptic flow since it is the largest component characterizing the ellipse shape of the azimuthal anisotropy, and v_3, v_4 and v_5 are triangular, quadrangular and pentagonal flow respectively. Elliptic flow, v_2, is the second harmonic coefficient in the description of particles azimuthal distribution w.r.t the reaction plane by Fourier expansion. It is argued that the centrality dependence of v_2 can be used to probe local thermodynamic equilibrium [62] and might provide a indication of the phase transition [63]. In this thesis, the centrality dependence of ϕ-meson v_n is presented in Chapter 6. Figure 1.18 shows the measured v_2 distribution as a function of p_T from minimum bias data in Au + Au collisions at $\sqrt{s}_{NN}$ = 200 GeV from STAR and PHENIX experiments [64, 65]. Identified particle v_2 are shown for $\pi^{\pm}$, k^0_s, $p(\bar{p})$ and $\Lambda(\bar{\Lambda})$. At a given p_T, the heavier particle has the smaller v_2 than the lighter particle up to 1.6 GeV/c. This characteristic of mass-ordering comes from radio flow which is predicted by the hydrodynamic calculations [66, 67, 68] represented by the dot-dashed lines. A particle type (baryon versus meson) difference in $v_2(p_T)$ was observed for identified hadrons (π, p, K^0_S, Λ) at the intermediate p_T. This particle type dependence of the $v_2(p_T)$ can be explained by assuming hadronization via quark coalescence or recombination [69, 70]. This

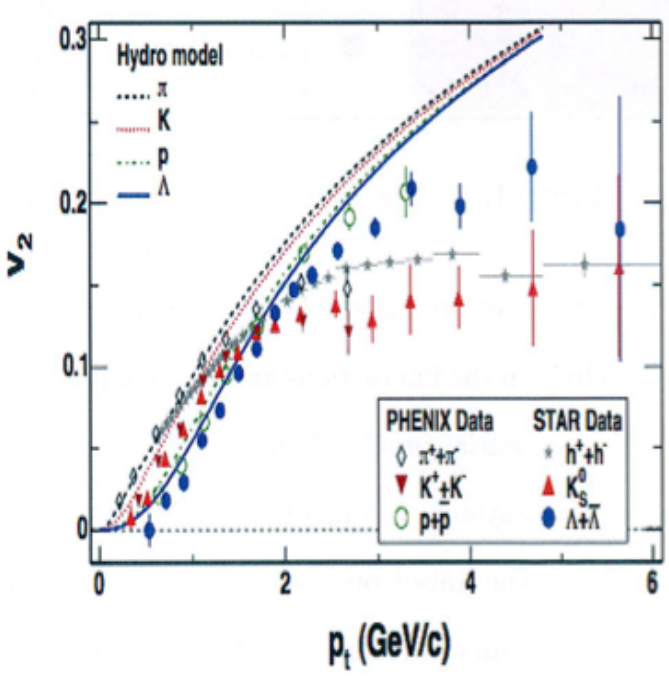

Figure 1.18: *Measurements of $v_2(p_T)$ for identified particles for $0-80\%$ centrality at RHIC. Hydrodynamic model calculation are shown by different lines. The figure is from [48].*

indicates that the collectivity has been developed at RHIC.

1.7 Models

In this section, we give a brief description of phenomenological models used in comparison with the data measurements.

1.7.1 Hydrodynamical Model

Hydrodynamics is a macroscopic approach to study the dynamical evolution of heavy ion collisions. In this model, the central assumption is that the strong interactions happen among the matter constituents, and shortly after that, the system reaches local thermalization. Only when the system is close to local thermal equilibrium,

the hydrodynamic properties, i.e, pressure, entropy density and temperature, are well defined. Only under these conditions, the equation of state of strongly interacting matter at high temperatures can be estimated. At relativistic heavy ion collisions, the approximate longitudinal boost invariant boundary conditions in central phase space simplify hydrodynamic equations greatly [71]. Based on the local conservation law for energy, momentum and other conserved quantities (e.g., baryon number)

$$\partial_\mu T^{\mu\nu}(x) = 0 \partial_\mu j^\mu(x) = 0 \tag{1.20}$$

the ideal fluid decompositions can be written as

$$T^{\mu\nu} = ((x) + p(x) +) u^\mu(x) u^\nu(x) - g^{\mu\nu} p(x) \tag{1.21}$$

$$j^\mu(x) = n(x) u^\mu(x) \tag{1.22}$$

where e(x) is the energy density, p(x) is the pressure and n(x) is the conserved number density at point x^{mu}=(t, x, y, z); $u^\mu(x)$=$\gamma(1, v_x, v_y, v_z)$ with $\gamma = 1/\sqrt{(}1 - v_x^2 - v_y^2 - v_z^2)$ is the local four velocity of the fluid. The great advantage of hydrodynamics is that it provides a covariant dynamics only depending on the equation of state (EOS) which is directly related to the lattice QCD calculations. While the disadvantage of hydrodynamics is that it can not describe the initial condition and the final freeze-out hypersurfaces, and all of these need to be modified by other models/assumptions.

1.7.2 Coalescence Model

In the coalescence model, the probability for forming a bound cluster from a many-particle system is determined by the overlap of the wave functions of coalescing particles with the internal wave function of the cluster. Its validity is based on the assumption that coalescing particles are statistically independent and the binding energy of formed cluster and the quantum dynamics of the coalescing process play only minor roles [72]. In this model, we assume that correlations among partons at

freeze-out are weak and binding energies of formed hadrons can be neglected. Furthermore, the coalescence model is considered as a perturbative approach, valid only if the number of partons coalesced into hadrons is small compared with the total number of partons in the system.

1.8 Comparison of the Models to Data

Figure 1.19 shows the v_2 versus p_T for collision centrality (30-40%) in Au-Au and Pb-Pb collisions at midrapidity for $\sqrt{s}_{NN}$ = 200 GeV and 2.76 TeV, respectively and the comparison of these data to a set of model calculations based on hydrodynamic approach (like THERMINATOR [73, 74]) and another set of calculations based on transport approach [75]. It is observed that hydrodynamic based models explain the v_2 measurements both at RHIC and LHC energies. Transport based models including partonic interactions (like AMPT [75]) also explain the v_2 measurements. However, those transport models which do not incorporate partonic interactions like

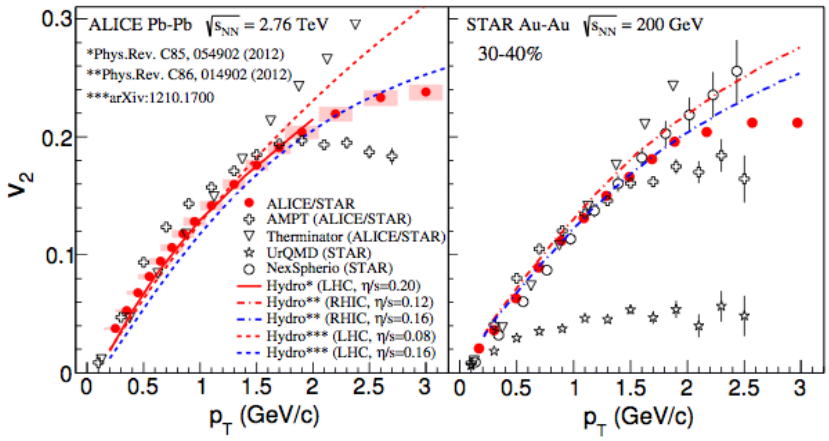

Figure 1.19: *The azimuthal anisotropy (v_2) as a function of p_T, measured in non-central heavy-ion collisions at midrapidity for RHIC and LHC energies. The comparison of data with various theoretical calculations based on hydrodynamic [76, 77, 78] and transport approaches [75] are also shown.*

UrQMD [79, 80] fail to explain the data. The model comparison also reveals that

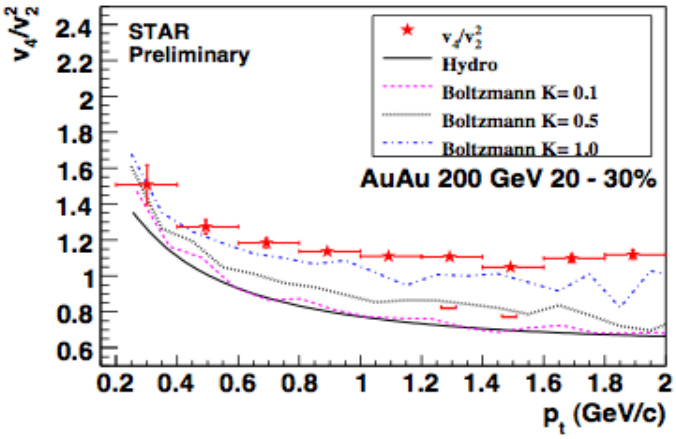

Figure 1.20: *The ratio of v_4/v_2^2 as a function of p_T for charged particles at $|\eta|<1.3$ in Au+Au collisions at $\sqrt{s}_{NN}$= 200 GeV. The brackets show the systematic uncertainty of non-flow effect. The curves correspond to two hydrodynamic calculations. The figure is from [81]*

the data favors a high degree of fluidity reflected by a small value of shear viscosity to entropy density ratio $(\eta/s) < 0.2$. A more detailed study and the comparison of the model calculations with various order azimuthal anisotropy parameters v_n would in near future give us a more quantitative picture of the temperature or energy dependence of transport coefficients of the system formed in the heavy-ion collisions. In ideal hydro calculation, the ratio v_4/v_2^2 will approach to 0.5 at high p_T [82]. Figure 1.20 shows the result of STAR data and ideal hydro calculation as a function of transverse momentum. The dashed lines are ratio come out of calculations by solving Boltzmann equations with Monte Carlo simulation, with different Knudsen number. When the Knudsen number is small, it recovers the hydrodynamic limit as indicated the solid line. The plot shows that the system exhibits considerable deviation from ideal hydrodynamic limit ($K \ll 1$), and the data is consistent with a incomplete thermalized system with $K > 0.5$.

1.9 Thesis Outline

In this thesis, the study of ϕ azimuthal anisotropy and two charged particle transverse momentum correlation in Au+Au at $\sqrt{s}_{NN}$ = 200 GeV and U+U at $\sqrt{s}_{NN}$ = 193 GeV collisions respectively are presented. The objective of the thesis is to understand the properties of thermalized system created in heavy-ion collisions. The thesis is organised as follows: *Chapter 1* of the thesis has introduced some basic concepts of particle physics, QCD and its phase diagram, and QGP signature. *Chapter 2* gives an overview of the Relativistic Heavy Ion Collider (RHIC) and will focus primarily on the STAR detector. *Chapter 3* In this chapter the review of the measurements of ϕ-meson production in heavy-ion experiments is presented. The energy dependence of ϕ-meson invariant yield and the production mechanism, strangeness enhancement, parton energy loss, and partonic collectivity in nucleus-nucleus collisions are discussed. Effect of later stage hadronic re-scattering on elliptic flow (v_2) of proton is also discussed relative to corresponding effect on ϕ-meson v_2. In *Chapter 4*, we discuss the data set, various kinematical cuts like event cuts, track cuts and particle identification method and ϕ-meson reconstruction in Au+Au collisions at $\sqrt{s}_{NN}$ = 200 GeV is discussed. *Chapter 5* gives various previous results on elliptical flow and the various method to obtain flow are discussed. In *Chapter 6*, we present the various corrections done to obtain ϕ-meson v_n, the p_T and centrality dependence of ϕ-meson v_n in Au+Au collisions at $\sqrt{s}_{NN}$ = 200 GeV. In addition, we also discuss the ϕ higher harmonic ratio and their possible implications. In *Chapter 7*, the results of transverse momentum correlations for U+U collisions at $\sqrt{s}_{NN}$ = 193 GeV are discussed. These results are compared with the published results from Au+Au and Cu+Cu collisions at $\sqrt{s}_{NN}$ = 200 GeV. *Chapter 8* finally summarizes and concludes all the results obtained in this thesis.

Chapter 2

The STAR Experiment

2.1 Introduction

The analysis done in the present thesis pertain to Au+Au and U+U data taken by the Solenoidal Tracker At RHIC (STAR) which is a detector installed at the RHIC accelerator facility. The Relativistic Heavy Ion Collider (RHIC) [83] is located in the Brookhaven National Laboratory (BNL) on Long Island, NY, USA. For almost six decades, BNL has been on the forefront of high energy nuclear and particle physics research. This program is driven by the Alternating Gradient Synchrotron (AGS) that has been operating since 1960. Apart from the fixed target experiments the AGS currently serves as an injector for Relativistic Heavy Ion Collider (RHIC). Approved in 1984, the construction of RHIC collider started in 1991 and the first Au+Au collisions for physics were provided in 2000. Until initiation of the LHC, it was the biggest heavy-ion collider in the world. In 15 years of its operation, the experiments at RHIC have collected huge amounts of physics data. The physics program at RHIC consists of 4 main branches: ultra-relativistic heavy-ion collisions (Au+Au, Cu+Cu), high energy spin physics (p+p collisions in various spin configurations), investigation of initial state of nuclear collisions (d+Au) and the beam energy scan (6 GeV-200

GeV). The STAR experiment [84] is one of the detectors collecting data from collisions provided by the RHIC collider. In this chapter the RHIC experimental facility and the STAR detector are described in detail.

2.2 Relativistic Heavy Ion Collider

The main goal of the heavy ion program at RHIC is to produce a new form of matter, QGP, and to QCD at high energies and temperatures. RHIC also collide spin-polarized proton beams, and is still the most powerful polarized-proton collider. The schematic diagram of the RHIC accelerator facility is shown in the Figure 2.1. The

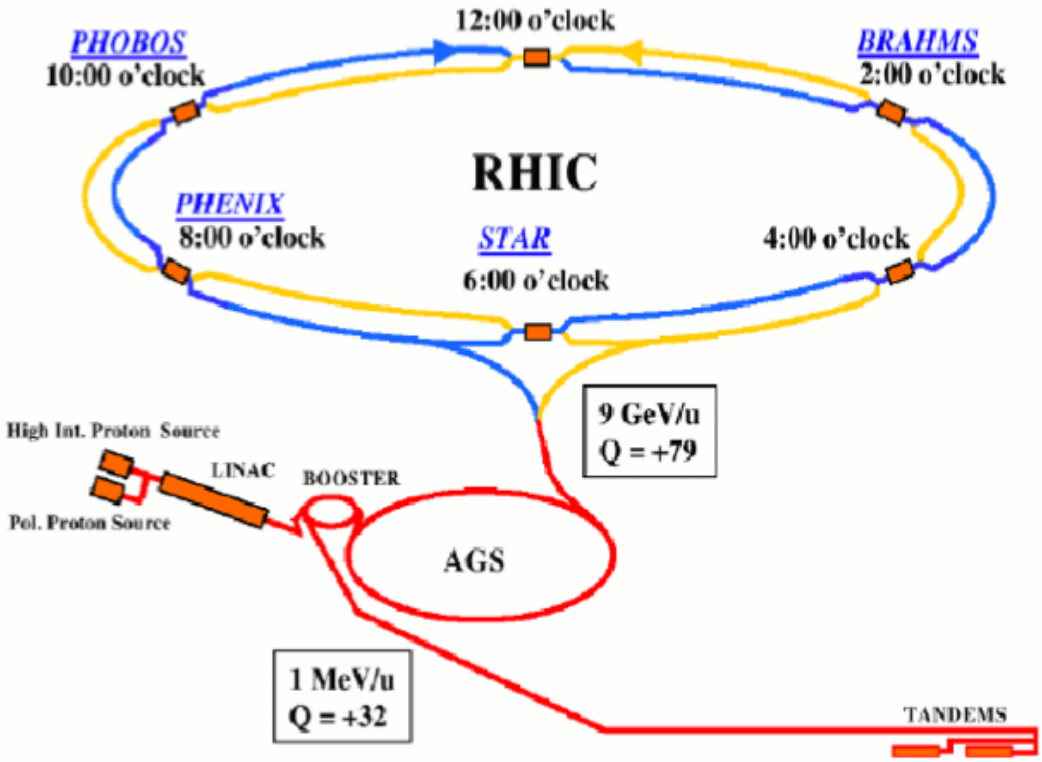

Figure 2.1: *The RHIC accelerator scheme. Figure taken from Ref. [85]*

3.8 km circumference RHIC tunnel houses an intersecting two-ring superconducting

hadron collider. The accelerator chain starts with an optically-pumped polarized H^- ion source [86] producing H^- ions at an energy of 35 KeV to be accelerated to 200 MeV with a radio-frequency quadrupole and Linear Particle Accelerator (LINAC). The ions are then stripped of electrons by passage through a foil, creating a proton beam for injection into the Booster synchrotron [87] which further accelerates it to 2 GeV, and then to the Alternating Gradient Synchotron (AGS) which boosts them to $\sim$ 23 GeV. Finally the proton beam is split and injected into the RHIC ring while the heavy ions to be collided originate from a pulsed sputter ion source [88] and than accelerated to 1 MeV/nucleon using the Tandem Van de Graaff accelerator, sent through the Tandem-to-Booster line to the Booster Synchrotron, further stripped and accelerated, and injected into the AGS. The ions are stripped of their remaining electrons, and ions are bunched together and accelerated to 10.8 GeV/A and transferred to RHIC. In the RHIC storage rings, the counter-rotating beams are steered and accelerated with the use of superconducting magnets, and intersect at six collision points on the ring. The maximum center-of-mass energy per nucleon RHIC can achieve with Au+Au collisions is 200 GeV, with U+U collisions it is 193 GeV and protons are accelerated upto $\sqrt{s}_{NN}$ = 500 GeV. In addition, RHIC can also collide heavy ions at lower energies. This has been utilized by the recent Beam Energy Scan (BES) program at RHIC, which has collided Au+Au ions at various energies from $\sqrt{s}_{NN}$ = 7.7 GeV to $\sqrt{s}_{NN}$ = 62.4 GeV. Since RHIC has independent rings and ion sources, it can also collide unequal ion species, such as Cu+Au, He+Au and d+Au. The d+Au has particular importance in exploring the Cold nuclear matter effects. In 15 years of its operation, numerous upgrades of the RHIC accelerator (such as stochastic beam cooling [89]) allowed to exceed the design luminosities and the luminosity is still being developed and improved. The Integrated nucleon-pair luminosity[1] for heavy-ions and proton-

[1]The nucleon-pair luminosity is defined as $L_{NN} = A_1 A_2 \mathrm{L}$, where L is the luminosity, and A_1 and A_2 are the number of nucleons of the ions in the two beams respectively.

proton collision is shown in Figure 2.2 [90]. There is planned upgrade to eRHIC, an

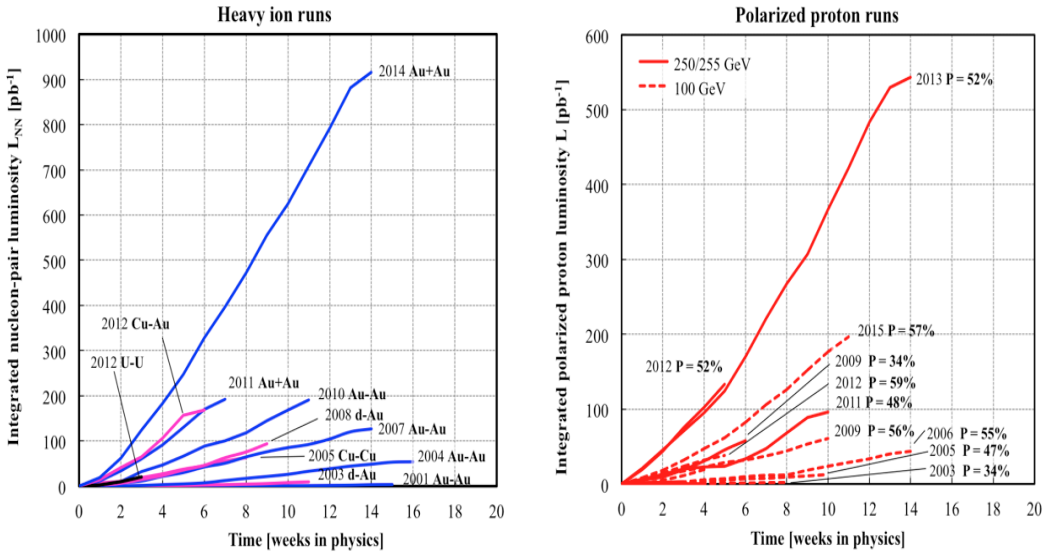

Figure 2.2: *RHIC integrated luminosity for heavy ion and proton-proton collision [90].*

electron-ion collider [91], which will further expand the range of collision species, and increase the range of momentun species (x) that can be probed at RHIC. This year, RHIC run 10.9 weeks of polarized p+p collisions at $\sqrt{s} = 200$ GeV, 5.1 weeks of p+Au collisions at $\sqrt{s_{NN}} = 200$ GeV with transverse polarization of the proton, and 1.9 weeks of p+Al collisions $\sqrt{s_{NN}}$= 200 GeV with transverse polarization of the proton. In 2016, RHIC will run 10 weeks of Au+Au collisions $\sqrt{s_{NN}} = 200$ GeV, 7 weeks of Au+Au and p+p collisions at $\sqrt{s_{NN}} = 62$ GeV, or 7 weeks of polarized p+p collisions at 510 GeV. The summary of RHIC runs is given in Ref [90]. The RHIC project houses experiments at four of the collision points: STAR [92], PHENIX [93], BRAHMS [94] and PHOBOS [95], with only STAR and PHENIX currently in operation. The STAR detector and its various subsystem are described in detail below:

2.3 The STAR Detector

The layout of The Solenoidal Tracker at RHIC (STAR) is shown in Figure 2.3. It is a large acceptance experiment that is designed to focus on interesting physics at midrapidity. The main physics goal is to study the formation, evolution and characteristics of the strongly coupled Quark Gluon Plasma (QGP). It is designed primarily for charged hadron production measurements with high precision tracking and momentum over a large solid angle. The whole detector is enclosed in a solenoidal magnet that provides a uniform magnetic field parallel to the beam direction. The STAR magnet [96] is designed as a cylinder with a length of 6.85 m and has inner and outer diameter of 5.27 m and 7.32 m, respectively. The maximum magnetic field along the z direction is $\mid B_z \mid = 0.5$ T. STAR has been run in full field, reversed full field and half field configurations.

The primary tracking detector is the Time Projection Chamber (TPC). The TPC has full azimuthal acceptance and a maximum acceptance in pseudorapidity of $\mid \eta \mid \leq 1.8$. The TPC extends from a radius of 50 cm to 200 cm from the beam axis and is 4.2 m in length along the beam axis. The TPC is only sensitive to charged particles, although the decay vertices from neutral hadrons can be reconstructed from tracks of charged decay products left in the TPC. In addition to the TPC, there are Forward Time Projection Chambers (FTPC) with coverage in pseudorapidity of $2.5 < \mid \eta \mid < 4$ and complete azimuthal coverage.

The Time Of Flight (TOF) detector is surrounding the TPC which has pseudorapidity coverage ($\eta < 0.9$) and full azimuthal coverage. The TOF improves the low and moderate p_T range particle identification, extends π/K separation from 0.7 GeV/c to 1.6 GeV/c and proton (π, K) separation from 1.1 GeV/c to 3 GeV/c. It has also two Electro-Magnetic Calorimeter, Barrel Electro-Magnetic Calorimeter (BEMC) located outside of the TPC covers $\mid \eta \mid < 1$ with complete azimuthal symmetry and the

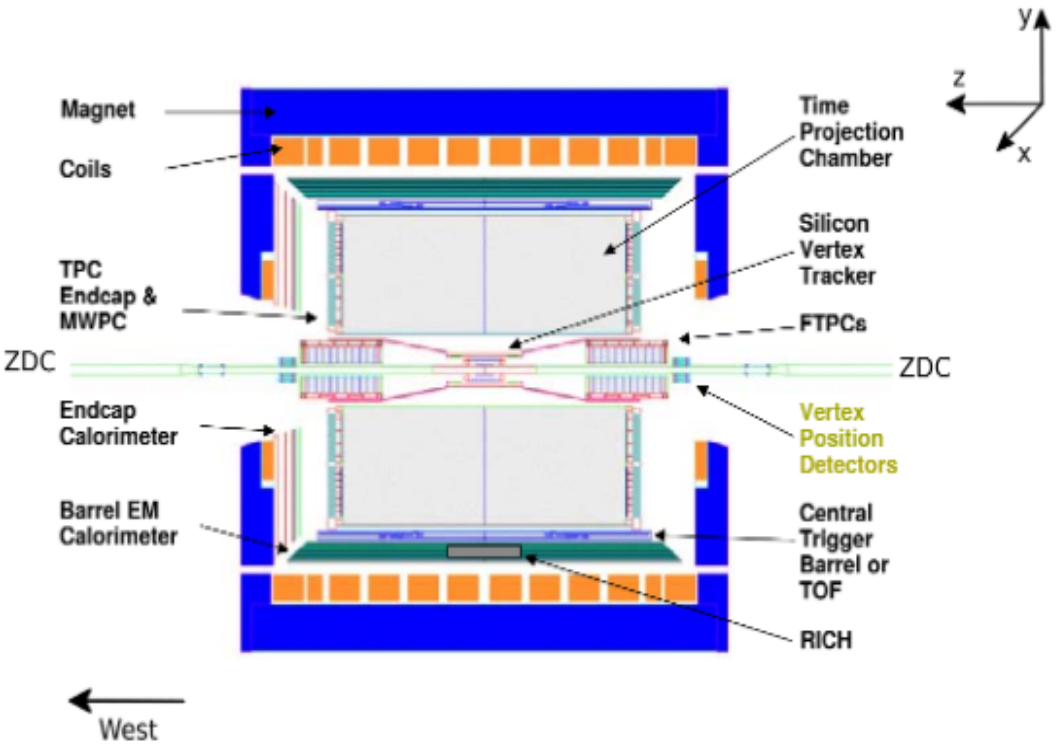

Figure 2.3: *An illustration of a cutaway side view of the STAR detector [97]*

Endcap Electro-Magnetic Calorimeter (EEMC) coverage for $1 <|\eta|< 2$, over the full azimuthal range. The EMCs are used to distinguish high momentum single photons from photon pairs of π and η meson decays and electrons from charged hadrons. The EMCs are also used as a high p_T hadron and electron trigger. Along the beam pipe, there are some trigger detectors: two upgraded pseudo Vertex Position Detectors (upVPD), a Beam Beam Counter (BBC), and two Zero-Degree Calorimeters (ZDC). The two upVPDs are installed 5.4 m away from the TPC center on both sides. It provides the start time to TOF for trigger purposes. The BBC consists of two scintillator annuli mounted on the east and west side out of the STAR magnets, with a pseudorapidity coverage of $3.3 <|\eta|< 5.0$. ZDC is the farthest detector from the collision center. The two ZDCs are located at 18 m from the TPC center, from east and west. They measure the shower energy deposited in scintillators by neutrons and serve as a trigger detector as well as a monitor of the RHIC luminosity. The STAR detector is an excellent mid-rapidity detector, with large pseudorapidity coverage and an excellent PID, which can detect nearly all particles produced at RHIC to study the spectra, flow and particle correlations. In this thesis, TPC and TOF are used for the analysis which are described below along with other detectors:

2.3.1 The Time Projection Chamber

The Time Projection Chamber is the primary tracking component of the STAR detector. As shown in Figure 2.4, the STAR TPC is cylindrical around the beam pipe and sits inside the STAR magnet with a magnetic field of up to 0.5 T parallel to the beam pipe. The TPC central membrane and field cage create an electric field of 135 V/cm that is parallel to the beam pipe. The TPC is 4.2 m long with an outer diameter of 4 m and an inner diameter of 1 m. The magnetic field bends charged particles as they move through the TPC, allowing determination of momentum. When a charged

particle traverses the gas volume, it liberates the electrons from the molecules in the gas. These ionization electrons are accelerated through the TPC by the electric field until they reach a constant speed which is a characteristic of the gas and the electric field. They move roughly two orders of magnitude faster than the ionized gas and

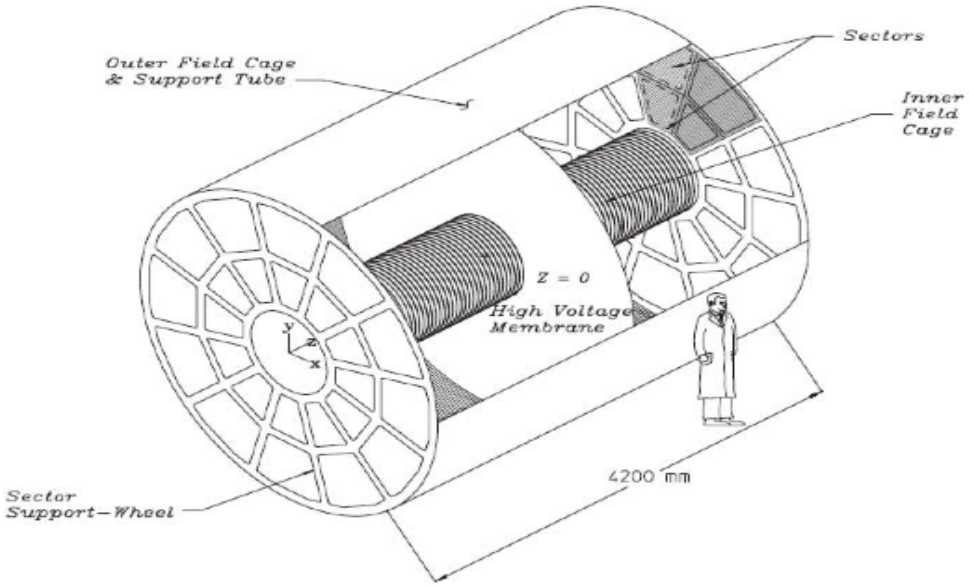

Figure 2.4: *The STAR TPC is 4.2 m long and 4 m in diameter, surrounding a beam-beam interaction region at RHIC [98]*

therefore will be collected first. For sufficiently low event rates, the ions can be neglected; for higher rates of events, ions can create significant local distortions in the electric field that alter the trajectory of nearby ionization electrons and can impair momentum resolution unless these field distortions are corrected for. The position in the plane perpendicular to the beam (the x-y plane) is determined by the location where the ionization electrons are collected on the readout pads. The position in the direction along the beam axis (the z-axis) is determined by the time that it takes the ionization electrons to reach the endcap, hence the name Time Projection Chamber.

The drift volume of TPC is filled with P10 gas (90% Ar, 10% CH4) at 2 mbar above the atmospheric pressure [98]. The P10 gas has an advantage of fast drift velocity which peaks at a low electric field. Operating on the peak of the velocity curve makes the drift velocity stable and insensitive to small variations in temperature and pressure. Low voltage greatly simplifies the field cage design. The drift velocity of P10 gas is 5.45 $cm/\mu s$. The transverse diffusion in P10 gas is about σ T = 3.3 mm after drifting 210 cm. The longitudinal diffusion of a cluster of electron that drifts the full length of the TPC is σ L = 5.5 mm.

The readout system of the TPC is based on Multi-Wire Proportional Chambers (MWPC) with pad readout [99], to gather drifting electrons for charged particle's energy loss and position measurement. The readout pads are in concentrical rows in 12 super sectors along the ϕ distribution. Each readout super sector consists of inner and outer radius sub-sectors, which are designed to optimize different measurements [99]. Figure 2.5 shows the inner and outer sub-sectors of one readout pad. The outer sub-sectors are designed to optimize the dE/dx measurement with continuous pad coverage. The inner sub-sectors are in the region of highest track density, thus they are optimized for good two-hit resolution to improve the two track resolution. The energy loss (dE/dx) in the TPC gas is used for particle identification. The Figure 2.6 shows the dE/dx as a function of momentum for particles in the TPC. The energy loss of a charged particle is measured by the deposit charge collected on the pad rows. The deposit charge are from drifting electrons liberated by the charged particles. The dE/dx is extracted from the energy loss measured on up to 45 pad rows. Energy loss of a charged particle for a given track length can be described by the Bichsel function [100] . However, the mean of the distribution is sensitive to the fluctuations in the tail of the distribution. Therefore, the most probable energy is measured by removing the highest 30% measured clusters.

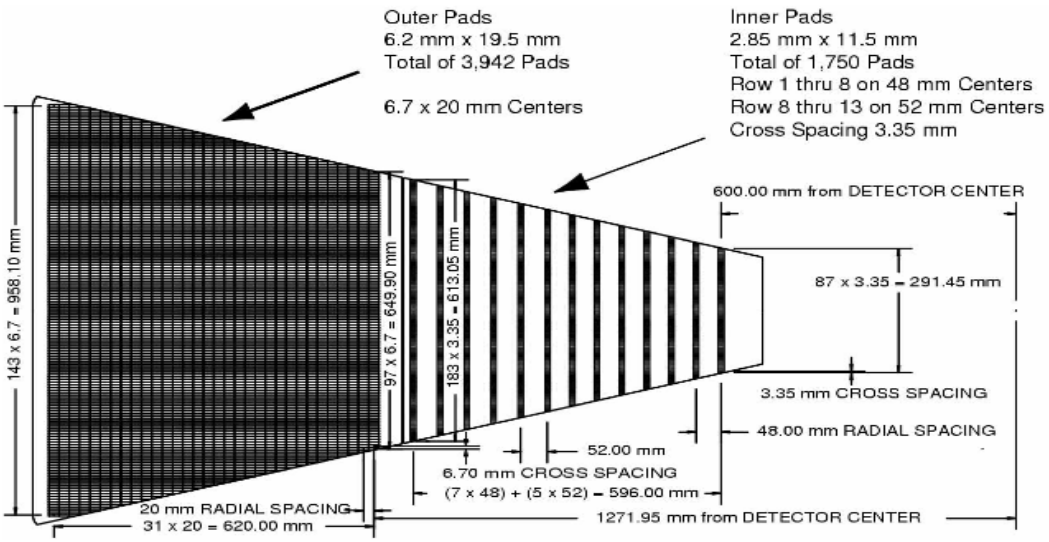

Figure 2.5: *The inner sub-sector is on the right and it has small pads arranged in widely spaced rows, the outer sub-sector is on the left and it is densely packed with larger pads [99]*

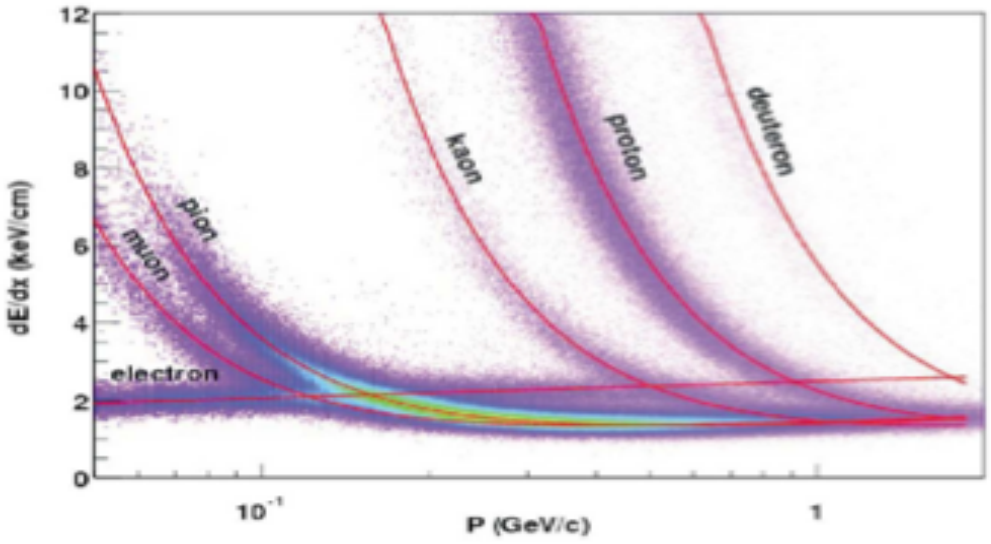

Figure 2.6: *Ionization energy loss of charged particles in STAR TPC [99]*

2.3.2 The Time-of-Flight Detector

A full-barrel Time-of-flight (TOF) system positioned just outside the TPC was built to extend the direct PID capabilities of STAR to higher momenta. It measures the flight time of the particle from the vertex of the collision till the particle hits the detector. The system consists of two separate detector subsystems. One is the upgraded Vertex Position Detector (VPD) (explained in detail in subsection 1.3.6.) which provides the start time. The other one is the Time of Flight detector (TOF), which provides the stop time. Figure 2.7 shows the time-of-flight system. The TOF

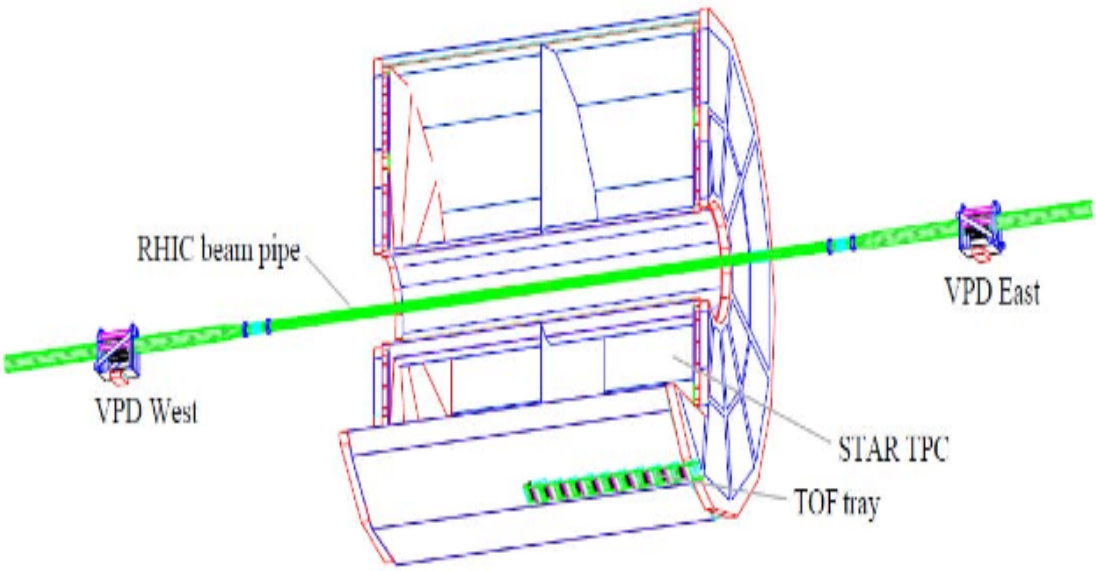

Figure 2.7: *A schematic diagram of the location of VPD and TOF detectors. The figure is taken from [101]*

detector are based on the Multigap Resistive Plate Chamber (MRPC) technology. The time intervals of interest for particle flight time measurement are defined by the electronic signals from these detectors. The VPD consists of two identical detector assemblies which are very close to the beam pipe, sitting on each side of the STAR

detector system with equal space [101]. In Au+Au collisions, a lot of high energy forward photons are produced, travelling away from the collision vertex effectively as a prompt pulse. Measuring the time of those forward particle pulses arrive at VPD on each side of the STAR provides the location of the collision vertex along the beam line. In the meanwhile, the average of the two arrival times is used as the collision time, or the start time of the event. The TOF trays are inside the STAR magnet and immediately outside the TPC, covering a pseudorapidity of ± 1.0 units. There are 120 trays, half of them are installed on the east side ($z < 0$), and half of them are installed on the west side ($z > 0$). Each tray covers 6 degree in azimuthal direction (ϕ) around the TPC. When the charged particle hit the TOF, it will trigger the trays, and the TOF provides the stop time for each particle. In central Au+Au collisions, the start time resolution from the VPD is about 28 ps, the end time resolution from TOF is about 82 ps, and the total time resolution of the TOF system is about 87 ps.

The primary particles produced in the heavy-ion collisions can be identified directly through the flight time along with particle momentum measured by TPC. The inverse velocity as a function of momentum for particle is shown in Figure 2.8. Pions, kaons and protons can be distinguished with a momentum up to about 1.5 GeV/c, and protons can be identified from pions and kaons up to about 3 GeV/c [101, 102]. On the other hand, the particle decayed from a secondary vertex, cannot be identified by TOF directly, because the flight time measured by the TOF system consists of the flight time of its parent particle. One way of using the TOF to identify weak decayed particle, is to reconstruct the parent and calculate the parents flight time. With the parent's flight time subtracted from the TOF measured time, the new time can be considered as the real flight time for the decay daughter. More details about TOF system can be found in Ref [101].

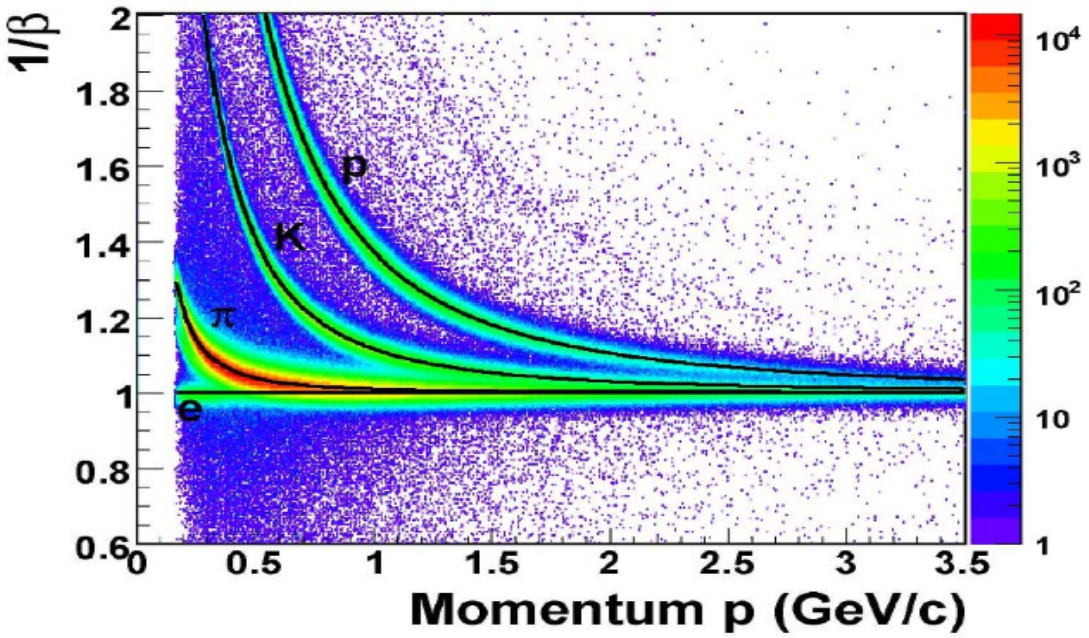

Figure 2.8: *Particle identification using the STAR Time of Flight (TOF) detector. Proton, kaon, pion and electron bands are clearly separated*

2.3.3 Barrel Electromagnetic Calorimeter

The Barrel Electromagnetic Calorimeter (BEMC) [103] is lead-scintillator calorimeter located between the TPC and STAR magnet and covering $\mid \eta \mid < 1$ and has full azimuthal acceptance. It is used to measure the energy deposits associated with jets, leading hadrons, direct photons, and electrons produced in large p_T processes. It measures the transverse energy deposited in electromagnetic showers from neutral and charged particles. Charged hadrons deposit a minimum amount of energy as a narrow electromagnetic shower in the lead scintillator material. Photon pair produced in the lead material and Bremsstrahlung resulting in further pair production creating a wider electromagnetic shower than hadrons.

The calorimeter consists of 120 modules, covering one unit of η and 0.1 rad in azimuthal. Each module is 26×293 cm^2 and 23.5 cm deep covering $\Delta\eta \times \Delta\phi = 1.0 \times 0.6°$. The modules consist of 40 towers. A tower covers $\Delta\eta \times \Delta\phi = 0.05 \times 0.05$ and consists of 20 layers of lead and 21 layers of Kuraray SCSN-82 scintillator layers interleaved as shown in Figure 2.9. The towers can measure the energy precisely and isolate electromagnetic showers but its spatial resolution is not fine enough to measure the shower shape and shower size to distinguish direct γ and π^0. The Shower Maximum Detector (SMD) was embedded into the BEMC to provide fine spatial resolution [103]. The conceptual design of the SMD is shown in Figure 2.10. The SMD sits at about 5 radiation length depth in the calorimeter modules, at $\eta = 0$, including all material in front of the calorimeter. The STAR SMD has a unique feature of double layer design. A two sided aluminum extrusion provides ground channels for two independent planes of proportional wires. In the η and ϕ directions, there are independent PC Board cathode planes with strips etched allowing two dimensional size measurement of the shower. The SMD is a wire proportional counter-strip readout detector using gas amplification. The aluminium extrusion has 5.9 mm wide channels

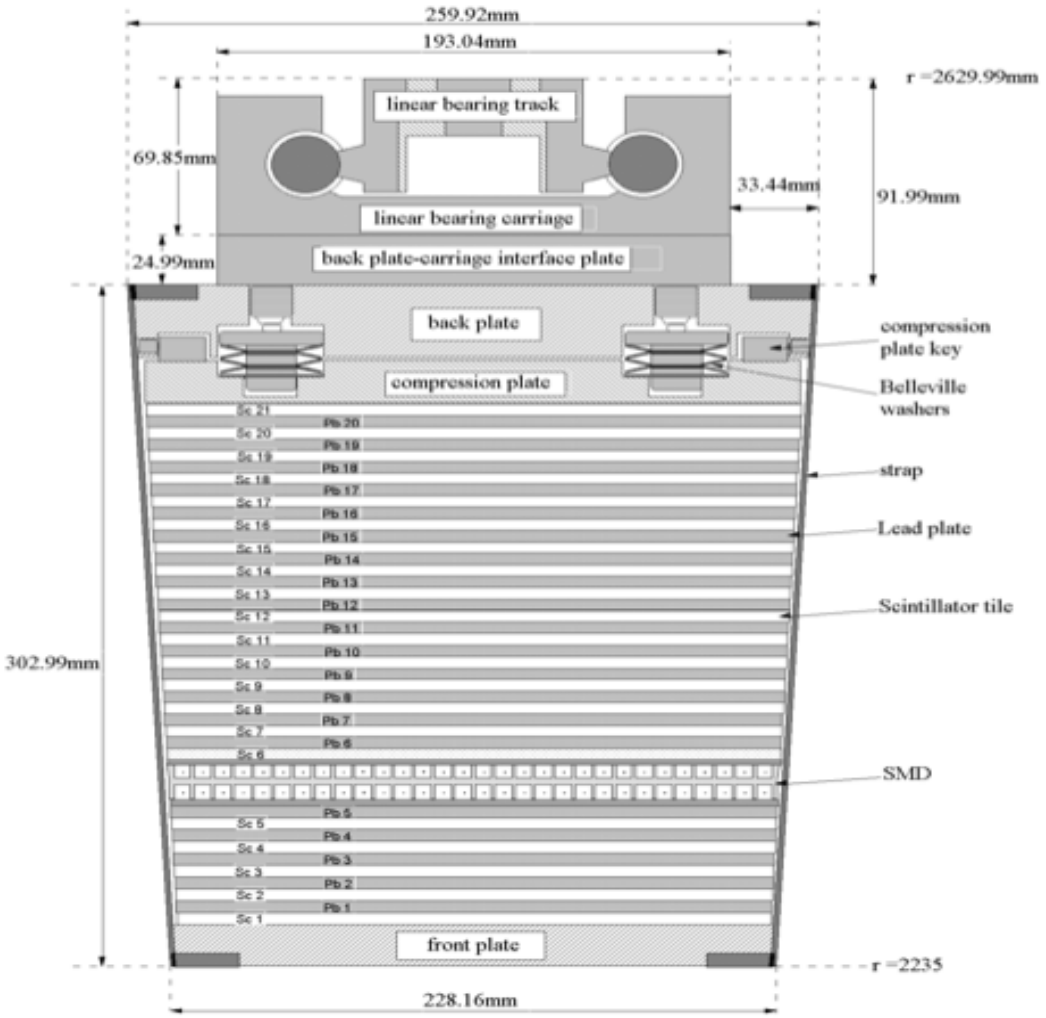

Figure 2.9: *Side view schematic of a BEMC module. The two layers comprising the shower maximum detector are labeled between the lead and scintillator layers [103]*

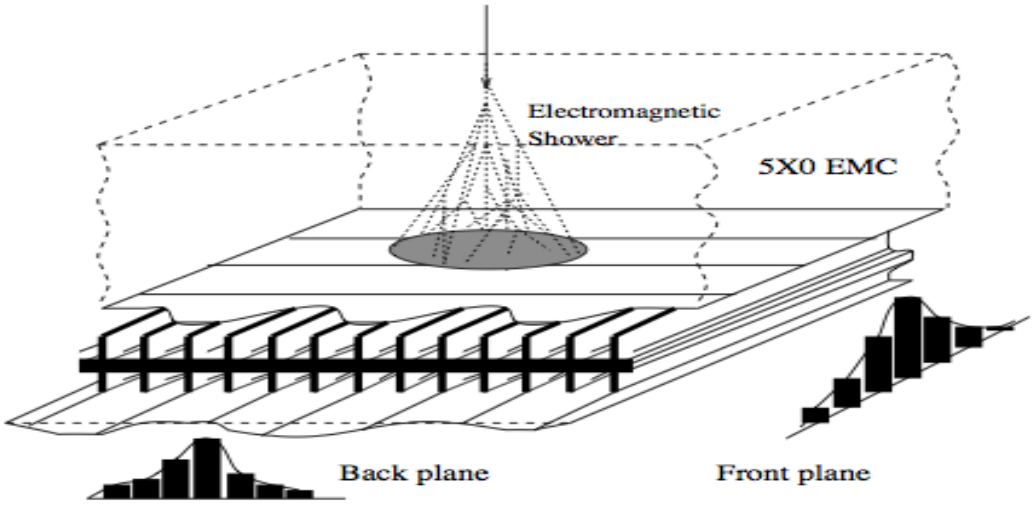

Figure 2.10: *Schematic view of the BEMC shower maximum detector. Two independent wire layers in the η and ϕ direction allow to measure electromagnetic showers more precisely [103]*

running in the η direction, and 50 μm gold-plated tungsten wires in the center. The detector strips sense the induced charge from the charge amplification near the wire. There are two sets of strips around the wire outside the aluminum extrusion, one is parallel to the wire channel while the other one is perpendicular to the wire, The two sets of strips provide an image of the shower spatial distribution in the η direction and ϕ direction. Each of these strips span 30 channels (30 wires), the strip perpendicular to wires has size of 0.1 radians in ϕ ($\approx$ 23cm, i.e. the module width) and 0.0064 in η($\approx$ 1.5cm at low η), the parallel strip is physically 1.33 cm wid and has length 0.1 units in η, while the wires are 1.0 units in η.

2.3.4 Endcap Electromagnetic Calorimeter

The EEMC has pseudorapidity coverage of $1 < \eta \leq 2$, over the full azimuthal range, supplementing the BEMC (discussed in the previous section). Within this accep-

tance, it will add the capabilities to detect photons and electromagnetically decaying mesons (π^0, η), to identify electrons and positrons, and to trigger on high-energy particles of these types. The EEMC will include a shower-maximum detector optimized to discriminate between photons and π^0 or η mesons over the 10-40 GeV energy region, as well as preshower and postshower layers intended for electron vs. hadron discrimination. Furthermore, it will significantly enhance the acceptance and triggering capabilities of STAR for jets. The further detail of EEMC detector can be found in Ref [104]

2.3.5 Beam Beam Counters

The Beam-Beam Counter (BBC) detector is a pair of scintillating counter that can be found 3.75 m from the center of the STAR detector on both the east and west sides of STAR. The center is defined at z = 0, where the z-axis is defined by the magnetic field. The BBC has an inner ring and an outer ring with different sized tiles on them, which can be seen in Figure 2.11. The pseudorapidity coverage (η) of these inner tiles is $3.4 <| \eta |< 5.0$. The BBC's mainly provide a minimum bias trigger for p+p collisions. In Au+Au collisions, many mid-rapidity tracks and spectator neutrons can be used as trigger, however these signatures are absent in p+p collisions. The signals from the tiles are sent down a fiber optic cable to magnetically-shielded photomultiplier tubes (PMTs) for readout. The coincidence of the signals in the east and west BBC's form a minimum bias trigger in p+p collisions with efficiency for non-singly diffractive events of $87 \pm 8\%$. This coincidence in the BBCs indicates that a collision has occured near the center of the detector.

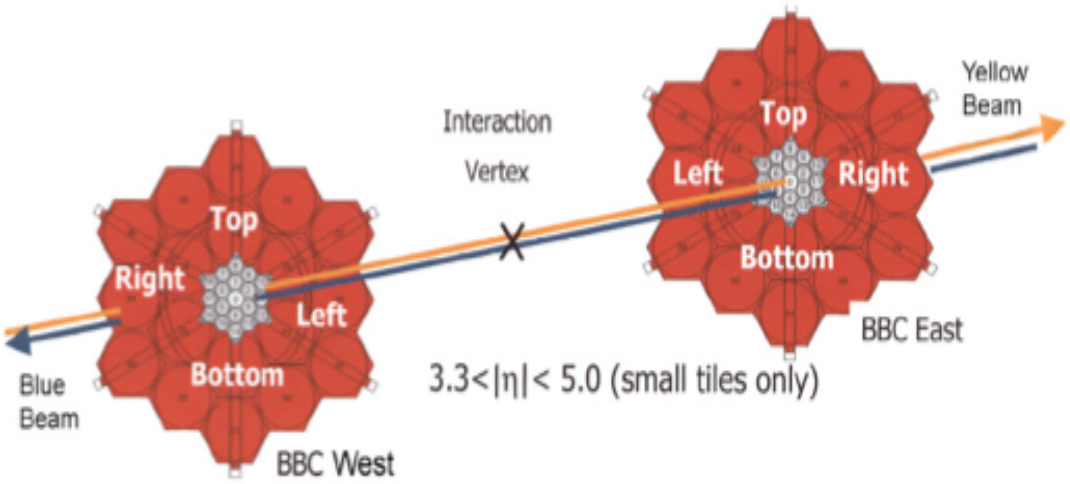

Figure 2.11: *Schematic of STAR's BBC East and BBC West [105]*

2.3.6 Vertex Position Detector

The Vertex Position Detectors (VPD) [106] exist as two identical detector assemblies, one on the east and one on the west of STAR at a distance of 5.6 m from z = 0. The VPD detectors use photomultiplier tubes to determine the start time of a collision/TOF. An East-West VPD coincidence is required for minimum-bias Au+Au events. The VPD can be used to determine the location along the z-axis where the collision that fired the VPD took place. This location is called the vertex location, with the z position being given the label V_z. The VPD can not determine V_x or V_y. The V_z from the VPD can be used in conjunction with the TPC to select in-time events [107]. Each VPD assembly consists of nineteen detectors, a side view of which is shown in Figure 2.12. Each detector housing is a 2 inch outer diameter and 0.049 inch thick aluminum cylinder with 3/8 inch thick aluminum front and back caps. Inside this cylinder is a 0.25 inch non-conducting spacer, then the active elements consisting of a 0.25 inch (1.13 radiation lengths) Pb converter, and a 1 cm thick

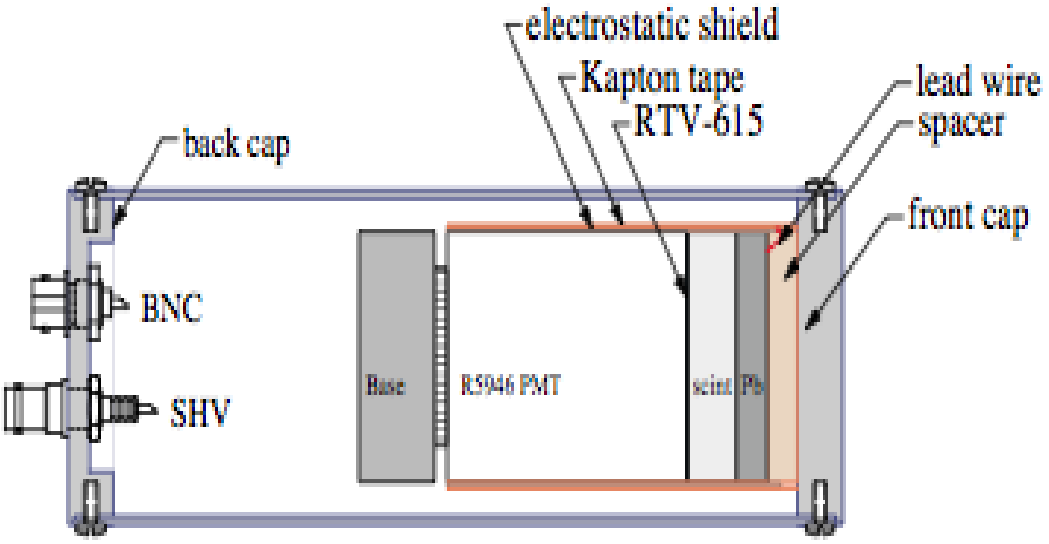

Figure 2.12: *A schematic side view of VPD detector [106]*

scintillator (Eljen EJ-204) coupled to a 1.5 inch diameter Hamamatsu R-5946 mesh dynode PMT via RTV-615 optically transparent silicone adhesive.

2.3.7 Zero Degree Calorimeter

Zero Degree Calorimeters (ZDCs) [108] are hadronic tungsten calorimeters used for detecting primarily neutrons. Two ZDC detectors are located 18 m away, past the DX magnets, on either side from the interaction point as shown in Figure 2.13. The DX magnets bend the charged particles allowing mostly neutral charged particles to hit the ZDC detectors. The ZDC detectors sample with a transverse area of 10×13.6 cm^2 with respect to the beam. ZDCs are composed of three modules made from alternating layers of tungsten absorber and Cerenkov fiber ribbons placed 45° relative to the incident beam. The fiber angle optimize the collection of Cerenkov light produced from the secondary showers [109]. A Shower Maximum Detector (SMD) resides between the first and second ZDC module. The SMD is composed of eight horizontal and seven vertical slats. Each horizontal(vertical) slat comprises of four(three) fiber

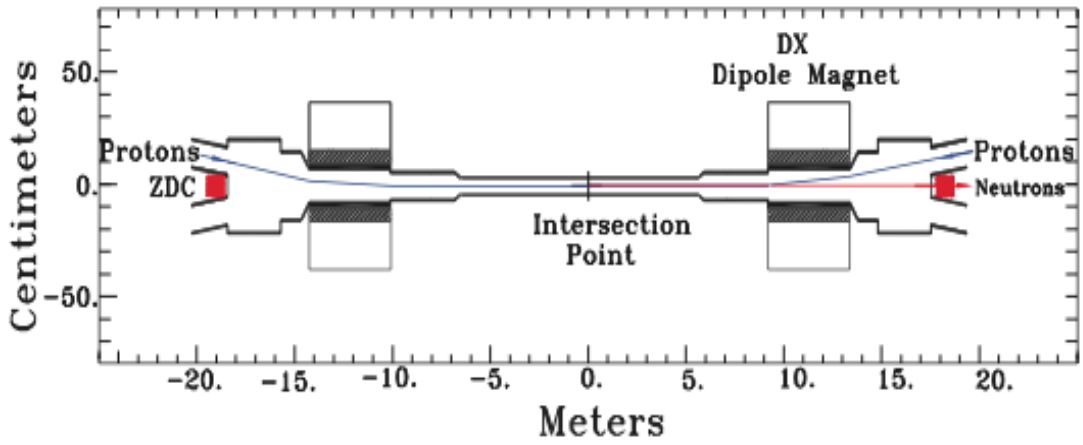

Figure 2.13: *Schematic layout of the ZDC detector at STAR. The red boxes show the location of the ZDC detectors. The charged proton beam shown by the blue line are bent by the DX magnets allowing only neutrons shown by the red line to traverse into the ZDC detectors [108]*

strips. The signal collected from the strips go to 16-pixel multi-anode photomultiplier tubes. The SMDs allow to determine the initial shower positions. The ZDCs measure the energy of neutrons associated with the spectator matter, and they are used for beam monitoring, triggering and locating interaction vertices [110, 111].

2.3.8 Recent Upgrade

In the year 2013-14, the STAR detector system has introduced two new subsystems i,e Muon Telescope Detector (MTD) and Heavy Flavor Tracker (HFT). MTD is installed in the most outside of all subsystem, which is specifically meant for the μ detection. MTD is based on the long-MRPC technology, it covers $|\eta|<0.5$ in terms of pseudorapidity and 2π in azimuthal direction. It uses the BEMC and the magnet steel as the absorber for electrons and hadrons. Its first prototype was installed in STAR in the year 2007 and showed good performance. In 2013, MTD had been fully

installed and tested, however the significant data set was taken with it in the year 2014. The most recent detector added into the STAR system is the HFT, which has been included in 2014, it is a inner vertex detector and is positioned between Beam pipe and TPC. The HFT is a state-of-art micro-vertex detector utilizing active pixel sensorsand silicon strip technology. The HFT consists of 4 layers of silicon detectors grouped into three subsystems with different technologies, guaranteeing increasing resolution when tracking from the TPC towards the vertex of the collision. The Silicon Strip Detector (SSD) is an existing detector in double-sided strip technology. It

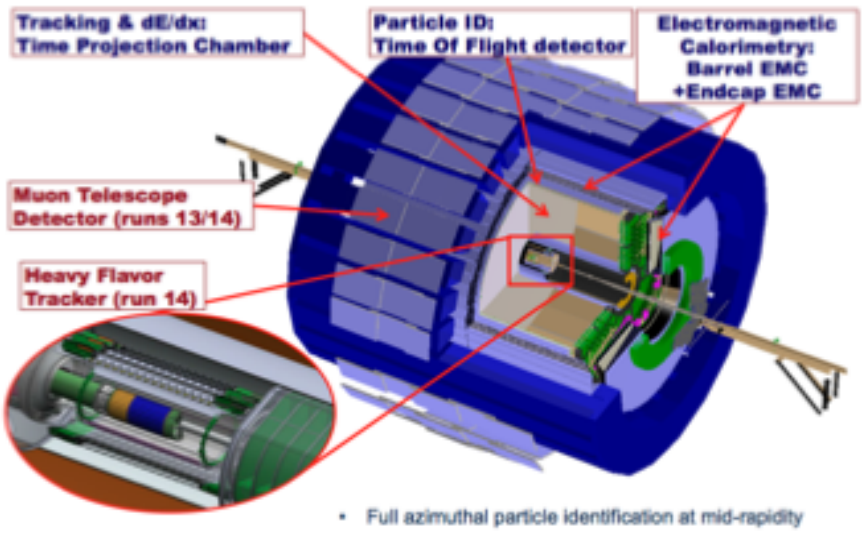

Figure 2.14: *Schematic view of the STAR system including the MTD and the HFT [112]*

forms the outermost layer of HFT. The Intermediate Silicon Tracker (IST), consisting of a layer of single-sided strip-pixel detectors, is located inside the SSD. Two layers of silicon Pixel detector (PXL) are inside the IST. The PXL detectors have the resolution necessary for a precision measurement of the displaced vertex. With the HFT, the TOF, the TPC, and the BEMC, the STAR will study the physics of mid-rapidity charm and bottom production. The schematic of the cutaway STAR-detector with

some of its main component detectors along with the MTD and the HFT is given in Figure 2.14. The primary motivation for the HFT is to extend STAR's capability to study heavy flavor production in p + p, p + A and A + A collisions by the measurement of displaced vertices and the direct topological identification of open charm hadrons. The yield and distribution of bottom hadrons will be estimated from the charm production and non-photonic electron measurements and also via the impact parameter reconstruction of their decay electrons. The primary physics topics to be addressed by the HFT include heavy flavor energy loss, flow, and a test of partonic thermalization at RHIC. These measurements have been identified as necessary goals for the RHIC program in the Nuclear Physics Long Range Plan and in the RHIC mid-term scientific plan [113].

2.4 STAR DAQ

The design and implementation of the STAR DAQ system [114, 115] was driven by the characteristics of STAR's main detectors, a large Time Projection Chamber (TPC), and to a lesser degree two smaller Forward TPCs (FTPC) [116] and a Silicon Vertex Tracker (SVT) [117]. Together, these detectors produce 200 MB of data per event and are able to read out events at 100 Hz. The RHIC Computing Facility (RCF) manages the storage of raw data for all of the RHIC experiments using an High Performance Storage System (HPSS) hierarchical storage system. By balancing the expected rate of offline data analysis with the rate of data production, resources were allocated to STAR to support sustained raw data rates of up to 30 MB/sec for steady state operation. The central task of the STAR DAQ system is then to read data from the STAR detectors at rates up to 20,000 MB/sec, to reduce the data rate to 30 MB/sec, and to store the data in the HPSS facility.

The large input data rate to the DAQ system demands parallel processing at the

DAQ front end. Multiple Receiver Boards [118] receive data in parallel on separate optical fibers from the detectors. The Receiver Boards (RBs) are grouped together in VME crates. Each crate is controlled by a Detector Broker CPU (DET). There are 12 DETs for the TPC, two each for the SVT and FTPC, and one for each additional detector. We use two strategies to reduce the data volume. First, we zero-suppress the data to reduce the event size to 10 MB for central events. Secondly, we apply a physics-based filter, the Level 3 Trigger (L3) [119], to choose which events to write to tape. The L3 must find on the order of 1500 tracks in the TPC and make trigger decisions based upon them within 200ms. This limits the time available for DAQ front-end processing, and creates the need for a farm of $\sim$50 CPUs integrated within DAQ dedicated to tracking.

The management of events within the DAQ system can be described in two phases according to whether the build decision for that event has been made by L3. Before the decision, the Global Broker (GB) handles the overall management of the event. At the same time as the data are read from the detectors into the DETs, the GB receives a token and trigger detector data from the Trigger/DAQ Interface (TDI) via the Myrinet network. The GB assigns L3 processors to analyze the event and waits for an event decision. If the event is rejected by L3, GB instructs the DETs to release the buffers associated with the event and returns the token to TDI for re-use. If the event is accepted by L3, responsibility for the management of the event is transferred to the Event Builder (EVB). The EVB collects and formats all of the contributions. At this time, EVB instructs the DETs to release the buffers associated with the event and passes the event to a Spooler (SPOOL) which handles the writing of the event to RCF.

Chapter 3

A Review on ϕ Meson Production in Heavy-Ion Collision

3.1 Introduction

Quantum Chromodynamics (QCD) [120, 121, 122, 123] predicts that at very high temperature (T) and/or at high density a deconfined phase of quarks and gluons is expected to be present, while at low T and low density the quarks and gluons are known to be confined inside hadrons. The heavy-ion collisions (A+A) provide a unique opportunity to study QCD matter in the laboratory experiments. The medium created in the heavy-ion collisions is very hot and dense and also extremely short-lived ($\sim$ 5 - 10 fm/c). In experiments we only able to detect the freely streaming final state particles. Using the information carried by these particles as probes, we try to understand the properties of the medium created in the collision. The ϕ vector meson, which is the lightest bound state of s and $\bar{s}$ quarks, is considered as good probe for this study. It was discovered at Brookhaven National Laboratory in 1962 through the reaction $K + p \rightarrow \Lambda + K + \bar{K}$ as shown in Figure 3.1 [124]. It has a mass of 1.019445$\pm$0.000020 GeV/c^2 which is comparable to mass of lightest baryons

proton (0.938 GeV/c^2) and Λ (1.115 GeV/c^2). The interaction cross-section of the ϕ meson with non-strange hadrons is expected to have a small value [125]. The data on coherent ϕ photo-production shows that $\sigma_{\phi N} \sim 10$ mb [126]. This is about a factor of 3 times lower than $\sigma_{\rho N}$ and $\sigma_{\pi N}$; about a factor 4 times lower than $\sigma_{\Lambda N}$ and σ_{NN} and about a factor 2 times lower than σ_{KN} . Therefore its production is expected to be less affected by the later stage hadronic interactions in the evolution of the system formed in heavy-ion collisions. A hydrodynamical inspired study of transverse momentum

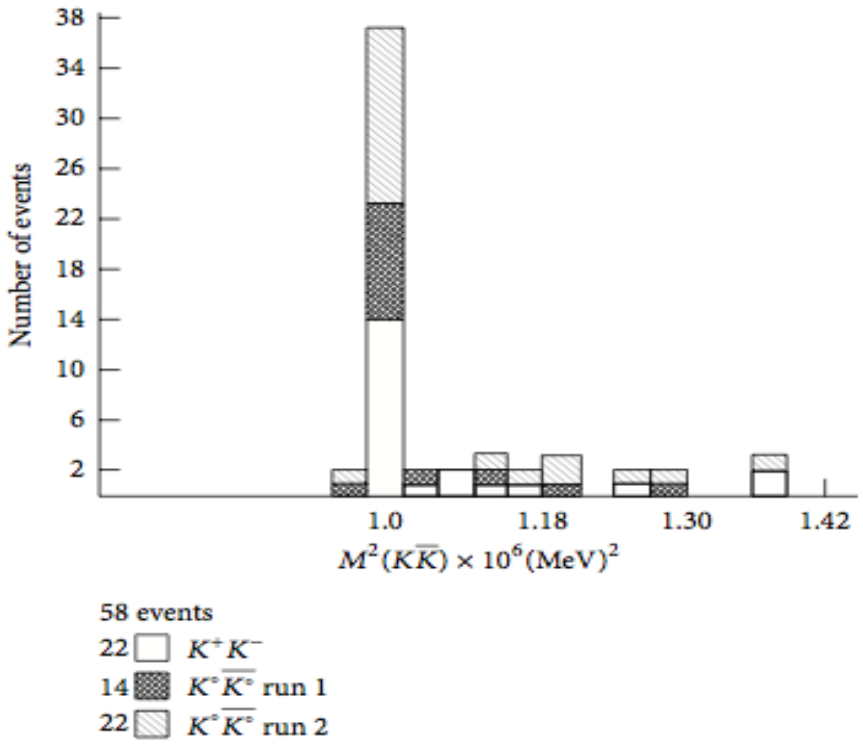

Figure 3.1: *Number of events versus square of invariant mass of $K\bar{K}^+$ pairs from the reaction $K + p \rightarrow \Lambda + K + \bar{K}$ in bubble chamber experiments at Brookhaven National Laboratory (BNL) [124]*

(p_T) distribution of ϕ meson seems to suggest that it freezes-out early compared to other hadrons [127]. The life time of the ϕ meson is ~ 42 fm/c. Because of longer life time the ϕ meson will mostly decay outside the fireball and therefore its daughters

will not have much time to re-scatter in the hadronic phase. Therefore, properties of ϕ meson are primarily controlled by condition in the early partonic phase and can be considered as a clean probe to investigate the properties of matter created in heavy-ion collisions.

Strange particle production is one of the observables expected to deliver detailed information on the reaction dynamics of relativistic nucleus-nucleus collisions [128]. In experiments at the CERN SPS accelerator it was found that the ratio of the number of produced kaons to that of pions is higher by a factor of about two compared to that in proton-proton reactions at the same energy [129, 130, 131, 132]. In the past, several possible reasons for this strangeness enhancement have been discussed. Firstly, if nucleus-nucleus reactions proceed through a deconfined stage, then strange-quark production should be enhanced relative to a no QGP scenario [133]. The idea of Canonical suppression of strangeness in small systems (proton-proton) as a source of strangeness enhancement in high energy nucleus-nucleus collisions have been proposed [134]. But $\phi(s\bar{s})$ mesons due to its zero net strangeness is not subjected to Canonical suppression effects. Therefore measurements of ϕ mesons in both nucleus-nucleus and proton-proton would give the answer for observed strangeness enhancement. Experimentally measured results on v_2 of identified hadrons as function of p_T shows that at low p_T (< 2 GeV/c), elliptic flow follows mass ordering (the lower v_2 for heavier hadrons than that of lighter hadrons) whereas at intermediate p_T all mesons and all baryons form two different groups [135]. When v_2 and p_T are scaled by number of constituent quarks (n_q) of the hadrons, the magnitude of scaled v_2 are same for all hadrons at the intermediate p_T. This observation, is known as number of constituents quark scaling (NCQ scaling). This effect has been interpreted as collectivity being developed at the partonic stage of the evolution of the system in heavy-ion collision [136, 137]. Since ϕ meson has mass (1.0194 GeV/c^2) comparable

to mass of the lightest baryons (protons, Λs) and at the same time it is meson, so study of ϕ-meson v_2 would be more appropriate to understand the mass type and/or particle type (baryon-meson) dependence of $v_2(p_T)$.

In this chapter, we have compiled all the available experimental measurements on ϕ-meson production in high energy heavy-ion collisions as a function of transverse momentum (p_T), azimuthal angle (ϕ) and rapidity (y).

3.2 Invariant Yield of ϕ Meson

3.2.1 Invariant Transverse Momentum Spectra

Figure 3.2 presents the invarint p_T spectra of ϕ meson measured in $p+p$, $d+A$ and $A+A$ system for different collision centralities at various centre-of-mass energies ($\sqrt{s_{NN}}$=17.3 GeV - 7 TeV) [138, 139, 140, 141, 142, 143, 144]. Only statistical errors are indicated by the error bars. The dashed black lines in Figure 3.2 are fits to the experimental data using an exponential function of the form

$$\frac{1}{2\pi p_T}\frac{d^2N}{dydp_T} = \frac{dN/dy}{2\pi T(m_0+T)} exp[-\frac{\sqrt{m_0^2+p_T^2}-m_0}{T}] \tag{3.1}$$

The blue solid lines in Figure 3.2 are the fits to the data with Levy function of the form given by

$$\frac{1}{2\pi p_T}\frac{d^2N}{dydp_T} = \frac{dN}{dy}\frac{(n-1)(n-2)}{2\pi nT(nT+m_0(n-2))}(1+\frac{\sqrt{p_T^2+m_0^2}-m_0}{nT})^{-n} \tag{3.2}$$

T is known as the inverse slope parameter, dN/dy is the ϕ-meson yield per unit rapidity, m_0 is the rest mass of ϕ meson and n is the Levy function parameter. Levy function is similar in shape to an exponential at low p_T and has a power-law-like shape at higher p_T. In fact, the exponential function is the limit of the Levy function as n approaches infinity. From Figure 3.2, it can be seen that the exponential and Levy

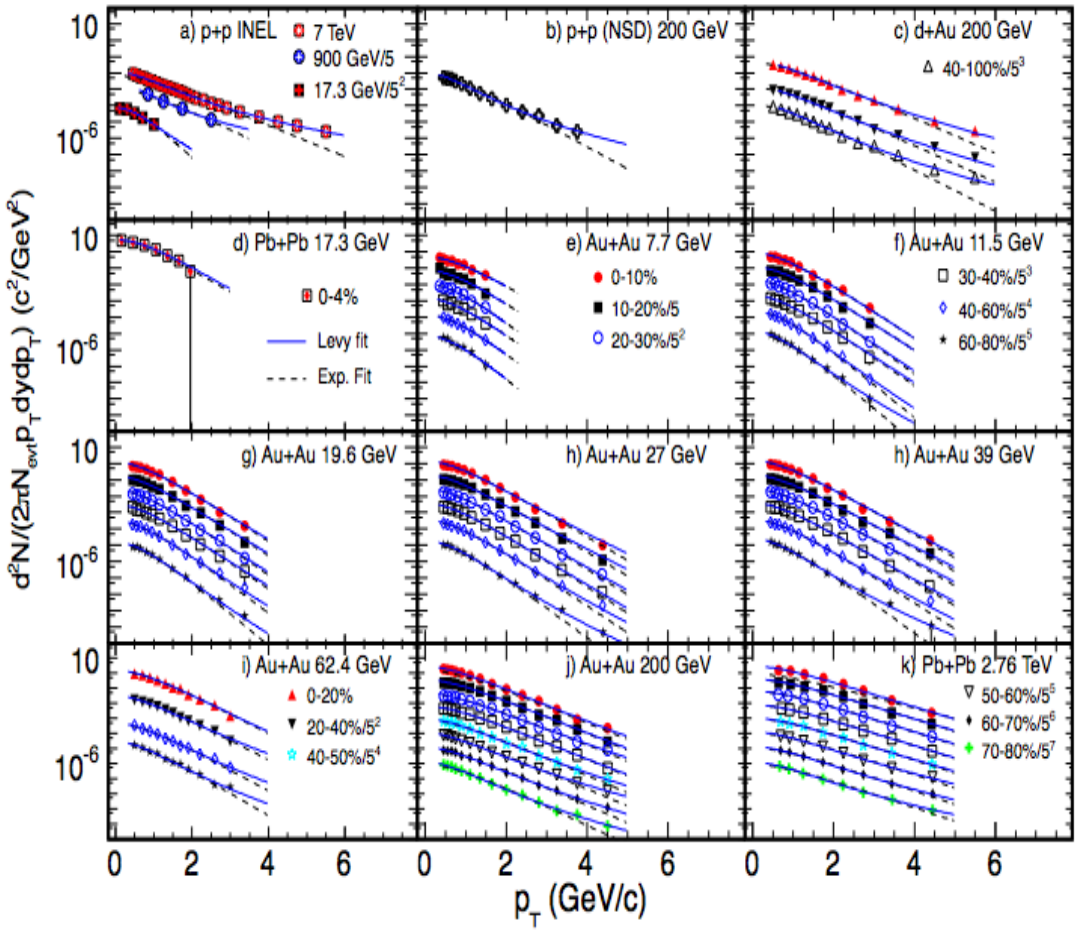

Figure 3.2: *The invariant yield of ϕ mesons as a function of p_T measured for different system and different centralities at various centre-of-mass energies [138, 139, 140, 141, 142, 143]. The black dashed (blue solid) line represents an exponential (Levy) function fit to the data.*

functions fit the central collision data equally well. However, with decreasing centrality, the exponential fits diverge from the data at higher transverse momentum and the Levy function fits the data better. The χ^2/ndf values are larger for exponential function fits in peripheral collisions compared to Levy function fits. This indicates a change in shape of the p_T spectra (deviations from exponential distribution and more towards a power law distribution) at high P_T for peripheral collisions. Tsallis function also describes the measured identified spectra equally well as Levy, which is shown in [145, 146]. Like Levy, Tsallis function describes both the low p_T exponential and the high p_T power law behaviors.

The Tsallis function has two parameters while number of parameters for Levy is three. The exponential function fails to explain data at high p_T for $p+p$ and $d+Au$ collisions whereas Levy function describes data for all p_T. This evolution in the shape of the spectra from exponential-like in central collisions to more power-law-like in peripheral collisions reflects the increasing contribution from pQCD (hard) processes to ϕ meson production in more peripheral collisions at higher p_T. Particle production at low p_T is expected to be due to non perturbative soft processes and with sufficient interactions the system could be thermalized, and that is why both exponential and Levy functions fit the data for all centralities at low p_T.

3.2.2 ϕ Meson Yield per Unit Rapidity

In Figure 3.3, we present all available measurements of p_T integrated ϕ meson yield (dN/dy) at midrapidity as a function of centre-of-mass energy in both nucleus-nucleus [138, 139, 140, 143] and proton-proton collisions [140, 141, 144, 147]. For A + A collisions, different centralities are shown by different marker styles in Figure 3.3(a). The measured midrapidity yield increases with centrality and for the same centrality it increases with the collision energy for both $A+A$ and $p+p$ collisions.

The rate of increases with $\sqrt{s}_{NN}$ is higher in $A + A$ collisions compared to $p + p$

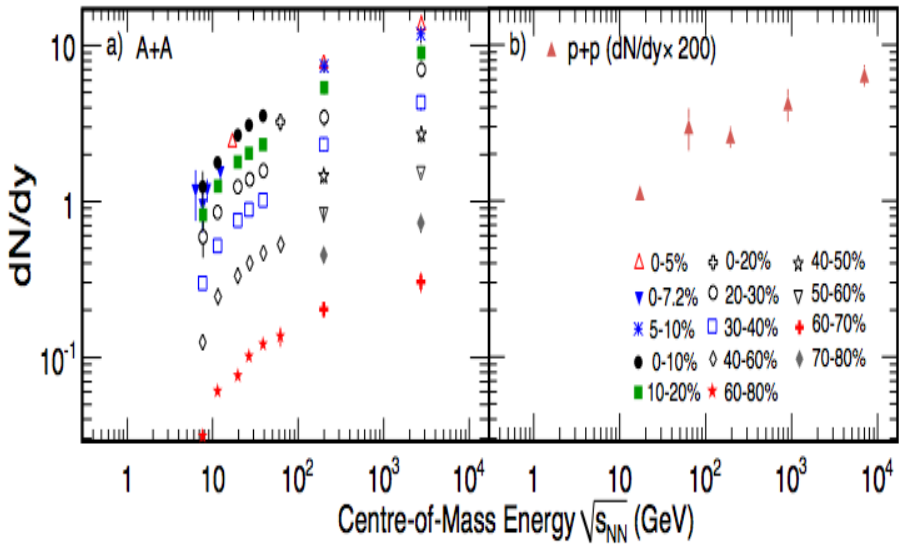

Figure 3.3: *The ϕ meson midrapidity yield (dN/dy) as a function of $\sqrt{s}_{NN}$ for $A + A$ [138, 139, 140, 142] and $p + p$ collisions [140, 141, 142, 144, 147]. For RHIC BES energies ($\sqrt{s}_{NN}$ = 7.7-39 GeV) only statistical errors are shown whereas for other energies systematic errors are added in quadrature with statistical errors.*

collisions. We have observed that the measured midrapidity yield per participant (N_{part}) pair, $(dN/dy)/(0.5N_{part})$, increases nonlinearly with centrality and for the same $N_{part}(dN/dy)/(0.5\text{part})$ increases with the collision energy of the $A + A$ collisions. The former suggests that particle production does not scale with N_{part} and the latter is expected because of the increase of energy available to produce the ϕ mesons.

3.2.3 Strangeness Enhancement

The ratio of strange hadron production normalised to $< N_{part} >$ in nucleus-nucleus collisions relative to corresponding results from $p + p$ collisions at 200 GeV [148] is shown in the left upper panel of Figure 3.4. The results are plotted as a function of $< N_{part} > K^-$, Λ and Ξ are found to exhibit an enhancement (value > 1) that

increases with the number of strange valence quarks. Furthermore, the observed enhancement in these open-strange hadrons increases with collision centrality, reaching a maximum for the most central collisions. However, the enhancement of ϕ meson production from $Cu+Cu$ and $Au+Au$ collisions shows a deviation in ordering in terms of the number of strange constituent quarks. Such deviation is also observed in central $Pb+Pb$ collisions at SPS energy (as shown in the right bottom panel of Figure 3.4). The difference in the ordering does not seem to be a baryon-meson effect, since K^- and Λ have similar enhancement, or a mass effect, since Λ and ϕ have similar mass but different enhancement factors. In heavy-ion collisions, the production of ϕ mesons is not Canonically suppressed due to its $s\bar{s}$ structure. The $p+p$ collisions at RHIC are at an energy which is ~ 25 times higher than energies where violations of the Okubo-Zweig-Iizuka (OZI) rule were reported [149, 150]. The observed enhancement of ϕ meson production then is a clear indication for the formation of a dense partonic medium being responsible for the strangeness enhancement in $Au+Au$ collisions at 200 GeV. Furthermore, ϕ mesons do not follow the strange quark ordering as expected in the Canonical picture for the production of other strange hadrons. The observed enhancement in ϕ meson production being related to medium density is further supported by the energy dependence shown in the lower left panel of Figure 3.4. The ϕ meson production relative to $p+p$ collisions is larger at higher beam energy, a trend opposite to that predicted in Canonical models for other strange hadrons. The right upper panel Figure 3.4 shows the enhancement in $Pb+Pb$ with respect to $p+p$ reference yields for ϕ, Λ, Ξ^- and $\Omega^- + \bar{\Omega}^+$ at $\sqrt{s}_{NN} = 2.76$ TeV [143]. The ϕ, Ξ and Ω yield in $p+p$ collisions at $\sqrt{s}_{NN} = 2.76$ TeV have been estimated by interpolating between the measured yields at $\sqrt{s}_{NN} = 0.9$ TeV and $\sqrt{s}_{NN} = 7$ TeV. The reference Λ yield in $p+p$ collisions at $\sqrt{s}_{NN} = 2.76$ TeV is estimated by extrapolating from the measured yield in (inelastic) + collisions available up to $\sqrt{s}_{NN} = 0.9$ TeV. Details

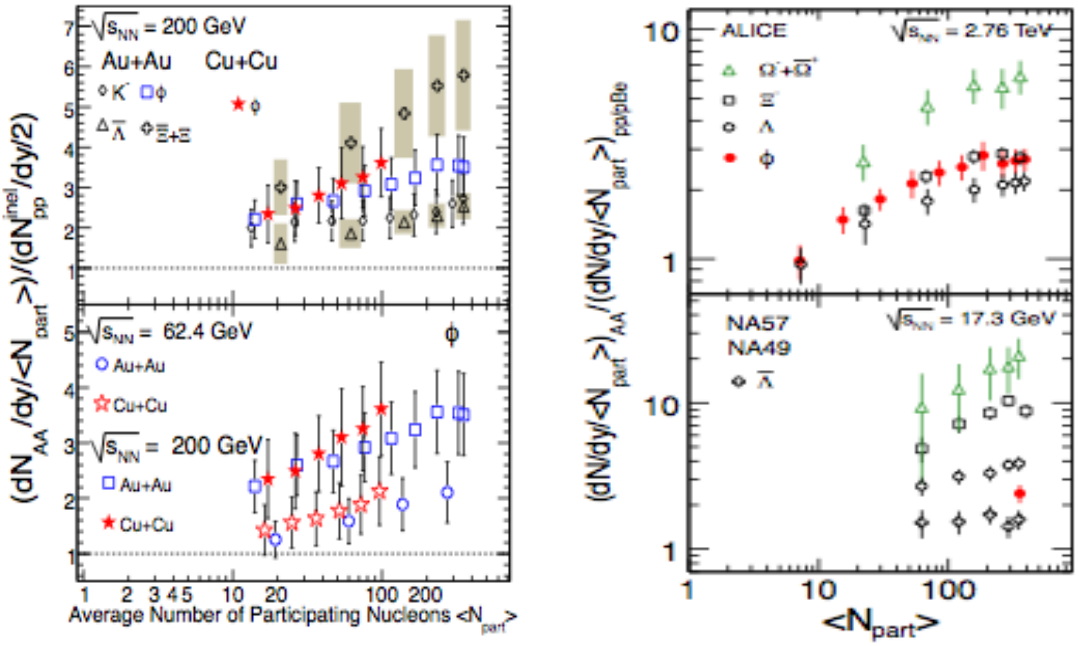

Figure 3.4: *Left Panel: The ratio of the yields of* $\bar{K}$, ϕ, λ, *and* $\Xi + \bar{\Xi}$ *normalised to* $< N_{part} >$ *nucleus-nucleus collisions and to corresponding yields in proton-proton collisions as a function of* $< N_{part} >$ *at 62.4 and 200 GeV [150]. Error bars are quadrature sum of statistical and systematic uncertainties. Right Panel: The ratio of* $< N_{part} >$ *normalised yield of* ϕ, Λ, $\bar{\Lambda}$, Ξ^-, $\Omega + \bar{\Omega}^-$ *and in Pb + Pb collisions to the corresponding yield in p+p (P + Be) collisions at 17.3 GeV (NA57 & NA49) and 2.76 TeV (ALICE) [143]. Only statistical uncertainties are shown.*

can be found in [143]. Enhancement factor increases linearly with N_{part} until N_{part} $\approx$ 100, then the enhancement values seem to be saturated for higher values of N_{part}. Unlike SPS and RHIC, the order of ϕ enhancement is the same as Ξ^- at LHC energy. We have observed that the ϕ enhancement at central collisions increases from SPS to RHIC energy but the enhancement factor is comparable, within errors, to the values at RHIC and LHC. These findings tell us that the observed ϕ meson enhancement is not due to the Canonical suppression effects. Therefore this enhancement is very likely due to the formation of a deconfined medium. Since other strange hadrons also

emerge from the same system, their enhancement is most likely also due to formation of deconfined matter or quark-gluon plasma (QGP) in heavy-ion collisions.

3.2.4 Nuclear Modification Factor

In order to understand parton energy loss in the medium created in high energy heavy-ion collisions for different centralities in $A + A$ collisions, the nuclear modification

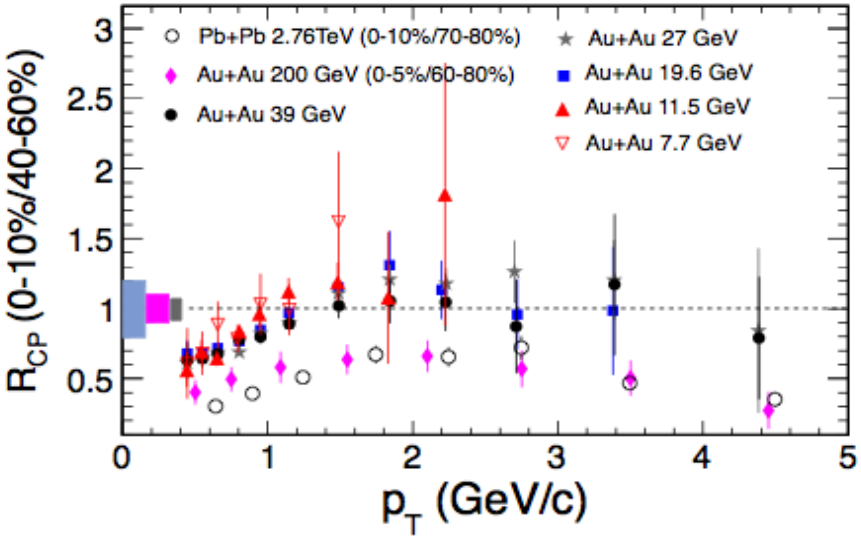

Figure 3.5: *The ϕ meson R_{CP} as a function of p_T in Au+Au [139, 140] and Pb + Pb [143] collisions at various beam energies. Error bars are only statistical uncertainties. Bands represent normalisation error from bin which is approximately 20% for $\sqrt{s}_{NN}$ = 7.7-39 GeV, ∼10% for 200 GeV, and ∼7% for 2.76 TeV.*

factor (R_{CP}) is measured which is defined as follows:

$$R_{CP} = \frac{Yield_{central}}{Yield_{peripheral}} \times \frac{< N_{bin} >_{peripheral}}{< N_{bin} >_{central}} \tag{3.3}$$

where $< N_{bin} >$ is the average number of binary collisions to the corresponding centrality. The value of N_{bin} was calculated from the Monte Carlo Glauber simulation [151]. $R_{\rm CP}$ is equal to one when a nucleus-nucleus collision are simply a superpo-

sition of nucleon-nucleon collisions. Therefore deviation of $R_{\rm CP}$ from the unity would imply contribution fron the nuclear medium effects specifically jet-quenching [152]. Nuclear modification factors (R_{CP}) of ϕ mesons at midrapidity in $Au + Au$ collisions at $\sqrt{s}_{NN}$ = 7.7, 11.5, 19.6, 27, 39, and 200 GeV [139, 140] and in $Pb + Pb$ collisions at $\sqrt{s}_{NN}$ = 2.76 TeV [143] are shown in Figure 3.5. We can see that the R_{CP} of ϕ

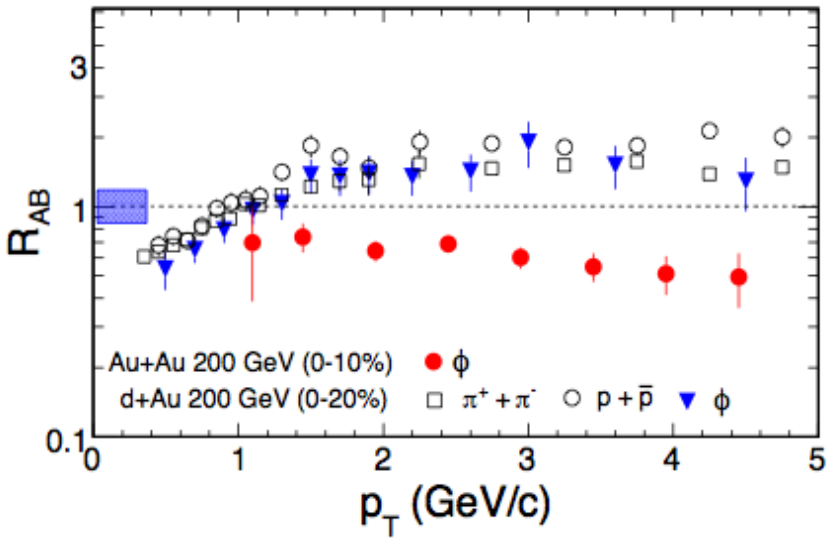

Figure 3.6: *The nuclear modification factor R_{AB} as a function of p_T in Au+Au and d+Au [139, 153] collisions at $\sqrt{s}_{NN}$ = 200 GeV. Rectangular bands show the uncertainties associated with estimation of number of binary collisions. Error bars are quadrature sum of statistical and systematic uncertainties for ϕ in d + Au and only statistical for three other cases.*

mesons goes below unity at 200 GeV and 2.76 TeV in nucleus-nucleus collisions. The most feasible explanation of this observation to date is due to the energy loss of the partons traversing the high density QCD medium. This implies that a deconfined medium of quarks and gluons was formed at 200 GeV and 2.76 TeV [139, 143]. For $\sqrt{s}_{NN} = \leq$ 39 GeV, ϕ meson R_{CP} is greater than or equal to unity at the intermediate p_T, which indicates that at low energy the parton energy loss contribution to R_{CP}

measurements could be less important. In order to confirm that the $R_{CP} < 1$ is due to parton energy loss or jet-quenching phenomenon, it is important to study R_{CP} in $A + A$ or $d + A$ collisions. Nuclear modifications in such systems are expected to be effected by the Cronin effect [153] and not by QGP effect. Due to the Cronin effect the value of R_{CP} at high p_T is expected to be greater than one.

Figure 3.6. presents the p_T dependence of the nuclear modification factor R_{AB} in $Au + Au$ and $d + Au$ collisions at $\sqrt{s}_{NN} = 200$ GeV [139, 154]. The definition of R_{AB} is the ratio of the yields of the hadron produced in the nucleus (A) + nucleus (B) collisions to the corresponding yields in the inelastic + collisions normalised by bin. The R_{AB} of ϕ mesons for $d + Au$ collisions show a similar enhancement trend as those for $\pi^+ + \pi^-$ and p + $\bar{p}$ at the intermediate. This enhancement in $d + Au$ collisions was attributed to be due to the Cronin effect [153]. The Cronin enhancement may result either from momentum broadening due to multiple soft [155] (or semihard [156, 157] scattering in the initial state or from final state interactions as suggested in the recombination model. These mechanisms lead to different particle type and/or mass dependence in the nuclear modification factors as a function of p_T. Current experimental measurements on ϕ meson R_{AB} in $d + Au$ do not seem to have the precision to differentiate between particle type dependence types [158, 159]. On the other hand, the R_{AB} in Au + Au (i.e., AA) at 200 GeV is lower than that in $d + Au$ at 200 GeV and is less than unity [154]. These features are consistent with the scenario of energy loss of the partons in a QGP medium formed in central $Au + Au$ collisions.

3.2.5 Mean Transverse Mass

Figure 3.7. shows the difference in mean transverse mass ($m_T = \sqrt{p_T^2 + m_0^2}$) and rest mass ($m_0$) i.e. $< m_T > - m_0$ for ϕ meson as a function of centre-of-mass energy for

p+p [140, 142, 145], Au+Au [139, 140] and Pb+Pb [138, 143] collisions. The data

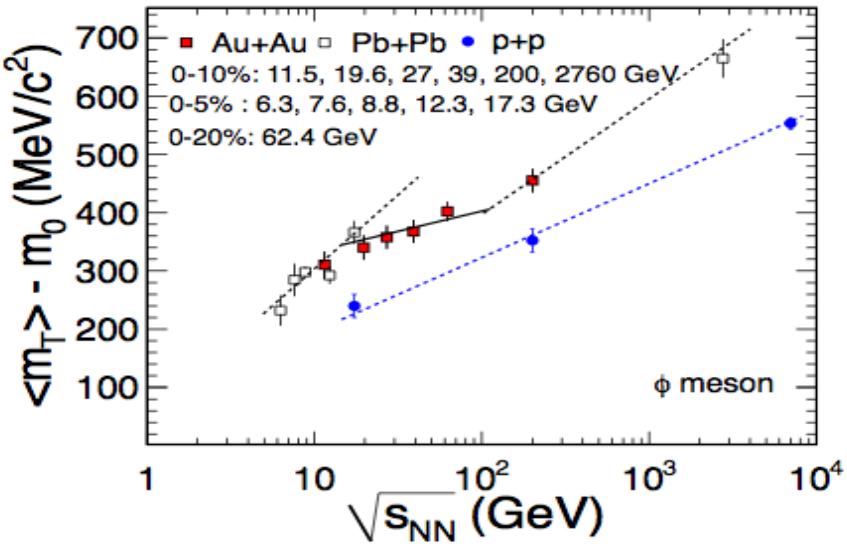

Figure 3.7: $< m_T > -m_0$ *as a function centre-of-mass energies in central* $A + A$ *and* $p + p$ *collisions. Only statistical errors are shown. The dashed and solid lines are the straight lines connected to the data to guide the eye of the reader.*

points in Figure 3.7 are connected by the lines to guide the eye of the reader. One can see that $< m_T > m_0$ increases monotonically with $\sqrt{s}_{NN}$ = in p+p collisions whereas the corresponding data in A+A collisions changes slope twice as a function of center-of-mass energy. In $A + A$ collisions, $< m_T > -m_0$ first increases with $\sqrt{s}_{NN}$ and then stays independent of energy from approximately 17 GeV to 39 GeV, followed by again an increase with $\sqrt{s}_{NN}$. For a thermodynamic system, the $< m_T > -m_0$ can be interpreted as a measure of temperature of the system, and dN/dy $\approx \ln(\sqrt{s}_{NN})$ may represent its entropy. In such a scenario, this observation could reflect the characteristic signature of a first order phase transition [160]. Then the constant value of $< m_T > -m_0$ for ϕ meson from 17 GeV to 39 GeV could be interpreted as a formation of a mixed phase of a QGP and hadrons during the evolution of the heavy-ion system.

3.2.6 Particle Ratios

3.2.6.1 ϕ/K^-

The mechanism for ϕ meson production in high energy collisions has remained an open issue. In an environment with many strange quarks, ϕ mesons can be produced readily through coalescence, bypassing the OZI rule [161]. On the other hand, a naive interpretation of ϕ meson production in heavy-ion collisions would be the ϕ production via kaon coalescence. In the latter case one could expect an increasing trend of ϕ/K^- ratio as function of collision centrality and centre-of-mass energy. Models that include hadronic rescatterings such as Ultrarelativistic Quantum Molecular Dynamics model (UrQMD) [162, 163] have predicted an increase of the ϕ/K^- ratio at midrapidity as a function of centrality [139]. Therefore, the ratio of ϕ meson yield to that of the kaons can be used to shed light on ϕ meson production mechanism. Figure **??**

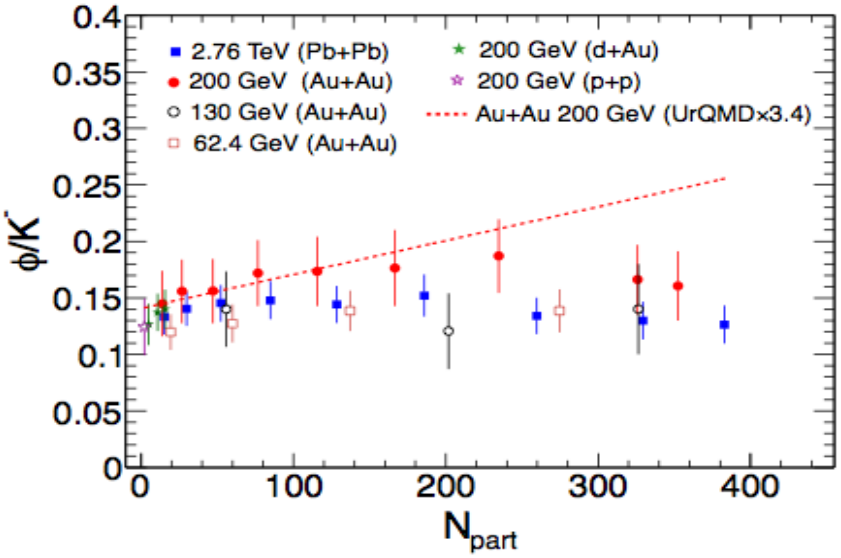

Figure 3.8: *ϕ/K^- ratio as a function of number of participants in Au + Au [139] and Pb + Pb [143] collision at various beam energies.*

shows the ϕ/K^- ratio as a function of number of participants for different centre-of-

mass energies [139]. Ultrarelativistic Quantum Molecular Dynamics model (UrQMD) model prediction for ϕ/K^- in $Au + Au$ 200 GeV collisions is shown by red dashed line. However, this prediction was disproved from experimental data. It is clear from figure 3.8 that ϕ/K^- is independent of centrality and also centre-of-mass energy. In addition, if ϕ production is dominantly from $K\bar{K}$ coalescence, one expects the width of the rapidity distribution of ϕ mesons to be related to those for charged kaons as $1/\sigma^2_\phi = 1/\sigma^2_{K^-} + 1/\sigma^2_{K^+}$. Measurements at SPS energies show a clear deviation of the data from the above expectation [164]. Finally, if ϕ production is dominantly from $K\bar{K}$ coalescence it would be reflected in elliptic flow (v_2) measurements. We observe at intermediate p_T that the v_2 of ϕ mesons and kaons are comparable (discussed in Section 3). All these measurements effectively rule out kaon coalescence as the dominant production mechanism for the ϕ meson for this energy region.

3.2.6.2 Ω/ϕ

The production mechanism of multistrange hadrons (e.g.,ϕ and Ω) is predicted to be very sensitive to the early phase of nuclear collisions [165], because both ϕ and Ω freeze out early, have low hadronic interaction cross-section, and are purely made of strange and antistrange quarks. Therefore the ratio $N(\Omega)$/N (ϕ) is expected to reflect the information of strange quark dynamics in the early stage of the system created in the nucleus-nucleus collision [166]. Figure 3.9 shows the baryon-to-meson ratio in strangeness sector, $\mathrm{N}(\Omega^- + \Omega^+)/2N(\phi)$, as a function of p_T in $Au + Au$ collisions at $\sqrt{s}_{NN}$ = 11.5 GeV to 2760 GeV [138, 140, 143]. The dashed lines are the results from the recombination model calculation by Hwa and Yang for $\sqrt{s}_{NN}$ = 200 GeV [166]. In this model the ϕ and Ω yields in the measured p_T region are mostly from the recombination of thermal strange quarks, which were assumed to follow an exponential p_T distribution. The thermal s quark distribution was determined by fitting the

low p_T data of kaon production. The contribution from hard parton scattering was assumed to be negligible unless p_T is large. Details of this recombination model have

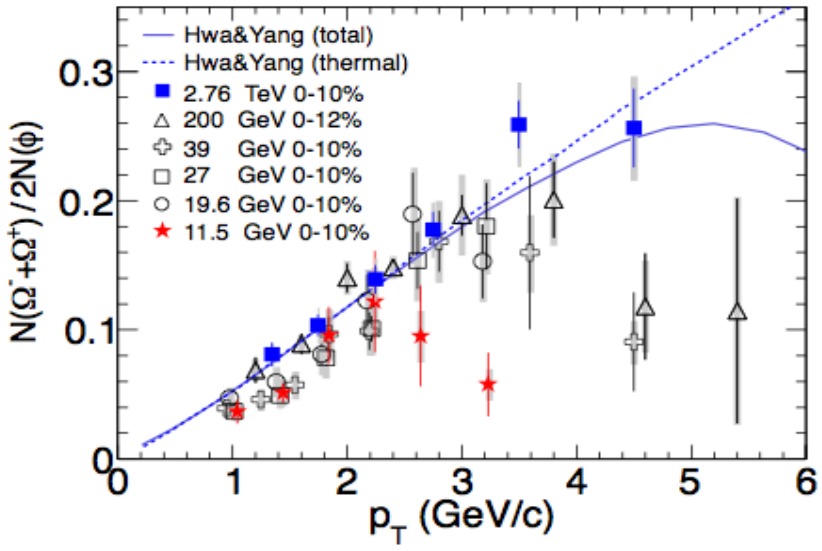

Figure 3.9: *The baryon-to-meson ratio, $N(\Omega^- + \Omega^+)/2N(\phi)$, as a function of p_T in midrapidity ($|\eta| < 0.5$) from central $A + A$ collisions at $\sqrt{s}_{NN}$ = 11.5, 19.6, 27, 39, 200, and 2760 GeV [138, 139, 143]. Gray bands denote systematical errors.*

been given in [166]. We can see from Figure 3.9 that, in central $A + A$ collisions at $\sqrt{s}_{NN} \leq$ 19.6 GeV, the ratios $N(\Omega^- + \bar{\Omega}^+)/2N(\phi)$ in the intermediate p_T range are explained by the recombination model with thermal strange quarks and show a similar trend. The model agrees well with the trend of the data up to $\sim$ 4 GeV/c which covers $\sim$95% of the total yields for the ϕ and Ω. The observations imply that the production of ϕ and Ω in central $Au + Au$ collisions is predominantly through the recombination of thermal squarks for $\sqrt{s}_{NN} \geq$ 19.6 GeV. But at $\sqrt{s}_{NN}$= 11.5 GeV, the ratio at the highest measured p_T shows a deviation from the trend of other energies. This may indicate a change in Ω and/or ϕ production mechanism at $\sqrt{s}_{NN}$ = 11.5 GeV.

3.3 Azimuthal Anisotropy in ϕ Meson Production

In non-central nucleus-nucleus collision, the initial spatial anisotropy is transformed into final state momentum anisotropy in the produced particle distributions because of pressure gradient developed due to the interactions among the systems constituents [167, 168, 169, 170, 171]. The elliptic flow (v_2) [172, 173, 174] is a measure of the second order azimuthal anisotropy of the produced particles in the momentum space. It can be used as probe for the properties of the medium created in the heavy-ion collisions. Because of its self-quenching nature, it carries information from the early phase. Although elliptic flow is an early time phenomenon, its magnitude might still be affected by the later stage hadronic interactions. Since the hadronic interaction cross-section of ϕ meson is smaller than the other hadrons [175] and freezes out relatively early [176], its v_2 remain almost unaffected by the later stage interaction. Therefore ϕ meson v_2 can be considered as good and clean probe for early system created in nucleus-nucleus collisions. Further the ϕ mesons seem to be formed by coalescence of strange quarks and antiquarks in a deconfined medium of quarks and gluons, hence the measurement of collectivity in ϕ mesons would reflect the collectivity in the partonic phase. In addition, its mass is comparable to the masses of the lightest baryon (p and Λ), therefore comparison of ϕ meson v_2 with that of proton and Λ will be helpful to distinguish the mass effect and/or baryon-meson effect in $v_2(p_T)$.

3.3.1 Differential ϕ Meson v_2

Elliptic flow of ϕ meson as a function of p_T measured at midrapidity [177, 178, 179, 180] is shown in Figure 3.10. The shape of ϕ $v_2(p_T)$ is similar for $\sqrt{s}_{NN}$ = 19.6 GeV to 2760 GeV. But at 7.7 GeV and 11.5 GeV, the ϕ v_2 values at the highest measured p_T bins are observed to be smaller than other energies. Various model studies predicted

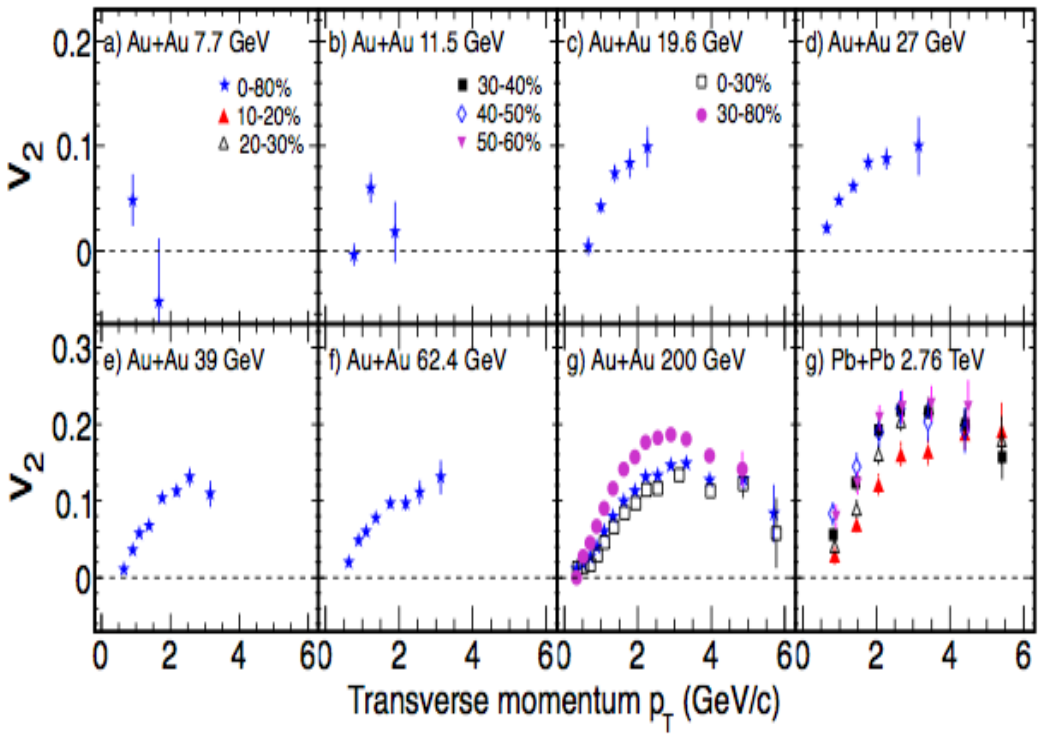

Figure 3.10: *The ϕ meson $v_2(p_T)$ at midrapidity in Au+Au collisions at $\sqrt{s}_{NN}$ = 7.7-62.4 GeV for 0-80% centrality [177] and at $\sqrt{s}_{NN}$ = 200 GeV for 0-80%, 0-30%, and 30-80% centralities [178, 179] and in Pb + Pb collisions at $\sqrt{s}_{NN}$ = 2.76 TeV [180] for different collisions centralities. The vertical lines are statistical uncertainties.*

that ϕ meson v_2 will be small for a system with hadronic interactions [181, 182]. Small interaction cross-section of ϕ meson in hadronic phase suggests that ϕ meson v_2 mostly reflects collectivity from the partonic phase; hence small ϕ meson v_2 indicates less contribution to the collectivity from partonic phase. So the large ϕ meson v_2 at $\sqrt{s}_{NN} \leq 15$ GeV indicates the formation of partonic matter and small v_2 at $\sqrt{s}_{NN} \leq 11.5$ GeV could indicate dominance of hadron interactions.

3.3.2 Number-of-Constituent Quark Scaling

In Figure 3.11, the v_2 scaled by number-of-constituent quarks (n_q) as a function $(m_T) - m_0/n_q$ for identified hadrons in $Au + Au$ collisions at $\sqrt{s}_{NN} = 7.7$-200 GeV are presented. We can see from Figure 3.11 that for $\sqrt{s}_{NN}$ 19.6-200 GeV the v_2 values follow a universal scaling for all the measured hadrons. This observation is known as the NCQ scaling. The observed NCQ scaling at RHIC can be explained by considering particle production mechanism via the quark recombination model and can be considered as a good signature of partonic collectivity [183, 184]. Therefore, such a scaling should vanish for a purely hadronic system if formed in the heavy-ion collisions at the lower energies. At the same time the study of NCQ scaling of identified hadrons from UrQMD model shows that the pure hadronic medium can also reproduce such scaling in v_2 [185, 186, 187]. This is due to modification of initially developed v_2 by later stage hadronic interactions and the production mechanism as implemented in the model [186]. Hence to avoid these ambiguities, the v_2 of those particles which do not interact with hadronic interaction will be the clean and good probe for early dynamics in heavy-ion collisions. Due to small hadronic interaction cross-section, ϕ mesons v_2 are almost unaffected by later stage interaction and it will have negligible value if ϕ mesons are not produced via and s and $\bar{s}$ quark coalescence [188, 189]. Therefore, NCQ scaling of ϕ mesons v_2 can be considered as

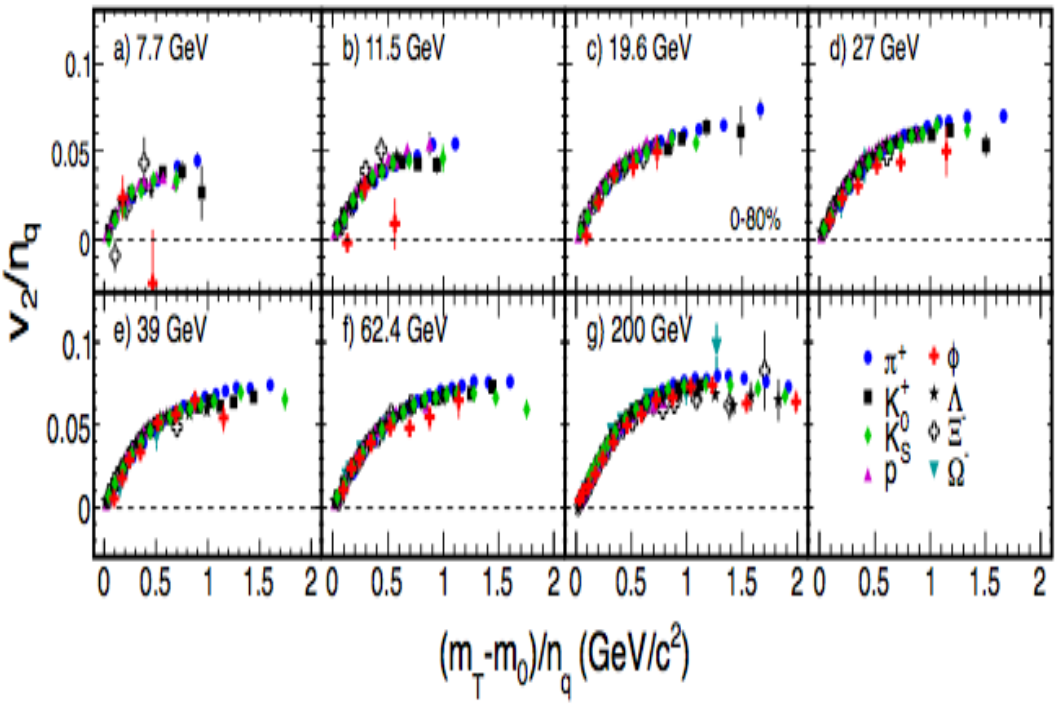

Figure 3.11: *The NCQ-scaled elliptic flow, v_2/n_q, versus m_T-m_0/n_q for 0-80% central Au + Au collisions for selected identified particles [177, 178, 179]. Only statistical error bars are shown.*

the key observables for the partonic collectivity in heavy-ion collisions. As we can see from Figure 3.11, at $\sqrt{s}_{NN} = 7.7$ GeV and 11.5 GeV, the ϕmeson v_2 deviates from the trend of the other hadrons at the highest measured p_T values by 1.8σ, respectively. This could be the effect for a system, where hadronic interactions are more important.

Figure 3.12 presents the $(m_T) - m_0/n_q$ dependence of v_2/n_q for 10-20% and 40-50% central $Pb + Pb$ collisions for selected identified particles [190]. It can be seen

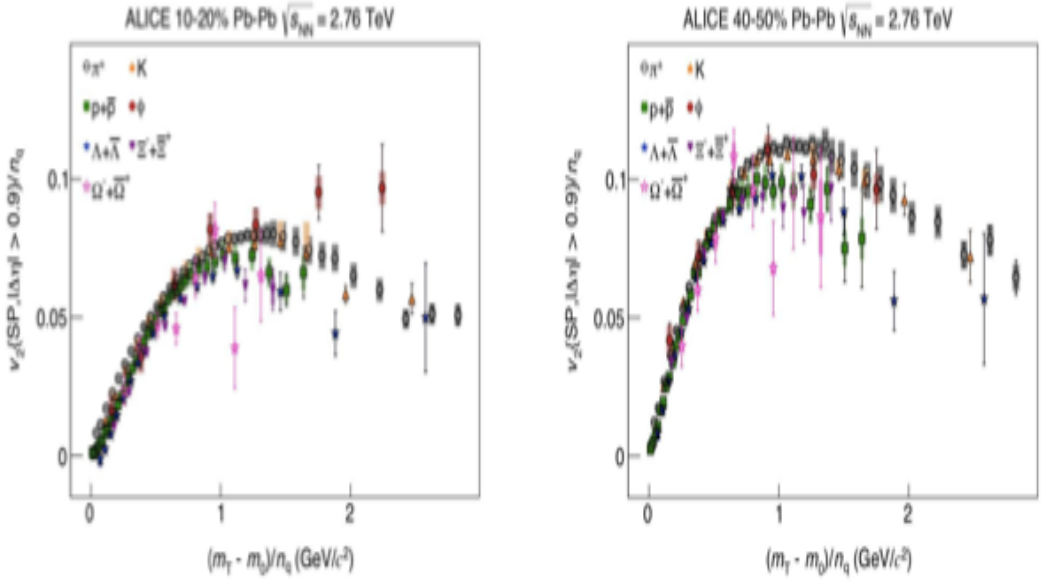

Figure 3.12: *The NCQ-scaled elliptic flow, v_2/nq, versus $(m_T$ - $m_0)/nq$ for 10-20% and 40-50% central Pb+Pb collisions for selected identified particles [190]. Only statistical error bars are shown. Figure has been taken from the presentation at Quark Matter 2014 by ALICE collaboration.*

that, at higher value of $(m_T) - m_0/n_q$, the scaling is not good compared to that observed at RHIC energies. There are deviations at the level of ±20% with respect to the reference ratio as shown in [190]. This larger deviation at LHC energy could be related to observed large radial flow at LHC compared to RHIC.

3.3.3 p_T Integrated ϕ Meson v_2

The p_T integrated elliptic flow ($< v_2 >$) can be calculated as

$$\langle v_2 \rangle = \frac{\int v_2(p_T)(dN/dp_T)dp_T}{\int (dN/dp_T)dp_T}, \tag{3.4}$$

Figure 3.13 shows p_T integrated ϕ meson (red star) and proton (blue circle) v_2 as a function of centre-of-mass energy for 0-80% centrality [191]. One can see that for both particle species the $< v_2 >$ increases with increasing beam energy. ϕ meson $< v_2 >$ from A Multiphase Transport Model (AMPT) for three different scenarios is shown by shaded bands. Green band corresponds to AMPT default model which includes only hadronic interaction whereas black and yellow bands correspond to AMPT with string melting scenario with parton-parton cross-sections of 3 mb and 10 mb, respectively. In contrast to observations from the data, the $< v_2 >$ values from model remain constant for all the energies. This is because they have been obtained for a fixed parton-parton interaction cross-section. The $< v_2 >$ of ϕ mesons for $\sqrt{s}_{NN}$ $\leq$ 19.6 GeV can be explained by the AMPT with string melting (SM) version, by varying the parton-parton cross-section. On the other hand, both the AMPT-SM and the AMPT default models overpredict data at $\sqrt{s}_{NN}$ = 11.5 GeV. The comparison to AMPT model results indicates negligible contribution of the partonic interactions to the final measured collectivity for $\sqrt{s}_{NN}$ 11.5 GeV. For $\sqrt{s}_{NN}$ >19.6 GeV, proton and ϕ meson show similar magnitude of $< v_2 >$. The proton is a baryon and ϕ is a meson; in addition they are composed of different quark flavours, yet they have similar $< v_2 >$; this is a strong indication of large fraction of the collectivity being developed in the partonic phase. However at $\sqrt{s}_{NN} \leq$ 19.6GeV, ϕ meson $< v_2 >$ values show deviation from that for proton and at $\sqrt{s}_{NN}$ 11.5 GeV ϕ meson $< v_2 >$ becomes small ($\sim$ 1.5%). This tells us that due to the lack of enough partonic interactions at lower beam energies a larger $< v_2 >$ could not be generated for ϕ mesons. The contribution to $\phi < v_2 >$ from hadronic interactions is small because

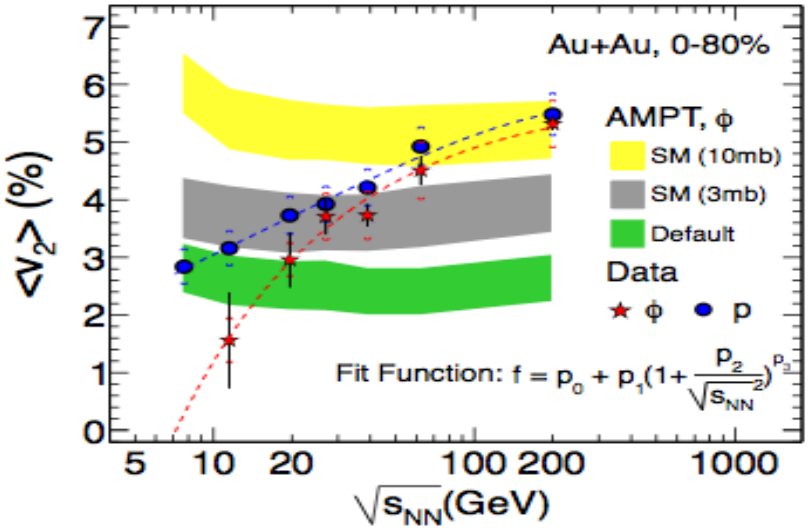

Figure 3.13: *The p_T integrated proton and ϕ meson v_2 for various centre-of-mass energies for 0-80% centrality in Au + Au collisions [191]. Vertical lines are the statistical error and systematic errors are shown by cap symbol. For lower RHIC energies, STAR preliminary p_T spectra were used for ϕ and proton $< v_2 >$ calculation [139, 192, 193]. The red and blue lines are the fit to the ϕ and proton v_2 by empirical function just to guide the eye of the reader.*

of small hadron interaction cross-sections. However the observed higher collectivity of protons compared to ϕ mesons at the lower beam energies could be due to the protons having larger hadronic interaction cross-section.

3.3.4 Hadronic Rescattering Effect on v_2

Recent phenomenological calculation based on ideal hydrodynamical model together with the later stage hadron cascade (hydro + JAM) shows that the mass ordering of v_2 could be broken between that of ϕ meson and that of proton at low p_T ($p_T < 1.5$ GeV/c) [194]. This is because of later stage hadronic rescattering effects on proton v_2. The model calculation was done by considering low hadronic interaction cross-section for ϕ meson and larger hadronic interaction cross-section for proton. The ratio between ϕ v_2 and proton v_2 is shown in Figure 3.14 for minimum bias $Au + Au$ collisions at $\sqrt{s_{NN}} = 200$ GeV. The data from the STAR experiment are shown by

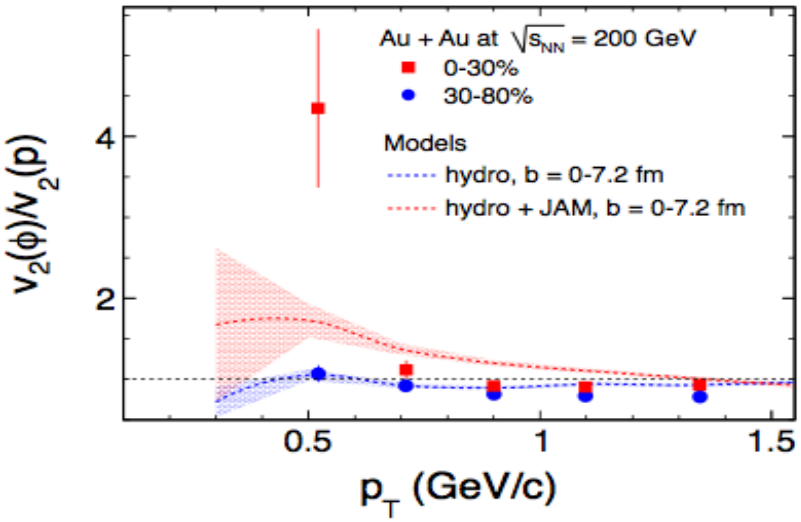

Figure 3.14: *Ratio between ϕ and proton v_2 for 0-30% and 30-80% centrality in Au + Au collisions $\sqrt{s_{NN}} = 200$ GeV [178, 179]*

solid red square and blue solid circle [178, 179]. Solid red square and blue solid circle

correspond to 0-30% and 30-80% centralities, respectively. The ratios are larger than unity at low p_T region (p_T <0.7 GeV/c) for 0-30% centrality although mass of the ϕ meson (1.019 GeV/c^2) is greater than mass of the proton (0.938 GeV/c^2). This is qualitatively consistent with the model calculation using hydro + JAM shown by red bands. Therefore this observation is consistent with the physical scenario of larger effect of hadronic rescattering on proton v_2 which reduces its value, as predicted in the theoretical model [189, 194]. Due to small hadronic interaction cross-section ϕ meson v_2 remains unaffected by later stage hadronic rescattering.

Chapter 4

ϕ Meson Reconstruction

4.1 Introduction

In this chapter, the reconstruction of ϕ-meson ($\phi \rightarrow K^+K^-$) has been studied for Au+Au collisions at $\sqrt{s}_{NN}$ = 200 GeV in STAR experiment. Prior to this, the brief information about the data set used as well as particle identification by TPC and TOF are also given.

4.2 Data Set

4.2.1 Event Selection

For the present study, the data taken by the the STAR experiment during RHIC run 2011 of data taking were analyzed. This data set is taken with a minimum bias trigger. The trigger detectors used are the Zero Degree Calorimeter (ZDC) [195] and Vertex Position Detector(VPD) [196]. The cuts on primary vertex position along the longitudinal beam direction (V_z) is 30 cm. The distribution of Z-positions of vertex is shown in Figure 4.1. In order to reject events which involves beam pipe interactions, the event vertex radius (defined as $V_r = \sqrt{V_x^2 + V_y^2}$, where V_x and V_y are the vertex

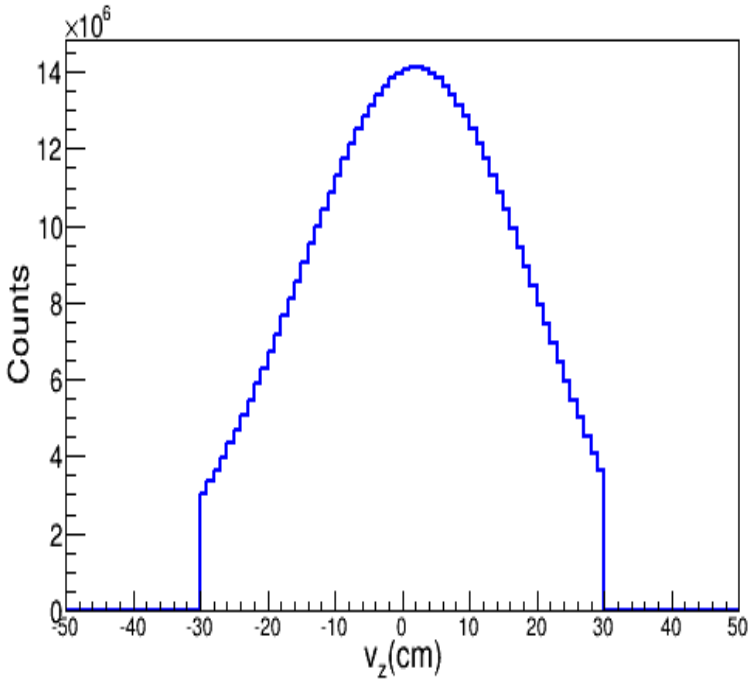

Figure 4.1: *Distribution of Z-component of event vertex in Au+Au collisions at* $\sqrt{s}_{NN}$ *= 200 GeV*

positions along the x and y directions) is required to be less than 2 cm. To remove pileup events, it was required that at least two tracks from the primary vertex were matched to the cells of the TOF detector. After all events selection cuts, number of minimum bias events are ∼562 million.

4.2.2 Centrality Selection

In heavy ion collisions, the system created in a head-on collisions is different from that in a peripheral collisions. Therefore, collisions are categorized by their centrality. The collision centrality is determined by comparing the measured raw charged hadron multiplicity uncorrected for efficiency and acceptance effects (named as RefMult or N_{raw}) from the TPC within a pseudo-rapidity window $|\eta| \leq 0.5$ with Glauber Monte Carlo simulations. A two-component model [197] is used to calculate the simulated

multiplicity distribution given by

$$\frac{dN_{ch}}{d\eta} = n_{pp}[(1-x)\frac{N_{part}}{2} + xN_{coll}] \tag{4.1}$$

where N_{part} is the number of participant nucleons and N_{coll} is the number of binary

bins	**Centrality Class**
1	0-5%
2	5-10%
3	10-20%
4	20-30%
5	30-40%
6	40-50%
7	50-60%
8	60-70%
9	70-80%

Table 4.1: *Centrality Classes in Au+Au collisions at* $\sqrt{s}_{NN}$ *= 200 GeV*

nucleon-nucleon collisions in the Glauber Monte-Carlo simulations. The fitting parameter n_{pp} is the average multiplicity per unit of pseudorapidity in minimum-bias p + p collisions and x is the fraction of production of charged particles from the hard component. The x value is fixed at 0.12±0.02 based on the linear interpolation of the PHOBOS results at $\sqrt{\mathbf{s}}_{NN}$ = 19.6 and 200 GeV [198]. The detailed procedures to obtain the simulated multiplicity are similar to that described in Ref.[199]. In this analysis, we have used *StRefMultCorr* class for centrality determination. The various centrality classes used in the analysis are given in Table 4.1. The charged multiplicity (RefMult) distribution for minimum-bias events is shown in Figure 4.2.

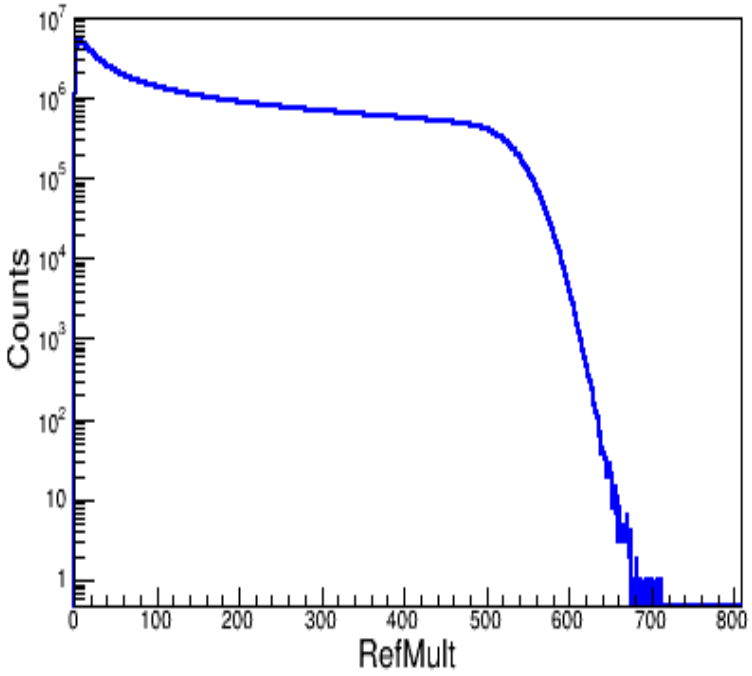

Figure 4.2: *The multiplicity distribution of charged particles in Au+Au collisions at* $\sqrt{s_{NN}}$ *= 200 GeV*

4.3 Particle Identification

4.3.1 Using TPC

The Time Projection Chamber (TPC) is the main tracking detector in the STAR experiment. It is capable of measuring charged particles within $\mid \eta \mid < 1.8$ and within full azimuthal coverage [200]. TPC operates within a constant magnetic field and hence it can measure the momentum of the charged tracks following their curvature. In this analysis, ϕ-meson are measured through the decay channel $\phi \rightarrow K^+ + K^-$. Kaons are identified by their ionization energy loss as a function of momentum inside the TPC gas volume. The mean specific energy loss in the TPC for different particles as a function of rigidity (charge×momentum) are shown in Figure 4.3. In this figure, the theoretical predictions of energy loss for the charged particles are also shown in solid lines. The theoretical values of specific energy loss are obtained from Bichsel

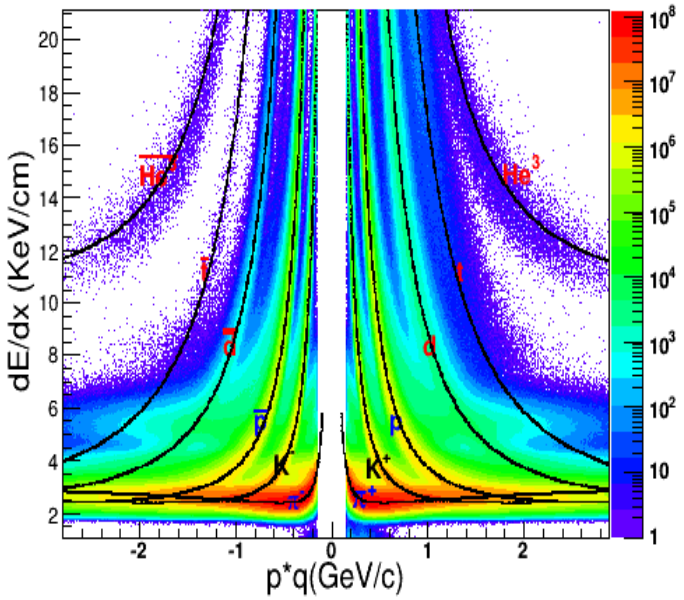

Figure 4.3: *The mean specific energy loss(dE/dx) as a function of rigidity (p*q) in Au+Au collisions at* $\sqrt{s}_{NN}$ *= 200 GeV*

function [201]. The Bichsel function is used to determine the nσ and is defined as

$$n\sigma = \frac{1}{R} \times \log[\frac{dE/dx_{measured}}{dE/dx_{theory}}] \tag{4.2}$$

where dE/dx is the specific ionization energy loss per unit path length and R is the dE/dx resolution. The kaons are shown in black text. The track quality cuts for kaons selection using TPC are listed in the Table 4.2. In order to ensure good track momentum reconstruction, short tracks were eliminated from the analysis by requiring all tracks to have $p_T > 0.15$ GeV/c and a minimum number of 15 fit points (nHitsFit) in TPC for each track. The effect of track-splitting due to the tracking algorithm is minimized by further requiring that the number of fit points is more than half of the number of total possible hit points for a track i.e. nHitsFit/Max.nHitsFit ≥ 0.52. In addition, all tracks with distance of closest approach (DCA) from primary vertex greater than 3.0 cm were removed to reject the tracks coming from sources other than primary vertex. Finally kaon tracks with $\eta < 1.0$, where the acceptance

Track Parameter	**Cut Value**
No. of fit points (nHitsFit)	≥ 15
nHitsFit/maximum possible nHitsFit	≥ 0.52
DCA from Primary Vertex(cm)	< 3.0
nσ	$\leq 2.0 \mid \sigma \mid$
Transverse momentum (p_T)	≥ 0.15 GeV/c
Pseudorapidity (η)	$\mid \eta \mid < 1.0$
dip angle between two kaons(in radians)	≥ 0.04
$m^2(GeV^2/c^4)$	$0.16 < m^2 < 0.36$

Table 4.2: *Kaon selection cuts for ϕ meson reconstruction*

of TPC is uniform, has been used in the analysis.

4.3.2 Using ToF

The ToF detector measures the time (τ) taken by a track to traverse the distance (L) from the primary vertex to the ToF. The ToF has full azimuthal coverage and works within $\mid \eta \mid < 0.9$ [202] . Using the time (τ), we can calulate the velocity (β) of the track as $\beta = \mathrm{L}/(\mathrm{c}\tau)$, where c is velocity of light. Using τ from ToF and corresponding momentum (p) from TPC, we calculate the mass (m) of the charged tracks using the relativistic equation:

$$m^2 = p^2(\frac{1}{\beta^2} - 1) \tag{4.3}$$

Therefore using this m^2, we can enhance the identification of the tracks in higher p_T(>1.0 GeV/c). The mass squared (m^2) as a function of momentum is shown in Figure 4.4. The m^2 cut which are applied for this analysis are also shown in Table 4.2.

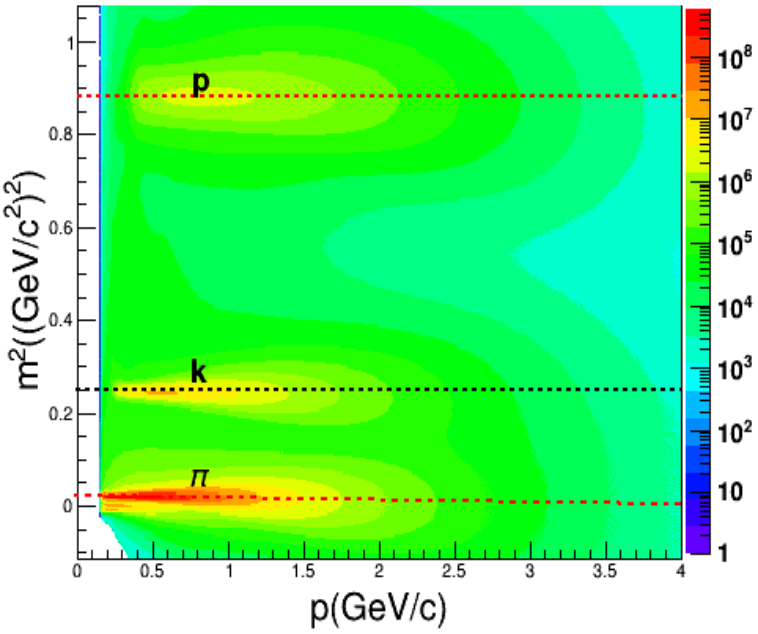

Figure 4.4: *The mass squared (m^2) as a function of momentum in Au+Au collisions at $\sqrt{s}_{NN}$ = 200 GeV. The dashed Black line corresponds to PDG mass value for kaons.*

4.4 ϕ Meson Reconstruction

The ϕ-mesons are reconstructed through their decay into two charged kaons (K^+K^-). For each event, the invariant mass distribution of the ϕ-meson was constructed using all combinations of positively charged kaon candidates with negatively charged kaon candidates. Since not all charged kaons in each event orginate from ϕ-meson decays, the ϕ-meson signal extracted this way sits above a large combinatorial background of uncorrelated pairs. Therefore one must subtract the large combinatorial background from the resulting same-event invariant mass distribution to observe the ϕ-meson signal. An event-mixing technique [203, 204] was applied to calculate the combinatorial background from the uncorrelated K^+K^- pairs, where the invariant mass was calculated by pairing two kaons from two different events with same primary vertex and

multiplicity bins. The data sample was divided into 9 raw multiplicity classes (i,e 0-5%, 5-10%,10-20%,20-30%,30-40%,40-50%,50-60%,60-70%,70-80%) and only mixing events within the same class to minimized multiplicity fluctuations effects. In order to minimize distortions due to acceptance effects, within each centrality class, the events were further sub-divided into 10(6) bins according to z-vertex position and mixed within those bins. The final mixed-event distribution for each centrality class was found by adding up all the m_{inv} distributions from each z-vertex bin. In order to reduce statistical uncertainty in the mixed-event, each event was mixed with 5 other events.

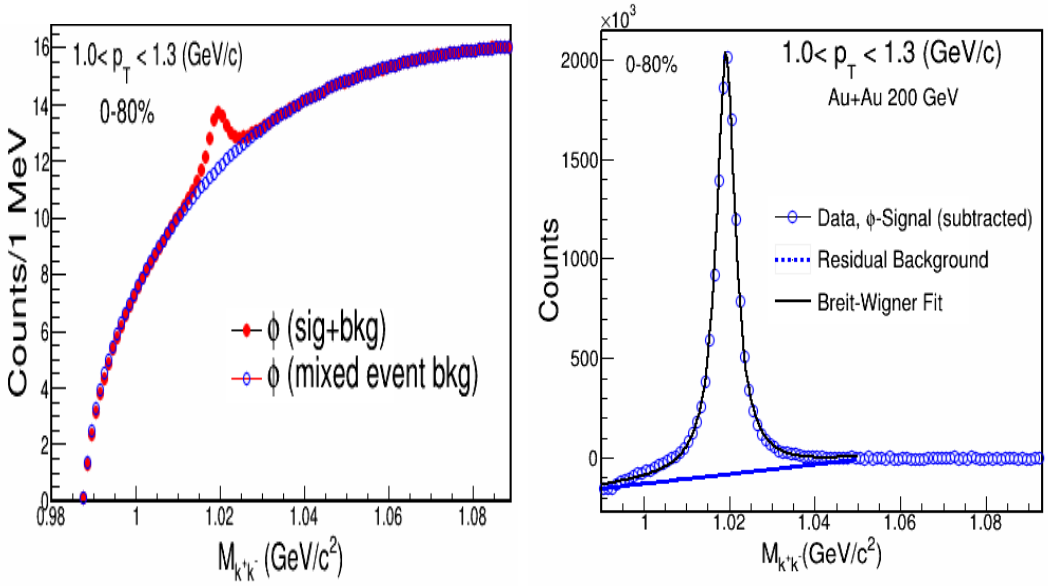

Figure 4.5: *Left Figure: Same event (Red marker) and normalized mixed event (Blue marker) K^+K^- invariant mass distributions in 0-80% centrality in Au+Au collisions at $\sqrt{s_{NN}}$ = 200 GeV, Right Figure: ϕ signal subtracted (Blue marker) fitted with B.W function and residual background (blue line) fitted with 1^{st} order polynomial in 0-80% centrality in Au+Au collisions at $\sqrt{s_{NN}}$ = 200 GeV*

To extract the ϕ-meson signal, first the mixed-event and the same-event K^+K^- invariant mass distributions were accumulated and than the mixed-event distribution

was normalized to the same-event distribution in the ϕ mass region by using scaling by the integral ratio method. In this method, the background distribution was scaled by the ratio of the integral of the signal to the integral of the background distribution in a fixed invariant mass region including the ϕ mass peak ($0.99 < m_{inv} < 1.05$ GeV/c^2). The background distribution was then subtracted from the signal distribution and the remaining signal was fitted with a Breit-Wigner (BW) function plus a straight line. Although the mixed-event background gives a good estimation of the combinatorial background due to uncorrelated kaon pairs, but it cannot account for the real correlated background from decay pairs due to Coulomb interactions, photon conversions ($\gamma \rightarrow e^+e^-$) and particle decays such as $K^{0*} \rightarrow K + \pi$, $\rho^0 \rightarrow \pi^+\pi^-$, $K^S_0 \rightarrow \pi^+\pi^-$, and $\Lambda \rightarrow p\pi^-$. For example, when both pions from a K^S_0 decay are mis-identified as kaons, the real correlation from decay will remain in the same-event as a broad distribution but will not be reproduced by the event-mixing method. Due to overlap of dE/dx bands for kaons and electrons around p = 0.5 GeV/c, the electrons/positrons are mis-identified as kaons in this momentum range. This leads to a residual background in the K^+K^- invariant mass distribution near the threshold from correlated e^+e^- pairs, mainly from photon conversions ($\gamma \rightarrow e^+e^-$). The δ-dip-angle between the photon converted electron and positron is usually very small. The δ-dip-angle is calculated from

$$\delta - dip - angle = cos^{-1}[\frac{p_{T_1}p_{T_2} + p_{z_1}p_{z_2}}{p_1 p_2}] \tag{4.4}$$

where p_1, p_2 represents the momenta of the two tracks, the other parameters with subscripts T and z representing the transverse and the longitudinal components, respectively. This δ-dip-angle represents the opening angle of a pair in the $p_z - p_T$ plane. We required the $\delta - dip - angle$ to be greater than 0.04 radians for the kaon candidate pairs. This cut is very effective in removing the photon conversion background. Figure 4.5 (Left) shows the K^+K^- invariant mass distributions from

same-event (Red marker) and mixed-event (Blue marker) and ϕ signal (subtracted) (Right Figure 4.5) (Blue marker) distribution in Au+Au collisions at $\sqrt{s}_{NN}$ = 200 GeV. The raw ϕ-meson yields are extracted by subtracting the scaled mixed-event background distributions from the signal distributions. After subtraction, the remaining distribution consists of the ϕ mass peak signal plus some residual background. To determine the raw yields for ϕ-meson, the distribution is fitted with a Breit-Wigner function superimposed on a linear background function:

$$BW(m_{inv}) = \frac{1}{2\pi}\frac{A\Gamma}{(m - m_{\phi})^2 + \Gamma/2} + B(M_{inv}) \tag{4.5}$$

where A is the area under the peak corresponding to the number of ϕ-mesons, Γ is the full width at half maximum (FWHM) of the peak and m_{ϕ} is the ϕ resonance mass. B (M_{inv}) denotes a linear [B$(M_{inv}) = p_0 + p_1 M_{inv}$] residual background function. The same event invariant mass distribution (Red marker) and mixed event invariant mass distribution (Blue marker) after proper normalisation are shown in various plots in Figure 4.6 - 4.7 for the 10 different p_T bins whereas the plots for the minimum bias raw background subtracted m_{inv} distributions in 10 p_T bins are shown in Figure 4.8 - 4.9. The various p_T bins are shown in plots.

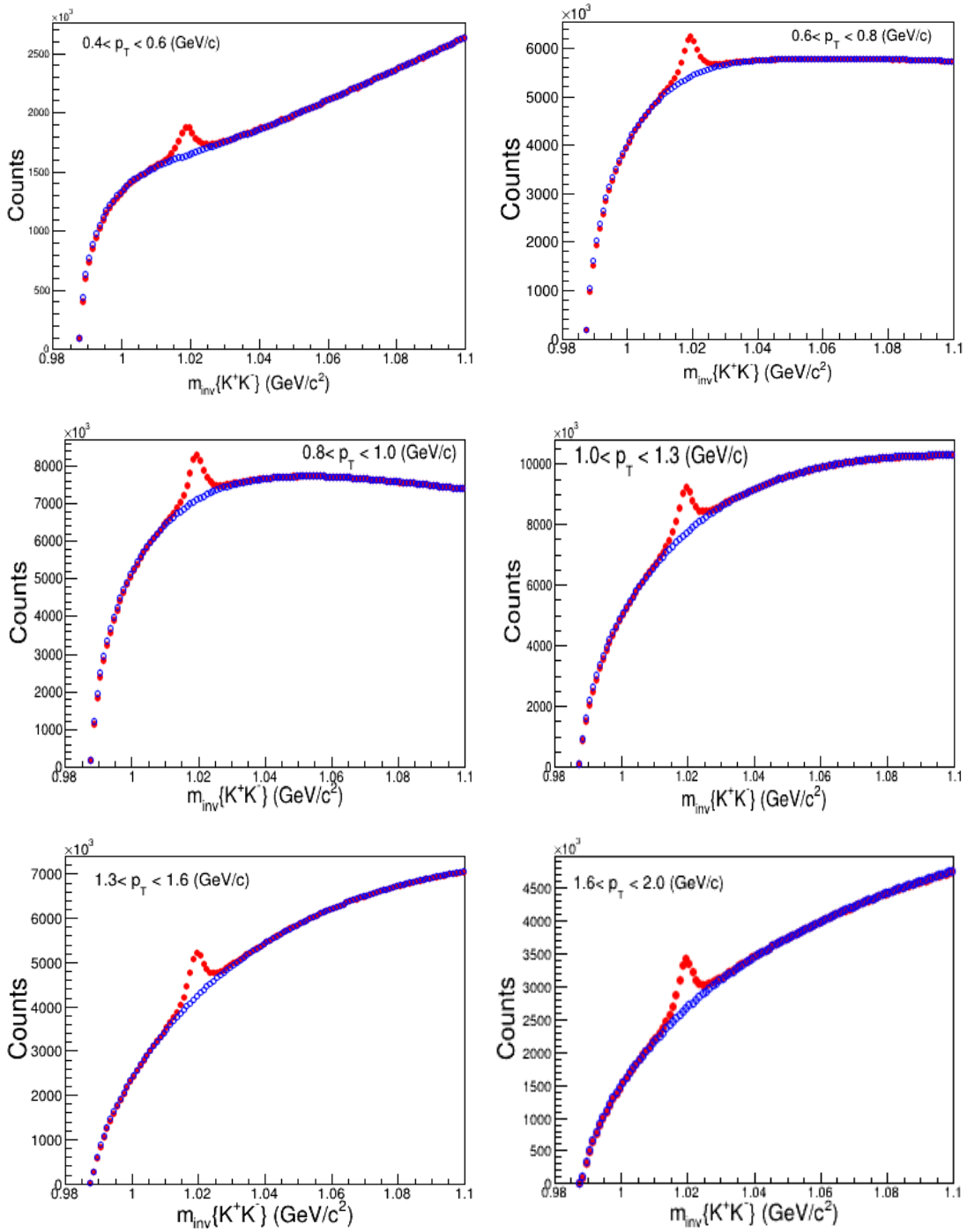

Figure 4.6: *Same event (Red marker) and normalized mixed event (Blue marker) K^+K^- invariant mass distributions in 0-80% centrality in Au+Au collisions at $\sqrt{s}_{NN}$ = 200 GeV for different p_T bins.*

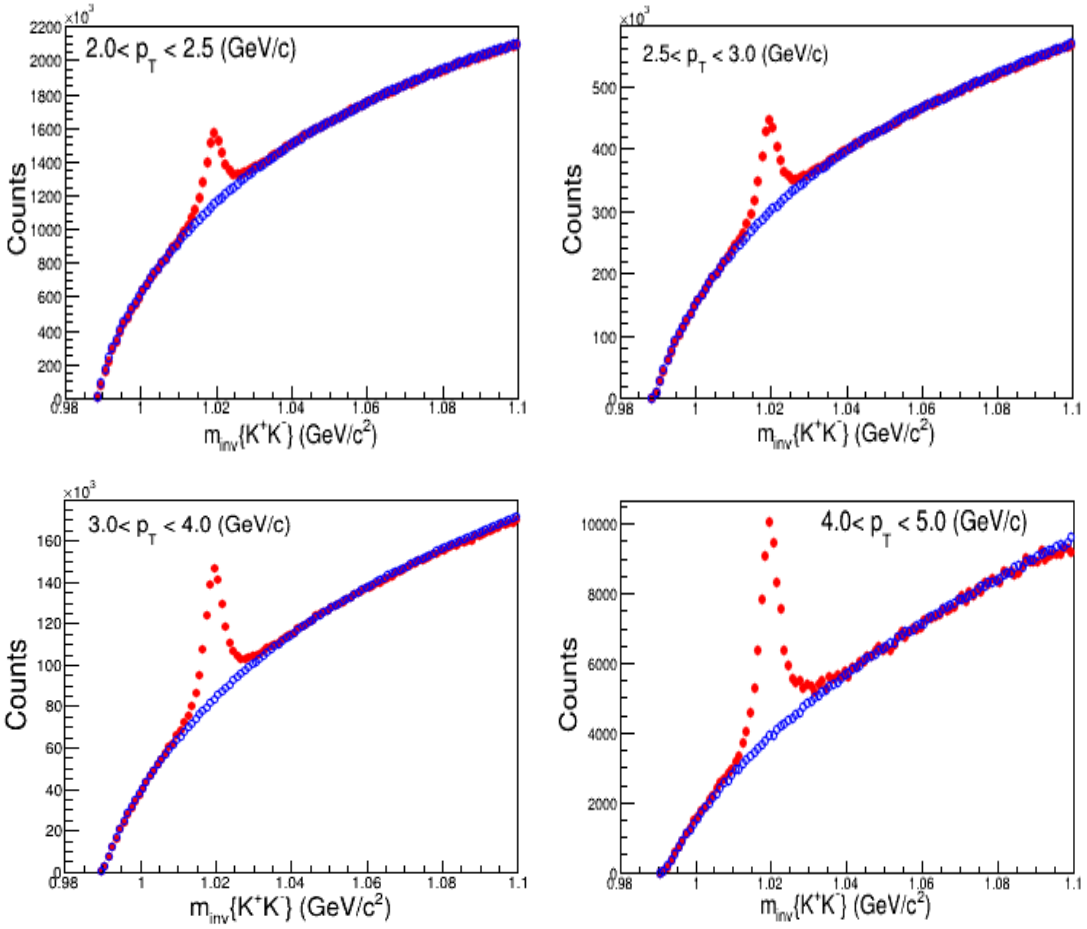

Figure 4.7: *Same event (Red marker) and normalized mixed event (Blue marker) K^+K^- invariant mass distributions in 0-80% centrality in Au+Au collisions at $\sqrt{s}_{NN}$ = 200 GeV for different p_T bins*

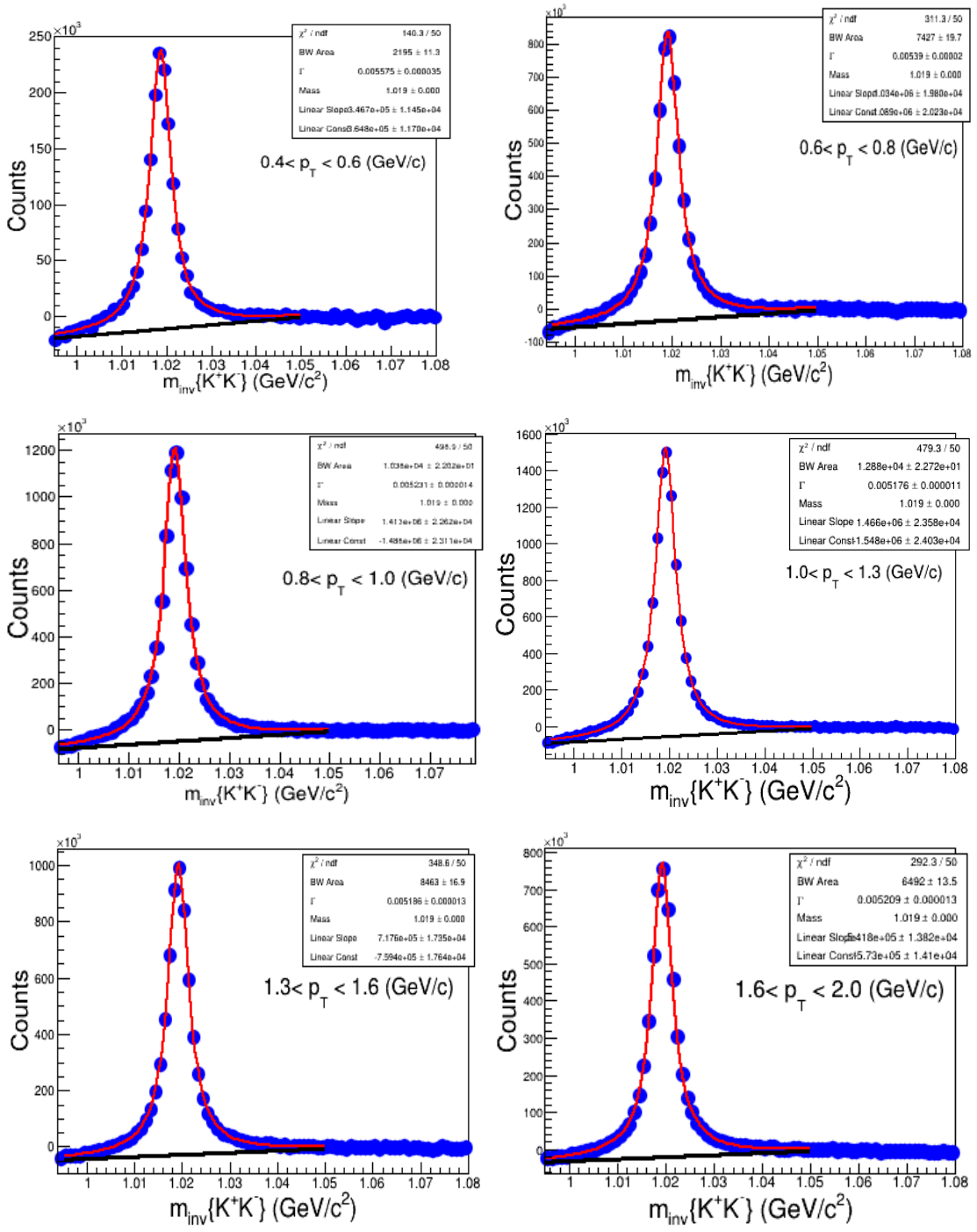

Figure 4.8: *ϕ signal subtracted (Blue marker) fitted with B.W function (Red Line) and residual background (black line) fitted with 1^{st} order polynomial in 0-80% centrality in Au+Au collisions at $\sqrt{s}_{NN}$ = 200 GeV for different p_T bins.*

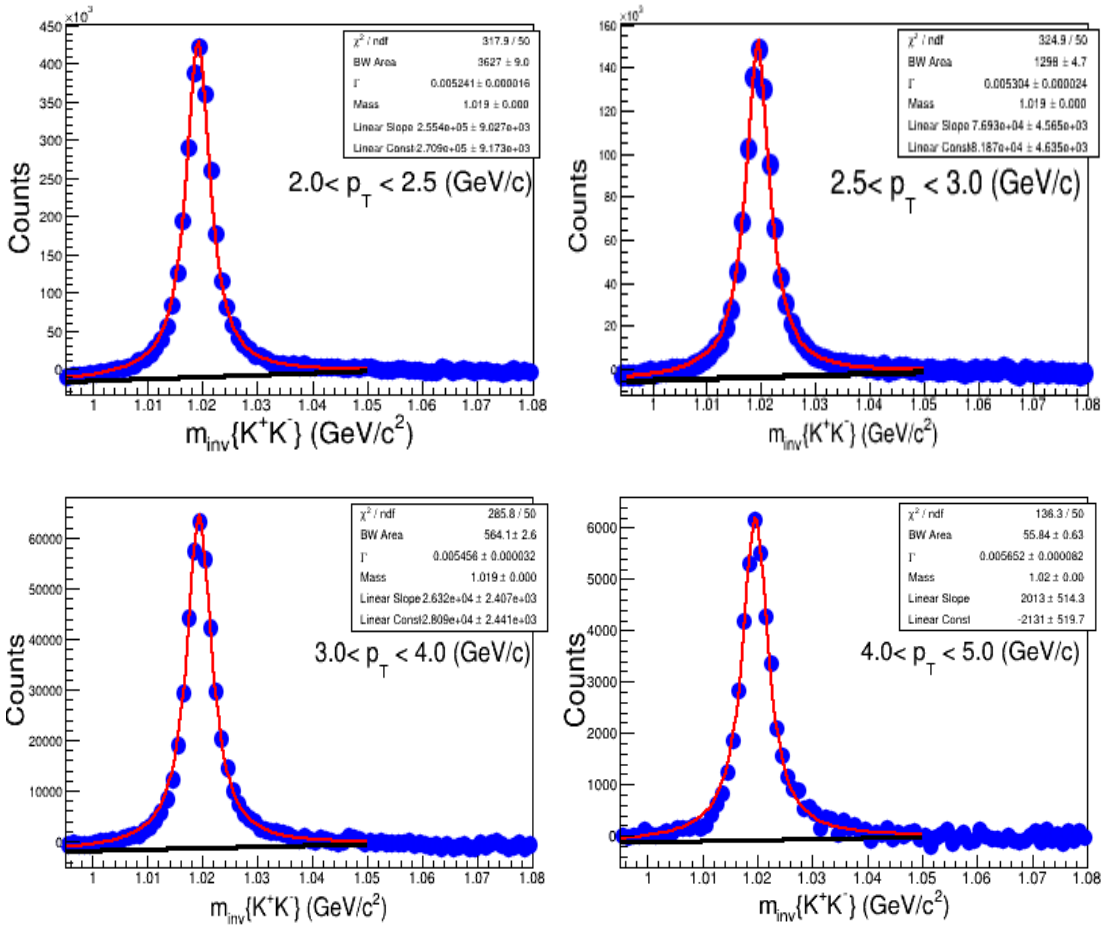

Figure 4.9: *ϕ signal subtracted (Blue marker) fitted with B.W function (Red Line) and residual background (black line) fitted with 1^{st} order polynomial in 0-80% centrality in Au+Au collisions at $\sqrt{s}_{NN}$ = 200 GeV for different p_T bins.*

Chapter 5

Flow in Heavy Ion Collisions

5.1 Introduction

Heavy-ion collisions provide a unique tool to create and study the hot QCD matter and its phase transition under controlled conditions. This hot and dense system created in heavy-ion collisions will thermalize and form a QGP which subsequently undergoes a collective expansion and eventually becomes so dilute that it hadronizes. This expansion is called "Collective Flow" and it provides experimental information on the EoS and the transport properties of created QGP. The collective motion or collective flow was first observed at Bevelac in 1984. It builds up over entire evolution of system and is therefore sensitive to combined effect of Equation of State (EoS) of the system in all its different phases. At low center of mass energies collective flow reflects the properties of hadronic matter whereas at higher center of mass energies the contribution from partonic phase (possibly QGP) becomes more dominant. The term "Collective flow" includes a common radial expansion, affecting the thermal spectra of outgoing particles and an anisotropic expansion affecting the spatial orientation of particle momenta. The first component is called radial flow, the second is anisotropic flow. The most dominant contribution to anisotropic flow is called elliptic flow. Az-

imuthal angles of the outgoing particles are generally correlated with the directions of the impact parameter in non-central nucleus-nucleus collisions. This phenomenon called "anisotropic flow" has been known for 20 years [205] and is of particular interest at RHIC which provides a unique evidence for QGP formation [206].

The main interest in anisotropic flow is due to its sensitivity to the system properties very early in its evolution. The origin of anisotropies in the particle momentum distributions lies in the initial asymmetries in the geometry of the system. Because the spatial asymmetries rapidly decrease with time, anisotropic flow can develop only in the first fm/c. Thus the anisotropic flow must be sensitive to the particle interactions which occur very early in the system evolution. Anisotropic flow is therefore, a unique hadronic observable providing direct information about the QGP formation. In this chapter, we review the contribution to flow and the analysis methods for the measurement of elliptical flow are discussed.

5.2 Radial Flow in Heavy Ion Collisions

In heavy ion collision, the system formed is surrounded by vacuum. This together with the density profile of the system gives rise to a pressure gradient from the dense centre to the boundary of the system. In central heavy ion collisions, this pressure gradient is radially symmetric and gives a boost to all particles that are formed in the system, pushing them radially outward. This means that on top of their thermal motion (governed by Classical Maxwell-Boltzmann statistics) the particles get a radial velocity component. The radial velocity component results in an increase of the momentum (p = mv) which is proportional to the mass of the particle. Therefore, the effect of radial flow is most pronounced for heavy particles. The transverse momentum spectra, in particular, of heavy particles, are influenced by radial flow, flattening them at low p_T. When thermodynamics is used to describe the evolution of the system the

measured transverse momentum spectra can be compared to the model predictions. The effect of different equations of state, which affect the radial flow through the pressure gradient, is more pronounced in the spectra of heavier particles and as such these particles can be used to constrain the models.

5.3 Anisotropic Flow in Heavy Ion Collisions

Flow signals the presence of multiple interactions between the constituents of the medium created in the collision. More interactions lead to a larger magnitude of the flow and bring the system closer to thermalization [207]. The magnitude of the flow is therefore a detailed probe of the level of thermalization and thus the possible signature of QGP.

In relativistic heavy ion collisions, when the two heavy nuclei collide, a large amount of energy is dumped into a very small volume. These collisions are pictured with various stages in between the initial stage and the end point, with particles observed in the detectors around the collision points, and many detectable signals and experimental observables are recorded at these stages. When the Lorentz contracted nuclei pass through each other, the vacuum left behind is filled with a colour field, indicates the attraction of the two nuclei and the energy of the colour field leads to the production of matter and anti-matter. Such a non-central heavy ion collision is illustrated in Figure 5.1. In the middle the reaction volume is elliptically Almond shaped, while the spectators (particles outside the overlap between the two nuclei) continue in the beam direction z.

In a collision between two protons particles are produced isotropically in the transverse plane. This means that in a heavy ion collision, where many protons collide, particle production is isotropic as well if all of these proton-proton collisions are independent of each other. If, on the other hand, in the collision system particles

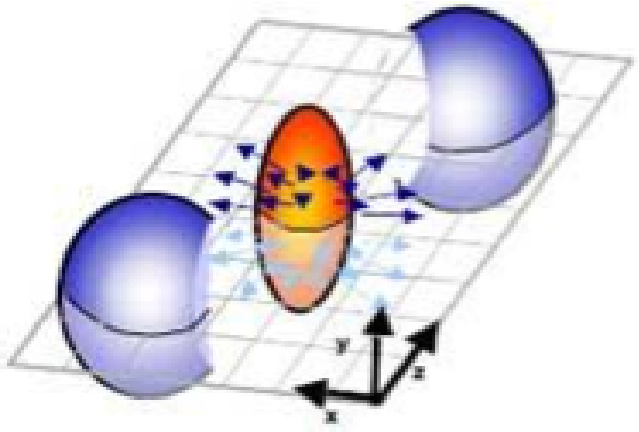

Figure 5.1: *Illustration of a non-central heavy ion collision with an elliptical reaction volume which is symmetric with respect to the reaction plane.*

undergo multiple interactions than the azimuthal transverse momentum distribution is modified due to the anisotropy of the reaction volume. This can be characterised by the Fourier expansion of the momentum distribution with respect to the reaction plane angle ψ_R. In this case the triple differential distribution, which measures the dependence of particle emission azimuthal angle measured with respect to reaction plane is written in the form of Fourier series as below:

$$E\frac{d^3N}{d^3\mathbf{p}} = \frac{1}{2\pi}\frac{d^2N}{p_T dp_T dy}(1 + \sum_{n=1}^{\infty} 2v_n \cos(n(\phi - \psi_R))) \tag{5.1}$$

where E is the energy, $\mathbf{p}$ the momentum, p_T its transverse component, y is the rapidity, ϕ the azimuthal angle and ψ_R is the azimuthal angle of the reaction plane (spanned by impact parameter (b) and beam direction (z)). v_n are the Fourier coefficients. Because of the symmetry with respect to the reaction plane the sine terms in the expansion vanish. The Fourier coefficients v_n are then given by:

$$v_n =< \cos(n(\phi - \psi_R)) > \tag{5.2}$$

The <> denote an average over all particles in the event. At zero impact parameter the reaction volume is spherical resulting in a uniform azimuthal distribution

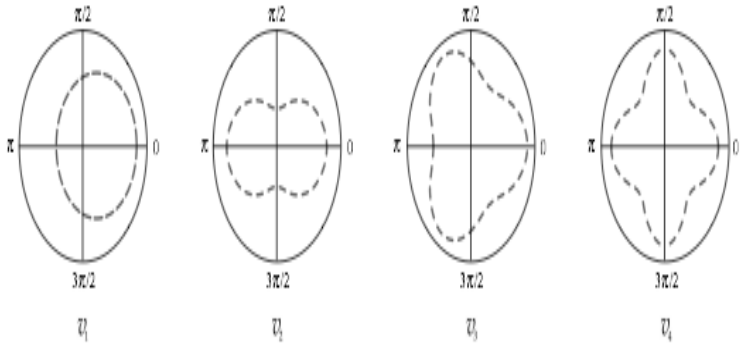

Figure 5.2: *Illustration of the first four harmonics in the transverse plane,* v_1*,* v_2*,* v_3 *and* v_4*.*

of particles, while at a finite impact parameter the reaction volume is anisotropic and the coefficients v_n will be non zero. Each Fourier harmonic co-efficient (in anology/contrast to the description at low energies, where three dimensional event shape is characterised using multipole terminology) reflects a different type of anisotropies. The first four harmonics are illustrated in Figure 5.2. The first harmonic v_1 represents an overall shift of the distribution in the transverse plane and is called directed flow. The word "directed" comes from the fact that such a flow has a direction. The second harmonic v_2 represents an elliptical volume and is called elliptic flow. The word elliptical is due to the fact that in polar co-ordinates the azimuthal distribution with non-zero harmonic is ellipse. The directed and elliptic flow are illustrated in Figure 5.3. The third harmonic (triangular flow) gives a triangular modulation and the fourth a squared. For matter at midrapidity (around $\eta = 0$) the second harmonic, elliptic flow, is dominant.

Directed flow is seen at small angles to the particle beam (large η) and it is zero at midrapidity because $< \cos(\phi) >$ is an odd function of pseudorapidity (η). v_1 is the result of pressure in the system and is therefore sensitive to the compressibility of the created matter. It depends on collision centrality and is maximum for semi-

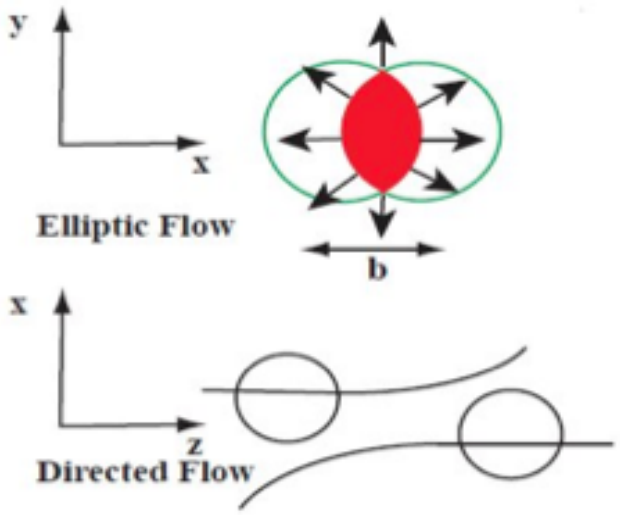

Figure 5.3: *Diagrams of elliptic and directed flow.*

central collisions and vanishes for central collisions. It also vanishes for very peripheral collisions due to the lack of a sizable pressure gradient.

5.4 Elliptic Flow in Heavy Ion Collisions

As discussed in previous section, the azimuthal anisotropy in particle production is the clearest experimental signature of collective flow in heavy-ion collisions [208]. This so-called anisotropic flow is caused by the initial asymmetries in the geometry of the system produced in a non-central collision. The second Fourier coefficient of the azimuthal asymmetry is called elliptic flow. Figure 5.4 illustrates that elliptic flow can only build up if an anisotropic reaction volume is present as well as multiple interactions between the particles. The Figure shows the elliptically shaped reaction volume and the way in which particles are emitted from that volume. The resulting azimuthal particle distribution is shown as well. The left side of the figure illustrates that when no secondary interactions are present, which means the mean free path of the particles is much larger than the typical size of the system, the azimuthal

distribution of the outgoing particles depends only on the symmetry of the production process and is not affected by the asymmetry of the reaction volume. When the mean free path is very small compared to the typical system size hydrodynamics can be used to describe the space-time evolution of the system and a pressure gradient is present in the reaction volume. The right side of the figure illustrates that more particles are emitted along the shorter axis where the pressure gradient is much larger than along the vertical axis, due to the geometry. The amplitude of the resulting modulation in the azimuthal distribution is the elliptic flow coefficient. Due to multiple interactions the initial spatial anisotropy of the reaction volume is transferred into an anisotropic transverse momentum distribution.

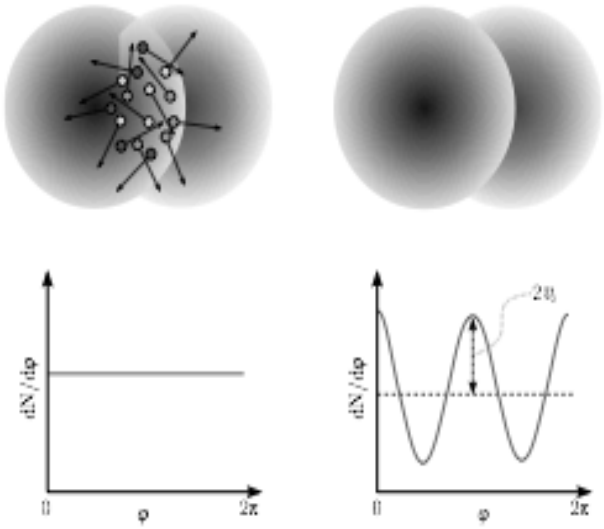

Figure 5.4: *Illustration of the azimuthal distribution of particles emitted from an anisotropic reaction volume in case of a large mean free path (left) and small mean free path (right).*

The initial spatial anisotropy, which is characterised by the spatial eccentricity ϵ_x, is defined by,

$$\epsilon_x = < \frac{y^2 - x^2}{y^2 + x^2} > \tag{5.3}$$

where x is taken in the impact parameter direction and y according to Figure 5.1 and the brackets denote an average over the transverse plane weighted with the initial density. If the system is elongated along the y-axis the spatial eccentricity is positive. The spatial eccentricity decreases during the evolution of the system because particles are emitted preferably along the short axis of the ellipse, making the particle distribution more and more spherical. At the same time the anisotropy in momentum space ϵ_p increases until it finally saturates. Most of the anisotropy in the transverse momentum distribution comes from the early stage of the evolution of the system making elliptic flow sensitive to the partonic phase, if present, of the system. By using hydrodynamics to describe the evolution of non-central heavy ion collisions and comparing these models to measure data one can learn about the equation of state of the matter and about the velocity of sound in the matter. According to ideal hydrodynamics v_2 is proportional to the initial spatial eccentricity [208],

$$v_2 \propto \epsilon_x \tag{5.4}$$

The proportionality constant depends on the speed of sound c_s in the matter. The speed of sound depends on the equation of the matter through

$$c_s^2 = \frac{dp}{d\epsilon} \tag{5.5}$$

where p is the pressure and ϵ the energy density. A softer equation of state, with smaller c_s, produces smaller elliptic flow.

5.5 Energy Dependence

At low centre of mass energies ($< 100MeV$), the collision interaction is dominated by the attractive nuclear mean field. The two nuclei are attracted towards each other and form a rotating system which emits particles in the rotating plane, producing in-plane

elliptic flow [209, 210]. At higher energies individual nucleon-nucleon collisions start to dominate, they produce a positive pressure which deflects the projectile and target fragments away from each other. Particles produced in the interaction region cannot escape in the reaction plane due to the presence of the spectator nucleons resulting in out of plane elliptic flow [211]. Figure 5.5 shows elliptic flow as a function of the centre of mass energy from many experiments [212]. Because of the Lorentz contraction of

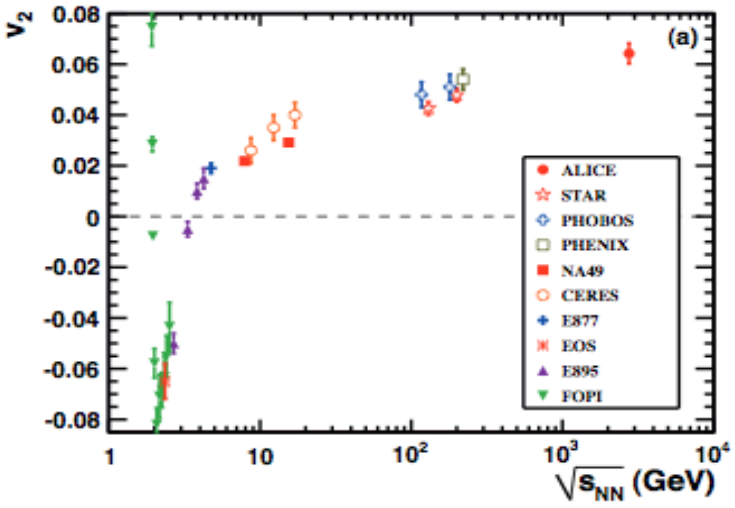

Figure 5.5: *v_2 as a function of the centre of mass energy from many experiments [212].*

the colliding nuclei, the spectators are also contracted. The spectators leave the interaction region after a time of the order $2R/\gamma$, where R is the nuclear radius and γ the Lorentz contraction factor. When the spectators are no longer present particles are free to move in any direction in the transverse plane. The pressure gradient which is largest in-plane pushes them in this direction producing in-plane elliptic flow. A transition from out of plane,$< cos(2\phi) >< 0$, to in-plane, $< cos(2\phi) >> 0$, occurs when the Lorentz contraction becomes significant. The in-plane elliptic flow increases with the centre of mass energy. At ultra-relativistic energies the nuclei are almost transparent and most of the energy stays in the longitudinal direction (along the beam direction). The transverse momenta of produced particles are mostly of the

order of a few hundred MeV while the longitudinal momenta are of the order of a few GeV. At such energies the transverse momentum dependence of elliptic flow is given by

$$\frac{dv_2(p_T)}{dp_T} \approx \frac{v_2}{< p_T >} \tag{5.6}$$

The results from STAR and ALICE experiments show that $v_2(p_T)$ does not in-

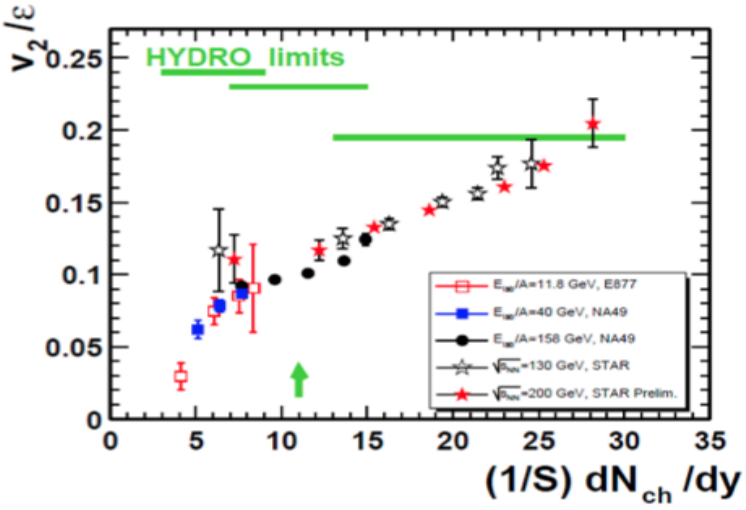

Figure 5.6: *v_2/ϵ as a function of the particle density at midrapidity. Green lines indicate ideal hydrodynamic predictions for AGS, SPS and RHIC collisions energies [214]*

crease [212], which means that the increase in v_2 of about 30%, is caused by an increase in the mean transverse momentum p_T of the produced particles. The mean p_T increases because the radial flow does increase with collision energy as a result of the higher initial energy density. By studying the ratio of v_2 over the spatial eccentricity one can test whether the system approaches the ideal hydrodynamic limit. The spatial eccentricity is in practise not measurable and has to be calculated, making it dependent on the assumed model. Figure 5.6 shows v_2/ϵ as a function of the multiplicity density (1/S) dN_{ch}/dy from several experiments [213]. Elliptic flow at different energies and impact parameters follows a single curve which reaches the hydrodynamic limit (Eq. 5.4) for Au data at 200 GeV. The disagreement between the

data and hydrodynamic calculations at lower energies is generally interpreted as a sign of incomplete thermalisation. In [214] the authors show that even for the most central Au+Au events at 200 GeV the data is best described by viscous hydrodynamics and that this viscous correction becomes more important at LHC energies because the contribution from the partonic phase of the system is expected to be larger. The viscosity can be constrained by viscous hydrodynamic model fits to v_2/ϵ as well as to $v_2(p_T)$.

5.6 Centrality Dependence

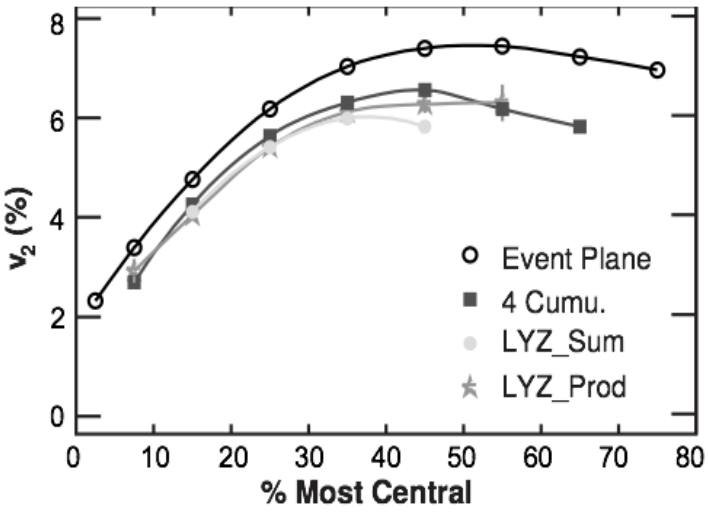

Figure 5.7: *Elliptic flow of charged hadrons as a function of the event centrality for Au-Au collisions at 200 GeV*

Elliptic flow (v_2) depends on the event centrality: multiple scattering increases with centrality while the spatial eccentricity decreases. These two effects combined make elliptic flow (v_2) low in central and in very peripheral collisions and maximum in mid-central collisions. Results of elliptic flow measurements as a function of centrality in Au-Au collisions at 200 GeV [215] are shown in Figure 5.7, where the elliptic flow

centrality dependence is seen.

5.7 Transverse Momentum and Particle Species Dependence

Figure 5.8 shows transverse momentum (p_T) dependence of elliptic flow for Au-Au collisions at 130 GeV [216]. At low p_T, v_2 rises linearly upto 1 GeV/c and this dependence at low p_T is well described by hydrodynamics. But at higher p_T, the contribution from particles that are not correlated to the reaction plane grows, which results in a deviation from thermodynamic behaviour. The particles that are not correlated to the reaction plane originate from the initial hard scatterings in the collision and because their energy is high they do not participate in many rescatterings. They are thus not thermalised nor do they participate in the collective motion. However, an azimuthal anisotropy in particle production is seen also at high p_T. At higher p_T, elliptic anisotropy is an interesting observable as it is believed that it reflects the path length dependence of high p_T parton energy loss [217]. At sufficiently high transverse momentum in Au+Au collisions, hadron yields are thought to contain a significant fraction originating from the fragmentation of high energy partons, resulting from initial hard scatterings. Calculations based on perturbative QCD (pQCD) predict that high energy partons traversing nuclear matter lose energy through induced gluon radiation [218, 219]. The energy loss (jet quenching) is expected to depend strongly on the color charge density of the created system and the traversed path length of the propagating parton. In non central heavy-ion collisions, the geometrical overlap region has an almond shape in the transverse plane, with its short axis in the reaction plane. Depending on the azimuthal emission angle,partons traversing such a system, on average, experience different path lengths and therefore different energy

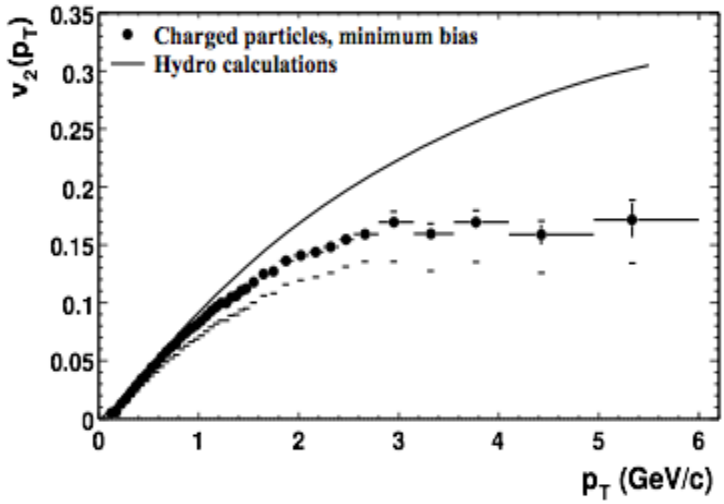

Figure 5.8: *Elliptic flow (v_2) of charged hadrons as a function of p_T for Au-Au collisions at 130 GeV compared to a hydrodynamic calculation [216].*

loss. This mechanism introduces an azimuthal anisotropy in particle production at high transverse momenta [217, 220, 221]. Figure 5.9 shows v_2 as a function of trans-

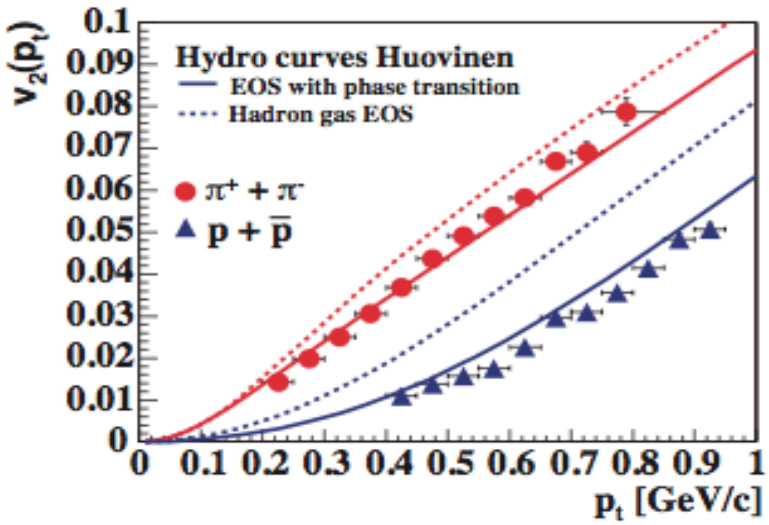

Figure 5.9: *Comparison of $v_2(p_T)$ dependence of pions and protons with hydrodynamic calculations for a hadron gas and also including a phase transition [222], [223]*

verse momentum for pions and protons for $p_T < 1$ GeV where it is well described

by hydrodynamics. As predicted by ideal hydrodynamics, at low p_T the elliptic flow clearly depends on the mass of the particle, with v_2 at a fixed p_T decreasing with increasing mass. The hydrodynamic model calculations of $v_2(p_T)$ for pions and protons are performed for two equations of state: the full curves are for an EoS which incorporates the effect of a phase transition from a QGP to a hadron gas, the dashed curves are for a hadronic EoS without phase transition. The hydro calculations clearly predict the observed behavior rather well with a better description of the measurements provided by the EoS incorporating a phase transition. For the pions the effect of a phase transition is less pronounced. The lighter particles are more affected by the temperature, thus less sensitive to the collective flow velocity but on the other hand the effect of the phase transition is more pronounced in the heavier protons because they are more influenced by the collective velocity which is sensitive to the equation of state.

At intermediate p_T, particle production by coalescence or recombination [224, 225] predicts that v_2 depends on the quark content of the particle [226], Coalescence

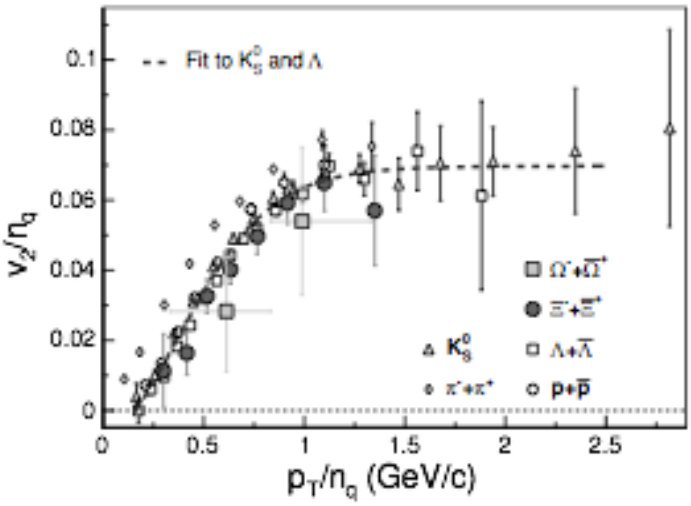

Figure 5.10: *v_2 as a function of p_T scaled by the number of quarks n_q for various particle species for Au-Au collisions at 200 GeV*

depends on the quark degrees of freedom being dominant at hadronisation and results in $v_{2,baryon} > v_{2,meson}$. Figure 5.10 shows scaling of v_2 with the number of constituent quarks versus a scaled p_T which result in all hadrons falling on a universal curve which indicates that collectivity is developed in the partonic stage of the collision [227].

5.8 Eccentricity Fluctuations

The eccentricity in general is quantified as the anisotropy of the collision geometry

$$\epsilon = < \frac{y^2 - x^2}{y^2 + x^2} > \tag{5.7}$$

Here x and y are the transverse coordinates along and perpendicular to the reaction plane respectively. For spherical nuclei the colliding system is symmetric under reflections with respect to the reaction plane. However, due to fluctuations in the positions of individual nucleons the distribution of particles in the reaction volume is not strictly symmetric on an event by event basis. Therefore the participant eccentricity is defined from the actual spatial distribution of the participants, the shifted coordinates in Figure 5.11, and can be different from the geometrical overlap region. The elliptic flow is caused by the rescattering of the particles produced in the initial nucleon-nucleon collisions. So the elliptic flow at low densities should be proportional to the particle density in the transverse plane [228, 229]. At high densities and vanishingly small mean free path, the elliptic flow signals are supposed to be saturated at a value imposed by hydrodynamical calculations. Also it is expected to be zero for azimuthally symmetric system, and for small anisotropies in the initial geometry the elliptic flow should be proportional to eccentricity. The size of fluctuations in the geometry can be estimated from Monte Carlo Glauber calculations. Due to these fluctuations in the spatial eccentricity for a fixed impact parameter, also the elliptic flow (v_2) will fluctuate and is given by a distribution rather than a single value. These

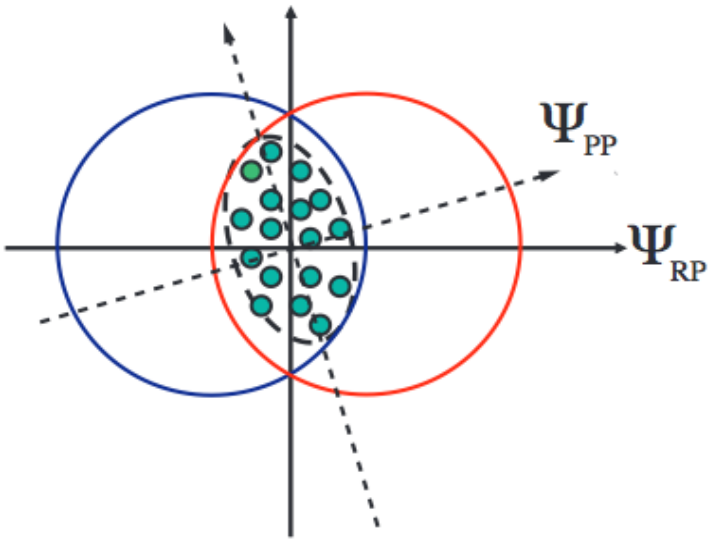

Figure 5.11: *Transverse view of a heavy-ion collision with the reaction plane ψ_{RP} oriented along the x-axis. Indicated are the participants in the overlap region that randomly define a particpant plane ψ_{PP} for each collision.*

fluctuations will be most pronounced in very peripheral collisions as the interaction region is small.

5.9 Analysis Method of Flow

As discussed in section 5.4 that the momentum anisotropy leads to the elliptical flow of produced particles. There are different methods that are used for measuring elliptical flow. These are enlisted below:

1. **Standard Event Plane Method**
2. **Scalar Product Method**
3. **Cumulant Method**
4. **Lee Yang Zeros Method**

5.9.1 Standard Event Plane Method

In the Standard event plane method [230, 231], the Fourier expansion of azimuthal distribution is used as it is impossible to determine the true reaction plane as we do not know the impact parameter vector. The essence of the method is to first estimate the reaction plane ψ_R. The estimated reaction plane is what we call the event plane. The method used to determine the anisotropy of event plane is known as Event Plane Method. In the standard event plane method ψ_R is replaced by the event plane angle in Eq. 5.2. So, one estimates the azimuthal angle of the reaction plane from the observed event plane which is further determined from the azimuthal distribution of the final state particles. The procedure to extract the event plane angle ψ_n from the produced particles starts with the reconstruction of the flow vector for each event and for each harmonic of the Fourier expansion. The event flow vector Q_n and the event plane angle ψ_n from the n^{th} harmonic distribution is defined by the equations:

$$Q_n \cos(n\psi_n) = Q_X = \sum_{i=1}^{N} w_i \cos(n\phi_i) \tag{5.8}$$

$$Q_n \sin(n\psi_n) = Q_Y = \sum_{i=1}^{N} w_i \sin(n\phi_i) \tag{5.9}$$

where w_i is the weight and N is the total number of particles in a event used for flow vector calculation. The event plane angle for each harmonic of the anisotropic flow is defined as:

$$\psi_n = \frac{1}{n} tan^{-1}[\frac{\sum_{i=1} w_i \sin(n\phi_i)}{\sum_{i=1} w_i \cos(n\phi_i)}] \tag{5.10}$$

The sum goes over the i particles used in event plane determination Since all the particles have not the same flow so weights w_i are introduced. The weight coefficients are used to enhance the contribution of particles with larger flow and hence make the Q vector a better defined observable. Experimentally it is observed that flow increases with the transverse momentum, therefore a good choice of the weights for

the calculation of flow vector Q_n is p_T itself. In present analysis weight $w_i = p_{Ti}$ (for $p_T < 2$ GeV/c) has been taken for event plane reconstruction. Usually the weights for odd and even harmonic planes are different.

5.9.2 The Scalar Product Method

The Scalar Product method [232, 233] is similar to the Event Plane method. It correlates particles to flow vector and uses length of flow vector as a weight in the average over events. As the length of the flow vector is proportional to the elliptic flow value, thus using it as a weight reduces the statistical error by maximising the measured elliptic flow signal. This method is based on scalar product of particle, u=$e^{\iota 2\phi}$, with the complex conjugate of flow vector Q^*

$$\begin{aligned} < uQ^* >_p = & \quad \frac{1}{M}\sum_{i=k}^{M} u_k \sum_{j=1,j\neq k}^{M} u_j^* \\ = & \quad \frac{1}{M}\sum_{k,j=1,j\neq k} e^{\iota 2(\phi_k-\phi_j)} \\ = & \quad \frac{1}{M}\sum_{k,j=1,j\neq k} e^{\iota 2(\phi_k-\psi_R-\phi_j)+\psi_R} \\ = & \quad \frac{1}{M}\sum_{k=1}^{M} e^{\iota 2(\phi_k-\psi_R)} \sum_{j=1,j\neq k}^{M} e^{\iota 2(\phi_j-\psi_R)} \\ = & \quad M v_2^2 \end{aligned} \tag{5.11}$$

This shows that 2-particle correlations in an event is used to estimate v_2 and is given by

$$v_2(p_T) = \frac{< Q_2 u_2^*(p_T) >}{2\sqrt{< Q_2^A Q_2^{B*} >}} \tag{5.12}$$

where $u_{2,i} = \cos(2\phi_i)+\iota\sin(2\phi_i)$ is a unit vector of ith particle, $Q_2 = \sum_k u_2, k$ is the flow vector with the sum running over all other particles k in the event. The superscript * denotes the complex conjugate of a complex number. A and B denote the two sub-events where the two vectors are constructed. The sub-events are chosen in different η intervals. In the case that Q_2 is normalized to a unit vector, Eq. 5.12 reduces to the Event Plane method. In the Scalar Product method, flow can be measured without

estimating the reaction plane. In this method, one can use a different (recentering) technique [234] to correct for detector effects, which presents an alternative to the weighting and shifting procedures. The Scalar Product method is applied to the v_2 measurement of charged hadrons. To avoid auto-correlation the particle has to be subtracted from Q in the numerator if it happens to be part of this sum. This subtraction has to be done before calculating the scaler product.

Following Eq. 5.11, the numerator of Eq. 5.11 gives v_2^2, the denomenator removes the square making $v_2[p_T]$ an estimate of v_2. $<Q_2^A Q_2^B> = <v_2^2>$ Taking the square root of denominator of the Eq. 5.12 implies that following should be valid $< v_2^2 >_e = < v_2 >_e^2$ which means that event with same elliptic flow value should be selected for measurement. Another event-by-event fluctuation arises due to the fact that the number of particles in each sub-event is different due to the statistical emission of particles in the two sub-events. These are corrected by dividing flow vectors event-by-event by their multiplicity.

The scalar product is sensitive to non-flow correlations, which are correlations not related to event plane. Non-flow typically involves few particles, in contrast to elliptic flow, which involves all particles in an event. As scalar product method uses 2-particle correlations to estimate elliptic flow, the non-flow also contributes to the measured correlations.

5.9.3 Cumulant Method

To overcome the biasing from non-flow multi-particle correlation methods have been developed. Multiple particle correlation method provides a less baised flow estimation as compared to two particle correlations. The cumulant method is proposed to measure flow by a cumulant expansion of multiparticle azimuthal correlations. The methods of flow analysis are sensitive to the non-flow effects. The cumulant method

is based on the fact that anisotropic flow is a correlation among all particles in an event whereas non-flow effects originate from a few particle correlations.

The principle of the cumulant method is that when cumulants of higher order are considered, the contribution of non-flow effects from lower order correlations will be eliminated [235, 236]. In the following we take a two and four-particle correlations as an example to illustrate how this approach works. Assuming a perfect detector, the measured two-particle correlations can be expressed as flow and non-flow components,

$$c_2 2 =< e^{\imath n(\phi_1-\phi_2)} >=< e^{\imath n(\phi_1-\phi_2)} >< e^{\imath n(\phi_1-\phi_2)} > +\delta_n = v_n^2 + \delta_n \tag{5.13}$$

where n is the harmonic. The average is taken for all pairs of particles in a certain rapidity and transverse momentum region (typically corresponding to the acceptance of a detector) and for all events in a event sample. The δ_n denotes the non-flow contributions to two-particle correlation. The measured four-particle correlations can be decomposed as follows:

$$c_2 4 =< e^{\imath n(\phi_1+\phi_2-\phi_3-\phi_4)} >= v_n^4 + 2.2.v_n^2\delta_n + 2\delta_n^2 \tag{5.14}$$

In this expression, two factors of "2" in front of the term $v^n 2\delta_n$ correspond to the two ways of pairing (1,3)(2,4) and (1,4)(2,3) and account for the possibility to have non-flow effects in the first pair and flow in the second pair or vice versa. The four-particle non-flow correlation is omitted in the expression.

From this it follows that the flow contribution can be obtained by subtracting the two-particle correlation from the four-particle correlation:

$$c_2 4 - c_2 2 =<< e^{\imath n(\phi_1+\phi_2-\phi_3-\phi_4)} >>=< e^{\imath n(\phi_1+\phi_2-\phi_3-\phi_4)} > -2 < e^{\imath n(\phi_1-\phi_3)^2} >= -v_n^2 \tag{5.15}$$

where the notation $<<\ >>$ is used for the cumulant. The cumulant of order two is just $< e^{\imath n(\phi_1-\phi_2)} >=< e^{\imath n(\phi_1-\phi_2)} >$. Cumulants of odd orders like $c_2 3$ vanish in average over many events because they include a factor $< \cos\psi_R >_e$, which is zero for

a detector with perfect acceptance. For cumulants of even order such dependence on reaction plane angle is cancelled out and thus only even cumulants are of interest. In practice, the cumulants are calculated by first constructing the generating function of the multiparticle correlations:

$$G_n(z) = \prod_{j=1}^{M}[1 + \frac{w_j}{M}(z^* e^{\iota n\phi_j} + z e^{-\iota n\phi_j}) \tag{5.16}$$

where z is an arbitrary complex number and z^* is its complex conjugate. M denotes the multiplicity in an event. w_j are weights like transverse momentum or rapidity to minimize the statistical error and maximize the flow signal. When the generating function is averaged over events and then expanded in powers of z, z^*, the coefficients of expansion yield the multiparticle correlations. Using these correlations, one can construct the generating functions of the cumulant,

$$M(< G_n(z) >)^{1/M} = \sum_k \frac{\mid z \mid^{2k}}{k!^2} << e^{\iota n(\phi_1 + ... \phi_k - \phi_{k+1} - ... - \phi_{2k}} >> \tag{5.17}$$

To study 2k particle correlation (k $\leq$1), the $(2k)^{th}$ order cumulants denoted by $c^n 2k$ can be derived by solving k equations with k different values $\mid z \mid$ in the complex plane. From the measured $c^n 2k$, one obtains an estimate of the integrated flow, which is denoted by $V_n 2k$.

$$V_n 2^2 = c_n 2, V_n 4^4 = -c_n 4, V_n 6^6 = c_n 6/4, ... \tag{5.18}$$

Given an estimate of the n^{th} order integrated flow V_n, one can obtain an estimate of differential flow $\acute{v_p}$ (flow in a restricted phase-space window) in any harmonic p = mn, where m is an integer. For instance, the 4^{th} order differential flow $\acute{v_4}$ can be analyzed using the integrated V_1, V_2, V_3 and V_4 as reference. The generating function of the cumulants for studying differential flow is given by

$$D_{p/n}(z) = \frac{< e^{ip\psi} G_n(z) >}{< G_n(z) >} \tag{5.19}$$

where ψ refers to the azimuth of the particle of interest. In the numerator, the average is performed over all particles of interest. On the other hand, the denominator is averaged over all events. Following the same procedure as in the case of the integrated flow, the cumulant $d_p 2k + m + 1$ involving 2k + m + 1 particles is computed. After this the differential flow $v_p^{'}$2k + m + 1 is estimated. For instance, the differential flow estimated from the lowest order cumulant is shown for two cases (m = 1 or m = 2):

$$v_{n/n}^{'}2 = d_{n/n}2/V_n, v_{n/n}^{'}4 = -d_{n/n}4/V_n^3 v_{n/n}^{'}3 = d_{2n/n}3/V_n^2, v_{n/n}^{'}5 = -d_{2n/n}5/2V_n^4 \tag{5.20}$$

The advantage of the generating functions is that they automatically involve all possible k-particle correlations when building the k-particle cumulants. Moreover, the formalism removes the non-flow correlations arising from detector inefficiencies. However, in practice, the use of higher order cumulants is often limited by statistics.

5.9.4 Lee-Yang Zero Method

The Lee-Yang Zero method [237, 238, 239] is based on a 1952 proposal of Lee and Yang to detect a liquid-gas phase transition [240]. As discussed above, the four-particle cumulant method, which is sensitive to the correlations of four particles, this method is sensitive to the correlations of all the particles. Thus it is supposed to remove non-flow correlations to all orders. Consider a generating function of azimuthal correlations

$$G^{\theta})(r) =< \prod_{j=1}^{M} [1 + \iota r w_j \cos(n(\phi_j - \theta))] > \tag{5.21}$$

where r is a real positive variable, $0 \leq \theta < \pi/$n an angle and the w_j is the weight attributed to the j_{th} particle to maximize the signal. The product runs over all particles in an event and the average denoted by the angular brackets is over events. If there is no collective flow the system consists of independent subsystems, and the product can be factorized to a product over the subsystems. Then the zeroes of G^{θ}

are the same as those of the subsystem function and their positions are independent of the system size (multiplicity). On the contrary, when there is collective flow, the generating function can no longer be factorized and the positions of its zeroes approach the origin as the multiplitiy increases. Therefore, the behavior of the zeroes reflects the presence or absence of collective flow in the system.

Now that the position of the first zero of G^{θ} is directly related to the presence and magnitude of anisotropic flow in the system, the first step to implement the Lee-Yang zeroes is to locate the first zero: calculate the modulus $\mid G^{\theta}(r) \mid$ as a function of r for several values of θ, so as to find for each θ the first minimum r_0^{θ}. This first minimum then yields an estimate of the integrated flow

$$V_n^{\theta}\infty = \frac{j_{01}}{r_0^{\theta}} \tag{5.22}$$

where $j_{01} = 2.40483$ is the first zero of Bessel function J_0. The integrated flow is then used as a reference to derive the estimates $v_{mn}\infty$ of differential flow $v_{mn}(p_T,\ \mathrm{y})$ by computing a function at r_0^{θ}. Averaging the various estimates $v_{mn}^{\theta}\infty$ over θ results in $v_{mn}\infty$ with reduced statistical errors. For more details see Ref [238].

Lee-Yang Zeroes provide a natural probe of collective behavior and are expected to give results similar to higher order cumulants. Its main limitation is the statistical errors, which can be significantly larger than with the standard method of flow analysis if the flow or the multiplicities are too small.

5.10 Non-flow Correlation

The method described so far are correct when correlation is induced by flow dominate all others i,e correlation due to momentum conservation [241], long and short range 2-particle correlation and many particle correlation due to quantum statistics, resonance, jets, minijets etc. Anisotropic flow is the correlation between all particles in

an event. Other correlations also exist between particles, but these typically involve a few particles. These azimuthal correlations between n-tuples of particles, that are not related to the reaction plane are collectively known as nonflow. The existence of nonflow correlations is important when measuring anisotropic flow, as these correlations need to be removed from the measurement. The characteristics of nonflow correlations are not well known and they cannot be calculated analytically as is done for flow correlations. These nonflow correlations are expected to exist mostly between few particles that are close to each other in pseudorapidity. In that respect they can be distinguished from flow correlations which extent over all particles independent of pseudorapidity. We generally start calculating the effects of non-flow by using MC data as it is difficult to measure by real data.

5.10.1 Non-flow Correlations in MC Generated Event

When the true reaction plane is known (as it is in any generated event) the contribution of non-flow correlations can be studied by analyzing correlations along the axis perpendicular to the reaction plane(y axis). For example, let us consider the correlation between Q^a and Q^b, the vectors defined by two independent sub-events. One can think of these vectors as the total transverse momentum of all particles of the sub-event (which is the case if the transverse momentum is defined as weight). If there are no other correlations except flow then

$$< Q^a Q^b >=< Q^a >< Q^b >=< Q^a_x >< Q^b_x > \tag{5.23}$$

It was assumed here that the two Q-vectors are totally uncorrelated except that both of them are correlated with reaction plane. If this is not true and there exists other correlations, then their contribution in first order would be the same to the

correlations of x components and y components. Then

$$\begin{aligned} &< Q_x^a Q_x^b >=< Q_x^a >< Q_x^b > + < Q_x^a Q_x^b >_{non-flow} \\ &\approx< Q_x^a >< Q_x^b > + < Q_y^a Q_y^b >_{non-flow}=< Q_x^a >< Q_{[}x^b > + < Q_y^a Q_y^b > \end{aligned} \tag{5.24}$$

$$< Q_x^a >< Q_x^b >\approx< Q_x^a Q_x^b > - < Q_y^a Q_y^b > \tag{5.25}$$

5.10.2 Non-flow Correlations in Real Data

The direct application of the above described method to real data is not possible. What can be done is the analysis of similar correlations using, instead of ψ_R, the event plane derived from the second harmonic, where as the analysis of different models shows, the contribution of non-flow effects is significantly less. Then with the (second harmonic) event plane resolution known one can carry out the above analysis.

There exists in the literature other methods for estimating and accounting for non-flow correlations [242, 243]. Here we briefly describe the method [243], which was applied to the data of the WA93 Collaboration [244]. It was proposed [243, 244] to characterize the non-flow correlation contribution by the value of the parameter given below:

$$c = \frac{< Q^a Q^b > - < Q_x^a >< Q_x^b >}{\sqrt{< (Q_a)^2 >< (Q_b)^2 >}} \approx \frac{< Q^a Q^b > - < Q_x^a}{N} \tag{5.26}$$

Where N is the sub-event multiplicity and for simplicity we assume w_i=1. The parameter c can strongly depend on the particular choice of sub-events, but if the non-flow contribution is dominated by two-particle correlations, it is largely independent of multiplicity [241]. For more detaits see [238]

Chapter 6

Azimuthal Anisotropy of ϕ-meson

6.1 Introduction

Azimuthal Anisotropy is an important tool for studying the hot and dense matter created in the early stages of high energy heavy-ion collisions at Relativistic Heavy ion Collider (RHIC) [245]. It describes the momentum space anisotropy of produced particles in non-central heavy ion collisions caused by the pressure gradient developed in the early stage of collisions. Although the azimuthal anisotropy is an early time phenomena but its magnitude might still be affected by the later stage hadronic interactions. Since the hadronic interaction cross section of ϕ-meson is smaller than the other hadrons, its v_n coefficients remain almost unaffected by the late stage interactions. Therefore ϕ-meson v_n will reflect the collective motion of the partonic phase. This makes the ϕ-meson a clean probe for the study of the properties of the matter created in heavy ion collisions. In this chapter the transverse momentum (p_T), centrality dependence of ϕ-meson v_n and higher harmonic ratios measured at mid-rapidity ($\mid y \mid < 1.0$) in Au+Au collisions at $\sqrt{s}_{NN} = 200$ GeV are discussed.

6.2 Data Set

The results presented in this chapter are based on data collected from Au+Au collisions at $\sqrt{s}_{NN} = 200$ GeV with the STAR detector in the year of 2011. The minimum bias trigger condition requires a coincidence of two Zero Degree Calorimeter (ZDC) which are located at ±18 m from the center of the interaction region along the beam line and the Vertex Position Detector(VPD). The event selection, centrality selection, track selection and other kinematic cuts are same as discussed in chapter 4. The Flow track selection cuts which we used to reconstruct flow vector for each event is discussed in next section.

6.3 Flow Track Selection Cuts

The tracks selection criteria for event plane reconstruction is listed in Table 6.1. In

Flow Track Selection Cuts	**Value**
No. of fit points (nHitsFit)	≥ 15
nHitsFit/Max. possible nHitsFit(nratio)	$0.52 \leq nratio \leq 1.02$
DCA from Primary Vertex(cm)	≤ 2.0
Transverse momentum (p_T)	$0.15GeV/c < p_T < 2.0GeV/c$
Pseudorapidity (η)	$\mid \eta \mid \leq 1.0$

Table 6.1: *Flow track selection cuts for event plane reconstruction*

order to minimize the contribution to the event plane determination from effects and phenomena which are not necessarily correlated with the event plane, called non-flow effects, for example jets, only particles with $p_T < 2.0$ GeV/c were used in the calculation. The various corrections done to obtain ϕ-meson v_n in Au+Au collisions at $\sqrt{s}_{NN} = 200$ GeV are discussed in the next two section.

6.4 Event plane flattening

The azimuthal angle distribution of event plane should be identical in all directions in the laboratory frame. Thus the event plane distribution has to be a flat distribution if the detectors have the ideal acceptance. But the biases due to the finite acceptance of the detector causes the particles to be azimuthally anisotropic in the laboratory. This anisotropy is not related to the true anisotropic flow arising due to pressure gradients developed in the system. Therefore it is necessary to ensure that event plane angle distribution should be flat or uniform in the laboratory frame. There are several different methods to make event plane angle distribution flat. Let us discuss them in detail:

1. **Phi Weighting**: In this method, we assume that the cumulative ϕ distribution from a large sample of events is flat in an ideal detector, this is generally true due to the random orientation of the impact parameter of the collision with respect to the laboratory frame. The ϕ dependence of the reaction plane reconstruction can be corrected by introducing the ϕ weights which are proportional to inverse of the azimuthal distribution of the particles averaged over many events of each ϕ bin. Each particle i gets the weight w(ϕ_i) calculated as:

$$w(\phi_i) = \frac{1}{N_{\phi_i}} \times \frac{\sum_{i=1}^{N_{bins}} N_{\phi_i}}{N_{\phi}} \tag{6.1}$$

   where ϕ_i is the azimuthal angle of the particle and N_{ϕ_i} is the discrete in the ϕ histogram. But this method will not work if the azimuthal distribution of the particles is zero or very low in some part of the phase-space. Exactly same problem happened for STAR detector system because of a few dead sector in the TPC during data collection in the year of 2010. For this reason it was not possible to use ϕ weight method for event plane correction.

2. **Recentering**: For non-flat distribution of event plane angle, the flow vector Q_n distributions over a large number of events are not centered around zero. In this method the Q_n-vector distributions are made to be centered by subtracting the average Q_n-vector i,e.

$$Q'_X = Q_X - < Q_X > \tag{6.2}$$

$$Q'_Y = Q_Y - < Q_Y > \tag{6.3}$$

where $Q_X = \sum_{i=1} w_i \cos(n\phi_i)$ and $Q_Y = \sum_{i=1} w_i \sin(n\phi_i)$ and Q'_X & $Q'Y$ are the new corrected position of Q_n vector. The averages $< Q_X >$ and $< Q_Y >$ are made over many events.

3. **Shift Correction**: In this method one has to fit the unweighted laboratory frame distribution of the event planes, summed over all events, to a Fourier expansion and devises an event-by-event shifting of the planes needed to make the final distribution isotropic. The equation for shift correction [246] for n^{th} harmonic event plane is:

$$n\Delta\psi_n = \sum_{i=1}^{i_{max}} \frac{2}{i}(- < \sin(in\psi_n) >< \cos(in\psi_n) > + < \cos(in\psi_n) >< \cos(in\psi_n)) > \tag{6.4}$$

These values are used to make shifts in the event plane angle. The corrected event plane angle after shift correction is given as:

$$\psi'_n = \psi_n + \sum_{i=1}^{i_{max}} \frac{2}{in}(- < \sin(in\psi_n) >< \cos(in\psi_n) > + < \cos(in\psi_n) >< \cos(in\psi_n)) > \tag{6.5}$$

In this analysis, the correction is done upto 20^{th} harmonic i.e. summation runs over i=1 to 20. Larger value of i is chosen to reduce the contribution from higher order harmonics.

In Figure 6.1, we have plotted the uncorrected, after recentering and after shift correction distribution of 2^{nd} order event plane angle. The ψ_2 distribution is

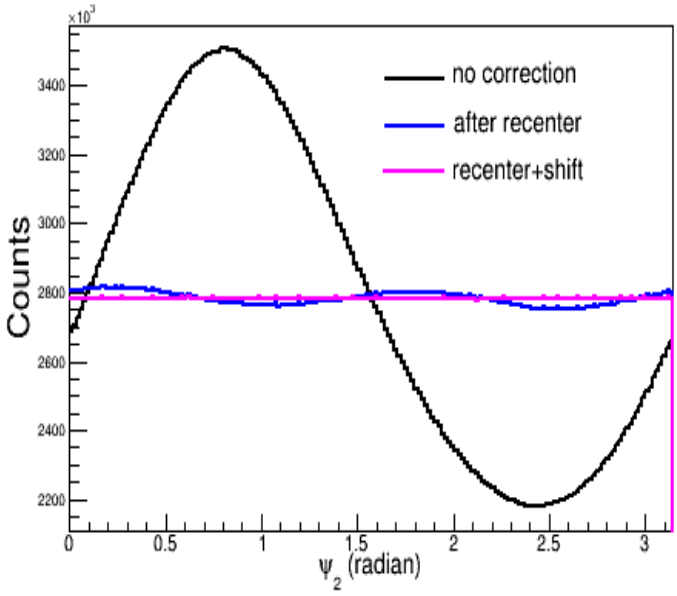

Figure 6.1: ψ_2 *distributions: uncorrected, recenter and recenter+shift corrected.*

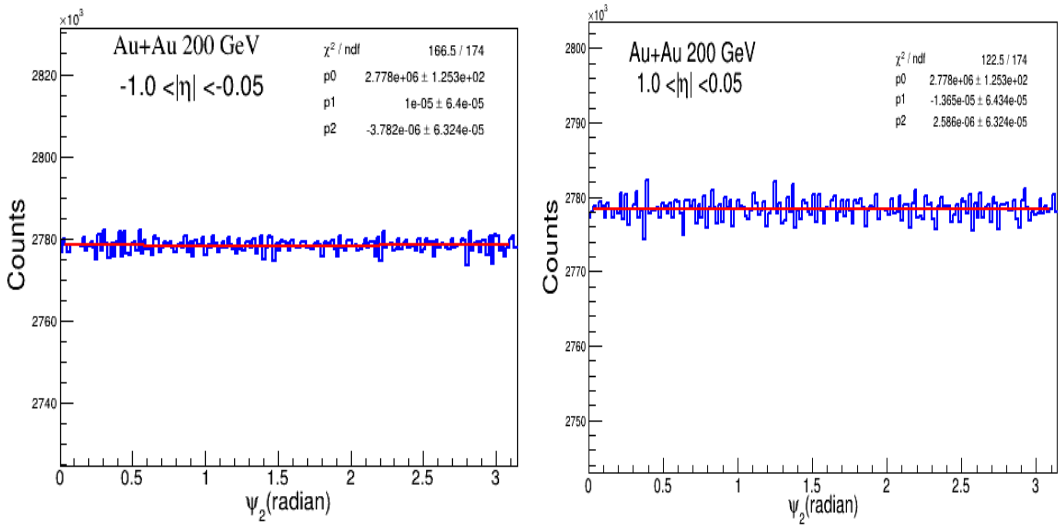

Figure 6.2: *Event plane distributions using flow tracks with* $-1.0 < \eta < -0.05$ *and* $0.05 < \eta < 1.0$ *respectively. Red line corresponds to the fit to the data*

flat after the shift correction followed by recentering. I am also showing the 2^{nd} order event plane (ψ_2) distributions constructed using flow tracks with -1.0 $< \eta <$ -0.05 and 0.05 $< \eta <$ 1.0, respectively in Figure 6.2. These event plane

distributions have been fitted with a function:

$$f = p_0[1 + 2p_1 \cos(2\psi_2) + 2p_2 sin(2\psi_2)] \tag{6.6}$$

where p_0, p_1 and p_2 are free parameters. Small values of parameters p_1 and p_2 indicate that event plane distributions are flat. The other higher order event plane (ψ_3, ψ_4, ψ_5) distributions are shown in Figure 6.3.

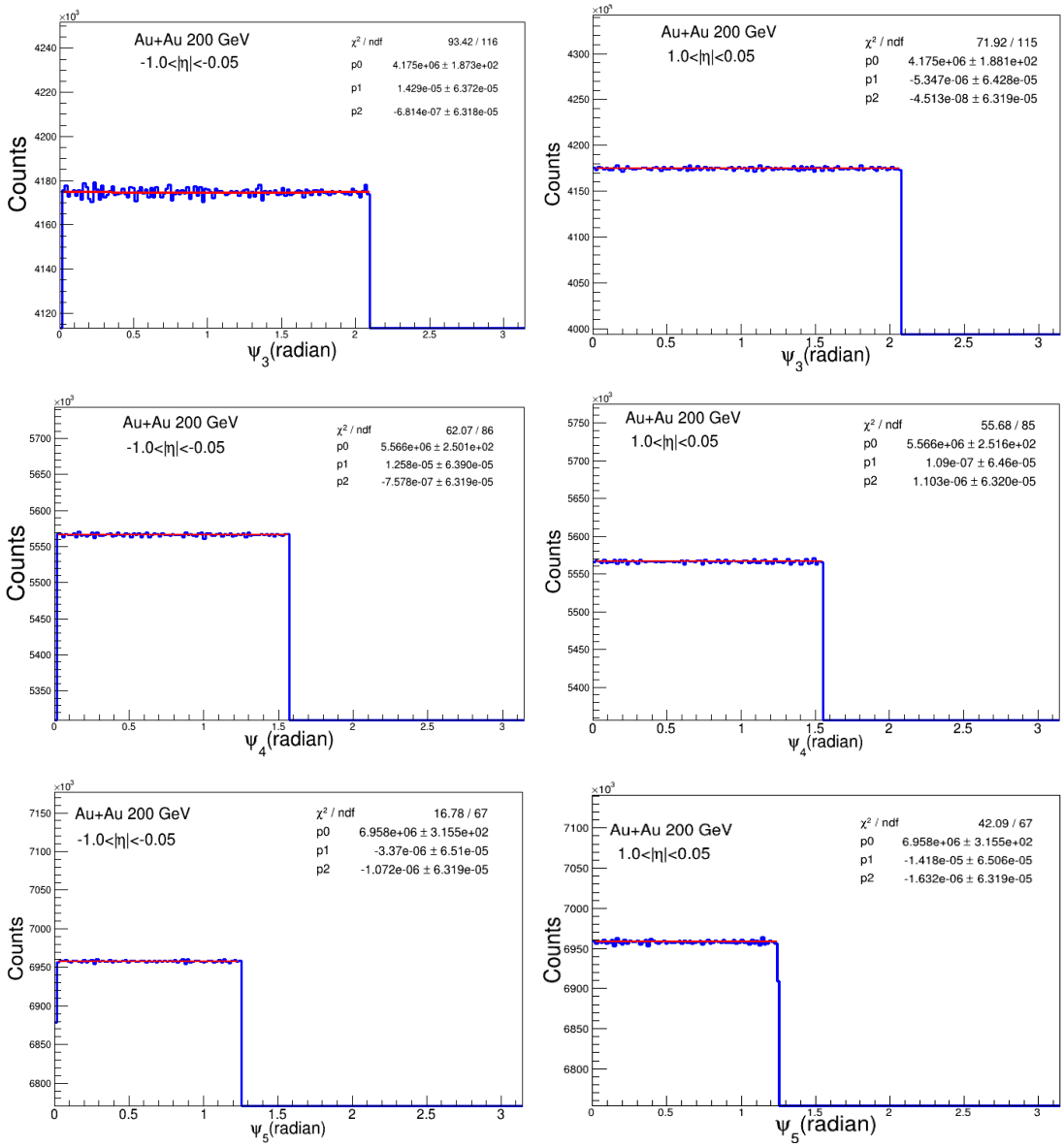

Figure 6.3: *ψ_3, ψ_4, ψ_5 event plane distributions using flow tracks with $-1.0 < \eta < -0.05$ and $0.05 < \eta < 1.0$ respectively. Red line corresponds to the fit to the data*

6.5 Event plane resolution

A finite number of particles are used to calculate the event plane in an event, which leads to a limited resolution in the measured event plane angle. Therefore, the observed v_n has to be corrected for the event plane resolution as:

$$v_n = \frac{v_n^{obs}}{< \cos[n(\psi_n - \psi_r)] >} \tag{6.7}$$

where ψ_r is true reaction plane angle. For this analysis, η-sub event method is used to calculate the event plane resolution. In this method, the full TPC event plane is divided into two subevents in η so that the multiplicity of each sub-event A and B are approximately the same and hence their respective resolutions should be equal. The two sub-events are positively correlated because each is correlated with the reaction plane and hence the event plane resolution is estimated by the correlation of the events planes of two sub-events A and B and is given by

$$R = \sqrt{< \cos[n(\psi_n^A - \psi_n^B >} \tag{6.8}$$

The Figure 6.4 shows resolution as a function of centrality in Au+Au collisions at $\sqrt{s}_{NN}$ = 200 GeV. The event plane resolution has been calculated for nine different centrality bins ($0-5\%, 5-10\%, 10-20\%, 20-30\%, 30-40\%, 40-50\%, 50-60\%, 60-70\%$ and $70-80\%$) as shown in Table 6.2. The resolution depends on the number of tracks used for event plane reconstruction. For the most peripheral collisions, the small multiplicity reduces the resolution while for the most central collisions, the small flow values weakens it (because event plane is calculated using the anisotropic flow of the event itself). Because of this two competing effects the final resolution first increases from peripheral to mid-central collision and then decreases. The resolution values for other order harmonics are shown in Table 6.3 - 6.5. The most common used method for resolution correction for an average v_n over a centrality range is

$$< v_n >= \frac{v_n^{obs.}}{< R >} \tag{6.9}$$

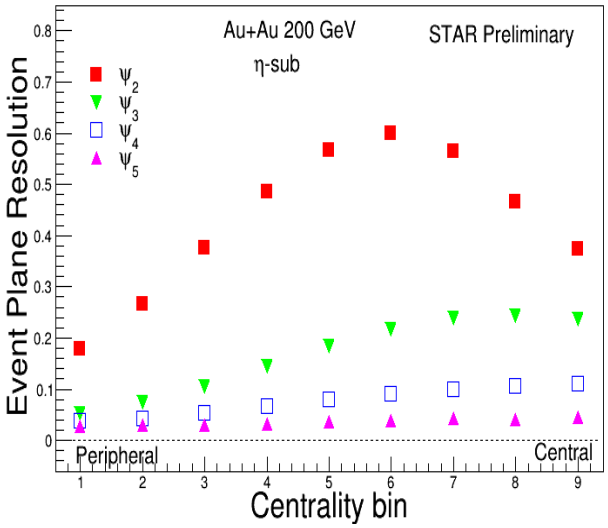

Figure 6.4: *The event plane resolutions as a function of centrality in Au+Au collisions at* $\sqrt{s_{NN}}$ *= 200 GeV*

Centrality Range	**Resolution values**
0-5%	0.373949
5-10%	0.465516
10-20%	0.563059
20-30%	0.598392
30-40%	0.565188
40-50%	0.484809
50-60%	0.376196
60-70%	0.264809
70-80%	0.177101

Table 6.2: *Second order event plane resolution in TPC from η-sub event method in Au+Au collisions at* $\sqrt{s_{NN}}$ *= 200 GeV*

Here $< R >$ is the mean resolution in wide centrality bin and can be calculated as:

$$< R >= \frac{\sum N_i < R >_i}{\sum N_i} \tag{6.10}$$

Where N_i and $< R >_i$ is the multiplicity and the resolutions of i^{th} narrow centrality bin, respectively. This procedure works well for narrow centrality bins, but fails for wider centrality bins, for example $0-80\%$. We use another approach known as event-by-event resolution correction for wide centrality bin [247]. In this method resolution correction for wide centrality bin has been done by dividing the term $cos(n(\phi - \psi))$ by the event plane resolution (R) for the corresponding centrality for each event.

$$< v_n >=< \frac{v_n^{obs.}}{R} > \tag{6.11}$$

Centrality Range	**Resolution values**
0-5%	0.234436
5-10%	0.241738
10-20%	0.236888
20-30%	0.215677
30-40%	0.182615
40-50%	0.143344
50-60%	0.103533
60-70%	0.072685
70-80%	0.051070

Table 6.3: 3^{rd} *order event plane resolution in TPC from* η*-sub event method in Au+Au collisions at* $\sqrt{s}_{NN}$ = *200 GeV*

6.6 Flow Method for short lived particles

The flow for unstable particles (for instance Λ, ϕ etc.) is studied through their decay products. One must first identify a correlation between daughter particles typically through an invariant mass plot and then study how this correlation depends

Centrality Range	**Resolution values**
0-5%	0.110642
5-10%	0.105791
10-20%	0.099713
20-30%	0.090441
30-40%	0.079968
40-50%	0.066035
50-60%	0.052624
60-70%	0.041885
70-80%	0.037489

Table 6.4: 4^{th} *order event plane resolution in TPC from* η*-sub event method in Au+Au collisions at* $\sqrt{s}_{NN}$ *= 200 GeV*

Centrality Range	**Resolution values**
0-5%	0.044249
5-10%	0.039941
10-20%	0.042200
20-30%	0.037634
30-40%	0.035919
40-50%	0.031262
50-60%	0.029786
60-70%	0.029041
70-80%	0.025997

Table 6.5: 5^{th} *order event plane resolution in TPC from* η*-sub event method in Au+Au collisions at* $\sqrt{s}_{NN}$ *= 200 GeV*

on azimuthal angle of decaying particles [248]. Two variations of event plane method can be used for extraction of flow for ϕ meson.

1. **ϕ- binning method**

2. **v_n vs m_{inv} method**

6.6.1 ϕ - binning method

In this ϕ - binning method [245] one has to measure the raw yield of the chosen particle as function of angle (ϕ - ψ_n), where ϕ is the azimuthal angle of the particle in laboratory-frame and ψ_n is the event plane angle. The extracted yield as a function (ϕ - ψ_n) can then be fitted by the following function to get the observed v_n

$$\frac{dN}{d(\phi - \psi} = p_0[1 + 2v_n \cos(n(\phi - \psi_n))] \tag{6.12}$$

Where p_0 and v_n are the parameters. In case of resonances, where the signal typically consists of a very small mass peak sitting above a large combinatorial background. It is difficult to extract the raw yields accurately. Again, the (ϕ - ψ_n) bin method of extracting v_n requires that for each p_T bin, the small signal is further divided into bins of (ϕ - ψ_n) angle. This can lead to a large systematic errors in the final v_n measurement as the systematic (or statistical) error in extracting the raw yield is large. Because of this reason, another method (v_n vs m_{inv}), described in the following section is used to extract the resonance v_n co-efficient.

6.6.2 v_n vs m_{inv} method

To extract v_n of ϕ-meson, v_n vs $m_{inv.}$ [248] method is used in the present analysis. For single particle, the probability distribution of the azimuthal angle ϕ (measured with respect to a fixed direction in the laboratory) can be written as:

$$p(\phi - \psi_r) = \frac{1}{2\pi} \sum_{n=+\infty}^{-\infty} v_n e^{in(\phi - \psi_r)} \tag{6.13}$$

where ψ_r is the reaction plane angle. If the system is symmetric w.r.t the reaction plane with real v_n, Eq. 6.13 reduces to:

$$p(\phi - \psi_r) = \frac{1}{2\pi}(1 + 2\sum_{n=1}^{\infty} v_n \cos(n(\phi - \psi_R))) \tag{6.14}$$

For pairs of particles, Eq. 6.13. can be extended as:

$$p(\phi_{pair} - \psi_r) = \frac{1}{2\pi}\sum_{n=+\infty}^{-\infty} v_n^{pair} e^{in(\phi_{pair} - \psi_r)} \tag{6.15}$$

where ϕ has been replaced with ϕ_{pair}. For resonance particle (e.g. ϕ-meson etc.) which decays to two daughter particles (e.g. $\phi \rightarrow K^+K^-$), ϕ_{pair} is the azimuthal angle of the parent resonance particle. In Eq. 6.15, v_n^{pair} are called "$pair - flow$" coefficients defined by v_n^{pair}=$< e^{-in(\phi_{pair} - \phi_R} >$, with the normalization v_0^{pair}=1. Since the probability distribution is real-valued so the coefficients also satisfy the property

$$v_{-n}^{pair} = (v_n^{pair})^* \tag{6.16}$$

But unlike the single-particle flow v_n, the pair-flow coefficient v_n^{pair} is in general not a real number. As a consequence, sine terms are also present in the real form of Fourier expansion and Eq. 6.15 is replaced by

$$p(\phi - \psi_r) = \frac{1}{2\pi}(1 + 2\sum_{n=1}^{\infty} v_{c,n}^{pair} \cos(n(\phi - \psi_r)) + (v_{s,n}^{pair} \sin(n(\phi - \psi_r)))) \tag{6.17}$$

where the real coefficients $v_{c,n}^{pair}$ =$< \cos(n(\phi - \psi_r)) >$ and $v_{s,n}^{pair} = \sin(n(\phi - \psi_r))$ are related to the complex v_n^{pair} by the relation $v_n^{pair} = v_{c,n}^{pair} - iv_{s,n}^{pair}$.

For a resonance particle which is identified through its mass peak in an invariant mass distribution consisting of all combinations of candidate decay daughter particle pairs, the invariant mass distribution can be separated into:

$$N_{pairs}(m_{inv}) = N_b(m_{inv}) + N_s(m_(inv) \tag{6.18}$$

where N_b is the number of combinatorial background pairs and N_s is the number of signal pairs. In similar way, for the ϕ-meson so we can write the contributions to the

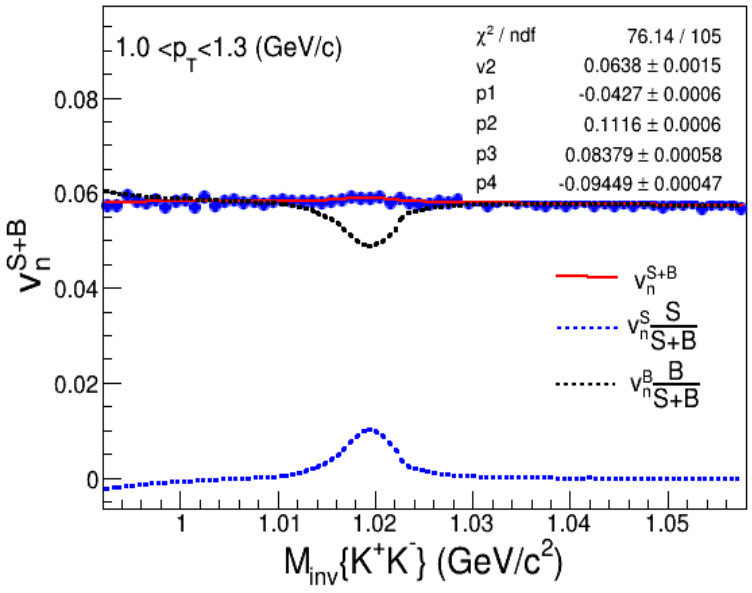

Figure 6.5: *v_n as a function of invariant mass. The red line is the fit to the data points.*

pair-flow coefficients as:

$$N_{pairs}(m_{inv})v_{c,n}(m_{inv}) = N_b(m_{inv})v^b_{c,n}(m_{inv}) + N_{\phi,n}(m_{inv})v^{\phi}_{c,n}) \tag{6.19}$$

$$N_{pairs}(m_{inv})v_{s,n}(m_{inv}) = N_b(m_{inv})v^b_{s,n}(m_{inv}) + N_{\phi,n}(m_{inv})v^{\phi}_{s,n}) \tag{6.20}$$

Symmetry with respect to the reaction plane for ϕ particles implies that $v^{\phi}_{s,n} = 0$, further if the background is composed of uncorrelated particles, then $v^b_{s,n} = 0$. The v_n distribution as a function of m_{inv} can then be fitted using the following equation(based on Eq. 6.19):

$$v_n^{S+B} = v_n^S \frac{S}{S+B}(m_{inv}) + v_n^B \frac{B}{S+B}(m_{inv}) \tag{6.21}$$

where S is the signal yield, B is background yield, v_n^S, v_n^B and v_n^{S+B} are the v_n of signal, background and total particles, respectively. The ratios $\frac{S}{S+B}$ and $\frac{B}{S+B}$ are functions of invariant mass. The term $v_n^B(m_{inv})$ is parametrized as a linear function in order to take care of the v_n^B value as a function of (m_{inv}). Here v_n^B has been taken

as a 3^{rd} order polynomial function of invariant mass. The fit result v_n^S is the final v_n. The each term of Eq. 6.21 is shown in Figure 6.5 for ϕ-meson in Au+Au collisions at $\sqrt{s}_{NN}$ = 200 GeV.

6.7 Systematic uncertainties

The systematic uncertainties in the analysis were performed by varying the track cuts, event cuts, track identification etc. Table 6.6 lists all the cuts (Track and Event cuts) that were applied for systematic study. The shape of residual background after mixed event subtraction varies with p_T. This is because of contamination in kaon selection. We used different methods to estimate the effect for raw ϕ yield extraction as given below:

Cut Name	**Default Cut**	**Varied Cut**	
		Cut 1	**Cut 2**
(nHitsFit)	$\geq$ 15	$\geq$ 18	$\geq$ 21
nHitsFit/ nHitsPoss	$\geq$ 0.52	$\geq$ 0.54	$\geq$ 0.56
DCA (cm)	$<$ 3.0	$<$ 2.0	$<$1.5
nσ	$\leq$ 2.0$\mid \sigma \mid$	$\leq$ 1.5$\mid \sigma \mid$	$\leq$ 2.5$\mid \sigma \mid$
Vertex Z $\mid Vz \mid$ (cm)	30	25	35
Etagap(η-gap)	0.1	0.2	0.3
$m^2(GeV)^2/c^4$	$0.16 < m^2 < 0.36$	$0.14 < m^2 < 0.36$	$0.18 < m^2 < 0.36$

Table 6.6: *Cuts for systematic study*

1. To vary fit function range for residual background

2. Using different fit function for residual background

   -Ist order polynomial (poly. 1)

-2nd order polynomial (poly. 2)

Finally, the systematic error is calculated as the root-mean-square value of the distribution for each data point.

6.8 Results and Discussions

6.8.1 Transverse momentum (p_T) dependence of ϕ-meson v_n

The ϕ-meson v_n as a function of transverse momentum (p_T) in Au+Au collisions for a minimum bias events ($0-80\%$) is presented in Figure 6.6. The vertical bars in each data point correspond to the statistical error and the bands correspond to the systematic error. From the Figure 6.6 we conclude that all v_n measurements of the

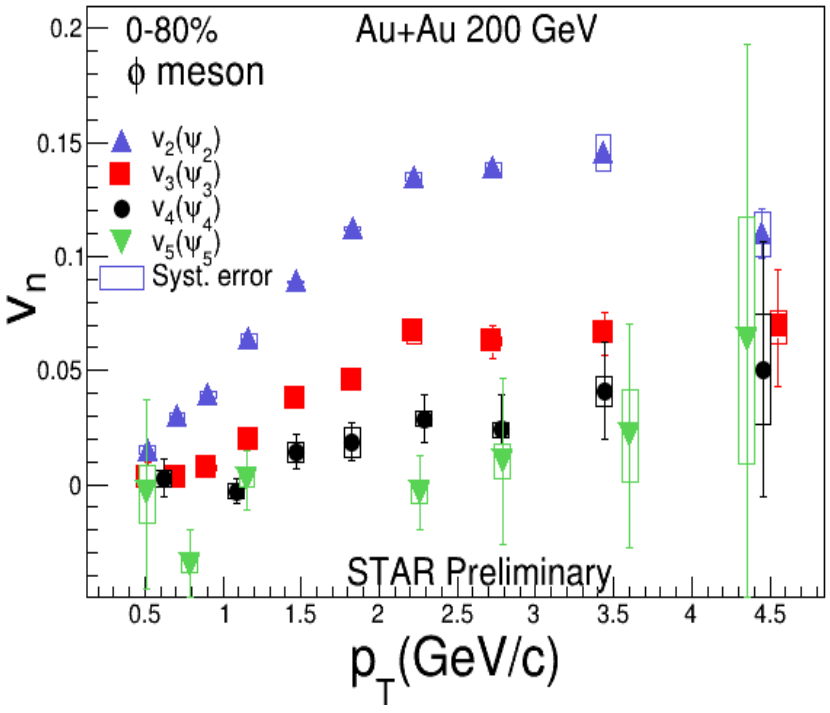

Figure 6.6: *ϕ-meson v_n as a function of transverse momentum (p_T) for $0-80\%$ minimum bias events in Au+Au collisions at $\sqrt{s}_{NN}$ = 200 GeV*

ϕ-meson show an increasing trend with increasing p_T i,e $v_n(p_T)$ at 200 GeV increases

with transverse momentum and reaches its maximum at intermediate p_t (~3 GeV/c). Further the magnitude of v_2 is greater than v_3, v_4 and v_5 ($v_2 > v_3 > v_4 > v_5$). However the v_n(n=2, 3 and 4) has a non-zero positive values but v_5 has a negative values and also consistent with zero within statistical uncertainty.

6.8.2 Centrality dependence of ϕ-meson v_n

Figure 6.7 shows centrality dependence of ϕ-meson $v_n(p_T)$ in Au+Au collisions at $\sqrt{s}_{NN}$ = 200 GeV for three different centrality bins: $0-10\%, 10-40\%$ and $40-80\%$. In this Figure, we can see that v_2 shows strong centrality dependence i,e ϕ-meson v_2 values for $40-80\%$ is larger than that of $10-40\%$ and $0-10\%$ centralities. This is

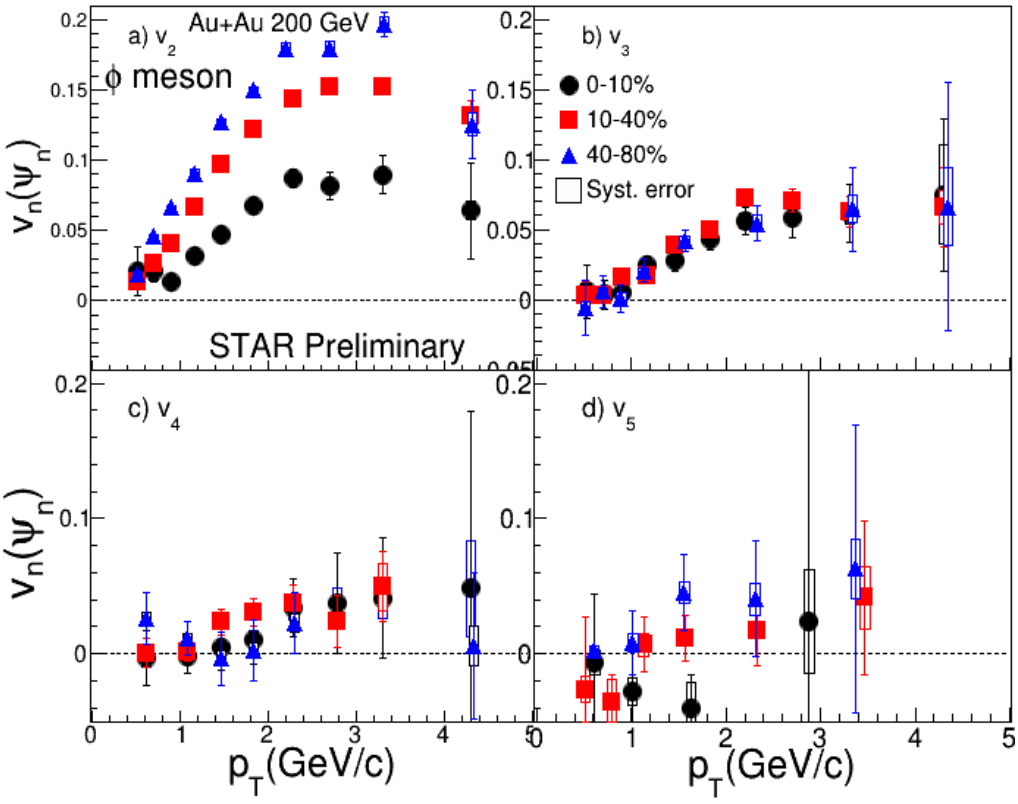

Figure 6.7: *Centrality dependence of ϕ-meson $v_n(p_T)$ in Au+Au collisions at $\sqrt{s}_{NN}$ = 200 GeV for three different centrality bins:* $0-10\%, 10-40\%$ *and* $40-80\%$.

expected because of the eccentricity of the initial nuclear overlap area which reflects

the initial spatial anisotropy is larger for $40-80\%$(mid central to peripheral) compared to $0-10\%$ (most central) and $10-40\%$ (central to mid peripheral) collisions. The flow coefficient v_3 exhibits no centrality dependence which suggests that its origin is entirely from fluctuations of the initial geometry of the system. Similarly the v_4 measured with respect to ψ_4 and $v_5(\psi_5)$ does not depend strongly on the collision centrality which refers to a strong contribution from the flow fluctuations.

6.8.3 Higher harmonic ratios and their comparison with ideal hydrodynamic and coalescence model

6.8.3.1 v_3/v_2 ratio

The Figure 6.8 presents ϕ-meson v_3/v_2 as a function of p_T for a minimum bias a) $0-80\%$ and b) $0-10\%$, c) $10-40\%$, d) $40-80\%$ centralities in Au+Au collisions at $\sqrt{s}_{NN} = 200$ GeV. From the plot, we can say that that ratio (v_3/v_2) is constant for $p_T > 1.5$ GeV/c which is consistent with hydrodynamical model.

6.8.3.2 $v_4(\psi_4)/v_2^2$ ratio

The ratio $v_4(\psi_4)/v_2^2$ is expected to reach 0.5 [249] in ideal hydrodynamic. Therefore, it is important to check the ratio $(v_4(\psi_4)/v_2^2)$ of data to see whether our system behaves like ideal hydro. Figure 6.9 shows ϕ-meson $v_4(\psi_4)/v_2^2$ as a function of p_T for a minimum bias $(0-80\%)$ and $0-10\%$, $10-40\%$,$40-80\%$ centralities in Au+Au collisions at $\sqrt{s}_{NN} = 200$ GeV. From the plot we can see that the ratio is more than unity or larger within uncertainities for all the centralities. The ratio $v_4(\psi_4)/v_2^2$ is larger than ideal hydrodynamic predictions. One of the explanation is that interactions among the produced particles are not strong enough to produce local thermal equilibrium, so that the hydrodynamic description breaks down and the resulting value is higher. It is also argued that elliptic flow fluctuations may enhance the value of $v_4(\psi_4)/v_2^2$.

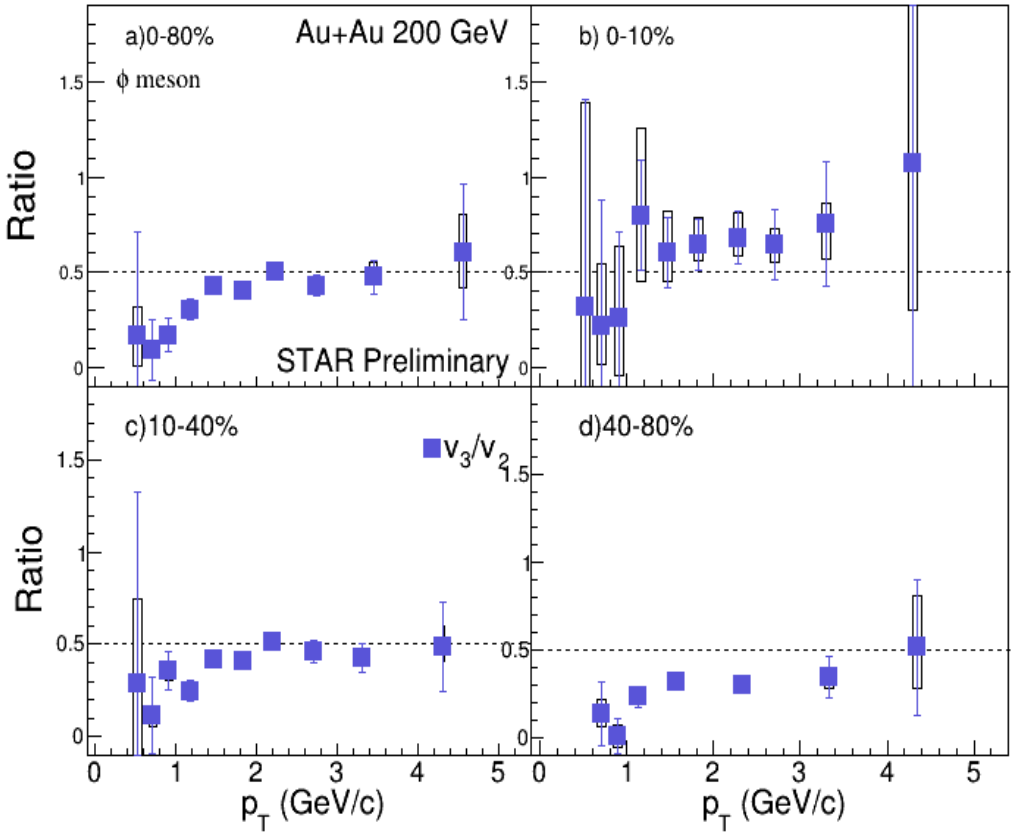

Figure 6.8: *ϕ − meson v_3/v_2 as a function of p_T for a minimum bias a) $0-80\%$ b) $0-10\%$, c) $10-40\%$, d) $40-80\%$ centralities in Au+Au collisions at $\sqrt{s}_{NN}$ = 200 GeV*

As per the calculations of coalescence model the value of the ratio $(v_4(\psi_4)/v_2)$ is $\approx$ 0.75[250], which is also lower than what we have observed in our measurement.

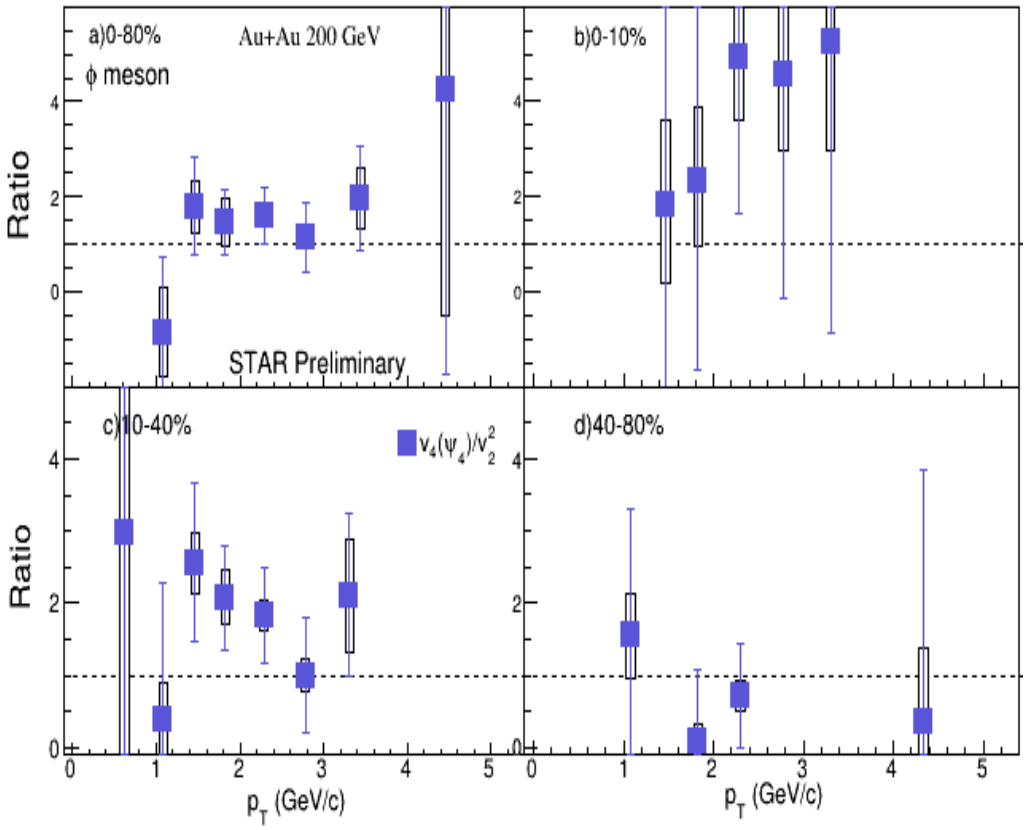

Figure 6.9: *$\phi-$meson $v_4(\psi_4)/v_2^2$ as a function of p_T for a minimum bias a) $0-80\%$ b) $0-10\%$, c) $10-40\%$, d) $40-80\%$ centralities in Au+Au collisions at $\sqrt{s}_{NN}$ = 200 GeV*

Chapter 7

Transverse Momentum Correlations

7.1 Introduction

The main goal of the ultra-relativistic nuclear collision program is the creation of the Quark Gluon Plasma (QGP), the state of deconfined quarks and gluons. The QGP is believed to be formed at the early stage of high energy heavy-ion collisions when the system is hot and dense. As the time passes, the system dilutes, cools down, and hadronizes. It is understood that such a state requires (local) thermalization of the system brought about by many rescatterings per particle during the system evolution. It is not clear when and if such a dynamical thermalization can really occur. The study of event-by-event fluctuations and correlations ia an important tool to understand thermalization and phase transition in heavy-ion collisions [251, 252, 253, 254, 255, 256]. Fluctuations of various quantities such as event wise mean transverse momentum ($< p_T >$), charged track multiplicity and conserved quantities such as net baryon and or net charge are considered as some of the probes in search of critical point in QCD phase diagram [257, 258, 259, 260, 261, 262]. The non-monotonic

change in transverse momentum (p_T) correlations as a function of centrality has been proposed as a possible signal of quark gluon plasma (QGP) formation [251]. In this chapter, two-particle transverse momentum correlations, $< \Delta p_{t,i} \Delta p_{t,j} >$ as a function of event centrality for U+U collisions at $\sqrt{s}_{NN} = 193$ GeV is discussed.

7.2 Data Selection

7.2.1 Event Selection

The data used in the present analysis is collected in the year 2012, for the U + U collisions at center of mass energy 193 GeV from the production $P12id$, with the minimum biased trigger with the trigger set up $UUproduction2012$ having the trigger $Id's$ $400005, 400025$ and 400035. Main detector used in the present analysis is the Time Projection Chamber (TPC) [263], the primary tracking device at STAR. TPC has full azimuthal coverage and uniform acceptance in ± 1.0 units of pseudorapidity. The charged particle momenta are measured by reconstructing their trajectories through the TPC. The more details of the STAR TPC and trigger detectors are given in chapter 2. The events with the primary collision vertex position along the beam direction (V_z) within 30 cm of the center of the detector are selected for this analysis. The primary vertex(v_Z) distribution is shown in Figure 7.1.

7.2.2 Centrality Definition

The centrality classes in U+U collisions at $\sqrt{s}_{NN} = 193$ GeV are determined by comparing the measured raw charged hadron multiplicity uncorrected for efficiency and acceptance effects (named as RefMult or N_{raw}) from the TPC within a pseudo-rapidity window $|\eta| \leq 0.5$ with Glauber Monte Carlo simulations [264]. The detailed procedure to obtain the simulated multiplicity are similar to that described in Ref[265].

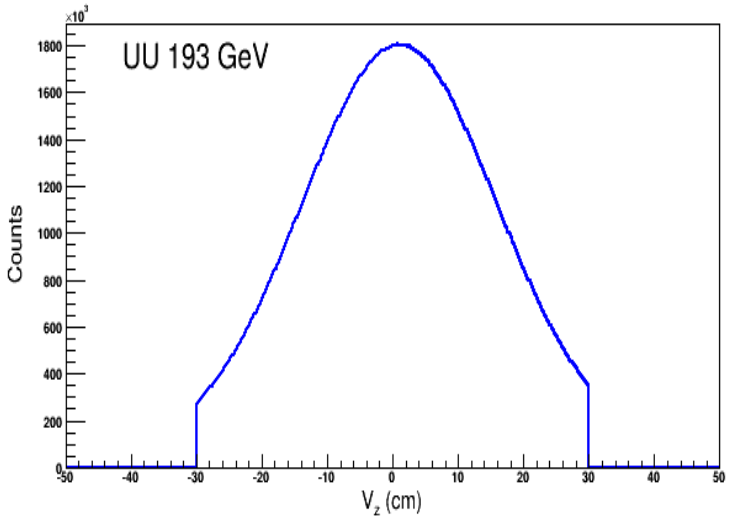

Figure 7.1: *Distribution of Z-component of event vertex in U+U collisions at* $\sqrt{s_{NN}}$ *= 193 GeV*

The centrality classes for U+U collisions at $\sqrt{s_{NN}} = 193$ GeV are 0-5% (most central), 5-10%,10-20%,20-30%,30-40%,40-50%,50-60%,60-70%,70-80%(most peripheral) [266]. Figure 7.2 shows the uncorrected multiplicity distribution with $\mid \eta \mid < 0.5$ in U+U collisions at $\sqrt{s_{NN}} = 193$ GeV. Each centrality bin is associated with an average number of participating nucleons ($< Npart >$) and average number of binary collisions ($< Ncoll >$) using the Glauber Monte Carlo simulations [264] employing the Woods-Saxon distribution for the nucleons inside the Uranium nucleus. The systematic uncertainties are determined by varying the Woods-Saxon parameters. Table 7.1 lists the $dN_{ch}/d\eta$, $<N_{part}>$ and $<N_{coll}>$ values for each centrality in U+U collisions at $\sqrt{s_{NN}} = 200$ GeV.

7.2.3 Track Selection

The various track cuts used in the analysis for the selection of charged particles are listed in Table 7.2. In order to have uniform detector performance, a pseudorapidity cut of $\mid \eta \mid < 1.0$ is applied in the data. It is important to avoid the admixture of

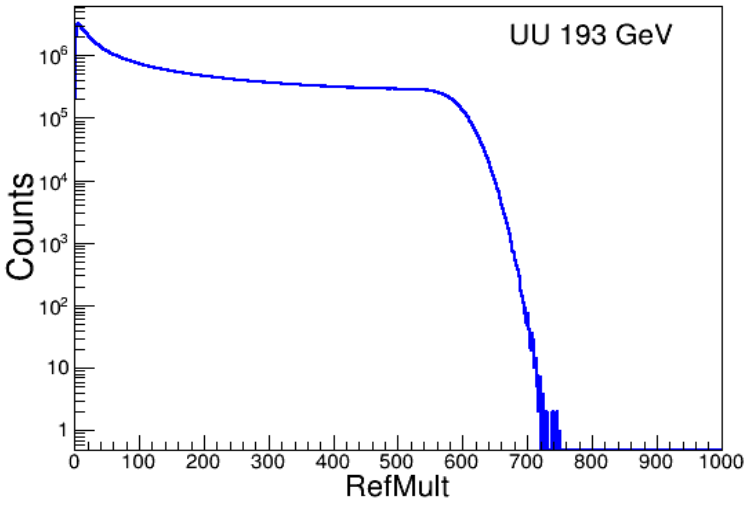

Figure 7.2: *Uncorrected multiplicity distribution with* $|\eta| < 0.5$ *in U+U collisions at* $\sqrt{s}_{NN} = 193$ *GeV*

Centrality	$\mathbf{d}N_{ch}/\mathbf{d}\eta$	$<N_{part}>$	$<N_{coll}>$
0-5%	$\geq$ 740	418±6	1341±105
5-10%	$\geq$ 609	358±14	1058±52
10-20%	$\geq$ 410	281±13	751±49
20-30%	$\geq$ 269	199±14	462±45
30-40%	$\geq$170	137±14	272±39
40-50%	$\geq$ 101	89±13	149±31
50-60%	$\geq$ 56	55±11	75±22
60-70%	$\geq$ 29	31±9	35±13
70-80%	$\geq$ 13	16±6	15±8

Table 7.1: *Summary of centrality bins based on the* $dN_{ch}/d\eta$, $<N_{part}>$ *and* $<N_{coll}>$ *for each centrality bin in U+U collisions* $\sqrt{s}_{NN} = 193$ *GeV [266]*

tracks from a secondary vertex. This is achieved by applying a condition on distance of closest approach (DCA) between each track and the event vertex. The charged

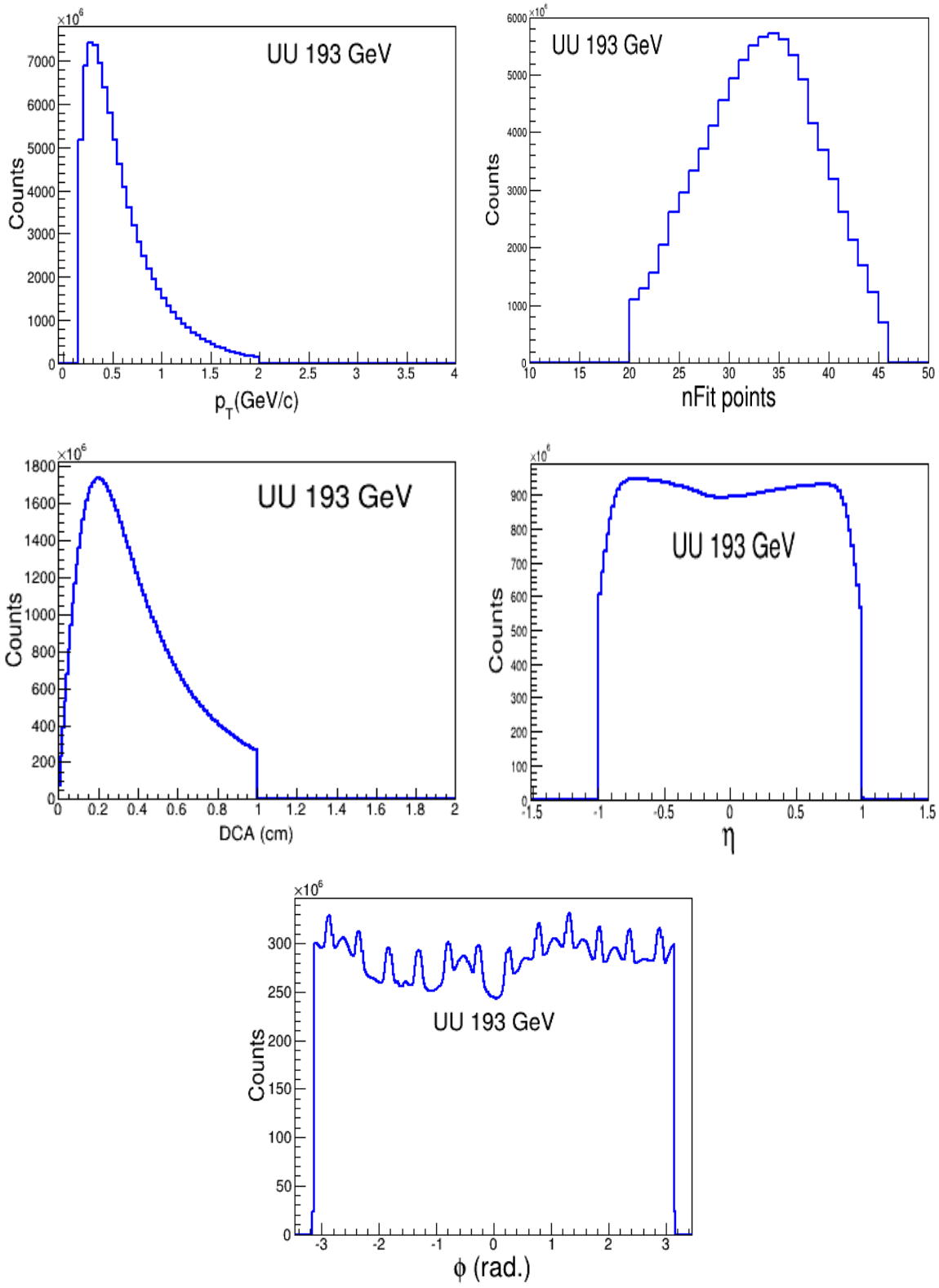

Figure 7.3: *Quality assurance distributions, p_T(top left), N_{Fit} points(top right), DCA(middle left), pseudorapidity(middle right) and phi(bottom) distributions for the U+U collisions at $\sqrt{s}_{NN}$ = 193 GeV.*

particle tracks are required to have originated within 1 cm of the measured event

Track Parameter	Cut Value
No. of fit points (nHitsFit)	> 20
DCA from Primary Vertex(cm)	< 1.0
Transverse momentum (p_T)	0.15 GeV/c $< p_T <$ 2.0 GeV/c
Pseudorapidity (η)	$\mid \eta \mid < 1.0$

Table 7.2: *Charged particle selection cuts used in the analysis*

vertex. The multiple counting of split tracks is avoided by applying a condition on the number of track points (N_{Fit}) used in the reconstruction of the track. Those charged particle tracks are selected for the analysis which satisfy $N_{Fit} > 20$. The transverse momentum range selected for the analysis is 0.15-2.0 GeV/c. Figure 7.3 shows the p_T (top left), N_{Fit} points (top right), DCA (middle left), pseudorapidity (middle right) and phi (bottom) distributions for the U+U collisions at $\sqrt{s}_{NN} = 193$ GeV.

7.3 Transverse Momentum Fluctuations

The p_T fluctuations in high-energy collisions can be measured using the distribution of the event-by-event mean transverse momentum defined as

$$< p_T >= \frac{1}{N} \sum_{i=1}^{N} p_{T,i} \tag{7.1}$$

where N is the multiplicity of accepted tracks from the primary vertex in a given event and $p_{T,i}$ is the transverse momentum of ith track. Figure 7.4 shows the event-by-event mean p_T distributions for U+U collisions at $\sqrt{s}_{NN} = 193$ GeV. The distributions become wider as we move on from central to peripheral collisions. This might indicate the presence of non-statistical fluctuations for all centralities in U+U collisions at $\sqrt{s}_{NN} = 193$ GeV.

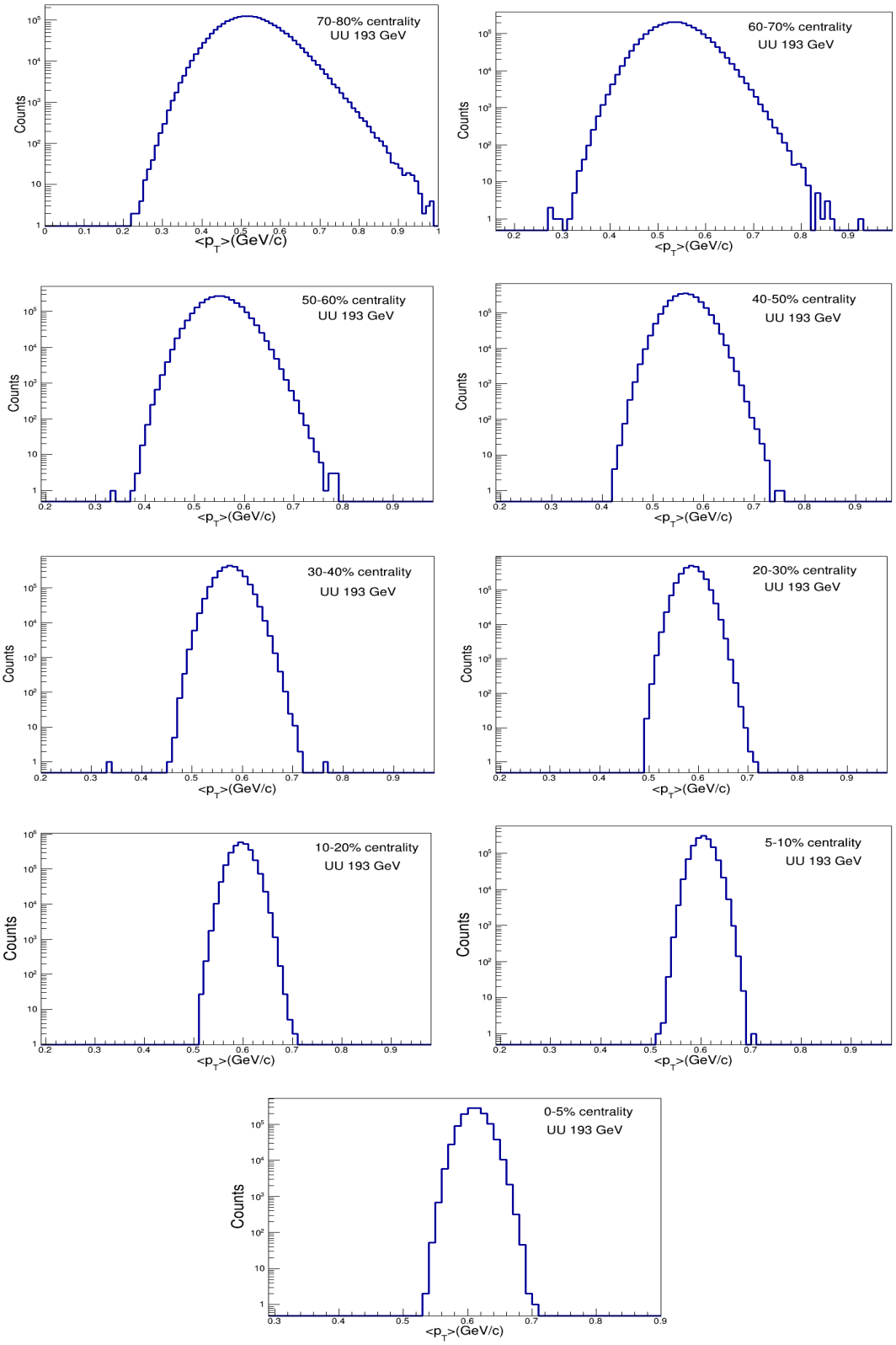

Figure 7.4: *Event-by-event* $< p_T >$ *distributions for various centralities in U+U collisions at* $\sqrt{s}_{NN}$ *= 193 GeV.*

7.4 Systematic Study

Systematic error on p_T correlations are evaluated by varying the different cuts used in the analysis, redoing the analysis using these changed cuts and determining the resulting changes in the values of p_T correlations. The resulting systematic uncertainties described below are shown in Table 7.3 as a percentage of the result for various centralities for U+U collisions at $\sqrt{s}_{NN}$ = 193 GeV. The v_z is varied to ± 50 cm from

Centrality	**DCA** %	N_{Fit} %	**poly** %	p_T %	η%
0-5%	2.15	0.4	2.98	3.4	27.42
5-10%	5.4	3.09	0.88	6.91	16.5
10-20%	0.12	1.98	5.11	3.48	20.062
20-30%	1.69	0.377	5.13	3.40	15.04
30-40%	3.13	0.80	5.94	3.4	13.11
40-50%	2.72	0.22	8.01	4.25	15
50-60%	0.04	0.33	11.40	3.04	15.12
60-70%	5.80	0.34	7.73	3.2	14.5
70-80%	14.01	11.34	5.37	14.13	6.68

Table 7.3: *Systematic error on p_T correlation for various centralities in U+U collisions at $\sqrt{s}_{NN}$ = 193 GeV*

the default (± 30 cm) value used for the analysis in order to obtain uncertainty due to the acceptance effect. We do not observe any change in p_T correlations by varying v_z. The effect of the cuts used to suppress background tracks is studied by changing the DCA cut from the default DCA <1 cm to < 1.5 cm and separately changing the required number of fit points along the track, N_{fit}, from the default $N_{fit} > 20$ to N_{fit}>15. The resulting systematic error due to these changes are listed in Table 7.3. The uncertainity due to change in η cut from default $\mid \eta \mid < 1$ to 0.5 is also estimated.

To estimate the systematic error due to changes in p_T cut, we vary the p_T range from default 0.15-2.0 GeV/c to 0.2-2.0 GeV/c, the resulting error due to this cut variation is also included.

The effect of size of centrality bin on the p_T correlations is addressed by fitting $<< p_T >>$ as a function of $< N_{ch} >$ and fitted with different polynomial (other than discussed in section 7.4) The parameters obtained from this fit are used to calculate $<< p_T >>$ (used in Eq. 7.3) on an event-by-event basis as a function of $< N_{ch} >$. The p_T correlation also include the contributions from the resonance decays and charge ordering. These correlations are obtained for pairs of particles having like (++ or --) and unlike (+ -) charges with respect to inclusive charged particles.

7.5 Results and Discussions

7.5.1 Transverse Momentum Correlations

The non-statistical or dynamical fluctuations can also be analyzed by using two-particle transverse momentum correlations [267]. It is proposed that non-monotonic change in p_T correlations as a function of centrality could be one of the possible signals of QGP formation [251]. Alternatively, analyses at RHIC based on p_T auto-correlations have indicated that basic correlation mechanism could be dominated by the process of parton fragmentation [268]. The two-particle p_T correlations are studied using the following equation [267]

$$< \Delta p_{T,i} \Delta p_{T,j} >= \frac{1}{N_{event}} \sum_{k=1}^{N_{event}} \frac{C_k}{N_k(N_k - 1)} \tag{7.2}$$

where C_k is the two-particle transverse momentum covariance for the kth event,

$$C_k = \sum_{i=1}^{N_k} \sum_{j=1, i \neq j}^{N_k} (p_{T,i} - << p_T >>)(p_{T,j} - << p_T >>) \tag{7.3}$$

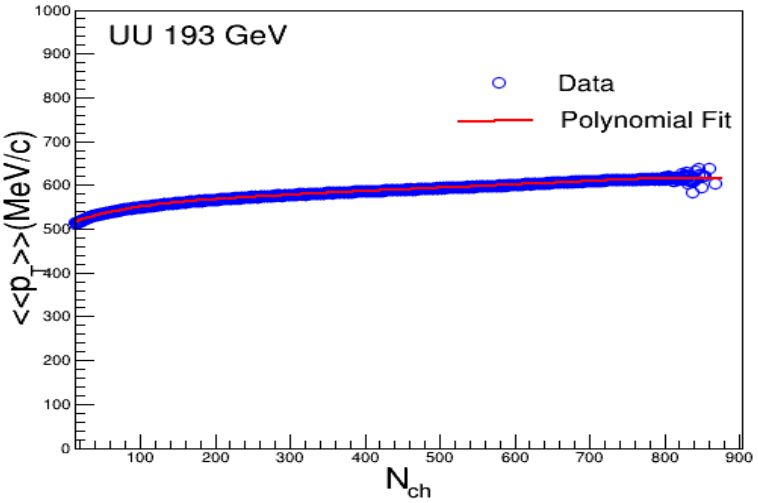

Figure 7.5: *The $<< p_T >>$ as a function of average charged particle multiplicity, $< N_{ch} >$ for U+U collisions at $\sqrt{s}_{NN}$ = 193 GeV*

where $p_{T,i}$ is the transverse momentum of the ith track in the kth event, N_k is the number of tracks in the kth event and N_{event} is the number of events. The overall event average transverse momentum ($<< p_T >>$) is given by

$$<< p_{T,i} >>= (\sum_{k=1}^{N_{event}} < p_T >_k)/N_{event} \tag{7.4}$$

where $< p_T >_k$ is the average transverse momentum in the kth event. The p_T correlation is obtained by using Eq. 7.2. These results are compared with the published results from Au+Au and Cu+Cu collisions [267, 269] to investigate the system-size dependence of the p_T correlations in heavy-ion collisions at RHIC.

The p_T correlation values may be influenced by the dependence of the correlation on the size of the centrality bin due to variation of $<< p_T >>$ with centrality. This dependence is removed by calculating $<< p_T >>$ as a function of $< N_{ch} >$, which is the multiplicity of charged tracks used to define the centrality. This multiplicity dependence of $<< p_T >>$ is fitted with a polynomial. The parameters obtained from the fit are used to calculate $<< p_T >>$ in Eq. 7.3 on event-by-event basis as a function of $< N_{ch} >$. Figure 7.5 shows the $<< p_T >>$ as function of $< N_{ch} >$ for U+U

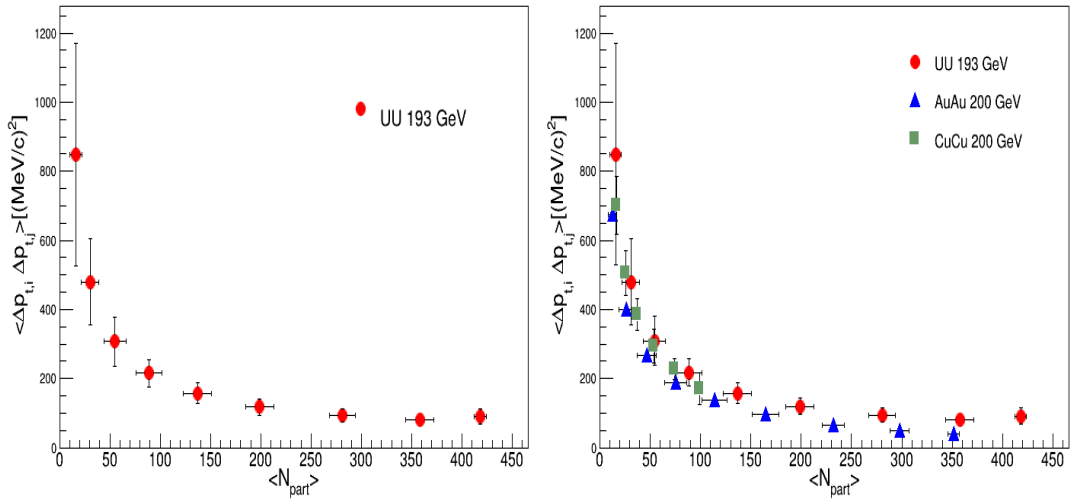

Figure 7.6: *Left: p_T correlation as a function of $< N_{part} >$ in U+U collisions $\sqrt{s}_{NN}$ = 193 GeV. Right: p_T correlation in U+U collisions compared with Au+Au and Cu+Cu collisions at $\sqrt{s}_{NN}$ = 200 GeV*

collisions at $\sqrt{s}_{NN}$ = 193 GeV. The red lines in the figure are the fit polynomials. A fourth order polynomial is used for fitting $< N_{ch} >$ versus $<< p_T >>$ in U+U collisions at $\sqrt{s}_{NN}$ = 193 GeV.

Figure 7.6 (Left) shows the p_T correlations plotted as function of $< Npart >$ for U+U collisions at $\sqrt{s}_{NN}$ = 193 GeV and its comparison (Right Figure 7.6) with the published results from Au+Au and Cu+Cu collisions at $\sqrt{s}_{NN}$ = 200 GeV respectively. We observe finite p_T correlations that decrease with increasing $< Npart >$. Similar behavior is observed for the Au+Au and Cu+Cu collisions at $\sqrt{s}_{NN}$ = 200 GeV. The decrease in correlations with increasing participating nucleons could be due to the fact that correlations are dominated by pairs of particles that originate from the same nucleon-nucleon collisions, and they get diluted when the number of participating nucleons increase [267]. It is also observed that p_T correlations in U+U collisions at $\sqrt{s}_{NN}$ = 193 GeV is more than the Au+Au and Cu+Cu collisions at $\sqrt{s}_{NN}$ = 200 GeV. The errors shown in Figure 7.6 have the statistical and systematic

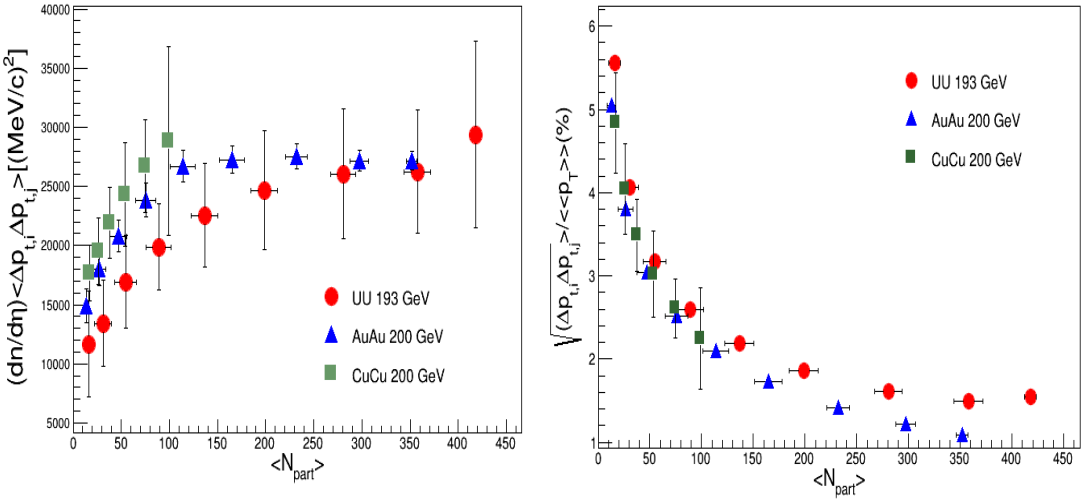

Figure 7.7: *Left: The p_T correlations multiplied by $dN/d\eta$ as function of average number of participating nucleons ($< N_{part} >$) for U+U, Au+Au and Cu+Cu collisions, Right: Square root of p_T correlations scaled by $<< p_T >>$ as function of average number of participating nucleons ($< N_{part} >$) for U+U, Au+Au and Cu+Cu collisions at $\sqrt{s}_{NN}$ = 193 GeV and 200 GeV respectively*

error added in quadrature. The statistical errors are small and are within symbol sizes.

7.5.2 Scaling of p_T correlations

Figure 7.7 (Left) shows the p_T correlations multiplied by dN/dη as a function of $< N_{part} >$. It is observed that this measure of correlations increases quickly with increasing collision centrality and saturates for central U+U collisions. The saturation of this quantity might indicate effects such as onset of thermalization [270], onset of jet quenching [271, 272], the saturation of transverse flow in central collisions [273], or other processes. It is also observed that for Cu+Cu collisions this quantity is larger than for Au+Au collisions, indicating more correlations for the smaller systems. The correlation measure $< \Delta p_{T,i} \Delta p_{T,j} >$ may change due any changes in $<< p_T >>$ with

collision centrality. To take care of these changes, we study the square root of the measured correlations scaled by $<< p_T >>$. Figure 7.7 (Right) shows the corresponding quantity $< \Delta p_{T,i} \Delta p_{T,j} > / << p_T >>$ plotted as a function of average number of participating nucleons ($< N_{part} >$) for U+U, Au+Au and Cu+Cu collisions at $\sqrt{s}_{NN}$ = 193 GeV and 200 GeV respectively. It is observed that the correlations scaled by $<< p_T >>$ is independent of collision system size but decreases with increasing collision centrality i,e $< N_{part} >$. The errors shown in Figure 7.7 have the statistical and systematic error added in quadrature. The statistical errors are small and are within symbol sizes.

Chapter 8

Summary and Conclusions

In this thesis work, ϕ meson azimuthal anisotropy and charged particle transverse momentum correlation analysis is done to understand the properties of hot and dense matter created in heavy-ion collisions at the RHIC. The data used for the analysis are Au+Au collisions at $\sqrt{s}_{NN}$ = 200 GeV and U+U collisions at $\sqrt{s}_{NN}$ = 193 GeV measured with the STAR detector at RHIC. The main sub-detector used for the given analysis are TPC and ToF. The ϕ meson production is measured through the decay channel $\phi \rightarrow K^+ K^-$. The Kaons are identified using the specific ionization energy loss (dE/dx) method in STAR's TPC detector. The ToF detector is used to identify the Kaons in higher p_T($>$ 1.0 GeV/c). The p_T correlations of charged particles at midrapidity in U+U collisions at $\sqrt{s}_{NN}$ = 193 GeV are studied. These results are compared to the published results from Au+Au and Cu+Cu collisions at $\sqrt{s}_{NN}$ = 200 GeV

We have measured ϕ meson azimuthal anisotropy co-efficients of various orders, v_n, as a function of transverse momentum and also studied its centrality dependence in Au+Au collisions at $\sqrt{s}_{NN}$ = 200 GeV. We observed that ϕ meson v_n show an increasing trend with increasing p_T. It is also found that the magnitude of ϕ meson v_2 is greater than v_3, v_4 and v_5. It is also observed that v_2 shows strong centrality

dependence whereas no centrality dependence is seen for v_3, v_4 and v_5 within statistical uncertainities.

In addition, we have also measured various higher harmonic ratio like v_3/v_2 and v_4/v_2^2. The ratio v_3/v_2 of ϕ meson is constant for $p_T>$ 1.5 GeV/c which is consistent with hydrodynamical model. The ratio v_4/v_2^2 is proposed as a more sensitive probe of ideal hydrodynamic behavior. Furthermore, it is argued that the ratio is directly related to the degree of thermalization. The measured ratio v_4/v_2^2 as function of p_T is found to be above the values expected for ideal fluid behavior, indicative of still incomplete thermalization at the full RHIC energies. This ratio seems to be higher for central collisions compared to peripheral collisions.

We have also measured two charged particle transverse momentum correlations in U+U at $\sqrt{s}_{NN}$ = 193 GeV. These results are compared with the published results from Au+Au and Cu+Cu collisions to study the system size dependence. We observed that event-by-event meant p_T distributions becomes wider as we move from central to peripheral collisions. This might indicate the presence of non-statistical fluctuations in U+U collisions at $\sqrt{s}_{NN}$ = 193 GeV. The p_T correlation is an important tool to understand thermalization in heavy ion collisions. We observed that the p_T correlations are finite and decreases with increase in the number of participants in U+U collisions as was observed in Au+Au collisions. This decrease in p_T correlations could be due to correlations being dominated from pair of particles coming from the same nucleon-nucleon collision which get diluted with increasing the number of participants. The p_T correlations scaled by dN/dη increases with collision centrality and then saturate in central U+U collision indicating the sign of thermalization. It is also observed that square root of p_T correlations scaled by mean p_T is independent of colliding ion size, but decrease with increase in collision centrality.

Bibliography

[1] G. D. Rochester and C. C. Butler, "Evidence for the Existence of New Unstable Elementary Particles", Nature **160**, 855 (1947).

[2] A. Pais and R. Jost, "Selection Rules imposed by Charged Conjugation and Charge Symmetry", Phys. Rev. **87**, 871 (1952).

[3] M. Gell-Mann,"Isotopic Spin and New Unstable Particles", Phys. Rev. **92**, 833 (1953) and T. Nakano and K. Nishijima, "Charge Independence for V-particles," Prog. Theoret. Phys. **10** 581 (1953).

[4] F. R. Brown, Frank P. Butler, Hong Chen, et al., Phys. Rev. Lett, **65**, 2491-2494,(1990).

[5] I. R. Kenyon,"Elementary Particle Physics",Routledge and Kegan Paul, (1987).

[6] J. Beringer et al., "Review of Particle Physics," Phys. Rev. D, **86**, 010001, (2012).

[7] P. Koch, B. Muller and J. Rafelski, Physics Reports, 142(4), 167-262, (1986).

[8] W. Pauli et al., "Zeeman-Effect and the Dependence of Electron-Mass on the Velocity", Z. Phys, **31** 373, (1925).

[9] R. C. Hwa and C. B. Yang,"Strangeness enhancement in the parton model", Phys. Rev. C, **66**, 064903, (2002).

[10] J. Rafelski and B. Muller,"Strangeness production in the Quark-Gluon Plasma",In Phy. Rev. Lett, **48**, (1982).

[11] M. E. Peskin, D. V. Schroeder,"An Introduction To Quantum Field Theory", Westview Press, (1995).

[12] G. Aad et al., (ATLAS Collaboration), Phys. Lett. B, **716**, 1 (2012).

[13] S. Chatrchyan et al., (CMS Collaboration), Phys. Lett. B, **716**, 30 (2012).

[14] M. Y. Han and Yoichiro Nambu, "Three Triplet Model with Double SU(3) Symmetry", Phys. Rev. **139**, B1006-B1010, (1965).

[15] J. Beringer et al.,"Review of Particle Physics", Phys. Rev. D, **86**, 010001 (2012).

[16] D. Perkins,"Introduction to High-Energy Physics", Cambridge University Press, Cambridge, (2000).

[17] E. V. Shuryak, "Quantum Chromodynamics and the Theory of Superdense Matter", Phys. Rept. **61**, 71 (1980).

[18] J. Adams et al., Nucl. Phys. A **757**, 102-183 (2005)

[19] K. G. Wilson, Phys. Rev. D, **10**, 2445-2459 (1974).

[20] F. Karsch and E. Laermann,"Thermodynamics and In-Medium Hadron Properties from Lattice QCD", (2004).

[21] J. D. Bjorken,"Highly relativistic nucleus-nucleus collisions", Phys. Rev. D, **27**, 140-151, (1983).

[22] F.Karsch, arXiv:hep-lat/9903031, (1998).

[23] I. R. Kenyon, "Elementary Particle Physics", (1987).

[24] H. Satz, Lect. Notes Phys, **785**, (2010).

[25] J. Kuti, J. Polnyi, and K. Szlachnyi, Phys. Lett. B, **98**, 199-204,(1981).

[26] L. D. M. and S. Benjamin, "A Monte Carlo study of SU(2) Yang-Mills theory at finite temperature", Phys. Lett. B, **98**,195-198,(1981).

[27] A. Schmah, "Highlights of the Beam Energy Scan from STAR", Eur. Phys. J,**10**.

[28] M. G. Alford, Ann. Rev. Nucl. Part. Sci. **51**, 131 (2001).

[29] B. C. Barrois, Nucl. Phys. B **129**, 390 (1977).

[30] M. Coleman Miller, arXiv:1312.0029v1 [astro-ph.HE], 1-51 (2013).

[31] J. D. Bjorken, "Highly relativistic nucleus-nucleus collisions", Physical Review D, **27**,140, (1983).

[32] M. Kliemant et al.,"Global Properties of Nucleus-Nucleus Collisions", Springer, (2010).

[33] M. L. Miller, K. Reygers, S. J. Sanders and P. Steinberg, Ann. Rev. Nucl. Part. Sci. **57**, 205 (2007).

[34] M. Nasim, "Probing the QCD phase diagram with measurements of ϕ-meson production and elliptic flow in heavy-ion collisions at STAR", Journal of Physics: Conference Series, 509, 10.1088/1742-6596/509/1/012070, (2014).

[35] B. I. Abelev et al.,"Measurements of ϕ meson production in relativistic heavy-ion collisions at the BNL Relativistic Heavy Ion Collider (RHIC)", Phys. Rev. C,**49**, 064903, (2009).

[36] B. B. Abelev et al.,"$K^*(892)0$ and $\phi(1020)$ production in Pb-Pb collisions at $\sqrt{s}_{NN}$= 2.76 TeV", Phys. Rev. C, **91**, 024609 (2015).

[37] X. N. Wang and M. Gyulassy, "Gluon shadowing and jet quenching in A+A collisions at $\sqrt{s}_{NN}$ = 200 AGeV", Phys. Rev. Lett, 68, (1992).

[38] E. L. Feinberg, "Direct Production of Photons and Dileptons in Thermodynamical Models of Multiple Hadron Production", Nuovo Cimento A, **34**, 391 (1976)

[39] T. Peitzmann, M. H. Thoma, "Direct Photons from Relativistic Heavy-Ion Collisions", Phys. Rept. **364** (2002) 175-246

[40] M. M. Aggarwal et al., (WA98 Collaboration), Phys. Rev. Lett, **85**, (2000) 3595.

[41] D. K. Srivastava and B. Sinha, Phys. Rev. C, **64**,(2001) 034902.

[42] T.Sakaguchi (Phenix Collaboration), "Direct Photons:Flow, Thermal Yield and High p_T R_{AA} from the PHENIX experiment at RHIC", J. Phys. Conf. Ser. 389 012020, (2012).

[43] T. Matsui and H. Satz, Phys. Lett. B, **178**,(1986).

[44] R. Rapp and van Hees H, Nucl. Phys. A, **827**,(2009).

[45] T. Matsui and H. Satz, Phys. Lett. B, 178:416 (1986).

[46] R. rapp, D. Blaschke and P. Crochet, Prog. Part. Nucl. Phys.**65**(2010).

[47] B. Munzinger and J. Stachel, (2009), 0901.2500.

[48] (STAR Collaboration), "Enhanced strange baryon production in Au+Au collisions compared to p+p at $\sqrt{s}_{NN}$ =200 GeV", Phys. Rev. C, **77**, p. 044908, (2008).

[49] J. Rafelski and B. Muller, Phys. Rev. Lett, **48**, 1066(1982).

[50] P. Koch, Muller, B., Phys. Rev. Lett, **48**, 1066 (1986).

[51] A. Wroblewski, ActaPhys. Polon. B **16**, 379 (1985).

[52] D. H. Rischke, Y. Pursun and J. A. Maruhn, Nucl. Phys. A, **595**, 383 (1995) Erratum-ibid A 596, 717 (1996)]; C. Spieles, H. Stocker and C. Greiner, Phys. Rev. C **57**, 908 (1998); M. Bluhm, B. Kampfer, R. Schulze, D. Seipt and U. Heinz, Phys. Rev. C, **76**, 034901 (2007).

[53] D. H. Rischke and M. Gyulassy, Nucl. Phys. A, **608**, 479 (1996).

[54] R. Hanburry Brown and R. Q. Twiss, Phil. Mag. **45**, 663 (1954).

[55] M. M. Aggarwal et al., (WA98 Collaboration), Phys. Rev. Lett, **85**, (2000) 3595.

[56] D. K. Srivastava and B. Sinha, Phys. Rev. C, **64**, (2001) 034902.

[57] T. Sakaguchi (Phenix Collaboration), J. Phys. Conf. Ser. 389 012020, (2012).

[58] J. D. Bjorken, Fermilab-pub-82-059-thy,(1982).

[59] X. N. Wang, M. Gyulassy, and M. Plumer, Phys. Rev. D, **51**, 3436 (1995).

[60] S. Cao et al., Phys. Rev. C, **88**, 044907 (2013).

[61] R. Abir et al., "Open heavy flavor and J/ψ at RHIC and LHC within a transport model", Phys. Lett. B, **715**, 183 (2012).

[62] S. A. Voloshin and A. M. Poskanzer. Phys. Lett. B, **474** 27, (2000).

[63] H. Sorge, Phys. Rev. Lett., **82**, 2048 (1999).

[64] J. Adams et al., Nucl. Phys. A, **757**, 102 (2005).

[65] S. S. Adler et al., Phys. Rev. Lett., **91**, 182301, (2003).

[66] P. Huovinen, P. F. Kolb, U. Heinz, P. V. Ruuskanen and S. A. Voloshin, Phys. Lett. B, **503** 58, (2001).

[67] S. Shusu (STAR collaboration), Nucl. Phys. A, **830**,187c-190c, (2009)

[68] P. Huovinen. Nucl. Phys. A, **761** 296, (2005).

[69] D. Molnar and S. A. Voloshin, Phys. Rev. Lett, **91**, 092301 (2003).

[70] R. J. Fries et al., Phys. Rev. Lett, **90**, 202303 (2003).

[71] J. D. Bjorken, Phys. Rev. D, **27**, 140 (1983).

[72] R. Mattiello, A. Jahns, H. Sorge, H. Stocker, and W. Greiner, Phys. Rev. Lett, **74**, 2180 (1995) and R. Mattiello, H. Sorge, H. Stocker, and W. Greiner, Phys. Rev. C, **55**, 1443 (1997).

[73] M. Chojnacki, A. Kisiel, W. Florkowski and W. Broniowski, Comput. Phys. Com-mun. **183**, 746 (2012).

[74] A. Kisiel, T. Taluc, W. Broniowski and W. Florkowski, Comput. Phys. Commun. **174**, 669 (2006).

[75] J. Xu and C. M. Ko, Phys. Rev. C **83**, 034904 (2011).

[76] C. Shen and U. Heinz, Phys. Rev. C 85, 054902 (2012) [Erratum-ibid. C **86**, 049903 (2012).

[77] V. Roy, A. K. Chaudhuri and B. Mohanty, Phys. Rev. C **86**, 014902 (2012).

[78] V. Roy, B. Mohanty and A. K. Chaudhuri, J. Phys. G **40**, 065103 (2013).

[79] S. A. Bass, M. Belkacem, M. Bleicher, M. Brandstetter, L. Bravina, C. Ernst, L. Gerland and M. Hofmann et al., Prog. Part. Nucl. Phys. **41**, 255 (1998).

[80] M. Bleicher, E. Zabrodin, C. Spieles, S. A. Bass, C. Ernst, S. Soff, L. Bravina and M. Belkacem et al., J. Phys. G, **25**, 1859 (1999).

[81] A. Tang. arXiv: 0808.2144.

[82] N. Borghini, J.-Y. Ollitrault. Phys. Lett. B, **642** 227, (2006).

[83] H. Hahn et al., "The RHIC design overview", Nucl. Instrum. Meth. A **499**, 245-263(2003).

[84] K. H. Ackermann et al., (STAR Collaboration), "Star detector overview", Nucl. Instrum. Meth. A **499**,624-632(2003).

[85] M. Harrison, T. Ludlam, and S. Ozaki., Nucl. Instr. Meth. A **499**, 235 (2003).

[86] Y. Mori et al., Rev. Sci. Instrum. **73**, 888 (2002).

[87] I. Alekseev et al., Nucl. Inst. Meth. A **499**, 392 (2003).

[88] P. Thieberger, M. McKeown, H.E. Wegner, "IEEE Transactions on Nuclear Science", (1983).

[89] M. Blaskiewicz, J. M. Brennan, and K. Mernick. Phys. Rev. Lett, **105**, 094801, (2010).

[90] http://www.rhichome.bnl.gov/RHIC/Runs/

[91] Abhay Deshpande, Richard Milner, Raju Venugopalan, and Werner Vogelsang. Ann. Rev. Nucl. Part. Sci, **55**, 165, (2005).

[92] STAR home page. http://www.star.bnl.gov./

[93] PHENIX home page. http://www.phenix.bnl.gov.

[94] BRAHMS home page. www4.rcf.bnl.gov/brahms/WWW/brahms.html.

[95] PHOBOS home page. http://www.phobos.bnl.gov.

[96] F. Bergsma et al. "The STAR detector magnet subsystem", Nucl. Instrum. Meth, A, **499**, 633-639, (2003).

[97] A. Schmah and Maria, "3D picture of the STAR detector", (2014).

[98] L. Kochenda et al., Nucl. Instrum. Meth. A, **499**, 703-712, (2003).

[99] M. Anderson et al., "The STAR time projection chamber: a unique tool for studying high multiplicity events at RHIC", Nucl. Instrum. Meth. A **499**, 659 (2003).

[100] H. Bichsel, "A method to improve tracking and particle identification in TPCs and silicon detectors", Nucl. Instrum. Meth., A, **562**, 154-197, (2006).

[101] W. J. Llope et al.,"The TOFp/pVPD time-of-flight system for STAR", Nucl. Instrum. Meth. A, **522**, 252 (2004).

[102] M. Shao et al., "Extensive particle identificaiton with TPC and TOF at the STAR experiment", Nucl. Instrum. Meth. A, **558**, 419 (2006).

[103] M. Beddo et al., (STAR Collaboration), "The STAR barrel electromagnetic calorimeter", Nucl. Instrum. Meth. A, **499** (2003) 725 (2003).

[104] C. E. Allgower et al., (STAR Collaboration),"The STAR Endcap Electromagnetic Calorimeter", Nucl. Instrum. Meth. A, **499**, 740 (2003).

[105] (STAR Collaboration,) J. S. C. C. A. Whitten, AIP Conference Proceedings **980**, 390 (2008).

[106] W. J. Llope et al., Nucl. Instrum. Meth. A **759** 23-28 (2014).

[107] W. Llope, Nuclear Instruments and Methods in Physics Research Section B: Beam Interactions with Materials and Atoms **241**, 306 (2005),

[108] A. Clemens et al., Nucl.Instrum. Meth. A **470** (2001), 488-499 nucl-ex/0008005

[109] M. Bai et al., Nucl. Instrum. Meth., A **499**, 372-387, (2003).

[110] F. S. Bieser et al., Nucl. Instr. Meth. A **499**,766 (2003), C. Alder et al., Nucl. Instr. Meth. A, **470**, 488 (2001) and J. W. Harris et al., Nucl. Phys. A,**566**, (1994).

[111] B. Christie, S. White, P. Gorodetzky and D. Lazic, STAR Note SN0175,(1994).

[112] S. Margetis, Conference Proceeding: ICNFP, Crete, Greece (2014).

[113] (STAR Collaboration), Technical Design Report, http://drupal.star.bnl.gov/STAR/starnotes/public/sn0600.

[114] A. Ljubicic Jr., M. Botlo, F. Heistermann, S. Jacobson, M. J. LeVine, J. M. Nelson, M. Nguyen, H. Roehrich, E. Schaefer, J. J. Schanback, R. Scheetz, D. Schmischke, M. W. Schulz and K. Sulimma,"Design and implementation of the STAR experiments DAQ", IEEE Trans. Nuc. Sci, **45** (1998).

[115] A. Ljubicic Jr, J. M. Landgraf, M. J. LeVine, J. M. Nelson, D. Roerich, J. J. Shamback, D. Schmische, M. W. Schulz, C. Struck, C. R. Consiglio, R. Scheetz and Y. Zhao,"The STAR experiment's data acquisition system", IEEE Trans. Nuc. Sci, **47**, (2000).

[116] K.H. Ackerman, et al., "The Forward Time Projection Chamber in STAR".

[117] R. Bellwied, et al.,"The Silicon Vertrax Tracker".

[118] M. J. LeVine, A. Ljubicic Jr., M. W. Schulz, R. Scheetz, C. Consiglio, D. Padrazo and Y. Zhao, "The STAR DAQ receiver board", IEEE Trans. Nuc. Sci., **47**, (2000).

[119] C. Adler et al., "The STAR Level 3 Trigger System", Nuc. Sci., **47**, (2000).

[120] F. Karsch, "Lattice results on QCD thermodynamics", Nucl. Phys. A, **698**,(2002).

[121] R. V. Gavai and S. Gupta, "On the critical end point of QCD," Phys. Rev. D, **71**, 114014,(2005).

[122] K. G. Wilson, "Confinement of quarks", Phys. Rev. D, **10**, (1974).

[123] S. Bethke, "Experimental tests of asymptotic freedom," Progress in Particle and Nuclear Physics, **58**, (2007).

[124] L. Bertanza, V. Brisson, P. L. Connolly et al., "Possible Resonances in the $\Xi\pi$ and K$\bar{K}$ Systems", Phys. Rev. Lett, (1962).

[125] A. Shor, "ϕ-meson production as a probe of the Quark-Gluon plasma," Phys. Rev. Lett, **54**, **11**, (1985).

[126] A. Sibirtsev, H.-W. Hammer, U.-G. MeiBner, and A.W.Thomas, "ϕ-meson photoproduction from nuclei",Eur. Phys.,**29**,(2006).

[127] J. Adams, M. M. Aggarwal, Z. Ahammed et al., "Experimental and theoretical challenges in the search for the quark-gluon plasma:The STAR Collaborations critical assessment of the evidence from RHIC collisions", Nucl. Phys. A, **757**, 102-183, (2005).

[128] P. Koch, B. Mullerb, and J. Rafelskic, Physics Reports, **142**,(1986).

[129] T. Alber, H. Appelsha, J. Bachler et al., "Strange particle production in nuclear collisions at 200 GeV per nucleon", Zeitschrift fur Physik C, **64**, (1994).

[130] P. G. Jones, "Hadron yields and hadron spectra from the NA49 experiment", Nucl. Phys. A, **610**, (1996).

[131] F. Sikler, J. Bachlerf, D. Barna et al., "Hadron production in nuclear collisions from the NA49 experiment at 158 GeV/c. A", Nucl. Phys. A, **611**, (1996).

[132] C. Hohne, "Strangeness production in nuclear collisions-recent results from experiment NA49", Nucl. Phys. A, **611**, (1999).

[133] J. Rafelski and B. Muller, "Strangeness production in the quark-gluon plasma", Phys. Rev. Lett, **48**, (1982).

[134] K. Redlich and A. Tounsi, Eur. Phys. C, **24**,(2002).

[135] J. Adams, C. Adler, M. M. Aggarwal et al., "Particle-type dependence of azimuthal anisotropy and nuclear modification of particle production in Au+Au collisions at $\sqrt{s_{NN}} = 200$ GeV", Phys. Rev. Lett, **92**, (2004).

[136] D. Molnar and S. A. Voloshin, "Elliptic flow at large transverse momenta from quark coalescence", Phys. Rev. Lett, **91**, (2003).

[137] R. J. Fries, B. Muller, C. Nonaka, and S. A. Bass,"Hadronization in heavy-ion collisions:recombination and fragmentation of partons", Phys. Rev. Lett, **90**, 202303, (2003).

[138] C. Alt, T. Anticic, B. Baatar et al., "Energy dependence of ϕ meson production in central Pb+Pb collisions at $\sqrt{s}_{NN} = 6$ to 17 GeV", Phys. Rev. C, **78**, (2008).

[139] M. Nasim,"Probing the QCD phase diagram with measurements of ϕ-meson production and elliptic flow in heavy-ion collisions at STAR", Journal of Physics: Conference Series, 10.1088/1742-6596/509/1/012070, (2014).

[140] B. I. Abelev et al., "Measurements of ϕ meson production in relativistic heavy-ion collisions at the BNL Relativistic Heavy Ion Collider (RHIC)", Phys. Rev. C, **49**, (2009).

[141] B. Abelev, A. Abrahantes Quintana, D. Adamova et al., "Strange particle production in protonproton collisions at $\sqrt{s_{NN}}$ = 0.9 TeV with ALICE at the LHC", Eur. Phys. C, **71**, 1594, (2011).

[142] B. Abelev, J. Adam, D. Adamova et al., "Production of $K^*(892)$ and $\phi(1020)$ in pp collisions at $\sqrt{s_{NN}}$ = 7 TeV", Eur. Phys. C, **72**, 2183, (2012).

[143] B. B. Abelev et al., "$K^*(892)0$ and $\phi(1020)$ production in Pb-Pb collisions at $\sqrt{s_{NN}}$ = 2.76 TeV", Phys. Rev. C **91**, 024609 (2015).

[144] S. V. Afanasiev, T. Anticicu, J. Bachler et al., "Production of ϕ-mesons in p + p, p + Pb and central Pb + Pb collisions at E_{beam} = 158 A GeV", Phys. Lett. B,**491**, (2000).

[145] V. Khachatryan, A. M. Sirunyan, A. Tumasyan et al., "Transverse-momentum and pseudorapidity distributions of charged hadrons in pp collisions at $\sqrt{s_{NN}}$ = 7 TeV", Phys. Rev. Lett, **105**, 022002, (2010).

[146] S. Chatrchyan, V. Khachatryan, A. M. Sirunyan et al., "Study of the inclusive production of charged pions, kaons, and protons in pp collisions at $\sqrt{s_{NN}}$ = 0.9, 2.76, and 7 TeV", The European Physical Journal C, **72**, 2164, (2012).

[147] T. Akesson, "Inclusive vector-meson production in the central region of pp collisions at $\sqrt{s_{NN}}$ = 63 GeV", Nucl. Phys. B, **203**, (1982).

[148] B. I. Abelev, M. M. Aggarwal, Z. Ahammed et al., "Energy and system size dependence of ϕ meson production in Cu+Cu and Au+Au collisions", Phys. Lett. B, **673**, pp. 183-191, (2009).

[149] V. Blobel, H. Fesefeldt, H. Franz et al., "Test of the Zweig selection rule in ϕ production by pp collisions", Phys. Lett. B, **59**, (1975).

[150] A. Sibirtsev, J. Haidenbauer, and U. -G. Meissner, "Aspects of phi-meson production in proton-proton collisions", Eur. Phys. A, **27**, (2006).

[151] M. L. Miller, K. Reygers, S. J. Sanders, and P. Steinberg,"Glauber modeling in high-energy nuclear collisions", Annual Review of Nuclear and Particle Science, **57**, (2007).

[152] X. N. Wang and M. Gyulassy, "Gluon shadowing and jet quenching in A+A collisions at $\sqrt{s_{NN}} = 200$A GeV", Phys. Rev. Lett,**68**, (1999).

[153] J. W. Cronin, H. J. Frisch, M. J. Shochet, J. P. Boymond, P. A. Piroue, and R. L. Sumner,"Production of hadrons at large transverse momentum at 200, 300, and 400GeV", Phys. Rev. D, **11**, 3105, (1975).

[154] A. Adare, S. Afanasiev, C. Aidala et al., "Nuclear modification factors of ϕ mesons in $d + Au$, $Cu + Au$, and $Au + Au$ collisions at $\sqrt{s_{NN}} = 200$", Phys. Rev. C, **83**, (2011).

[155] M. Lev and B. Petersson, "Nuclear effects at large transverse momentum in a QCD parton model", Zeitschrift fur Physik C Particles and Fields, **21**, (1983).

[156] A. Accardi and M. Gyulassy, "Cronin effect vs. geometrical shadowing in d + Au collisions at RHIC", Phys. Lett. B, **586**, (2004).

[157] G. Papp, P. Levai, and G. Fai, "Saturating Cronin effect in ultrarelativistic proton-nucleus collisions", Phys. Rev. C,**61**, (1999).

[158] R. C. Hwa, C. B. Yang, and R. J. Fries, "Forward production in d+Au collisions by parton recombination", Phys. Rev. C,**71**, (2005).

[159] B. I. Abelev, J. Adams, M. M. Aggarwal et al., "Rapidity and species dependence of particle production at large transverse momentum for d + Au collisions at $\sqrt{s_{NN}}$ = 200 GeV", Phys. Rev. C,**76**, 054903,(2007).

[160] L. van Hove, "Multiplicity dependence of p_T spectrum as a possible signal for a phase transition in hadronic collisions", Phys. Lett. B, **118**, (1982).

[161] N. Isgur and H. B. Thacker, "Origin of the Okubo-Zweig-Iizuka rule in QCD", Phys. Rev. D, **64**, (2001).

[162] S. A. Bass, M. Belkacem, M.Bleicher et al.,"Microscopic models for ultrarelativistic heavy ion collisions", Progress in Particle and Nuclear Physics, **41**, (1998).

[163] M. Bleicher, E. Zabrodin, C. Spieles et al., "Relativistic hadron-hadron collisions in the ultra-relativistic quantum molecular dynamics model", Journal of Physics G, **25**,(1999).

[164] C. Alt, T. Anticic, B. Baatar et al., Phys. Rev. Lett, **94**,052301,(2005).

[165] J. Adams, C. Adler, M. M. Aggarwal et al.,"Multistrange Baryon Production in Au-Au Collisions at $\sqrt{s_{NN}}$ = 130 GeV", Phys. Rev. Lett, **92**, (2004).

[166] R. C. Hwa and C. B. Yang, "Production of strange particles at intermediate p_T in central Au+Au collisions at high energies", Phys. Rev. C, **75**, (2007).

[167] P. F. Kolb and U. Heinz, "Emission angle dependent HBT at RHIC and beyond", Nucl. Phys. A, **715**,(2003).

[168] D. Teaney, J. Lauret, and E. V. Shuryak, "Flow at the SPS and RHIC as a quark-gluon plasma signature", Phys. Rev. Lett, **86**, (2001).

[169] P. F. Kolb and U. Heinz, "Hydrodynamic description of ultrarelativistic heavy-ion collisions", http://arxiv.org/abs/nucl-th/0305084.

[170] P. F. Kolba, P. Huovinend, U. Heinza, and H. Heiselberge, "Elliptic flow at SPS and RHIC from kinetic transport to hydrodynamics", Phys. Lett. B, **500**, (2001).

[171] H. Sorge, "Elliptical flow: a signature for early pressure in ultra-relativistic nucleus-nucleus collisions", Phys. Rev. Lett, **78**,(1997).

[172] J. Y. Ollitrault,"Anisotropy as a signature of transverse collective flow", Phys. Rev. D,**46**, 229, (1992).

[173] P. Huovinen, P. F. Kolb, U. Heinz et al., "Radial and elliptic flow at RHIC: further predictions", Phys. Lett. B, **503**, (2001).

[174] A. M. Poskanzer and S. A. Voloshin, "Methods for analyzing anisotropic flow in relativistic nuclear collisions", Phys. Rev. C, **58**,(1998).

[175] A. Shor, "ϕ-meson production as a probe of the Quark-Gluon plasma", Phys. Rev. Lett,**54**, (1985).

[176] J. Adams, M. M. Aggarwal, Z. Ahammed et al., "Experimental and theoretical challenges in the search for the quark-gluon plasma: The STAR Collaboration's critical assessment of the evidence from RHIC collisions", Nucl. Phys. A, vol. **757**,(2005).

[177] L. Adamczyk, J. K. Adkins, G. Agakishiev et al., "Elliptic flow of identified hadrons in Au+Au collisions at $\sqrt{s}_{NN}$ = 7.7-62.4 GeV", Phys. Rev. C, vol. **88**, 014902,(2013).

[178] M. Nasim and The STAR Collaboration, "Systematic investigation of partonic collectivity through centrality dependence of elliptic flow of multi-strange hadrons in Au + Au collisions at $\sqrt{s}_{NN}$ = 200 GeV", Nucl. Phys. A, (2013).

[179] R. Haque and M. K. Sharma, STAR presentation at QM2014.

[180] B. Abelev.,"Elliptic flow of identified hadrons in Pb-Pb collisions at 2.76 TeV", http://arxiv.org/abs/1405.4632.

[181] B. Mohanty and N. Xu, "Probe of the QCD phase diagram with phi-mesons in high-energy nuclear collisions", Journal of Physics G, **36**,064022, (2009).

[182] M. Nasim, B. Mohanty, and N. Xu, "Elliptic flow of ϕ mesons as a sensitive probe for the onset of the deconfinement transition in high energy heavy-ion collisions", Phys. Rev. C, **87**, (2013).

[183] D. Molnar and S. A. Voloshin, "Elliptic flow at large transverse momenta from quark coalescence", Phys. Rev. Lett,**91**, (2003).

[184] R. J. Fries, B. Muller, C. Nonaka, and S. A. Bass,"Hadronization in heavy-ion collisions: recombination and fragmentation of partons", Phys. Rev. Lett, **90**,(2003).

[185] P. Bhaduri and S. Chattopadhyay, "Differential elliptic flow of identified hadrons and constituent quark number scaling at the GSI Facility for Antiproton and Ion Research (FAIR)", Phys. Rev. C, **81**,(2010).

[186] K. J. Wu, F. Liu, and N. Xu, Nucl. Phys. A, **834**,(2010).

[187] M. Bleicher and X. Zhu, "Is constituent quark scaling a unique sign of parton recombination?", Eur. Phys. C, **49**,(2007).

[188] B. Mohanty and N. Xu,"Probe of the QCD phase diagram with ϕ-mesons in high-energy nuclear collisions", Journal of Physics G, **36**, 064022, (2009).

[189] M. Nasim, B. Mohanty, and N. Xu, "Elliptic flow of ϕ mesons as a sensitive probe for the onset of the deconfinement transition in high energy heavy-ion collisions", Phys. Rev. C,**87**,(2013).

[190] B. Abelev,"Elliptic flow of identified hadrons in Pb-Pb collisions at $\sqrt{s}_{NN}$ = 2.76 TeV".

[191] M. Nasim, "Using ϕ-meson elliptic flow to map the strength of the partonic interaction", Phys. Rev. C, **89**, (2014).

[192] L. Kumar, "STAR results from the RHIC beam energy scan-I", Nucl. Phys. A, **904-905**,(2013).

[193] S. Das and The STAR Collaboration, "Study of freeze-out dynamics in STAR at RHIC beam energy scan program", Journal of Physics: Conference Series,**509**, 012066, (2014).

[194] T. Hirano, U. Heinz, D. Kharzeev, R. Lacey, and Y. Nara, "Mass ordering of differential elliptic flow and its violation for ϕ-mesons", Phys. Rev. C,**77**, 044909, (2008).

[195] C. Adler et al., Nucl. Instrum. Methods A **499**, 433 (2003);

[196] W. J. Llope et al., Nucl. Instr. Meth. A **522**, 252 (2004).

[197] D. Kharzeev and M. Nardi, Phys. Lett. B **507**, 121 (2001).

[198] B. B. Back et al. (PHOBOS Collaboration), Phys. Rev. C, **70**, 021902(R) (2004)

[199] H. Masui and A. Schmah, arXiv: 1212.3650v1 [nucl-ex]

[200] M. Anderson et al., Nucl. Instrum. Meth. A **499**, 659 (2003).

[201] H. Bichsel, Nucl. Instr. and Meth. A **562**, 154 (2006).

[202] B. Bonner et al., Nucl. Inst. and Meth. A **508**, 181 (2003).

[203] D. L' Hote, Nucl. Instrum. Methods A **337**, 544 (1994) and D. Drijard, H. G. Fischer, and T. Nakada, Nucl. Instrum. Methods A **225**, 367 (1984).

[204] B. I. Abelev et al., Phys. Rev. C, **79**, 064903 (2009).

[205] H. A. Gustafsson et al., Phys. Rev. Lett, **52**, 1590 (1984).

[206] M. Gyulassy and L.D. Mclarrean, nucl-th/0405013

[207] R. Snellings, "Elliptic flow: A brief review", New J. Phys. **13**, 055008 (2011).

[208] J.-Y. Ollitrault, "Anisotropy as a signature of transverse collective flow", Phys. Rev. D, **46**,(1992).

[209] M. B. Tsang et al., "Azimuthal correlations between light particles emitted in ^{12}O induced reactions on ^{12}C and ^{197}Au at 400 MeV", Phys. Lett. B, **148**, 265-269 (1984).

[210] C. B. Chitwood et al., Phys. Rev. C, **34**: 858871 (1986).

[211] H. H. Gutbrod et al., "A new component of the collective flow in relativistic heavy-ion collisions", Phys. Lett. B, **216**: 267-271 (1989).

[212] (ALICE collaboration), "Elliptic Flow of Charged Particles in Pb-Pb Collisions at 2.76 TeV", Phys. Rev. Lett,**105**: 252302 (2010).

[213] P. F. Kolb, J. Sollfrank and U. W. Heinz, Phys. Rev. C, **62**, 054909 (2000).

[214] H. Masui, J.-Y. Ollitrault, R. Snellings, and A. Tang,"The centrality dependence of v_2/ϵ: the ideal hydro limit and η/s", Nucl. Phys. A, **830**, (2009).

[215] (STAR collaboration), "Centrality dependence of charged hadron and strange hadron elliptic flow from $\sqrt{s}_{NN} = 200$ GeV Au + Au collisions", Phys. Rev. C, **77**, 054901 (2008).

[216] (STAR Collaboration), "Azimuthal Anisotropy and Correlations in the Hard Scattering Regime at RHIC", Phys. Rev. Lett, **90**(3):032301 (2003).

[217] R. J. M. Snellings, A. M. Poskanzer and S. A. Voloshin, arXiv:nucl-ex/9904003.

[218] M. Gyulassy and M. Plumer, Phys. Lett. B, **243**, 432 (1990).

[219] X. N. Wang and M. Gyulassy, Phys. Rev. Lett, **68**,1480 (1992).

[220] X. N. Wang, Phys. Rev. C **63**, 054902(2001).

[221] M. Gyulassy, I. Vitev, X. N. Wang and P. Huovinen, Phys. Lett. B, **526**, 301 (2002).

[222] P. Huovinen, P. F. Kolb, U. W. Heinz, P. V. Ruuskanen and S. A. Voloshin, Phys. Lett. B, **503**, 58 (2001).

[223] R. Snellings, (STAR Collaboration and ALICE Collaboration), Eur. Phys. C, **49**, 87 (2007).

[224] V. Greco, C. M. Ko, and P. Le vai, "Parton Coalescence and the Antiproton/Pion Anomaly at RHIC", Phys. Rev. Lett, **90**, (2003).

[225] R. J. Fries, B. Muller, C. Nonaka, and S. A. Bass, Phys. Rev. Lett., **90**, 202303 (2003).

[226] S. A. Voloshin, Anisotropic flow, Nuclear Physics A, **715**, (2003).

[227] (STAR Collaboration), "Multistrange Baryon Elliptic Flow in Au+Au Collisions at $\sqrt{s}_{NN}$ = 200 GeV", Phys. Rev. Lett, **95**:122301 (2005).

[228] S. Afanasiev et al., "Elliptic flow for q mesons and (anti)deuterons in Au+Au collisions at $\sqrt{s}_{NN}$ = 200 GeV", Phys. Rev. Lett, **99**, 052301 (2007).

[229] B. B. Back et al., "Charged hadron transverse momentum distributions in Au + Au collisions at $\sqrt{s}_{NN}$= 200 GeV", Phys. Lett. B, **578**, (2004).

[230] J. Barrette et al., Phys. Rev. C, **55**, 1420 (1997).

[231] A. M. Poskanzer and S. A. Voloshin, Phys. Rev. C, **58**, 1671 (1998)

[232] C. Adler et al. (STAR Collaboration), Phys. Rev. C, **66**, 034904 (2002).

[233] J. Adams et al. (STAR Collaboration), Phys. Rev. C, **72**, 014904 (2005).

[234] J. Adams et al. Phys. Lett. B, **612** 181, (2005).

[235] N. Borghini, P. M. Dinh, J. Y. Ollitrault Phys. Rev. C, **64**, 054901 (2001).

[236] N. Borghini, P. M. Dinh, and J. Y. Ollitrault, Nucl. Phys. A, **715**, (2003).

[237] R. S. Bhalerao, N. Borghini, and J. Y. Ollitrault, Phys. Lett. B, **580**, 157 (2004).

[238] R. S. Bhalerao, N. Borghini, and J. Y. Ollitrault, Nucl. Phys. A, **727**, 373 (2003).

[239] N. Borghini, R. S. Bhalerao, and J. Y. Ollitrault, J. Phys. G, **30**, S1213 (2004).

[240] C. N. Yang and T. D. Lee, Phys. Rev. **87**, 404 (1952).

[241] P. Danielnicz and G. Odyniec, Phys. lett. B, **157** 146 (1985).

[242] P. Danielewicz et al., Phys. Rev. C, **38**,120 (1988).

[243] J.-Y. Ollitrault, Nucl. Phys. A, **590**,561c (1995).

[244] W. H. van Heeringen, PhD thesis, Utrecht University, 1996 and M. M. Aggarwal et al., Phys. Lett. B, **403**, 390 (1997).

[245] A. M. Poskanzer and S. A. Voloshin, Phys. Rev. C, **58**, 1671 (1998).

[246] J. Barrette et al., Phys. Rev. C, **56**, 3254 (1997).

[247] H. Masui and A. Schmah, arXiv: 1212.3650v1 [nucl-ex].

[248] N. Borghini and J. Y. Ollitrault, Phys. Rev. C, **70**, 064905, (2004).

[249] C. Lang et al., Eur. Phys. J. C, **74**, (2014).

[250] L. W. Chen et al., Phys. Rev. C, **73**, (2006).

[251] H. Heiselberg, Phys. Rep, **351**, (2001).

[252] H. Appelshauser et al., (NA49 Collaboration), Phys. Lett. B, **459**, 679 (1999). **727**, 97 (2003) and K. Adcox et al., (PHENIX Collaboration), Phys. Rev. Lett, **89**, 212301 (2002).

[253] S. S. Adler et al., (PHENIX Collaboration), Phys. Rev. Lett, **93**, 092301 (2004).

[254] J. Adams et al., (STAR Collaboration), Phys. Rev. C **71**, 064906 (2005).

[255] M. M. Aggarwal et al., (WA98 Collaboration), Phys. Rev.C, **65**, 054912 (2002).

[256] K. Adcox et al., (PHENIX Collaboration), Phys. Rev. C, **66**, 024901 (2002).

[257] S. A. Voloshin, V. Koch and H. G. Ritter, Phys. Rev. C, **60**, 024901 (1999).

[258] S. A. Bass, M. Gyulassy, H. Stocker and W. Greiner, J. Phys. G, **25** (1999).

[259] S. A. Bass, P. Danielewicz and S. Pratt, Phys. Rev. Lett,**85**, 2689 (2000).

[260] S. Jeon and V. Koch, Phys. Rev. Lett. **85**, 2076 (2000).

[261] M. Asakawa, U. Heinz and B. Muller, Phys. Rev. Lett,**85**, 2072 (2000).

[262] Z.W. Lin and C. M. Ko, Phys. Rev. C, **64**, 041901 (2001).

[263] M. Anderson et al., Nucl. Instr. Meth. A **499**, 659 (2003).

[264] B. I. Abelev et al., (STAR Collaboration), Phys. Rev. C, **79**, 034909 (2009) and D. Kharzeev and M. Nardi, Phys. Lett. B, **507**, 121 (2001).

[265] H. Masui and A. Schmah, arXiv: 1212.3650v1 [nucl-ex].

[266] H. Masui et. al., Phys. Lett. B **679**, 440(2009).

[267] J. Adams et al., (STAR Collaboration), Phys. Rev.C, **72**, 044902 (2005).

[268] J. Adams et al., (STAR Collaboration), J. Phys. G, **33**, 451 (2007); J. Phys. G, **32**, (2006).

[269] L. Adamczyk et al., Phys. Rew. C **87**, 064902 (2013).

[270] S. Gavin, Phys. Rev. Lett. **92**, 162301 (2004).

[271] Q. Liu and T. A. Trainor, Phys. Lett. B, **567**, 184 (2003).

[272] S. S. Adler et al., (PHENIX Collaboration), Phys. Rev. Lett, **93**, 092301 (2004).

[273] S. A. Voloshin, Phys. Lett. B, **632**, 490 (2006).